A Predictive Model for Waste Package Terminal Velocity in Deep Borehole Disposal

by

Adam F. N. Squires

Thesis

for the award of

DOCTOR OF PHILOSOPHY

The University Of Sheffield.

Supervised by Dr. Karl P. Travis

Department of Materials Science and Engineering

University of Sheffield

May 2019

Word Count: 46000

Acknowledgements

My gratitude is first and foremost given to Dr Karl Travis; Karl's keen enthusiasm and befitting knowledge over a vast range of computational mechanics has been invaluable throughout the previous 4 years, and I am indebted to Karl for his unwavering perseverance in regards to my academic development. These gratitudes are naturally extended to the DBD team at the University of Sheffield, headed by Prof Fergus Gibbs whose enthusiasm for DBD has been continuously inspiring - an enthusiasm closely rivalled by Dr Nick Collier, whose pro-active interest in all aspects of DBD were warmly welcomed in the laboratory. A huge appreciation must also be given to Dr David Burley for his mathematical expertise and generous contributions to the analytical sinking models using fluid mechanics.

I am also indebted to the contributions of Frank Fletcher, whose time and effort in regards to the development of experiment circuitry is highly appreciated. These thanks are extended to the welcoming staff of the Quarrell laboratory led by Dr Lisa Hollands, whose patience regarding flooded laboratories will not go forgotten.

Laboratory excursions aside, I am wholesomely appreciative of the day-to-day companionship provided by the residents of H7, both past and present, and the extended members of the MESAS modelling group - many of whom have time and again provided selfless acts of encouragement, support, and entertainment. None of these more so than Matthew – whose mantra of '*bug, fix, pub*' is unquestionable.

I am exceedingly fortunate to have two of the most well-rounded, supporting parents I could wish for. I would undoubtedly not be in this position if not for their commitment and sacrifices made to provide every possible opportunity to me throughout the years. Last but certainly not least my appreciation goes to my long-term partner Freya, whose enduring love and support is matched only by her tolerance to patiently cohabite amongst a shameful myriad of half-finished DIY projects during the completion of this thesis.

Table of Contents

Table of Figures

Summary

The aim of this work is to provide insight into the sinking rate of waste packages in Deep Borehole Disposal (DBD). An investigation was performed using simplified, scaled down experiments, analytical modelling and molecular modelling.

The experiments systematically varied a range of cylinder parameters to understand their influences upon the sinking rate of the cylinder. Results showed that this sinking velocity varied as a function of cylinder diameter, length and density, with diameter being the predominant factor in dictating the sinking rate.

An analytical model was subsequently developed using the experiment data as validation. The model was developed by solving the Navier-Stokes equations for the flow within the annular gap, in addition to characterising pressures applied at the front of the cylinder. Results showed good levels of accuracy for low values of clearance, although velocity was increasingly over predicted as clearance increased.

Molecular dynamics simulations were used as a method of gaining pseudo-experiment data and further insight into the fluid flow. Sinking disc simulations provided several correlating results with experiments; confirming that sinking velocity decreases linearly with diameter at sinker-container ratios greater than 0.6, and that density appears to increase sinking velocity towards a plateau. Stationary disc simulations illustrated that highly turbulent flow regimes occurred at the wake of objects in confined boundary systems. Several of these flow regimes occurred at significantly lesser streaming velocity for finite boundary systems as opposed to infinite boundary systems. This shows the importance of accounting for turbulence in finite boundary systems, and provides a logical path for the future development of a predictive sinking velocity model.

1: Introduction

The United Kingdom continues to produce both intermediate (ILW) and high-level waste forms (HLW), which include *both* spent fuel[1] and vitrified reprocessed waste. These waste inventories have been described in detail during recent reports produced by the United Kingdom Department for Business, Energy and Industrial Strategy alongside the Nuclear Decommissioning Authority [1]. The UK ILW stockpile is reported to be 99,000 m^3 (or 120,000 tonnes), with future projections predicting an increase to 290,000 m^3 (310,000 tonnes) by the year 2125. The contents of ILW can vary due to the nature of decommissioning, however a large portion of the waste (30,100 m^3) is currently immobilized within concrete and placed within a total of 60,407 stainless steel or concrete containers [2].

The UK has a further 1960 m^3 (3,700 tonnes) of HLW. Although a relatively lesser volume of waste in comparison to ILW, HLW contributes to over 95% of the total radioactivity in UK nuclear wastes [1]. Over half of the HLW has been processed to date, with the majority being vitrified into glass blocks and stored within steel containers. This process effectively reduces the final volume of waste by two thirds, and is one of the reasons behind future HLW projections predicting to decrease to 1,150 m^3 (3,000 tonnes) by 2125. However, the UK has an additional stockpile of 113,000 tonnes of Uranium and 103 tonnes of Plutonium not currently classified as nuclear waste [3]. This Plutonium inventory has been produced through spent fuel reprocessing with the original purpose of fuelling fast-breeder reactors, however, readily available Uranium has made this fuel cycle gratuitous. Although Uranium and Plutonium stockpiles could conceivably be used to create a mixed oxide fuel, there are no current reactors in the UK which could accept such a fuel. In addition, it is reasonable to believe that projected abundancies in available Uranium will result in much of these stockpiles adding to the HLW inventories in the coming years.

Such expansive inventories of nuclear waste are not limited to the UK; following the first civil nuclear power plant in 1954, the global number of operational power plants has grown to over 440 [4]. This highlights the growing urgency for a

[1] In the United Kingdom spent fuel was historically *not* classified as waste.

readily available disposal route for both ILW and HLW, although an operational solution still remains elusive despite over six decades of accumulated waste.

The disposal of both ILW and HLW waste forms has proven time and again to be problematic, thanks to both the intensity and lifetime of present radioactive elements. The current consensus for the long-term disposal of these waste forms is to deposit them within a mined engineered repository 200 – 1000 m underground [5]. However, Deep borehole disposal (DBD) is a potentially safer and more cost effective alternative to conventional mined repositories for HLW disposal [6], [7].

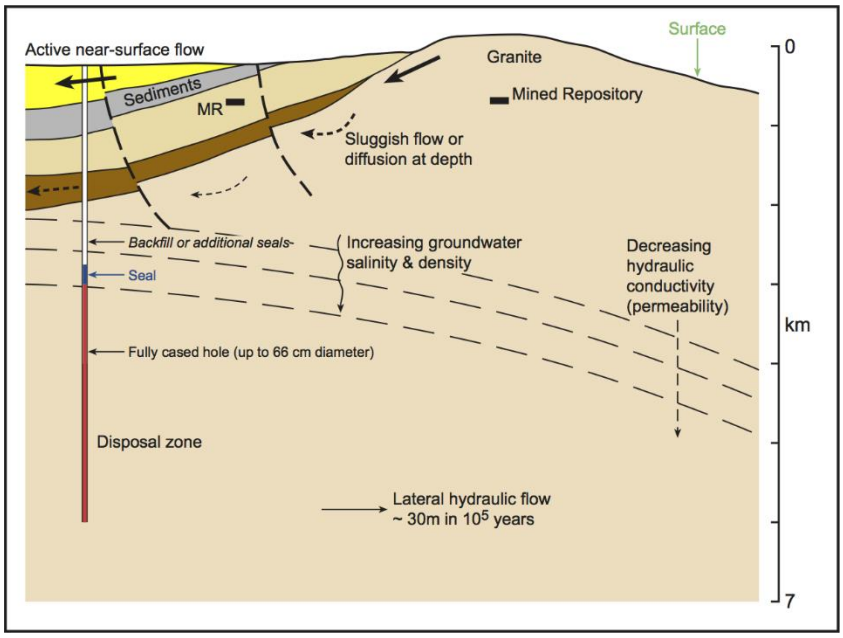

Figure 1.1: Diagram of the DBD concept, including the disposal zone and surrounding groundwater flow regimes. Image taken from external source [7].

In DBD waste forms are placed in deep (4 - 5 km), geological boreholes. Holes are drilled vertically into crystalline rock formations with a relatively large diameter in comparison to those traditionally used in the oil industry[1]. Throughout the drilling process the borehole is lined with a rigid steel casing, which is perforated over the depth range associated with waste emplacement (the disposal zone) [8]. Waste packages are subsequently deposited into the deepest 1 – 2 km region of the borehole, as illustrated in figure 1.1. Once waste packages are deployed, they are sealed in two stages. Firstly, a

[1] The largest proposed diameter for DBD is 0.85 m (Harrison, 2000).

suitable material is used to fill the annuli between waste packages, bore lining and host rock. This material is referred to as a sealing and support matrix (SSM), due to its secondary purpose of providing structural support to the heavy, stacked waste packages. There are several different variants of DBD developed by different research groups, particularly at the University of Sheffield. The disposal zone for the Sheffield concept is shown in figure 1.2, where two SSM methods are illustrated [9]. The second stage of waste package containment occurs above the disposal zone, separating and sealing the disposal zone from the upper borehole. This is to ensure any escaping wastes are unable to use the borehole as a means of circumventing the geologically imposed confinements and returning to the biosphere.

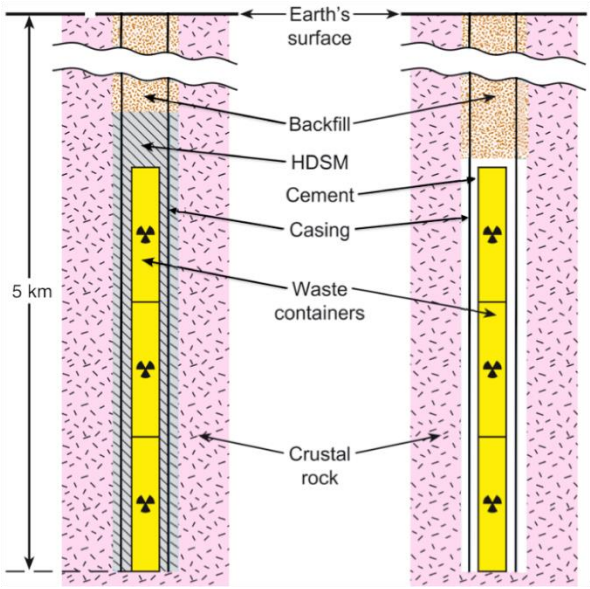

Figure 1.2: Schematic diagram of two of the Sheffield SSM concepts [10]. For waste packages of sufficient heat generation, a high-density lead based alloy is proposed (left image). A high-temperature cement is used as an alternative for lower heat-output waste packages (right image). Figure after external source [9].

The greater depth of disposal in DBD takes advantage of natural geological barriers. At such depths, low bulk hydraulic conductivity retards the movement of groundwater. Furthermore, salinity gradients provide additional retardation to vertical flow movement; this counters the convective flow induced by the heat output of waste forms [11]. These natural containment methods effectively eliminate the need for additional engineered barriers, but these are included in DBD as a precautionary, additional form of containment. As a result, there are greater containment requirements specifically

upon the engineered barriers used in mined repositories, giving rise to fewer compatible waste forms in comparison to DBD [6], [7].

In addition to a more robust safety case, DBD potentially provides a more economical solution as opposed to mined repositories. The main costs of DBD include an initial investment of a sufficient drilling rig (although this could potentially be reduced through rental) and the unpredictability of drilling due to both economic and machinery variables. However, drilling rig aside, conservative estimates predict a drilling cost of $40 million per borehole [12]. A quantitative comparison with the Swedish KBS-3 concept using spent nuclear fuel estimates DBD to be approximately 5 times cheaper per tonne of heavy metal [13]. Where DBD particularly comes into strength is in the nature of modularity; the freedom to create as many or as few boreholes required not only makes for a more versatile disposal solution, but makes DBD orders of magnitudes more economical for countries with small waste inventories.

Geologically the requirements of DBD are relatively relaxed, needing reasonably un-fractured granite below the depth of 2 km. This gives DBD a greater volume of potentially suitable geological locations than its competitors, which would aid in the location of a suitable disposal site (a proven issue for many countries, including the United Kingdom [14]). Furthermore, these relaxed geological requirements could potentially allow for DBD to be performed on-site at a reactor power station, removing transportation complications and expenses.

The DBD research group at the University of Sheffield have developed several DBD concepts, defining various geometries, borehole diameters and waste package parameters to accommodate different types of nuclear waste. These include (but are not limited to) concepts that accommodate complete pressurised water reactor (PWR) fuel assemblies, boiling water reactor assemblies, consolidated fuel rods and vitrified high level waste forms [6], [7]. These variants accommodate a range of waste package outer diameters between 0.24 and 0.45 m, and canister heights of 1.39 – 4.85 m. Other notable concepts include a similar USA complete PWR assembly concept, in which a single borehole could accommodate 400 PWR assemblies [15]. Of particular interest is the USA Cs-Sr assembly stockpile; it has been reported that these assemblies are at the highest risk of catastrophic failure [16], yet the entire stockpile could be disposed inside a singular borehole, without the need for reprocessing.

Despite a wealth of DBD concepts, there are certain limitations to viable waste forms. The most obvious limitation is waste geometry, with decommissioning wastes in particular being larger than currently obtainable boreholes. Fortunately, much of this waste is classified as low-level waste, much of which can be disposed of within designated near-surface disposal sites [17]. There are exceptions however, such as reactor core components which contain higher levels of radioactivity. Similarly, several complete spent fuel assemblies would not be suitable for DBD disposal, and although consolidating spent fuel rods could alleviate this issue, the increase in cost may make mined repositories a more economical solution. Despite these limitations, DBD should remain a consideration for countries requiring a mined repository; co-disposal can be advantageous for focused problem wastes such as the aforementioned Cs-Sr inventories, and potentially highly fissile materials such as Pu due to security. Furthermore, DBD provides an early disposal option during mined repository construction.

The DBD group at the University of Sheffield has been involved with a wide range of research. This includes the development of rock welding methodology [18], in which a finite section of the casing is removed and the hole is backfilled with crushed granite which is then melted along with part of the host rock. This essentially creates a containment layer continuous with that of the surrounding host-rock, removing the potential for any escaping waste to circumvent conventional seal designs through micro fractures located at the interface between host rock and seal [19]. The University of Sheffield also continues with the development of SSM concepts, including the lead-based alloy and high-temperature cements shown in figure 1.2. The latter in particular has presented recent advances with impermeable grouts with specific setting times to accommodate waste package deployment [20].

Several key components of the DBD method remain in contention and must be addressed before the disposal method is ready for implementation [21], [12]. The method of emplacing waste packages into the disposal zone (depths of 3 – 5 km) is one such area of contention. A simple approach is to use the wireline method, where waste packages are deployed using braided cable and are mechanically released. Despite its simplicity, the wireline method is restricted in payload weight and provides less control in comparison to alternatives [7]. Certain research groups are in favour of the drill pipe method, in which pipe segments are systematically deployed and attached to one another [12]. The drill pipe method has long been one of the more common and robust

methods of borehole deployment, however the connection rate of the 9 - 12 m pipe segments limits the deployment rate to a maximum of 1000 m h^{-1} [7]. The slow rate of deployment in addition to reliance upon mechanical release mechanisms has resulted in justifiable opposition to the drill pipe method [21]. A promising alternative is to use coiled tubing, which would be slightly slower than wireline but substantially faster than drill pipe methods. Coiled tubing provides a high level of control and would conveniently allow for electrical conductors to be shielded within the hollow tube, allowing for automated canister release and the use of various electrical sensors [7]. Freefall has been considered as a deployment method [22], but is unlikely to be given serious consideration due to a lack of control and unnecessary risk.

Irrespective of the deployment method, the free fall velocity of a sinking waste package does remain an important component of the DBD safety case, as it is critical in regard to the scenario of a deployment system failure where a package is dropped. Furthermore, understanding the rate of free fall deployment will give the upper limit to the deployment rate of *any* of the aforementioned methods, as none of these methods force waste packages to sink faster than their free fall sinking rate. It is still important to be mindful of the different deployment methods when considering freefall, as their concurrent deployment capabilities also determine the freefalling deployment objects parameters (length and mass).

There have been several rough-estimates of the free-fall deployment rate for waste packages. A study from the Camborne School of Mines noted that for a sinker-to-bore diameter ratio (κ) of 0.82, a concrete plug took approximately 15 minutes to descend to the bottom of a 2225 m deep borehole [23]. This gives a sinking velocity of approximately 2.5 ms^{-1}. Similarly, a preliminary estimate from Sandia National Laboratories [11] predicted that waste packages with $\kappa = 0.85$ would be expected to sink at approximately 0.5 – 1.5 ms^{-1}. The discrepancy of up to 500 % for these preliminary investigations illustrates high sensitivity of sinking rate to the various system variables. This signifies that a more detailed study is necessary to accurately predict the sinking rate for a broad range of waste packages and boreholes.

At a high-level, the aim of this project is to guide improvements to the estimates of waste package sinking rates in boreholes, by providing insight into the phenomena and associated physics that govern theses sinking rates. Several methods are used to fulfil these aims:

1) Analytical fluid dynamics.
2) Computational fluid dynamics.
3) Laboratory experiments.

Analytical fluid dynamics can theoretically be used to describe the flow properties throughout a given system by applying the Navier-Stokes equations. The frictional forces applied to a sinking object may then be determined once the fluid properties are known, which in turn can be used to give the sinking rate of an object. The Navier-Stokes equations are therefore presented in chapter 2 followed by examples of their application to objects sinking through a fluid. These methods are later used to construct a tractable analytical model that attempts to define the correct functional dependencies of a cylinder sinking through a column of fluid, which is presented in chapter 4.

Chapter 2 also describes the methods of Molecular Dynamics, a computational method which can be used to simulate fluid at a particle level and avoids the complex application of the Navier-Stokes equations. This allows for the construction of simulations including a disc sinking through a fluid and a fixed disc within a streaming fluid, as presented in chapter 6. The former is used to obtain pseudo-experiment data which would be difficult to obtain in a laboratory, whilst the later provides a convenient frame of reference that allows for a detailed analysis of flow regimes and fluid properties. This information provides a deeper understanding of fluid flow past objects in confined boundary systems, and gives guiding insight into future iterations of sinking velocity prediction models.

It is paramount to obtain an extensive collection of experiment data in order to validate any analytical and computational results given in chapters 4 and 6. In chapter 3 the terminal velocity of cylinders sinking through fluid are therefore determined experimentally in a highly controlled laboratory setting, where parameters are systematically varied to quantify their effects upon terminal velocity.

It is also important to obtain the relevant transport coefficients of the Molecular Dynamics force potential used during simulations in chapter 6. These are required in the calculation of dimensionless numbers that describe the flow, which theoretically allow for comparisons with experiments performed in different length scales. This data is provided in chapter 5 using non-equilibrium Molecular Dynamics simulations.

Finally, the key results throughout the project are discussed in chapter 7 in addition to recommendations for future work.

2: Background Literature

2.1 Introduction

To better understand how the sinking rate of a waste package in DBD is determined, an analytical model is presented in chapter 4 that predicts the sinking rate of a cylinder through a column of fluid. This aims to provide a tractable solution which defines the key functional dependencies of the simplified cylindrical object and column of fluid.

To determine the sinking rate of a cylinder analytically, the friction applied to the cylinder is first required. An accurate description of the fluid surrounding a sinking cylinder is necessary to determine this friction applied to the cylinder from the fluid. It is shown in this chapter how the Navier-Stokes equations for an incompressible fluid are derived. When supplied with appropriate boundary conditions, these equations are capable of describing the velocity, pressure, temperature and density of a given fluid.

Following the derivation of the Navier-Stokes equations, several examples of their application to sinking objects are given. Foremost is the application of Stokes Law, which describes the sinking of a sphere through an infinite boundary fluid. This illustrates how the Navier-Stokes equations may be used to obtain the sinking rate of an object sinking through a fluid. Other methods are then presented which expand upon the many limitations of Stokes Law, such as accounting for advective flows, finite boundaries and alternate sinker geometries.

The fluid dynamics section of this chapter is concluded with a simple dimensional analysis of an object sinking through fluid. This determines whether any preliminary dependencies upon system variables (such as sinker density and length scales) can be obtained, prior to performing a complete numerical study of fluid flow.

It is later shown that the analytical model presented in chapter 4 has several shortcomings, the origins of which must be identified before the iteration of future models. Computational methods are favourable for this cause, as they not only allow for pseudo-experiments to be performed which would be difficult in a laboratory, but also allow for detailed measurements of fluid properties to be obtained with relative ease. Several popular methods of computational fluid dynamics are therefore discussed in the latter part of this chapter, along with their applications in relevant studies to assess their applicability. Finally, the theory necessary to perform simulations using the Molecular

Dynamics method is presented. This allows for the application of these methods in both the sinking disc and fixed disc simulations described in chapter 6.

2.2 Fluid Dynamics

At a fundamental level, matter consists of particles. Modelling can be used to simulate each and every particle, however, even with the incorporation of state of the art supercomputers, the magnitude of necessary calculations limits such treatments to the microscale [24]. It is therefore important to simplify the engineering problem at hand, whilst maintaining the desired level of accuracy.

Fortunately, at length scales appropriate to engineering, a continuum description is found to be adequate. Continuum mechanics uses assumed constitutive relations in conjunction with the laws of continuity to describe the state of a continuum using partial differential equations [25].

The principles behind the equations of continuity can be traced back to the concepts of Da Vinchi, which were notably followed by Castelli in the 17th century [26]. Throughout the 18th century the fundamental methods of hydrodynamics were established through contributions by both Euler and Bernoulli, forming the continuity laws in the form of partial differential equations [27], [28]. The continuity equations of fluid mechanics include the equations of mass, momentum and energy conservation, given as follows respectively:

$$\frac{d\rho}{dt} = -\rho(\boldsymbol{\nabla} \cdot \boldsymbol{v}) \tag{2.1}$$

$$\rho \frac{d\boldsymbol{v}}{dt} = -\boldsymbol{\nabla} \cdot \boldsymbol{P} \tag{2.2}$$

$$\rho \frac{\partial e}{\partial t} = -\boldsymbol{\nabla} \cdot \left[\boldsymbol{J}_Q - \boldsymbol{P}\boldsymbol{v}\right] \tag{2.3}$$

where ρ is fluid density, $\boldsymbol{v}$ the fluid velocity vector, t time, $\boldsymbol{P}$ the pressure tensor, e is the energy per unit mass and $\boldsymbol{J}_Q$ the vector of heat flux. A detailed derivation of these equations is given in appendix A.

The constitutive relations describe the relationships between the fluxes and forces within a fluid using empirically determined coefficients. One of the most significant constitutive equations is the law of viscosity, which describes the internal resistance of fluids and originates from Newton [29] in the 17th century, before being presented mathematically by Cauchy later in the 19th century [30]. Other important constitutive equations include Fourier's law of heat conductivity, which relates the rate of heat flow to temperature differences [31] and Fick's law of diffusion [32]. These constitutive relations are given in greater detail in appendix B.

In the following section it is shown how the continuity and constitutive equations are used to derive the Navier-Stokes equations. It is assumed that the fluid is homogeneous and inert throughout.

2.2.1 Linear Irreversible Thermodynamics

When deriving the source strength of entropy σ (see appendix A.4), it is clear that the contributing fluxes are of different tensoral character, and are therefore uncoupled [33]. Entropy may therefore be given as:

$$\psi = \sum_i J_i X_i \tag{2.4}$$

where ψ is the entropy source strength, J_i is a thermodynamic flux and X_i is a conjugate thermodynamic force. A postulate of Linear Irreversible Thermodynamics is Curies principle, which states that all forces are linearly related to fluxes:

$$\boldsymbol{J}_i = \sum_j L_{ij} X_j \tag{2.5}$$

where L_{ij} are the phenomenological transport coefficients. Substituting equation 2.5 into equation 2.4 gives:

$$\psi = \sum_i \sum_j \boldsymbol{X}_i \boldsymbol{L}_{ij} \boldsymbol{X}_j \tag{2.6}$$

The energy source strength may only be positive; it is therefore clear from equation 2.6 that the transport coefficients must also be positive.

Curies principle determines that for an isotropic fluid, the symmetry applied unto the second rank tensor $\boldsymbol{X}_j$ can be decoupled to separate linear equations. These linear equations represent the symmetric, antisymmetric and trace contributions of force and fluxes. Assuming the fluid is homogenous (diffusivity is unnecessary) and the stress tensor is *not* antisymmetric, the decoupled linear equations are:

$$\boldsymbol{J}_Q = L_Q \boldsymbol{X}_Q = -L_Q \frac{\nabla T}{T^2} \tag{2.7a}$$

$$\boldsymbol{\Pi}^{os} = L_{\Pi}^{os} X_{\Pi}^{os} = -L_{\Pi} \frac{\boldsymbol{\nabla v}^{os}}{T} \tag{2.7b}$$

$$\Pi = L_{\Pi} X_{\Pi} = -L_{\Pi} \frac{3\boldsymbol{\nabla \cdot v}}{T} \tag{2.7c}$$

where Π and $\boldsymbol{\Pi}^{os}$ are the trace and the traceless symmetric components of the non-equilibrium pressure tensor $\boldsymbol{\Pi}$, and T is temperature. The linear relationships of 2.7 were determined phenomenologically prior to Curies principle. The phenomenological forms are:

$$\boldsymbol{J}_Q = -k\nabla T \tag{2.8a}$$

$$\boldsymbol{\Pi}^{os} = -2\mu \boldsymbol{\nabla v}^{os} \tag{2.8b}$$

$$\Pi = -\mu_v \boldsymbol{\nabla \cdot v} \tag{2.8c}$$

2.8a is Fourier's law as shown in appendix B.2, with k the thermal conductivity. 2.8b is the vector form of Newton's law of viscosity as shown in section B.2, where μ is the fluid viscosity. The linear constant μ_v is the bulk viscosity, which is an additional viscosity independent of Newton's Law. This describes the fluctuations in entropy as a result of flow compressibility [34].

2.2.1.1 Navier-Stokes Equations

In this section it is shown how the combination of the continuity and constitutive equations yield the Navier-Stokes equations. These Navier-Stokes equations may be

considered complete, in the sense that with the appropriate initial and boundary conditions, they may be solved to yield the continuum flow properties within a system.

Although not strictly one of the Navier-Stokes equations, the previously given mass continuity equation (equation 2.1) is often referred to as such, and is necessary when describing a continuum fluid.

The left hand side of the momentum continuity equation (equation 2.2) may be expressed in terms of the partial derivatives, giving:

$$\rho \frac{d\boldsymbol{v}}{dt} = \rho \left[\frac{\partial \boldsymbol{v}}{\partial t} + \boldsymbol{v} \cdot \boldsymbol{\nabla} \boldsymbol{v} \right] \tag{2.9}$$

Inserting equation 2.9 back into 2.2 gives:

$$\rho \left[\frac{\partial \boldsymbol{v}}{\partial t} + \boldsymbol{v} \cdot \boldsymbol{\nabla} \boldsymbol{v} \right] = -\boldsymbol{\nabla} \cdot \boldsymbol{P} \tag{2.10}$$

The pressure tensor can be decomposed in terms of the hydrostatic pressure p and the non-equilibrium pressure tensor, $\boldsymbol{\Pi}$ such that

$$\boldsymbol{P} = p\boldsymbol{I} + \boldsymbol{\Pi} \tag{2.11}$$

As the non-equilibrium pressure tensor is also a second-rank tensor, it too may be decomposed, therefore:

$$\boldsymbol{\Pi} = \Pi \boldsymbol{I} + \boldsymbol{\Pi}^{os} \tag{2.12}$$

Simply substituting equation 2.12 into 2.11 gives the fully decomposed pressure tensor:

$$\boldsymbol{P} = (p + \Pi)\boldsymbol{I} + \boldsymbol{\Pi}^{os} \tag{2.13}$$

Equation 2.13 can now be inserted into 2.10, giving:

$$\rho \left[\frac{\partial \boldsymbol{v}}{\partial t} + \boldsymbol{v} \cdot \boldsymbol{\nabla} \boldsymbol{v} \right] = -\boldsymbol{\nabla} \cdot [(p + \boldsymbol{\Pi})I + \boldsymbol{\Pi}^{os}] \tag{2.14}$$

The constitutive relationships of Newton's law of viscosity and the bulk viscosity relationship (equations 2.8b and 2.8c) are inserted into equation 2.14.

$$\rho\left[\frac{\partial \boldsymbol{v}}{\partial t} + \boldsymbol{v}\cdot\nabla\boldsymbol{v}\right] = -\nabla\cdot p\boldsymbol{I} + \nabla\cdot(\mu_v\nabla\cdot\boldsymbol{v})\boldsymbol{I} + \nabla\cdot 2\mu\boldsymbol{\nabla v}^{os} \tag{2.15}$$

Finally, equation 2.15 can be simplified to give the Navier-Stokes momentum equation,

$$\rho\left[\frac{\partial \boldsymbol{v}}{\partial t} + \boldsymbol{v}\cdot\boldsymbol{\nabla v}\right] = -\nabla p + \mu_v\boldsymbol{\nabla}^2\boldsymbol{v} + \left(\frac{\mu}{3}+\mu\right)\nabla(\boldsymbol{\nabla}\cdot\boldsymbol{v}) \tag{2.16}$$

The final Navier-Stokes equation is the equation of energy. Analogous to the momentum Navier-Stokes equation derivation, the decomposed pressure tensor, equation 2.13 is inserted into the energy continuity equation, equation 2.3. The viscosity constitutive equations, 2.8b and 2.8c may then be inserted with Fourier's law of heat conductivity, equation 2.8a, giving:

$$\rho\frac{\partial u}{\partial t} = \nabla[k\nabla T] - [\mu_v\boldsymbol{\nabla}(\boldsymbol{\nabla}\cdot\boldsymbol{v}) + 2\mu\boldsymbol{\nabla}\cdot(\boldsymbol{\nabla v}^{os})]:\boldsymbol{\nabla v} \tag{2.17}$$

where *u* is the internal energy. The velocity vector of equation 2.17 is expanded and rearranged to give the final form of the Navier-Stokes energy equation in vector Cartesian co-ordinates,

$$\rho\frac{\partial u}{\partial t} = k\nabla^2 T = p(\boldsymbol{\nabla}\cdot\boldsymbol{v}) + \mu_v(\boldsymbol{\nabla}\cdot\boldsymbol{v})^2 + 2\mu\boldsymbol{\nabla v}^{os}:\boldsymbol{v}^{os} \tag{2.18}$$

The polar co-ordinate and cylindrical polar co-ordinate forms of the Navier-Stokes equations are stated in Appendix C.

2.2.2 Objects Sinking Through Fluids

The Navier-Stokes equations derived in section 2.2.1.1 give a mathematical description of a moving fluid's continuum properties, which can theoretically be used to determine the frictional forces applied to an object sinking through a fluid. In reality, the complexity of the Navier-Stokes equations makes their application problematic, and

assumptions and simplifications are often required to reach a numerical solution in all but the simplest of use cases[1].

Although not the first of its kind, Lamb provides several examples of applying the Navier Stokes equations to objects moving through fluids. These applications are instructive to discuss thanks to their simplicity, beginning from a simplified dimensional frame of reference.

Lamb applied the Navier-Stokes equations to a moving object within a fluid to determine flow distributions and external pressures [35]. Lamb investigated a cylinder travelling perpendicularly to its *infinite* length; this effectively reduced the scenario to 2 dimensional co-ordinates. The 2 dimensional disc traverses a continuous plane of fluid, which is at rest at an infinite distance from the disc.

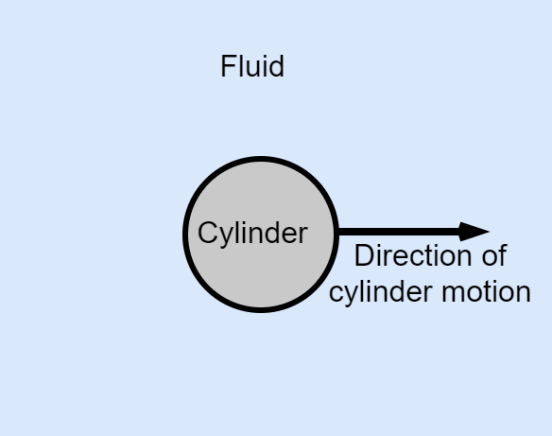

Figure 2.1: An infinite cylinder passing through a continuous medium of fluid, in a direction perpendicular to its longitudinal axis.

Lamb used the continuity arguments of the Navier-Stokes equations to derive what was referred to as a 'velocity potential'. This potential can be used to give the *x* and *y* components of the fluid velocity by differentiation with respect to the relevant axis. The derived velocity potential is equal to $\frac{Ua^2}{r} cos\theta$, where a is the radius of the cylinder, r and θ are the radial distance and relative angle to the origin and U is the cylinder velocity. Lamb showed how differentiating the fluid velocity over the cylinder boundary can give the pressure applied to the cylinder as a function of cylinder velocity,

[1] Notable examples of complete solutions to the Navier-Stokes equations include poiseuille and Couette flow, both of which are shown, amongst others, by Berker [159].

which could theoretically be used to derive the object velocity as a function of its' driving force (such as gravity).

Lamb continued to apply the Navier-Stokes equations in pseudo 2-dimensions, including the flow of an infinite elliptical cylinder and a cylinder traversing in a spiralling motion. Nevertheless, the incorporation of a finite boundary in 2-dimensions is notably omitted, despite the simplified reference frame - an early suggestion of the intricacies involved in the application of the Navier-Stokes equations to finite boundary systems.

2.2.2.1 Stokes Law and Spherical Sinking Objects

One of the most popular applications of the Navier-Stokes equations is Stokes law, which gives the relationship between the speed of a spherical object and its radius as it moves through a viscous medium [36]. Despite Stokes law only applying to 'creeping' flow regimes, it is instructive to derive Stokes law in order to understand the assumptions used to achieve a numerical solution, and to illustrate how the Navier-Stokes equations can be used to obtain the sinking velocity of a free-fall object. This provides a basis for constructing a numerical solution which predicts the sinking rate of a cylinder within a finite tube, as presented in chapter 4.

Because of the equivalence of inertial frames, the movement of an object through a stationary fluid is mathematically equivalent to the flow of a fluid past a stationary object. This latter viewpoint is simpler to treat and therefore we begin by considering this case.

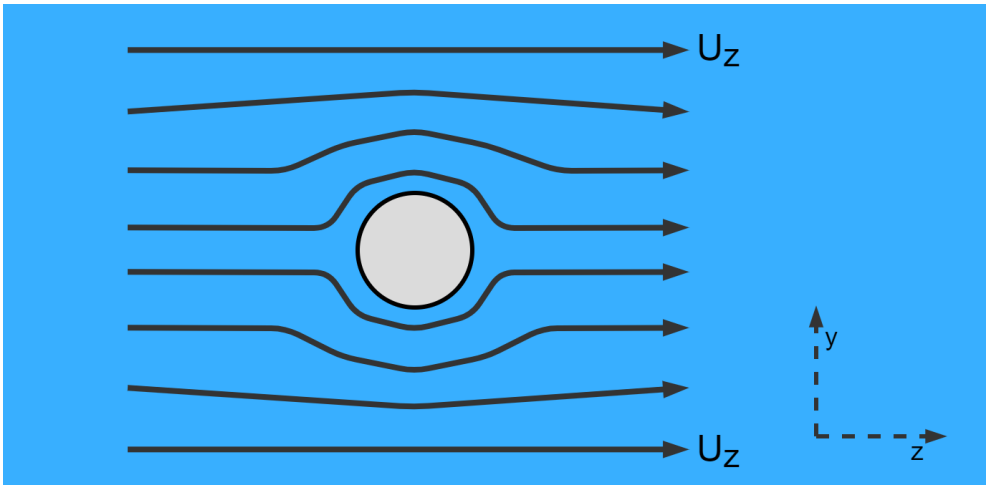

Figure 2.2: Flow paths of a fluid with an initial, unperturbed terminal velocity U_z past a stationary sphere. As the radial distance from the sphere trends towards infinity, the fluid velocity is again U_z.

For a fluid in steady state, the $\rho\left({}^{\partial \boldsymbol{v}}/_{\partial t}\right)$ component of the Navier-Stokes momentum equation vanishes. For such a fluid in a gravitational field, the Navier-Stokes equation becomes

$$\rho \boldsymbol{v}(\boldsymbol{v} \cdot \boldsymbol{\nabla}) = -\nabla p + \mu \nabla^2 \boldsymbol{v} - \boldsymbol{g}\rho \tag{2.18}$$

Under the assumption of creeping flow, the advective term in equation 2.18 (the left hand side) is negligible in comparison to viscous forces. Equation 2.18 may therefore be approximated, such that

$$\nabla p = \mu \nabla^2 \boldsymbol{v} - \boldsymbol{g}\rho \tag{2.19}$$

Which, in addition to the incompressibility condition:

$$\boldsymbol{\nabla} \cdot \boldsymbol{v} = 0 \tag{2.20}$$

completes the field equations. The divergence of equation 2.19 gives Laplace's equation for pressure,

$$\nabla^2 p = 0 \tag{2.21}$$

Pressure can be redefined to incorporate hydrostatic contributions, such that

$$P' = p - \rho g h \tag{2.22}$$

Where P' is the redefined pressure. This redefinition simplifies the following derivations, whilst still satisfying Laplace's equation. Assuming boundaries are non-slip, fluid velocity would be identical to that of the spherical object at the interface yet uninterrupted at large distances from the object, therefore

$$p = 0 \text{ as } z \to \infty \tag{2.23}$$

$$\boldsymbol{v} = U_z \text{ as } z \to \infty \tag{2.24}$$

$$\boldsymbol{v} = 0 \text{ as } z \to r \tag{2.25}$$

Where U_z is the un-perturbed far-field flow velocity, *z* is the distance from the origin (centred within the spherical object) and *r* the object radius. By obtaining a solution for *p*, equation 2.19 may be used to derive the velocity distribution.

To apply Laplace's equation to the fluid volume, it is convenient to change from Cartesian coordinates to spherical polar.

$$x = r sin\theta cos\phi \tag{2.26a}$$

$$y = r sin\theta sin\phi \tag{2.26b}$$

$$z = r cos\theta \tag{2.26c}$$

The value of angle ϕ cannot change the distance of a point in space from the sphere. Pressure dissipates uniformly from the sphere, therefore pressure cannot be dependent on ϕ. As a result, the component of the polar-coordinate Laplace's equation describing pressure as a function of ϕ can be ignored, giving

$$\frac{\partial^2 p}{\partial r^2} + \frac{2}{r}\frac{\partial p}{\partial r} + \frac{1}{r^2}\frac{\partial^2 p}{\partial \theta^2} + \frac{cos\theta}{r^2 sin\theta}\frac{\partial p}{\partial \theta} = 0 \tag{2.27}$$

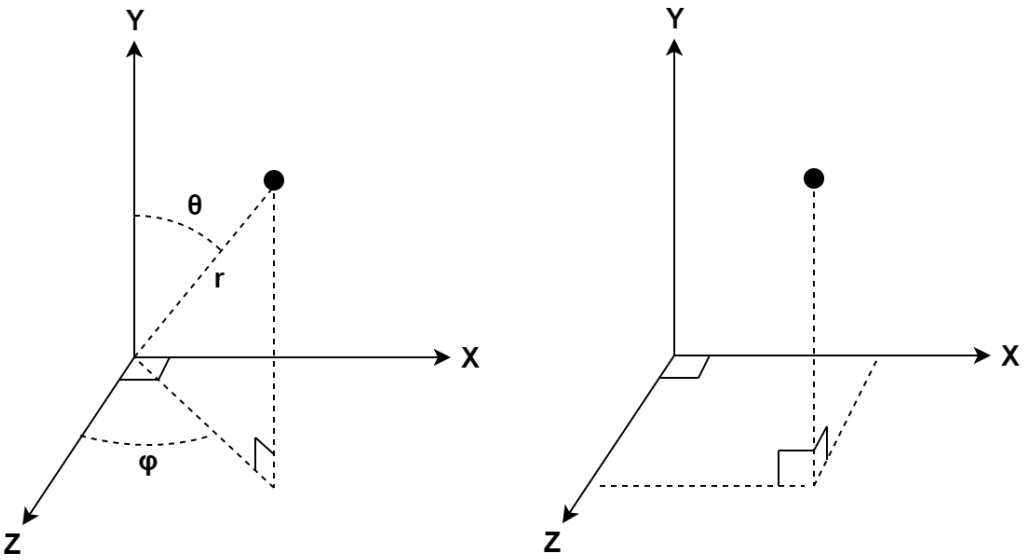

Figure 2.3: A point in identical position within a three dimensional space as described by spherical co-ordinates (left) and Cartesian co-ordinates (right). Co-ordinate systems are interchangeable using the relationships in equations 2.26.

Making the substitution to the form of $p = R(r)\Phi(\theta)$ gives

$$r^2 \frac{d^2R}{dr^2} + 2r\frac{dR}{dr} - \beta R = 0 \tag{2.28}$$

$$\frac{d^2\Phi}{dt^2} + \frac{cos\Phi}{sin\theta} - \beta\Phi = 0 \tag{2.29}$$

Where β is the separation constant between equations 2.28 and 2.29, the solutions in terms of each arbitrary function *R* and Φ. Equation 2.28 is the Cauchy-Euler equation, whilst equation 2.30 is a form of Legendre's equation. The partial derivatives from equation 2.27 have effectively been transformed into ordinary differential equations. The solutions of Legendre's equation and the Cauchy-Euler equation are well known [37], and therefore the pressure can be written as

$$p = \sum_{i=0}^{\infty} \left(A_i r^p + B_i r^{-(p+1)}\right) p_i(cos\theta) \tag{2.30}$$

where A_i and B_i are arbitrary constants, and $p_i(cos\theta)$ are Legendre polynomials. The A_i component of equation 2.30 must vanish whenever *i* is greater than zero, otherwise *p* would be infinity as *r* reaches infinity. Equation 2.30 therefore expands to

$$p = \left(A_0 + \frac{B_0}{r}\right) + \left(\frac{B_1}{r^2} cos\theta\right) + \left(\frac{B_2}{r^3}\frac{1}{2}(3cos^2\theta - 1)\right) \tag{2.31}$$

The velocity can be expressed in spherical co-ordinates, such that

$$\boldsymbol{v} = Ucos\theta d\boldsymbol{r} + Usin\theta d\boldsymbol{\theta} \tag{2.32}$$

To be compatible with the boundary condition in equation 2.32, *p* must take the form

$$p = \frac{B_1}{r^2} cos\theta \tag{2.33}$$

Equation 2.33 can then be used with the Navier-Stokes momentum equation (2.16) to show that

$$p = -\frac{3}{2}\frac{\mu a U}{r^2} cos\theta \tag{2.34}$$

$$v_r = \left(1 - \frac{3}{2}\frac{a}{r} + \frac{1}{2}\frac{a^3}{r^3}\right) Ucos\theta \tag{2.35}$$

$$v_\theta = -\left(1 - \frac{3}{4}\frac{a}{r} - \frac{1}{4}\frac{a^3}{r^3}\right) Usin\theta \tag{2.36}$$

With the velocity field determined, the stress elements can be calculated. For cylindrical polar co-ordinates, these take the form [38]

$$\eta_{\mathrm{rr}} = \mu\left[2\frac{\partial \mathrm{v_r}}{\partial \mathrm{r}}\right] - \mathrm{p} \tag{2.37}$$

$$\eta_{r\theta} = \mu\left[r\frac{\partial}{\partial r}\left(\frac{v_\theta}{r}\right) + \frac{1}{r}\frac{\partial v_r}{\partial \theta}\right] \tag{2.38}$$

Inserting equations 2.34, 2.35 and 2.36 into equations 2.37 and 2.38 yields

$$\eta_{rr} = \frac{3a}{2r^2}\left[3 - \frac{2a^2}{r^2}\right]\mu U cos\theta \tag{2.39}$$

$$\eta_{r\theta} = -\frac{3}{2}\frac{a^3}{r^4}\mu U sin\theta \tag{2.40}$$

At the sphere-fluid boundary, equations 2.39 and 2.40 become

$$\eta_{rr|r=a} = \frac{3}{2a}\mu U cos\theta \tag{2.41}$$

$$\eta_{r\theta|r=a} = -\frac{3}{2a}\mu U sin\theta \tag{2.42}$$

To get the total stress vector in the *r* direction equations 2.41 and 2.42 are summed to give

$$\boldsymbol{\eta}_{r|r=a} = \frac{3}{2a}\mu \boldsymbol{U}[d\boldsymbol{r}cos\theta - d\boldsymbol{\theta}sin\theta] \tag{2.43}$$

Far-field velocity *U* can be expressed as a vector, encompassing the respective *r* and θ components of equation 2.43 using:

$$\eta_{r|r=a} = \frac{3}{2a}\mu \boldsymbol{U} \tag{2.44}$$

The magnitude of the total drag force F_D applied to the surface is obtained by multiplying equation 2.44 by the surface area of a sphere ($4\pi a^2$).

$$F_D = 6\pi\mu a U \tag{2.45}$$

The roles of the fluid and spherical object may now be reversed, such that the fluid is stationary and the spherical object is sinking under the effects of gravity.

The sinking ball will lose energy due to friction and eventually move at a constant velocity, at which point the forces must be in balance, due to Newton's law of inertia. The forces acting upon the sphere can be described by a force balance equation, such that

$$F_G = F_B + F_D \tag{2.46}$$

where F_G is the gravitational force, F_B the buoyancy force and F_D the drag force. Equation 2.45 can be inserted into equation 2.46 as the drag force. Buoyancy and gravitational forces are expressed as the product of sinker volume and respective densities, yielding:

$$U = \frac{2}{9}\frac{(\rho_s - \rho_f)}{\mu} g a^3 \tag{2.47}$$

which is the terminal velocity of a sphere sinking through fluid under creeping flow conditions. In theory, the methods used to derive this drag force (and subsequent terminal velocity) may be applied to any geometry, however these are analytically unsolvable for all but a limited number of cases. The 2-dimensional disc submerged in a fluid is one such case; the same methodology used in the 3-dimensional example can gives the pressure around the disc as:

$$p \propto \frac{\boldsymbol{q}}{r^2} \tag{2.48}$$

where $\boldsymbol{q}$ is the Cartesian position vector [39]. In polar co-ordinates, this gives a radial pressure dependency of:

$$p \propto \frac{1}{r} \tag{2.49}$$

These relations will be used in the analysis of 2-dimensional computational modelling.

It is instructive to compare the applicability of the spherical Stokes law to preliminary measurements of cylinders sinking through a borehole, despite their obvious differences. This helps to ascertain whether there is a need for incorporating additional complexities (such as finite boundaries or more complex object geometries) to a numerical solution, or if the basic solution of Stokes law is already reasonably accurate. A hypothetical sphere is formulated with the same volume and density as a waste package. For the DBD reference package[1] the diameter of the sphere would be 0.98 m. Stokes law predicts the terminal velocity of this sphere to be 6 orders of magnitude greater than the preliminary estimates given in section 1. This illustrates that Stokes law is an insufficient method for determining the sinking velocity of cylinders within a tube, and that one, if not all, of the simplifications made to the Navier-Stokes

[1] The DBD 'reference package' refers to the Sheffield 2018 standard; this is a consolidated fuel rod concept sharing the canister geometry of the Sheffield PWR complete assembly concept [7]. The key parameters of this package are an outer diameter of 0.36 m, height of 4.81 m and a mean density of 6749 kg m^{-3}.

equations, object geometry or boundary omission must be improved upon for an accurate solution.

One of the limitations of Stokes Law arises from the assumptions made regarding the simplification of the Navier-Stokes equation. The assumption that the advective term of the Navier-Stokes equation can be negligible is true when the Reynolds number (*Re*) of the fluid is less than 0.1 [40]. The Reynolds Number is a dimensionless number that characterizes the magnitude of turbulence in a given system [41]. The dimensionless nature of *Re* makes it a useful method to reduce the number of variables that describe a given system, simplifying comparisons between different systems. The *Re* can be used to identify which hydrodynamic methods are applicable to a given system, and is defined by

$$Re = \frac{U d_h \rho}{\mu} \tag{2.50}$$

where d_h is the hydraulic diameter. For an incompressible fluid (therefore of constant density) it is clear from equation 2.50 that for a low Reynolds number both the velocity and diameter of the sinking object are required to be relatively low. The aforementioned example of the sinking reference waste package would have a *Re* of 3×10^{12}, many orders of magnitude over the accurate range of Stokes law.

Several methods have been developed to extend the Reynolds number range of the Stokes flow solution. These extended methods are not derived from the underlying physics, but instead rely upon empirical data to transform the Stokes equation to that of large Reynolds number systems. A common such expression takes the form:

$$U = \sqrt{\frac{8}{3}\left(\frac{\rho_s}{\rho_f} - 1\right)\frac{ag}{C_D}} \tag{2.51}$$

where C_D is the dimensionless drag coefficient [40]:

$$C_D = \frac{24}{Re} + \frac{5}{\sqrt{Re}} + 0.3 \tag{2.52}$$

The right hand side of equation 2.52 contains 3 terms. The first represents Stokes law, the second represents a thin laminar boundary layer and the third represents a constant

terminal form drag. This solution is accurate up to $Re \approx 10^4$. Because equation 2.52 makes *U* a function of *Re*, which is already a function of *U* as shown by equation 2.50, the solution cannot be solved analytically and instead becomes implicit. The empirical nature of this solution means that the drag coefficient is now disassociated with the theory of hydrodynamics, and the incorporation of any additional physics becomes difficult. Furthermore, the iterative nature of the solution not only makes the seeking of solutions more complex (and often ambiguous), but also complicates the tractability of sinking velocity dependence on system variables.

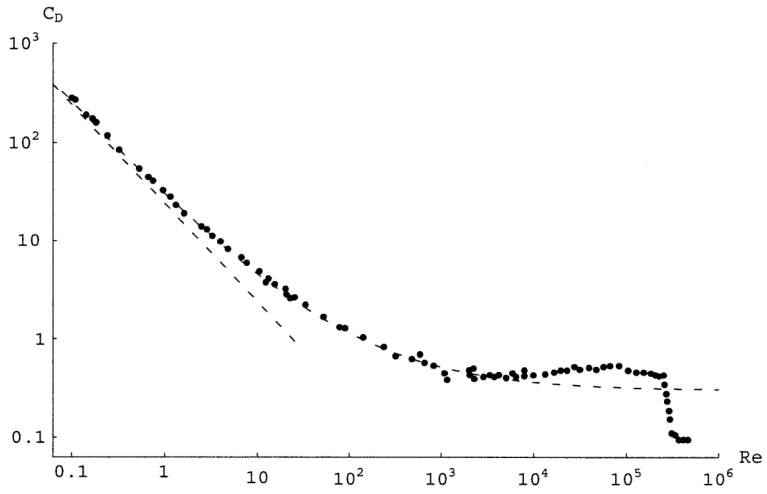

Figure 2.4: Drag coefficient as a function of *Re*. The straight dashed line represents Stokes Law. The dots represent experimental data and the curved dashed line represents the frictional drag given by the interpolated function (equation 2.52). This figure is taken from an external source [40].

Another omission of Stokes law is boundary effects, as the surrounding medium is assumed infinite at all times. Studies into this so called 'wall effect' on sinking rates date back to Newton in 1687 [29]. It has been consistently proven that terminal velocity is reduced at an increasing rate as wall effects become significant, arguably for diameter ratios of 0.15 and above [42].

In an analogous fashion to his works in 2-dimensions described earlier in this section, Lamb applied the Navier-Stokes equations to a travelling sphere within a concentric, finite boundary. The final velocity potential is $\propto (\frac{a^3 r}{R^3 - a^3} + \frac{a^3 R^3}{2r^2(R^3 - a^3)}) cos\theta$, where *R* is the radius of the container. In comparison, an analogous application of the Navier-Stokes equations in an infinite boundary system yields a velocity potential of

$\frac{Ua^3}{r^2}cos\theta$. Lamb made similar assumptions of non-advective flow as described in the derivation of Stokes law, yet the final velocity potential clearly increases in complexity drastically. This fundamental example illustrates the difficulty in incorporating finite boundaries to analytical sinking solutions.

Several researchers have instead created empirical solutions with various levels of success, many of which are validated against a vast volume of experiment data produced by Fidleris and Whitmore [43]. The authors concluded that the most consistently accurate solution is that of Francis, which contains the correction formula:

$$U \propto U_\infty - \kappa^4 \tag{2.53}$$

where U_∞ is the sphere velocity derived using conventional Stokes flow and κ is the ratio of sphere to container diameter [44]. This method proved to be accurate to within 0.5% of experimental data, but became increasingly inaccurate when $\kappa > 0.4$ and flow is non-laminar.

Francis and Whitmore concluded that finite-boundary effects became *less* important with an increase in *Re*, and alternative solutions showed greater accuracy. Munroe derived a formula to describe the sinking rate of grains in jigging in the late 19th century, after discovering various non-boundary formulas underpredicted the sinking rate when $\kappa > 0.1$ [45]. Munroe derived several empirical equations for different ranges of κ after collection over 600 sinking measurements. The most popular of Munroe's models is convenient due to its simplicity, where:

$$\frac{U}{U_\infty} = 1 - (\kappa)^{3/2} \tag{2.54}$$

Munroe originally estimated his solution to be accurate to up to 0.3 κ, yet Francis and Whitmore proved the solution to have an accuracy of up to 97.5% when $\kappa < 0.6$, and to have the greatest accuracy over various solutions between $1000 < Re < 3000$. These values of *Re* are likely more applicable to later sinking experiments described in chapter 3, and will be used provide a link between apparatus and literature.

Although more recent works have investigated wall effects at greater κ [46], the complexity of the solutions are considerably increased, and flow regimes are again restricted to smaller Reynolds numbers.

2.2.2.2 Cylindrical Sinking Objects

The sinking of cylindrical objects within a finite container is in some ways mathematically simpler than those of spheres. Bird, Stewart and Lightfoot [38] provide an analytical solution to the flow between concentric very long tubes, which assumes end effects to be negligible and flow to be laminar. A velocity gradient is shown to exist in the annulus as a function of radial position *only*. The authors derive the radial fluid velocity distribution as a function of the radial and axial pressure difference over a given length. This is used to give the average flow rate, total axial through-flow, and friction applied to both cylindrical surfaces. It is important to note that the cylinders were considered to be stationary in this example, and flow through the annulus was imposed by an arbitrary pressure gradient, *not* via the fluid displacement of a sinking cylinder.

Finite concentric cylinders have also been studied in the application of the falling cylinder viscometer. A study by Lohrenz, Swift and Kurata [47] gave a complete analytical methodology to obtain the viscosity of a fluid by measuring the velocity of a cylinder sinking through a concentric tube. They used a similar methodology to the infinite concentric cylinder of Bird, Stewart and Lightfoot in addition to a continuity argument of fluid flowing through the annulus due to the displacement of fluid at the front face. The Navier-Stokes equations and non-slip boundary conditions were used to give the radial velocity distribution in the annular region, which in turn was used to give the frictional force applied to the cylinder via the fluid. This approach does *not* account for any frictional forces applied to either face. Results showed 'sufficient' agreement to previous data, but the viscometer consistently over predicted viscosity[1], and was inaccurate when flow became turbulent.

[1] Although this study focuses upon the measurement of viscosity to quantify accuracy, viscosity is interchangeable with sinking velocity as the two are inversely proportional.

The research of Lohrenz, Swift and Kurata gave rise to a multitude of further studies in finite cylindrical flow. Chen, Lescarboura and Swift [48] focused upon the observed, and analytical solutions to, eccentricity in cylinder flow path. Their observations led to the conclusion that the coupling of radial and longitudinal freedom induced an angular dependent shear stress at the cylinder wall. This resulted in cylinder 'tilt'. The eccentricity and tilt were seen to oscillate, with these oscillations being inversely dependent upon viscosity. It was postulated, therefore, that an infinitely long cylinder would remain concentric. In an attempt to remove these inaccuracies from the viscometer, the author states that cylinders are centred using 'pins or fins'. Despite efforts to centralise cylinders, the authors still observed a certain degree of oscillation, which their study attempts to quantify. The study took an analytical approach of expressing the distance from concentric origin of the radially displaced cylinder edge as a function of angle and cylinder radius.

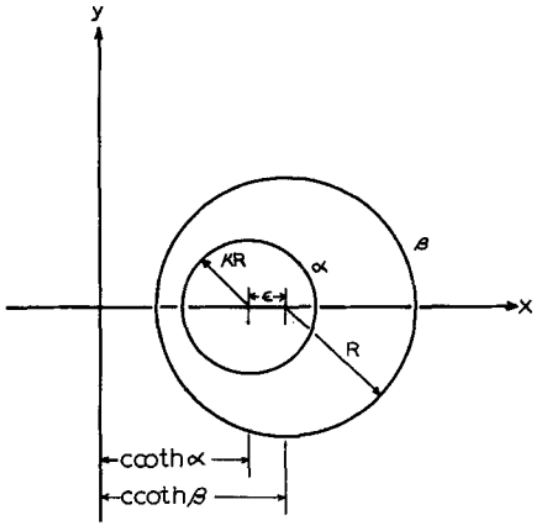

Figure 2.5: A cylinder eccentrically positioned within a tube. The radial position of the inner cylinder is related to the radial distance from the *concentric* origin as a function of angle, cylinder radius and eccentricity magnitude. Figure taken from external source [48].

The same analytical procedure as described for the concentric viscometer is applied using the dynamic radii. This resulted in a dimensionless correction factor C_e to the original analytical solution:

$$C_e = \frac{\left(\frac{1}{2}\right)(\kappa R)^2(\beta - \alpha)}{1/(\beta - \alpha)S - 1} \tag{2.55}$$

where α and β are the aforementioned dynamic radii, and

$$S = \frac{(1-\kappa^4)}{4\phi^2(1-\kappa)^2 sinh^2\beta} + \frac{1}{(\beta - \alpha)} + 4\sum_{n=1}^{\infty} \frac{n}{e^{2n\beta} - e^{2n\alpha}} \tag{2.56}$$

with ϕ the ratio of eccentricity to clearance. The solution showed very good agreement with experiments, with an accuracy > 99% for Newtonian fluids where $\kappa > 0.9$ and flow is laminar.

Attempts have been made to apply the sinking cylinder viscometer to non-Newtonian fluids. Ashere, Bird and Lescarboura [49] tried this under the premise that, at high values of κ, the annular gap can be simplified to a 2 dimensional slit. 2 non-Newtonian models, the Ellis (see [50]) and power law [51] models are applied to the slit region. This resulted in a partially empirical correction factor, which can be applied to the viscosity equation given in previous models. Results for both models were compared with volume flow data from experiments in polymer fluids, where it was concluded that the Ellis model was consistently more accurate than the power law model. The work of Eichstadt and Swift [52] later criticised this approach, proving that it was inaccurate at larger scales. These authors postulated that although the slit approximation at such κ ranges is reasonable, it is a poor approximation at even the slightest levels of eccentricity. They proposed an alternative analytical solution using the conventional annular reference frame for both power-law and Bingham fluids that gave < 1% error for strictly laminar flow within the $\kappa > 0.9$ range.

It is clear from the research regarding the falling cylinder viscometer that the applicability of the various given analytical solutions appear to have the following constraints:

1) Low *Re*, analytical solutions repeatedly become inaccurate as *Re* increases to beyond the laminar flow range.

2) Large κ, analytical solutions sharply decrease in accuracy as κ falls below 0.9.

More recent research in this field is that of Park and Irvine [53], who expands upon these limitations by incorporating the frictional forces applied to the front cylindrical face into the analytical solution. This was achieved using frictional values applied to a disc via work from Brenner [54], which is used to give a dimensionless correction factor to the terminal velocity equation. The work of Brenner is, however, an empirical solution, therefore the sinking velocity is no longer related to the fundamental hydrodynamics. The applied work of Brenner is also only performed for $\kappa < 0.18$. To extend this method over a wider κ range the author applies asymptotic boundary conditions at $\kappa = 0$ and $\kappa = 1$, and performs a Taylor expansion over the entire range of κ. This gives a front face correction factor C_F of:

$$C_F = 1.003852 - 1.961019\kappa + 0.9570952\kappa^2 \tag{2.57}$$

Final results agree with experiments within 0.6% error, however these experiments were performed exclusively in the laminar flow regime. The Taylor expansion was also found to produce unreasonable results at $\kappa > 0.9$, where the correction coefficient *increases* velocity. Related research has been limited in recent years, likely due to the rise of the spherical-front face variant of the viscometer, referred to as the needle point viscometer [55].

The flow through concentric cylinders at higher *Re* than those investigated in viscometry has also been the subject of previous investigation. Much of the work has been experimental, such as those of Quarmby [56] who studied flow within both horizontal and vertical concentric cylinders. The inner tube of these experiments spanned the entirety of the system. The author investigated cylinders of κ between 0.11 to 0.35 and *Re* between 6,000 and 450,000, using gas as the inlet fluid. Quarmby notably concluded that the frictional factor is completely independent of *Re* (and thus throughput velocity) within the available accuracy at these flow regimes. Quarmby also noted that the maximum fluid velocity differed to that of laminar flow, with discrepancies between the 2 regimes being a function of both *Re* and container diameter.

Shortly following his experimental investigation, Quarmby [57] created a numerical solution to turbulent flow through concentric annuli defining 2 flow regions within the annulus, with separate turbulent flow solutions applied to each of them. The Deissler turbulence model [58] is applied to the first flow region neighbouring the inner tube wall. The Von Karmen turbulence model (see [59]) is applied to the outer region. The solution becomes highly complex; the Deissler model is a function of an empirical dampening factor, which in turn is a function of *Re* and diameter ratio. The solution becomes unsolvable analytically, and relies upon numerical iteration.

For a given set of tube diameters, each model predicted the annular velocity profile, friction factor and *Re*. This solution not only determined the radial location of the peak fluid velocity, but also discovered that this maximum has an effective radial width, both of which are a function of *Re* and κ. Quarmby confirmed analytically that the friction applied to the inner cylinder is constant at *Re* greater than 5×10^4.

The method of dual-turbulent phase regions within concentric annuli has also been investigated by Lee and Park [60] who applied the Deissler diffusivity model to the inner turbulent region. In contrast to the work of Quarmby, Lee and Park applied the Reichardt eddy diffusivity model [61] to the outer annulus flow region. Using in-house experiments to validate the model, the authors noted that the shape of the front face of the inner concentric object made a substantial difference to the turbulent flow regimes. A rounded, spherical front face to the inner concentric object was proven to give a laminar flow pattern within the annulus, which progressed to turbulent at a certain distance along the annulus as shown in figure 1.6. In contrast, disturbing the flow prior to reaching the concentric object removed any laminar flow region within the annulus.

It was also observed that flow in the outer region had minimal radial variance. The authors concluded that the zero-shear region would *not* coincide with the velocity maximum, more so for rough surfaces. In comparison to the analytical solution, there was ‘good’ agreement in radial velocity profiles, ‘very good’ agreement with eddy diffusivity lengths and ‘excellent’ agreement for the annular friction coefficient. In its final form the model is highly complex, validated exclusively for gaseous fluids, and omits end effects.

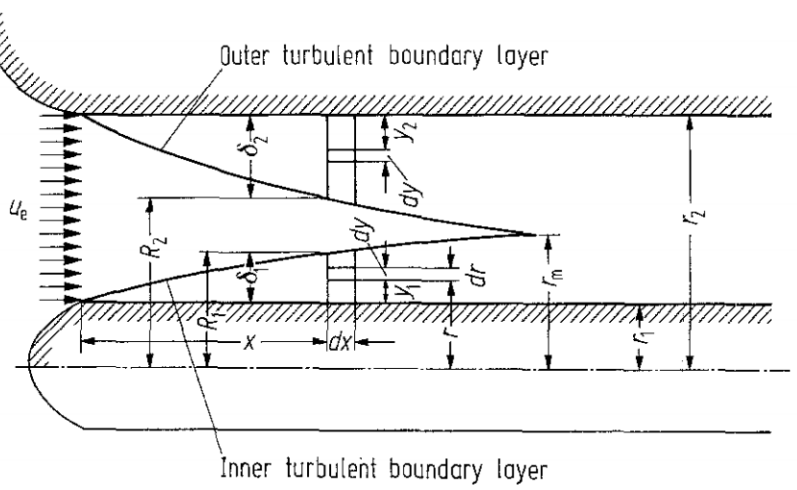

Figure 2.6: Flow diagram of a turbulent duel-flow regime at the entrance to an annulus. Image taken from external source [60].

Sud and Chaddock [62] investigated turbulent flow through concentric annuli for the application of theoretical transport media. Unlike previous studies, these authors created an analytical solution inclusive of end effects, giving rise to a third turbulent flow region. This work was later improved by Kotlow and White [63]. Both studies use the same methodology for the fully developed turbulence phase: Deissler's turbulence model for the inner radial core and Karman's similarity hypothesis for the outer core. This creates a complex numerical solution for the fully developed flow region, which results in a nested-iterative solution. Both studies assume a smooth initial laminar flow pattern at the entrance of the annulus, such as those observed by Lee and Park for rounded front-face concentric objects. Kotlow and White criticized the work of Sud, declaring that the local mass and momentum balances were not adequately satisfied. Kotlow uses these mass and momentum balances to derive a new laminar flow regime at the entrance to the annular region. This results in an *additional* separate, nested iterative solution to determine the velocity profile in the entrance region. Velocity profiles and subsequent frictions observed in each region are smooth functions of both κ and *Re*, giving excellent agreement with previous experimental data.

The solution of Kotlow and White uses the *simplest* geometric form of the front face possible, yet a 3-phase, multiple iterative solution is required to get a strong agreement with experiment data. Furthermore, these solutions have mainly been confined to gaseous, perfectly concentric systems. It is clear that extremely complex,

iterative solutions are necessary to describe friction within high *Re* annular flow to a high degree of accuracy. The complexity of these solutions makes the addition of additional phenomena, such as complex front face flows and dynamic eccentricity, likely impossible to implement into a sinking velocity model. A simpler approach is clearly necessary in order to achieve an analytical solution that describes the sinking rate of a cylinder in terms of its functional dependencies on system variables.

Bates recently studied the terminal velocity of sinking cylinders, also for application in DBD [22]. Bates used the empirical Colebrook [64] formula to give the frictional forces applied to the annular surface of the cylinder. Bates also used an empirical look-up table to give what is referred to as the 'form-loss coefficient', which quantifies energy lost through the displacement of fluid into the annular gap. Although the empirical solution is relatively simple and shows good agreement with the range of experimental sinkers used, the solution is not directly related to the theory of hydrodynamics. Furthermore, the Colebrook formula is a function of the *Re*, which relies upon the unknown sinker velocity. This makes the solution implicit, requiring numerical iteration. There is clearly a need to improve upon the model created by Bates and to develop an explicit solution that provides a link to hydrodynamics and the associated physics.

2.2.3 Dimensional Analysis

Dimensional analysis may be used to determine the proportional relationship of terminal velocity and relative variables. This is done by finding the necessary combination of variables that combine to the same units as the dimension of interest (in this instance, terminal velocity). For a cylinder deploying through an infinite fluid, the dependent variables are cylinder radius *a*, force *F*, cylinder height *h*, cylinder density ρ_c, fluid density and fluid viscosity, which comprise of the following dimensions

$$U \propto LT^{-1} \tag{2.58a}$$

$$a \propto L \tag{2.58b}$$

$$h \propto L \tag{2.58c}$$

$$\rho_c \propto ML^{-3} \tag{2.58d}$$

$$\rho_s \propto ML^{-3} \tag{2.58e}$$

$$\mu \propto FL^{-2}T \tag{2.58f}$$

$$g \propto FM^{-1} \tag{2.58g}$$

where *L* is length, *T* is time and *M* is mass [65]. From equations 2.58 it is easy to identify 2 dimensionless products as a result of identical dependencies for medium densities and cylinder dimensions. Because these dimensions are identical, velocity must be dependent on an unknown function of each of these dimensionless products, such that

$$U \propto f_1\left(\frac{\rho_c}{\rho_s}\right) \tag{2.59a}$$

$$U \propto f_2\left(\frac{a}{h}\right) \tag{2.59b}$$

The remaining dimensionless product is obtained by combining the dimension of interest *U* with four other quantities, seeking the dimensionless product of

$$Ua^{\alpha}{\rho_c}^{\beta}\,\mu^{\gamma}g^{\delta} \tag{2.60}$$

where α, β, γ and δ are variables to be determined through dimensional analysis. It is now possible to create a dimensionless product of each dimension within equations 2.58. Beginning with *T* and using the dimensional dependency of velocity and viscosity;

$$(T^{-1})(T)^{\gamma} = 0 \tag{2.61}$$

$$\therefore\ \gamma = 1$$

Force is dependent on viscosity and gravity therefore

$$(F)^{\gamma}(F)^{\delta} = 0 \tag{2.62}$$

$$where\ \gamma = 1\ \therefore\ \delta = -1$$

Mass is dependent on density and gravity, therefore

$$(M)^{\beta}(M^{-1})^{\delta} = 0 \tag{2.63}$$

$$where\ \delta = -1 \therefore\ \beta = -1$$

Finally, length is dependent on velocity, diameter, density and viscosity, therefore

$$(L)(L)^{\alpha}(L^{-3})^{\beta}(L^{-2})^{\gamma} = 0 \tag{2.64}$$

$$where\ \beta = -1\ and\ \gamma = 1 \therefore\ \alpha = -2$$

Combining the determined exponent values with the dimensionless products gives the dimensional analysis of a cylinder deploying through an infinite fluid:

$$U = \frac{a^2 \rho_c g}{\mu} f_1\left(\frac{\rho_c}{\rho_s}\right) f_2\left(\frac{a}{h}\right) \tag{2.65}$$

As both functions in equation 2.65 are arbitrary, the relationship between cylinder velocity with sample density, radius and height may not be exactly determined. However, the first component in the right hand side of equation 2.65 shows that the combined dimensionality of length and density are to the power 2 and 1 respectively. It would therefore be reasonable to assume that the velocity of cylinders will have a greater dependence on geometry in comparison to density. Furthermore, the unaccounted for effects of the container size would only increase the geometry dependence.

This analysis provides a starting point for the selection and variation of cylinder variables in experiments; if terminal velocity has the greatest dependency on cylinder geometry, experiment resource should be focused on investigating geometric variables. However, because this analysis proves that cylinder geometry is coupled to cylinder density in the sinking rate equation, experiments should be repeated across multiple densities.

2.3 Computational Methods

In section 2.1 it is shown how the continuum laws of hydrodynamics are derived and several examples of their applications to objects sinking through fluids are given. Despite the eventual incorporation of both implicit and empirical methods, the only

reasonably accurate methods of predicting the sinking rate of a cylinder using hydrodynamics are limited to particular ranges of *Re* and κ. Chapter 4 attempts to further the development of an analytical sinking model, however, it will later be shown that a purely analytical model is not conclusive, and alternative methods are necessary to guide future efforts. This leads to a computational investigation, which allows for local fluid parameters such as pressure and velocity to be closely analysed.

Computational methods provide convenient, alternative approaches to solving the laws of hydrodynamics. Finite volume methods (FVM) are one of the most popular computational methods in continuum mechanics [66]–[68], where partial differential equations are *approximated* throughout a given continuum region. The frequency of these approximations is determined by discretizing the domain into a mesh of control volumes, with the field variable of interest located at the centre of each control volume [69]. The partial differential equations which govern the field variable of interest (such as the Navier-Stokes equations and fluid velocity) are then interpolated throughout the domain.

Turbulence requires careful consideration when using FVM to model fluid dynamics. As turbulence increases, so does the internal rotations within the fluid, eventually to the extent that localized eddy currents and vortices form. These additional rotations in the fluid give rise to a random and chaotic variance in field variables and an increased amount of energy is lost due to the transfer of fluid motion to thermal energy.

Field variables experiencing turbulence can be quantified as a sum of their conventional values and turbulent fluctuations. This allows for a re-derivation of the Navier-Stokes equations- a somewhat lengthy process, but a full derivation can be found in Versteeg and Malalasekra [70]. The resulting equations of motion are commonly referred to as the Reynolds-Averaged Navier Stokes equations (RANS), which include 6 additional stresses.

Various RANS methods exist which are capable of accounting for the effects of turbulence on the mean flow rate, using models to determine the additional stresses in the RANS equations of motion. Turbulence models date back to the early 20th century, including the popular mixing length model proposed by Prandtl [71], which calculates additional stresses without the use of partial differential equations. Other common turbulence models include the k-ϵ model, which has been used extensively in a wide

variety of engineering applications, including wind turbine [72], pollution dispersion [73] and chemical mixing [74]. The k-ϵ model includes 2 additional partial differential equations (one to determine the turbulent kinetic energy, and another to determine the turbulent kinetic energy dissipation rate). The k-ϵ model has been used to simulate flows past objects in several studies, including a study by Rahman and Karim comparing simulations to experiments between 1000 – 3900 *Re*. The authors found good agreement with experiment results when determining drag coefficients and lift. In addition, the k-ϵ model provided adequate visualization of vortex shedding, although alternative turbulence models showed better agreement at greater values of *Re*. A study by Lukes, Hart, Potts and Haake [75] applied 2 variants of the k-ϵ turbulence model to simulate the flow around a thin disc to determine lift, drag and pitching coefficients. The authors found good agreement with experiment data for one of the k-ϵ models, which was also successfully used to visualize flow detachment observed in experiments. However, data from the alternative k-ϵ model showed a lesser degree of correlation.

Large Eddy Simulations (LES) are an increasingly popular alternative to RANS methods that involve the spatial filtering of eddies [76]. Large eddies are computed in the time dependent simulation, making the computing time relatively large. Contributions to the mean flow from smaller eddies are incorporated using various 'sub-grid' models, or even hybrid models which incorporate RANS [77]. Notable LES applications to objects submerged in fluid include a study by Rajani, Kandasamy and Majumdar [78] which investigated the flow past a circular cylinder at 3900 *Re*. Results showed reasonable agreement of flow properties with experiment data at the near-wake region, however divergence was observed at greater distances from the cylinder. In a similar study, Mukrami, Iizuka and Oooka used LES for the modelling of flow past a square cylinder [79]. The authors compared conventional LES method with dynamic sub-grid methods, which had previously been proven to greatly improve upon the accuracy of conventional LES methods. These dynamic LES methods were ultimately unstable for flows past the square cylinder. The authors implemented an improvement to the dynamic LES method, involving the averaging of trajectories in the Lagrangian frame of reference, which greatly improved the stability of simulations.

It is clear from the literature in regards to flows past objects that *both* RANS and LES methods suffer from the same shortcomings; there is clearly no 'one size fits all' method of modelling turbulence, especially in regards to flows past submerged objects.

The common process in the discussed literature is to compare various methods with finely tuned experiment data. For many applications this approach acceptable, however, with the sinking of cylinders through a tube, the frame of reference is not consistent between experiment and modelling. The mesh created during pre-processing means that the cylinder position is fixed using RANS / LES simulations, and a true comparison with experiment data is not achievable. There are relatively recent methods that are somewhat more universal; Direct Numerical Simulations (DNS) extends the approach of LENS by incorporating eddies directly into the time-dependent simulations, by incorporating *all* eddies of sufficient magnitude to cause energy dissipation[1] [80]. The direct incorporation of such small eddy flows results in extremely fine meshes and small time-scales, drastically increasing the computational processing time. This has resulted in DNS modelling traditionally being limited to the development of models used for simulation validation, and select experiments which are impossible in conventional laboratories [81].

The computational cost of DNS remains relatively large, despite its increasing popularity and the continual advances computational processing. Furthermore, as with RANS/LENS methods, DNS is mesh-driven, restricting simulations to a dissimilar frame of reference to sinking experiments performed in a laboratory.

Mesh-free alternatives in continuum mechanics are limited. One method gaining popularity is Smoothed Particle Applied Mechanics, or SPAM. SPAM is a mesh-free method in which the partial differential equations of continuum mechanics are replaced by a finite number of ordinary differential equations. Domains are discretised using free-to-move particles, each of which are considered as the centre of mass for a continuum section of co-moving matter [82]. Continuum variables can be evaluated at any location using a weighted average of nearby particles. The convenience of performing simulations in a mesh-free, Lagrangian frame of reference originally made SPAM the computational method of choice for this study. Unfortunately, flow instabilities occurring in the wake of sinking objects hindered the study. At the time of publishing the cause of these instabilities is inconclusive, and the SPAM related research is therefore omitted from this project. The SPAM code developed for this

[1] The length scales of eddiest at which energy dissipiation occurs is defined by the Kolmogorov smoothing length [160].

purpose is complete and the aforementioned studies have been documented should they be desired for any future projects.

An alternative approach is to use particle based simulations as opposed to continuum mechanics. Molecular dynamics (MD) is a particle based tool for simulating matter at the atomic level, avoiding the need to solve the continuum equations of motion. The method entails the numerical solution of the motion equations of classical mechanics for a set of 'particles' using finite differences where each particle can be considered as a point of mass. The technique is exact for a given inter-particle force law and therefore MD can be considered to generate pseudo experimental data. Statistical mechanics provides the link between time ordered sets of potentials and momenta from simulations and thermodynamic quantities. MD has been extensively applied to hydrodynamics, and has been used to simulate several fundamental flow patterns that arise from continuum mechanics, including Rayleigh-Bénard convection [83], [84] and Taylor-Couette flow [85]. This provides an additional method to conventional experiments to aid in the validation and development of continuum theory.

MD has also been previously applied to flows past submerged objects; Rapaport both independently [86] and co-dependently with Clementi [87] used MD to investigate the flow past an infinite cylinder, which is reduced to a 2 dimensional simulation of flow past a disc. Rapaport and Clementi used what was at the time a leading edge simulation size of 16×10^4 particles to detect flow patterns in the wake of the disc. A fixed-velocity inlet fluid and external field were used to maintain flow past the disc object. The pair potential used to describe the inter-particle forces is the WCA potential, named after Weeks, Chandler and Anderson [88]- a modified form of the Lennard Jones potential, truncated and shifted at its minimum so that it is exclusively repulsive. Rapaport and Clementi investigated the flow past a disc at a *Re* of approximately 25 and observed several flow patterns, beginning with the development of a stationary eddy flow at the wake of the sphere, developing into an oscillatory wake, with vortices shedding and propagating downstream of the disc. Furthermore, they observed a density drop of 25% at the centre of eddy vortices. These turbulence observations were in agreement with those observed in experiments and occurred at similar values of *Re*. This shows that MD is a quantitatively suitable computational method for simulating turbulent flow schemes that occur in nature, despite the limitation of simulations being performed in the microscale.

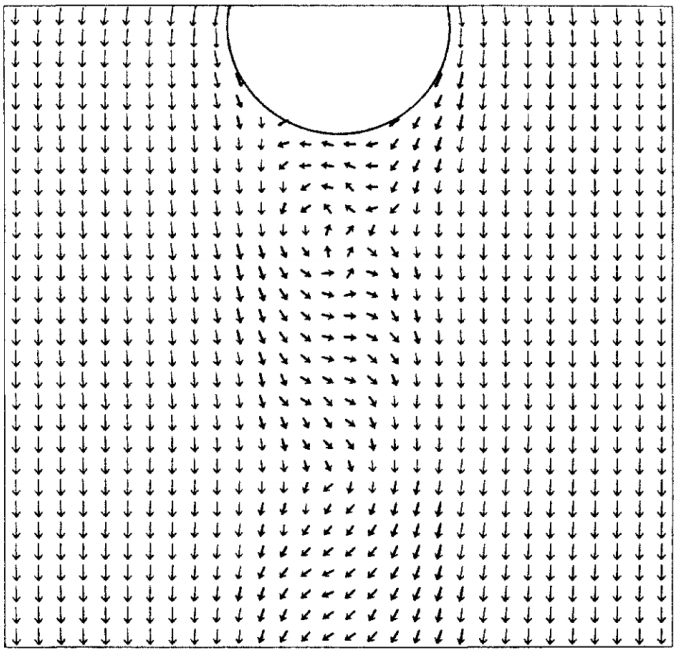

Figure 2.7: The observed turbulent flow regime of flow past a stationary circle. Eddy vortices are seen in the wake of circle. These vortices develop at both sides of the circle before shedding, causing the observable oscillatory flow at the wake. Figure taken from external source [87].

Following on from the work of Rapaport and Clementi, Cui and Evans [89] (1992) investigated 2-dimensional flow past a stationary, off-set plate, again using a WCA fluid. The authors had success in using significantly fewer particles in comparison to Rapaport and Clementi when observing turbulent flow regimes, showing that turbulence observation is *not* limited to simulations performed on large-scale supercomputers. The authors observed laminar flow up to 15 *Re*. As *Re* increased, alternating vortices were observed, shedding from the boundary layer alternatively at *Re* of 30 – 60. Cui and Evans observed a region of lower fluid velocity before the plate, and region with a velocity of 2-3 times that of the inlet at the outer edges of the plate. Density appeared uniform, with the exception of vortex centres.

Ishiwata and Murakami [90] later compared similar simulations to those performed by Rapaport & Clementi, flow past an infinite cylinder in a 2-dimensional frame of reference, with experiments. The authors extended the investigation to a wider range of *Re* using a simplified hard-sphere potential. Symmetrical laminar flow was observed at a *Re* of 1, and stationary vortices at the wake of the disc at *Re* between 6 and 33. At a greater *Re* of 106 they observed oscillatory vortex shedding as observed by

Rapaport & Clementi and Cui & Evans. Ishiwata, Murakami, Yukawa and Ito [90] later compared simulations with experimental data quantitatively, using the calculated friction applied to the infinite cylinder. Simulations were shown to agree within 15% of experiments; this relatively good agreement with experiments (considering the simplified potential used) further validates the applicability of turbulent flow studies in MD. The authors noted that the friction calculations decreased in accuracy when using a boundary less than 5 times the diameter of the disc, showing that finite boundaries affect friction coefficients in MD simulations, as they have previously been shown to in experiments.

Due to the computational cost of simulating a fluid using molecular dynamics at a large enough scales to observe eddy flows, there has been limited research into the sinking of 3-dimensional objects. One such study by Satoh [91] investigated flow past a stationary sphere in 3-dimensions, but was unable to simulate a large enough volume to completely remove the effects of the boundaries, despite implementing a simplified elastic collision model.

Unlike other atomistic simulation tools (such as the Monte-Carlo method), MD allows for the calculation of time dependent properties [92]–[94]. In particular, MD can be used to determine transport properties for use in continuum mechanics. If the pair-potential used for MD simulations and the obtaining of transport properties is consistent, simulations could potentially be performed in the macroscale (using methods such as SPAM) that are analogous to MD simulations, validating any observations to greater length scales. Obtaining transport coefficients also allows for the calculation of dimensionless variables such as *Re*, which allow for results to be compared with alternative length-scale experiments or simulations.

For the various aforementioned advantages discussed in this chapter, MD is the preferred computational method for this project, and will be used for the following simulations:

1) To simulate sinking experiments in finite boundary systems that are impractical to obtain in a laboratory (section 6.1).
2) To obtain detailed flow insight for objects sinking through a fluid in finite boundaries (section 6.2).

3) Obtaining transport coefficients for characterising results from section 6, and potentially allowing for their application in future continuum methods such as SPAM (section 5).

The remainder of this section will describe the MD theory necessary to implement the aforementioned simulations.

2.3.1 Molecular Dynamics Equations of Motion

The equations of motion are used to describe the position and momenta of a particle as a function of the inter-particle force law. The classical equations of motion for a position $\boldsymbol{q}$ in arbitrary co-ordinates can be expressed in both Lagrangian and Hamiltonian forms. The Lagrangian equation of motion were developed in the 18th century by Lagrange [95], and describe motion via:

$$\frac{d}{dt}\left(\frac{\partial L}{\partial \dot{\boldsymbol{q}}}\right) - \left(\frac{\partial L}{\partial \boldsymbol{q}}\right) = 0 \tag{2.66}$$

It can be seen in equation 2.66 that the Lagrangian is a function of both position $\boldsymbol{q}$ and the rate of change of position $\dot{\boldsymbol{q}}$. The Lagrangian is described by potential and kinetic energy components, such that:

$$L = K - \Phi \tag{2.67}$$

where K represents the kinetic energy and Φ represents the potential energy, as discussed in further detail in sections 2.2.4 and 2.2.2 respectively.

For Cartesian co-ordinates using the usual definitions of kinetic and potential energy, the Lagrangian equation of motion becomes

$$m_i \ddot{\boldsymbol{r}}_i = \boldsymbol{F}_i \tag{2.68}$$

where $\boldsymbol{r}_i$ is the position of a particle i in Cartesian co-ordinates. The force acting upon each particle can be derived in terms of the potential derivative,

$$F_i = \boldsymbol{\nabla}_{\boldsymbol{r}i} L = -\boldsymbol{\nabla}_{\boldsymbol{r}i} \Phi \tag{2.69}$$

where $\boldsymbol{\nabla_{ri}}$ is the gradient of particle *i* at position $\boldsymbol{r}$. The momentum is also given through the Lagrangian via:

$$\boldsymbol{p}_k = \frac{\partial L}{\partial \dot{\boldsymbol{q}}_k} \tag{2.70}$$

where $\boldsymbol{p}_k$ is the momentum in arbitrary co-ordinates. This completes the Lagrangian equations of motion.

An alternative method to describe the equations of motion was develop by Hamilton in the early 19th century [96]. The Hamiltonian (*H)* can be related to the Lagrangian via:

$$H = \sum_k \dot{\boldsymbol{q}}_k \boldsymbol{p}_k - L \tag{2.71}$$

Unlike the Lagrangian equation of motion, the Hamiltonian is a direct function of position and momentum. The Hamiltonian equations of motion are given using

$$\dot{\boldsymbol{q}}_k = \frac{\partial H}{\partial \boldsymbol{p}_k} \tag{2.72}$$

$$\dot{\boldsymbol{p}}_k = -\frac{\partial H}{\partial \boldsymbol{q}_k} \tag{2.73}$$

Assuming the potential is independent of velocity and time, in Cartesian co-ordinates these equations reduce to

$$\dot{\boldsymbol{r}}_i = \frac{\boldsymbol{p}_i}{m_i} \tag{2.74}$$

$$\dot{\boldsymbol{p}}_i = -\boldsymbol{\nabla}_{\boldsymbol{r}i}\, \Phi = \boldsymbol{F}_i \tag{2.75}$$

Newton's equation of motion is derived by differentiating equation 2.74 in respect of time and substituting into equation 2.75. This gives:

$$\ddot{\boldsymbol{r}}_i = \frac{\boldsymbol{F}_i}{m_i} \tag{2.76}$$

The Hamiltonian equations of motion are first order differential equations, in contrast to the second order differentials used in the Lagrangian equations of motion. The first-

order derivatives of the Hamiltonian often lead to simpler equations of motion as opposed to the second-order derivatives of the Lagrangian.

2.3.2 Molecular Potentials

It is shown in section 2.2.1 that both of the methods used to determine the equations of motion use the force applied to each particle given from a potential, Φ. This potential is a function of particle positions, and can be broken down such that

$$\Phi = \sum_i \Phi_1(\boldsymbol{r}_i) + \sum_i \sum_j \Phi_2(\boldsymbol{r}_i, \boldsymbol{r}_j) + \sum_i \sum_j \sum_k \Phi_3(\boldsymbol{r}_i, \boldsymbol{r}_j, \boldsymbol{r}_k) \ldots \tag{2.77}$$

[97]. The first component of equation 2.77, Φ_1, is a function of individual particle position; this usually represents a boundary condition or external force applied to the particle. The second component Φ_2 is the pair potential, which is a function of the separation distance r_{ij} between 2 particles. This is therefore commonly denoted as Φ_{ij}.

For *N* number of particles, the double summation required to calculate the dependent positions would, using the most basic computational algorithm, result in an N^2 number of operations[1]. Φ_3 is the triplet component of the potential, which would similarly require a computational loop of order N^3. Both the second and third components of potential energy are defined as inter-particle potentials. Φ_2 is the most important of the inter-particle potentials, as it accounts for the largest contribution of inter-particle interactions. In reality, the triplet component accounts for approximately 10% of potential energy in the liquid phase, which is relatively low considering the associated increase in computational time [97]. Instead, pair potentials are often modified to include an average of triplet effects, sometimes referred to as the 'effective' pair potential. Further summations such as the quadruplet are known to exist, but have been proven to be insignificant in magnitude to the initial 3 potential terms [98].

There are many pair potentials commonly used in computational molecular dynamics. Although some are more accurate at replicating the behaviour of real life

[1] This can be reduced using several algorithms, such as taking advantage of the fact that distances between particles *ij* are equivalent to those between *ji*, as well as manipulating any potential cut-off distances to only loop over particles within defined neighboring areas (see section 2.2.8).

matter, simple potentials are often used for theoretical or empirical applications in computational molecular dynamics. A key characteristic of any pair potential is the maximum separation distance required to evaluate the potential at any given particle. Larger cut-off distances will result in a larger number of neighbouring particles located within each particles cut-off distance. This subsequently increases the number of calculations required to evaluate the potential, and therefore the computational cost.

The most basic potential is the hard-sphere potential, Φ_{HS}, which is zero beyond a cut-off distance σ (particle diameter), but infinite everywhere else. This was the potential used in the first known implementation of computational molecular dynamics, by Alder and Wainwright in 1957 [99].

$$\phi_{HS} = \begin{cases} \infty & r_{ij} \leq \sigma \\ 0 & r_{ij} > \sigma \end{cases} \tag{2.78}$$

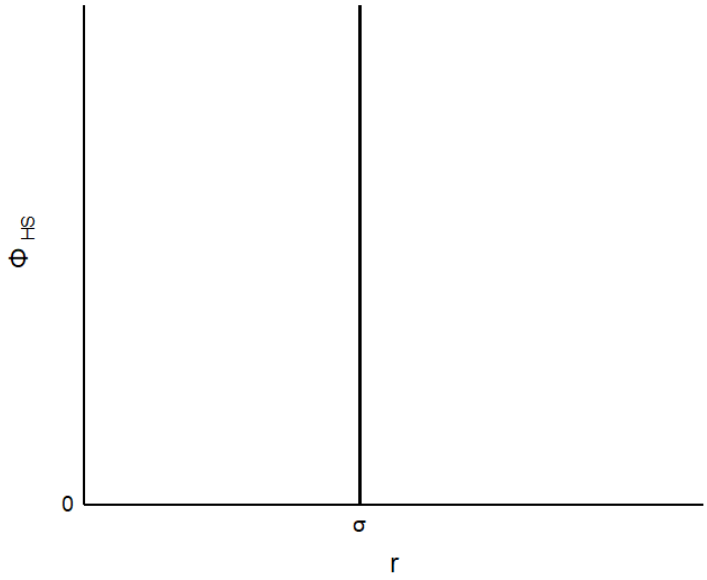

Figure 2.8: The potential energy as a function of distance for the hard sphere potential.

Two years later Alder and Wainright improved upon their initial molecular dynamics approach using a new potential known as the ‘finite square well’ [100]. Although still very much a simplified potential, the square well potential includes a finite attractive region before the infinite repulsive force region, such that

$$\phi_{SW} = \begin{cases} \infty & r_{ij} < \sigma \\ -\varepsilon & \sigma \leq r_{ij} < \lambda\sigma \\ 0 & r_{ij} \geq \lambda\sigma \end{cases} \tag{2.79}$$

where ε is the depth of the attractive region and λ is a parameter which defines the well width relative to the hard sphere diameter.

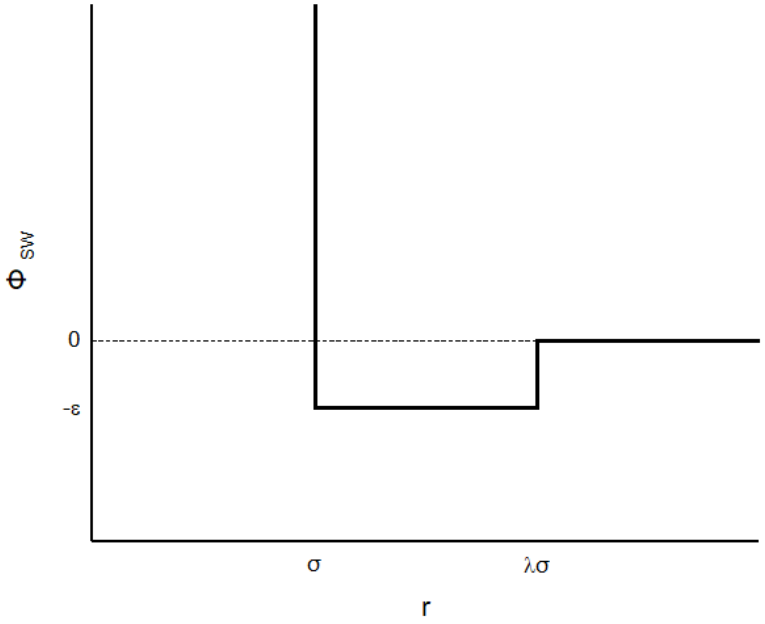

Figure 2.9: The finite-square well potential as a function of inter-particle separation r_{ij}, as described in equation 2.79.

The soft sphere potential is another simplified potential which has seen widespread use in MD thanks to its simple form. By omitting the attractive potential region, a simple equation is used to give a gradual potential increase:

$$\phi_{SS} = \varepsilon \left(\frac{\sigma}{r}\right)^k \tag{2.80}$$

where *k* may be an arbitrary constant which defines the 'hardness' of the potential [88]. The potential replicates the hard sphere model as $k \to \infty$. Although the potential does not approach absolute zero for a long distance, it is normally truncated at a finite cut-off distance. An example of the potential for $k = 6$ can be seen in figure 2.10.

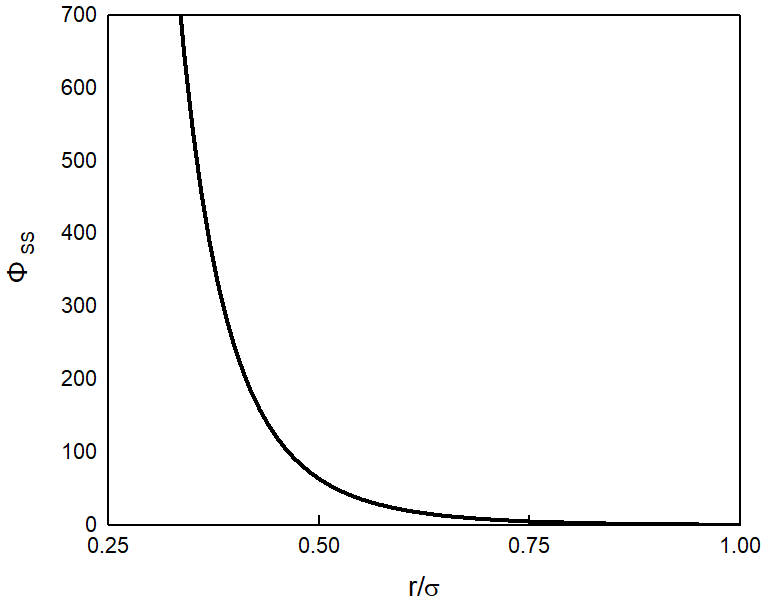

Figure 2.10: The soft-sphere potential as a function of particle separation distance r_{ij}. The steepness of the curve is defined by *k*, which is 6 in this example.

A more recent potential, somewhat similar to the soft-sphere, is known as the 'soft-repulsive' potential. Instead of going to infinity, the soft-repulsive potential approaches a given maximum, ε, at zero. Furthermore, the soft-repulsive potential has the benefit of trending exactly toward zero at the given cut-off distance, denoted σ.

$$\phi_{ij} = \begin{cases} \left[1 - \left(\frac{r_{ij}}{\sigma}\right)^2\right]^4 & r_{ij} < \sigma \\ 0 & r_{ij} \geq \sigma \end{cases} \tag{2.81}$$

The soft-repulsive potential is again considered a simple potential in the sense that it is computationally cheap and easy to use.

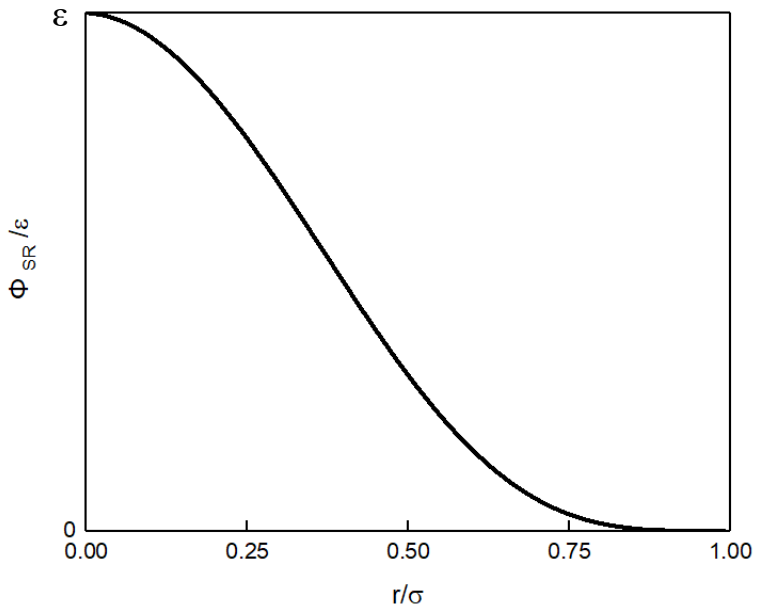

Figure 2.11: The soft-repulsive potential as a function of separation distance r_{ij}. Below the cut-off σ the potential gradually trends to the maximum ε.

A more realistic and widely used pair potential is that proposed in 1926 by John Lennard-Jones:

$$\phi_{LJ} = 4\varepsilon\left[\left(\frac{\sigma}{r_{ij}}\right)^{12} - \left(\frac{\sigma}{r_{ij}}\right)^{6}\right] \tag{2.82}$$

The Lennard-Jones potential was first used in computational molecular dynamics in 1964 by Rahman [101], where the potential and relevant parameters were developed to approximate experimental data of an Argon gas. The first inner-bracket term in corresponds to the repulsive part of the potential; this was originally an exponential term, but was simplified for computational ease. The second inner-bracket term corresponds to the attractive well. Despite its relatively high level of accuracy, the attractive potential gives rise to large cut-off distances, making simulations computationally expensive.

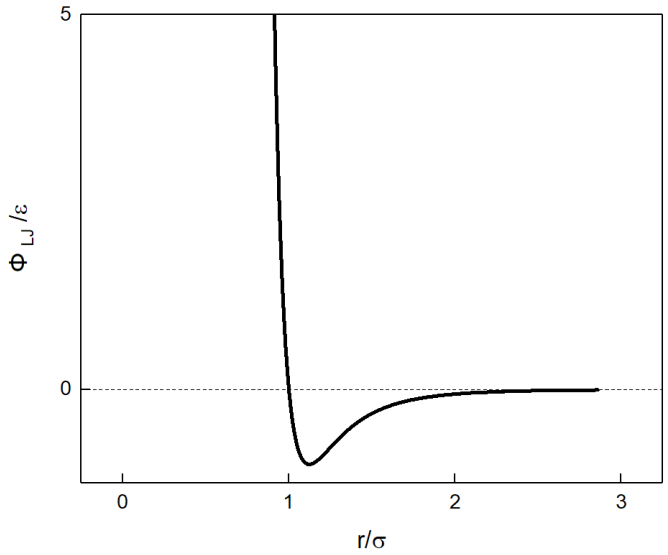

Figure 2.12: The Lennard Jones potential as a function of separation distance r_{ij}. The potential exhibits an attractive and repulsive component, which can closely replicate experiment data using carefully chosen input variables.

2.3.3 Boundary Conditions

A given container, or 'unit cell' of particles allowed to evolve without boundary conditions will experience several inconsistencies over time. Most obvious is that of particles being likely to exit the unit cell as time evolves, altering the density of matter. Furthermore, molecules near boundaries will experience lesser inter-particle forces than molecules at the centre of the unit cell. Boundary conditions must therefore be imposed onto MD containers to mitigate these inconsistencies.

Several types of boundary conditions exist, some replicating different types of boundaries found in nature, as well as handling these boundaries at different levels of complexity. In this section the boundary conditions applicable to this study are described.

2.3.3.1 Periodic Boundaries

The periodic boundary method is a tool used to simulate continuous blocks of matter, created by a given unit cell being replicated in all directions. This is materialised by reinserting any particle which exits the given unit cell instantaneously at the *opposing*

face. The method is visualised in figure 2.13 for a finite section of an infinitely repeating lattice.

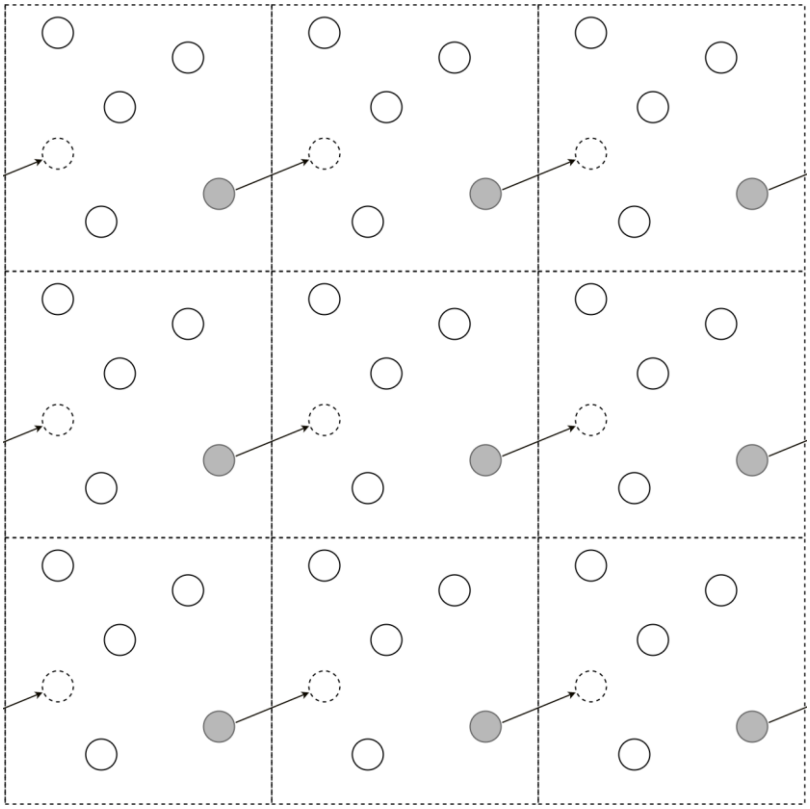

Figure 2.13: A repeating periodic boundary unit-cell. The grey particle represents a particle undergoing a boundary interaction, where it can be seen to re-enter the same unit cell at the opposing side.

An example of a particle crossing a periodic boundary is shown in dark grey. The dark grey circle represents the particle at a given time, whereas the dotted circle represents the same particle after an iteration of the simulation, which has re-entered the given unit cell at the opposing face.

As with particles themselves, inter-particle forces must also transcend across each periodic boundary, so as not to give rise to phase-space irregularities and errors in energy conservation.

Consider a repeating periodic cell where $L > 2r_{cut}$ (r_{cut} is the pair potential cut-off distance). In this example, particles cannot interact with the same particle multiple times. As a result, the nearest image of any given particle must be the only image of *that* particle close enough to interact. Only particles within a distance L / 2 from the origin of a particle therefore need to be considered, as illustrated by the solid, particle-

centred square in figure 2.14. This is known as minimum image convention. Furthermore, the considered area is even smaller than that of the square, due to the spherical nature of the pair potential.

The extended boundary forces are visualised in figure 2.14, showing the inter-particle interaction area of a given particle with $r_{cut} = L / 2$.

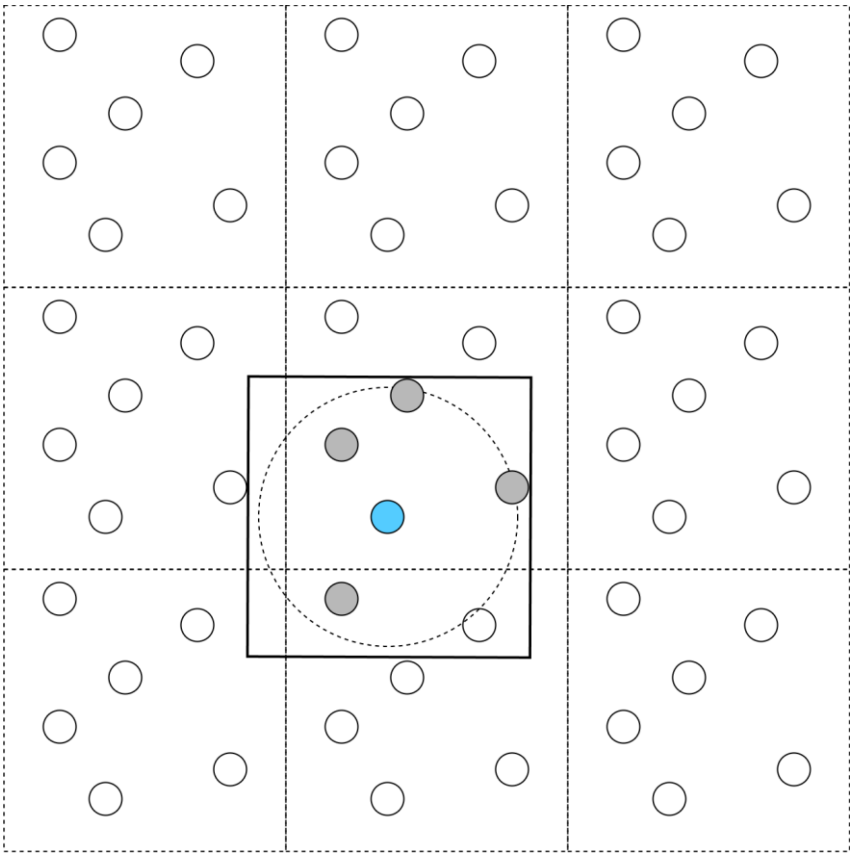

Figure 2.14: Inter-particle forces extended over a periodic boundary. The blue coloured particle has a force interaction area as shown by the dotted circle. Each particle interacting with the blue particle is shaded grey.

Each interacting particle is shaded grey; it can be seen that one of the interacting particles is located over a periodic boundary. The incorporation of cross-boundary particles is achieved using the condition:

$$if \quad x_{ij} < \frac{L}{2} \quad then \quad x_{ij} = x_{ij} + L \tag{2.83a}$$

$$if \quad x_{ij} > \frac{L}{2} \quad then \quad x_{ij} = x_{ij} - L \tag{2.83b}$$

where x_{ij} is the x-component of the inter-particle separation.

2.3.3.2 Elastic Boundaries

Elastic boundaries conserve kinetic energy, and are a simple method of simulating the interaction between a non-porous containment barrier. A particle is reflected from a flat elastic surface at an angle from the normal equal to the angle of incidence as illustrated by figure 2.15.

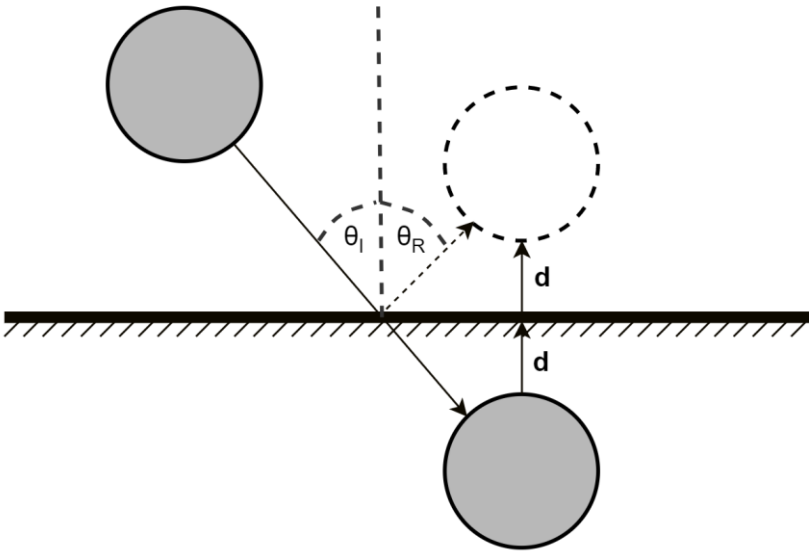

Figure 2.15: An elastic boundary condition in the *x* axis. The grey particle travels from below to above the boundary during a simulation evolution. The elastic boundary repositions the final particle position as if an elastic collision occurred, as shown by the dashed outline particle.

For an interaction with a boundary perpendicular to a Cartesian co-ordinate axis, the angles of incidence θ_I and reflection θ_R are equal. As such, the boundary condition becomes highly simplified; for a collision with a boundary perpendicular to the *x* axis, the condition becomes:

$$y_i' = y_i - 2d \tag{2.84}$$

Where y_i' is the position of a particle after a boundary interaction and *d* is the distance from the particle to the boundary in the *y* direction. The *y* component of momentum must also be inverted, simply using:

$$p'_{yi} = -p_{yi} \tag{2.85}$$

There are several other boundary methods of note; these include stone-wall boundaries, where the normal velocity component of a particle is removed when interacting with the boundary. Mirror boundaries are another boundary method, where a particle is created at an equal distance from a neighbouring boundary at the opposing side. The drawback of this method is it being computationally expensive (due to additional theoretical particles) as well as being comparatively complex. Furthermore, if a finite potential such as the soft-repulsive potential is used, an interaction with a strength exceeding that of the finite potential will result in particles escaping a boundary.

2.3.4 Temperature Control

In MD temperature is calculated using the thermal kinetic energy, *K*,

$$K = \sum_{i=1}^{N} \frac{\boldsymbol{p}_i^2}{2m_i} \tag{2.86}$$

where $\boldsymbol{p}_i$ is the momentum vector of particle *i*, as introduced in section 2.2.1. Temperature is related to the time averaged Kinetic Energy through the Boltzmann equipartition. For a simulation with d degrees of freedom per particle, this deduces to

$$\langle K \rangle = \frac{Ndk_BT}{2} \tag{2.87}$$

where k_B is the Boltzmann constant, and $\langle K \rangle$ is the average kinetic energy. The instantaneous temperature is therefore:

$$T(t) = \frac{1}{Ndk_B} \sum_{i=1}^{N} \frac{\boldsymbol{p}_i^2}{m_i} \tag{2.88}$$

It is clear from equation 2.88 that Temperature is directly related to particle momentum. The Hamiltonian equations of motion conserve total energy, which when used with energy conserving boundary conditions (such as periodic and elastic), create a

thermodynamically isolated system (also referred to as a microcanonical ensemble[1]). When a source of energy is added to such a system (ie through an external force) particle momentum (and therefore temperature) will increase continously. This is true for an object sinking through fluid, where the steady conversion of gravitational potential energy to kinetic energy would cause the system temperature to increase, making a steady state unobtainable. Fortunately, thermostats can be applied to the simulation to add or remove kinetic energy at such a rate that ensures the system is kept at a constant temperature. Several thermostats which have been developed for this purpose will therefore be presented in the following sub-sections, each with varying degrees of complexity.

2.3.4.1 Momentum Rescaling

The most intuitive method to control temperature is to simply scale the kinetic energy. This is achieved by multiplying the momenta of each particle by a scaling coefficient λ:

$$\boldsymbol{p}_i' = \boldsymbol{p}_i \lambda \tag{2.89}$$

It is clear from equation 2.88 that:

$$T \propto \langle \boldsymbol{p}^2 \rangle \tag{2.90}$$

The scaling coefficient can therefore be calculated using:

$$\lambda = \sqrt{\frac{T_{required}}{T(t)}} \tag{2.91}$$

Momentum is rescaled *after* temperature is allowed to deviate away from a specific value, therefore the ad-hoc thermostat does not generate a known canonical ensemble.

[1] Ensemble is a term used to describe a collection of particle systems with various microscopic states, but identical macroscopic states. An ensemble can be described as microcanical when the particle count, volume and energy are kept constant.

2.3.4.2 Gaussian Thermostat

The Gaussian Thermostat, also referred to as the Gaussian Isokinetic Thermostat, was created simultaneously and independently by Hoover [102] and Evans [103]. The Gaussian thermostat keeps a constant temperature *before* fluctuations occur, maintaining a canonical phase-space distribution. This is achieved by modifying the equation of motion, such that

$$\dot{\boldsymbol{p}}_i = \boldsymbol{F}_i - \lambda \boldsymbol{p}_i \tag{2.92}$$

To satisfy the temperature constraint, the instantaneous scaling parameter λ must be equal to:

$$\lambda = \frac{\sum_i \boldsymbol{F}_i \cdot \boldsymbol{p}_i}{\sum_i \frac{\boldsymbol{p}_i{}^2}{m_i}} \tag{2.93}$$

A Gaussian thermostat prevents temperature from fluctuating – a necessary requirement for generating the canonical ensemble. However, Evans has proved that the Gaussian thermostatted linear response is similar to one obtained using a thermostat which *does* generate the canonical ensemble [104].

2.3.4.3 Nosé-Hoover Thermostat

Nosé developed a form of mechanics more general than Newton, Lagrange, Hamilton and Gauss. Nosé mechanics allows thermodynamic constraints to be easily incorporated into the dynamics. A Nosé thermostat was developed by extending the phase space to include the effect of a thermostat and its coupling. In the extended phase space, the Hamiltonian becomes:

$$H_{Nosé} = \sum_i^N \frac{\boldsymbol{p}_i{}^2}{2m_i} + \phi + \frac{p_s{}^2}{2Q} + k_B T(Nd+1) ln(s) \tag{2.94}$$

where p_s is the coupling momentum and s is a scaling coefficient. Q can be considered as the associated mass of a fictitious heat sink; this effectively defines the strength of interactions with the molecular ensemble [105]. Nosé suggested Q values of $\sim 6Nk_BT$.

The +1 in the final right hand side component reflects the additional degree of freedom associated with the heat bath. Using the Hamiltonian to calculate *s*, the momentum is scaled using

$$\boldsymbol{p}_i' = \boldsymbol{p}_i s \tag{2.95}$$

The Hamiltonian in equation 2.94 leads to equations of motion which involve an awkward time scaling. Hoover later improved the method to replace this scaling with a friction term ζ [106]. The Nosé-Hoover Hamiltonian is:

$$H_{N-H} = \sum_i^N \frac{\boldsymbol{p}_i{}^2}{2m_i} + \phi + \frac{\zeta^2 Q}{2} + k_B T N d \, ln(s) \tag{2.96}$$

The equations of motion are derived from the Hamiltonian to be

$$\dot{\boldsymbol{r}}_\iota = \frac{\boldsymbol{p}_i}{m_k} \tag{2.97}$$

$$\dot{\boldsymbol{p}}_\iota = -\boldsymbol{\nabla}_{ri}\, \phi - \zeta \frac{\boldsymbol{p_i}}{\boldsymbol{m_i}} \tag{2.98}$$

$$\dot{\zeta} = \frac{\sum_i^N \frac{\boldsymbol{p}_i{}^2}{2m_i} - N d k_B T}{Q} \tag{2.99}$$

It is clear that ζ is proportional to particle momentum (and thus velocity), which has a constant rate of change when kinetic energy is at the required value. High values of Q result in a strong-coupling thermostat, similar to that of the Gaussian re-scaling. Low values of Q give rise to a weak-coupling thermostat, which allows for fluctuations in temperature and the creation of a canonical ensemble.

2.3.5 Pressure Calculation

In molecular dynamics the pressure of an ensemble usually refers to the *macroscopic* pressure, which is commonly calculated using an average of the *instantaneous* pressure calculated at each particle [107]. Expressing this average using a simple arithmetic mean, the macroscopic pressure *P* is given by:

$$P = \left\langle \frac{N k_B T}{V} \right\rangle + \left\langle \frac{1}{Vd} \sum_i \sum_j \boldsymbol{r}_{ij} \cdot \boldsymbol{F}_{ij} \right\rangle \tag{2.100}$$

where d is the dimensions of space. The first term on the right hand side of equation 2.100 is the pressure contribution through kinetic energy. The second term is the residual pressure contributions through particle interactions; assuming there are no additional external force fields, $\boldsymbol{F}_{ij}$ is simply given through the pair potential.

2.3.6 Initial Conditions

The Hamiltonian equations of motion given in section 2.2.1 are a coupled set of first order ordinary differential equations in positions and momenta. These $6N$ degrees of freedom require initial values. For simplicity, a 2-dimensional lattice is described in this section, although the same principles can be applied to 3-dimensions.

For a self-starting MD algorithm to resemble a fluid either the particle positions or velocities require a randomised initial distribution. It is advantageous to initialise particles in a defined lattice structure with randomized velocity, then allow the system to reach an equilibrium. This ensures an even distribution of the pair potential. In practice, the chaotic nature of fluids makes the particular choice of lattice superfluous, as particles should hold no resemblance to their initial configuration after the equilibrium phase[1]. In 2 physical dimensions there are only 2 regular lattices, square and triangular (see figure 2.16). The square lattice is the easiest and most convenient choice for a fluid.

[1] With the assumption that particles are distributed in a consistent manner such that density is continuous throughout the system.

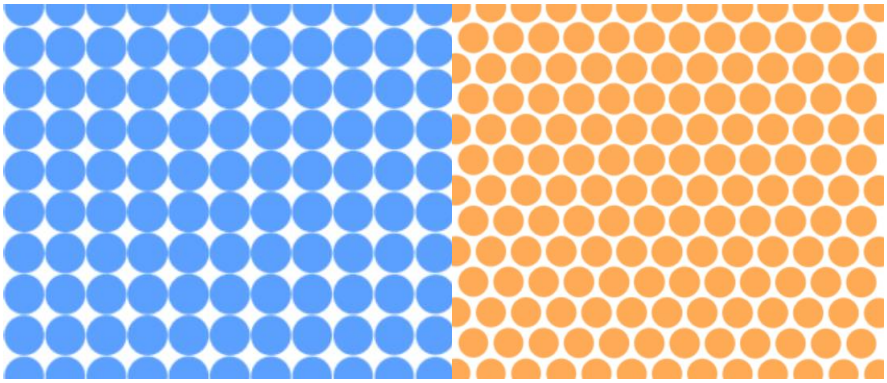

Figures 2.16: Lattice configurations in 2-dimensions, including a square lattice (left) and triangular lattice (right).

The easiest and most convenient method of constructing a square lattice is by placing a given number N_x of particles in the x direction. This row of particles can then simply be repeated N_Y number of times. The spacing of both columns and rows can be adjusted to the desired fluid density.

Giving each particle in a MD simulation a random starting velocity ensures the molecules quickly equilibrate to a fluid representation. The initial velocity can be given using a pseudo-random number generator as given by Hoover [108]. The function returns non-sequential values between 0 and 1, which can be replicated exactly using given starting parameters (the ensures that multiple simulations running on the same program are on an equal footing). Simply subtracting the initial value by 0.5 before scaling temperature is an efficient method to randomize direction.

A caveat of the random velocity initialization is that there is no guarantee of equal direction distribution. The linear momentum can be made to vanish exactly via

$$\boldsymbol{p}_i' = \boldsymbol{p}_i - \frac{\langle \boldsymbol{p} \rangle}{N} \tag{2.101}$$

where $\langle \boldsymbol{p} \rangle$ is the average momentum vector prior to the momentum scaling. Once the net momentum has been zeroed, the velocities of particles may be adjusted to the desired temperature. This can be easily performed using the momentum rescaling thermostat.

2.3.7 Integration Methods

The approach to solving the Hamiltonian equations of motion are based on finite differences, where time is discretised into intervals of duration Δt. The position of a particle at time $t + \Delta t$ can then be written as a Taylor series expansion, where

$$\boldsymbol{r}_i(t + \Delta t) = \boldsymbol{r}_i(t) + \dot{\boldsymbol{r}}_i(t)\Delta t + \dot{\boldsymbol{r}}_i(t)\frac{\Delta t^2}{2!} + \dot{\boldsymbol{r}}_i(t)\frac{\Delta t^2}{3!} + .. \tag{2.102}$$

Numerical methods derived from this Taylor expansion may be used to solve the Hamiltonian equations of motion, several of which are described in this section.

2.3.7.1 Euler Integration

The simplest method of integration is the Euler algorithm. Euler is a self-starting method of integration, meaning that it is independent of any previous particle information. The algorithm uses the Taylor expansion (equation 2.102) truncated after the 1st derivative term, giving an error of order Δt^2 [109]. For positions and velocity, these equations of motion become:

$$\boldsymbol{r}_i(t + \Delta t) = \boldsymbol{r}_i(t) + \dot{\boldsymbol{r}}_i(t)\Delta t \tag{2.103a}$$

$$\boldsymbol{v_i}(t + \Delta t) = \boldsymbol{v_i}(t) + \dot{\boldsymbol{v}}_i(t)\Delta t \tag{2.103b}$$

It is clear from equations 2.103 that the respective derivatives (velocity and acceleration) are assumed to be constant throughout the time step. For a molecular dynamics simulation this is seldom the case, as a change in particle separation results in a change in inter-particle forces. The Euler method must therefore be used with low time steps in order for the acceleration approximation to be reasonably accurate.

2.3.7.2 Verlet Integration

The Verlet integration algorithm is a recurring algorithm in physics, and one of the most common algorithms used in Molecular Dynamics following its creation by Loup Verlet [110], [111]. The Verlet algorithm is derived from summing a forward and backwards Taylor Expansion for position.

$$\boldsymbol{r}_i(t+\Delta t) = \boldsymbol{r}_i(t) + \dot{\boldsymbol{r}}_i(t)\Delta t + \ddot{\boldsymbol{r}}_i(t)\frac{\Delta t^2}{2!} + \dddot{\boldsymbol{r}}_i(t)\frac{\Delta t^2}{3!} + .. \quad (2.104a)$$

$$\boldsymbol{r}_i(t-\Delta t) = \boldsymbol{r}_i(t) - \dot{\boldsymbol{r}}_i(t)\Delta t + \ddot{\boldsymbol{r}}_i(t)\frac{\Delta t^2}{2!} - \dddot{\boldsymbol{r}}_i(t)\frac{\Delta t^2}{3!} + .. \quad (2.104b)$$

The resulting expression is truncated at the term in Δt^2. Rearrangement then gives:

$$\boldsymbol{r_i}(t+\Delta t) = 2\boldsymbol{r_i}(t) + \ddot{\boldsymbol{r}}_\iota(t)\Delta t^2 - \boldsymbol{r_i}(t-\Delta t) \quad (2.105)$$

Verlet is superior to Euler in that a centred difference approximation is used for the acceleration, whilst the omission of a velocity calculation results in an insignificant increase in computational cost compared to the Euler method. A drawback of this velocity omission is that the Verlet algorithm is therefore not self-starting, and each particle must be assigned a random velocity at the initial step. Furthermore, the velocity of particles is often required during MD simulations, in this case an additional calculation is required to derive velocity using previous particle positions, where:

$$\boldsymbol{v}_i(t) = \dot{\boldsymbol{r}}_i(t) = \frac{\boldsymbol{r}_i(t+\Delta t) - \boldsymbol{r}_i(t-\Delta t)}{2\Delta t} \quad (2.106)$$

There are many adaptations and improvements to the Verlet algorithm, including the leap-frog algorithm which introduces velocity into the equations of motion using an intermediate calculation of velocity. These algorithms are not covered in detail, as attention is instead turned to the Runge-Kutta family of algorithms.

2.3.7.3 Runge-Kutta Integration

The Runge-Kutta algorithms are a family of integration methods developed in the early 20th century by Runge [112] and Kutta [113], who applied novel root finding techniques to methods of integration. Unlike the Verlet and Euler algorithms, the Runge-Kutta methods use a series of calculations *during* the time step to perform averaging. This makes the integration method self-starting.

The Runge-Kutta algorithms use the Taylor expansion truncated following the first term to calculate the intermediate stages of integration. Each intermediate calculation therefore takes the same form as that of the Euler method. For a second

order Runge-Kutta method (RK2), the first of the intermediate steps $\boldsymbol{r}_i(1)$ and $\boldsymbol{v}_i(1)$ are:

$$\boldsymbol{r}_i(1) = \boldsymbol{r}_i(t) + \dot{\boldsymbol{r}}_i(t)\Delta t \tag{2.107}$$

$$\boldsymbol{v}_i(1) = \boldsymbol{v}_i(t) + \dot{\boldsymbol{v}}_i(t)\Delta t \tag{2.108}$$

The second stage of the RK2 algorithm repeats the technique of the previous step, but using the intermediate position $\boldsymbol{r}_i(1)$ and velocity $\boldsymbol{v}_i(1)$:

$$\boldsymbol{r}_i(2) = \boldsymbol{r}_i(t) + \dot{\boldsymbol{r}}_i(1)\Delta t \tag{2.109}$$

$$\boldsymbol{v}_i(2) = \boldsymbol{v}_i(t) + \dot{\boldsymbol{v}}_i(1)\Delta t \tag{2.110}$$

Finally, the 2 intermediate steps are summed using a weighted averaged.

$$\boldsymbol{r}_i(t + \Delta t) = \boldsymbol{r}_i(t) + \frac{[\dot{\boldsymbol{r}}_i(1) + \dot{\boldsymbol{r}}_i(2)]}{2}\Delta t \tag{2.111}$$

$$\boldsymbol{v}_i(t + \Delta t) = \boldsymbol{v}_i(t) + \frac{[\dot{\boldsymbol{v}}_i(1) + \dot{\boldsymbol{v}}_i(2)]}{2}\Delta t \tag{2.112}$$

The fourth order Runge-Kutta (RK4) methods are calculated in a similar manner, using four intermediate steps. The first step is calculated identical to that of Euler and RK2. The following steps again repeat the process using the intermediate particle positions, using additional steps to calculate positions and velocities at half of Δt, where

$$\boldsymbol{r}_i(2) = \boldsymbol{r}_i(t) + \dot{\boldsymbol{r}}_i(1)\frac{\Delta t}{2} \tag{2.113a}$$

$$\boldsymbol{v}_i(2) = \boldsymbol{v}_i(t) + \dot{\boldsymbol{v}}_i(1)\frac{\Delta t}{2} \tag{2.113b}$$

$$\boldsymbol{r}_i(3) = \boldsymbol{r}_i(t) + \dot{\boldsymbol{r}}_i(2)\frac{\Delta t}{2} \tag{2.113c}$$

$$\boldsymbol{v}_i(3) = \boldsymbol{v}_i(t) + \dot{\boldsymbol{v}}_i(2)\frac{\Delta t}{2} \tag{2.113d}$$

$$\boldsymbol{r}_i(4) = \boldsymbol{r}_i(t) + \dot{\boldsymbol{r}}_i(3)\Delta t \tag{2.113e}$$

$$\boldsymbol{v}_i(4) = \boldsymbol{v}_i(t) + \dot{\boldsymbol{v}}_i(3)\Delta t \tag{2.113f}$$

Each intermediate step is again averaged, using

$$\boldsymbol{r}_i(t+\Delta t) = \boldsymbol{r}_i(t) + \left[\frac{\dot{\boldsymbol{r}}_i(1)}{6} + \frac{\dot{\boldsymbol{r}}_i(2)}{3} + \frac{\dot{\boldsymbol{r}}_i(3)}{3} + \frac{\dot{\boldsymbol{r}}_i(4)}{6}\right]\Delta t \tag{2.114}$$

$$\boldsymbol{v}_i(t+\Delta t) = \boldsymbol{v}_i(t) + \left[\frac{\boldsymbol{v}_i(1)}{6} + \frac{\boldsymbol{v}_i(2)}{3} + \frac{\boldsymbol{v}_i(3)}{3} + \frac{\dot{\boldsymbol{v}}_i(4)}{6}\right]\Delta t \tag{2.115}$$

RK4 algorithms have an associated error of order Δt^5, a significantly greater accuracy in comparison to the RK2 method (Δt^3) and the Verlet method (Δt^2). This increase in accuracy comes at a greater computational cost, with the RK2 and RK4 methods requiring two and four evaluations of the equations of motion per time step, respectively. This makes the RK2 method twice as computationally expensive as the Euler and Verlet methods, yet similar in accuracy to the latter. For most applications of computational physics, the accuracy of RK4 provides the best trade-off between computational cost and accuracy, despite being four times as computationally expensive as the Verlet method [114], [115].

2.3.8 Simulation Optimisation

For an MD pair-wise potential described in section 2.2.2, the force applied to each particle i is given by the sum of contributions from every other particle j. For a simulation of N particles, calculating this separation distance would naturally lead to an N^2 loop of floating point operations.

The link-cell method is a commonly used algorithm that greatly reduces the number of pair interactions [116]. The link-cell method first discretizes a domain into smaller sectors as shown in figure 2.17.

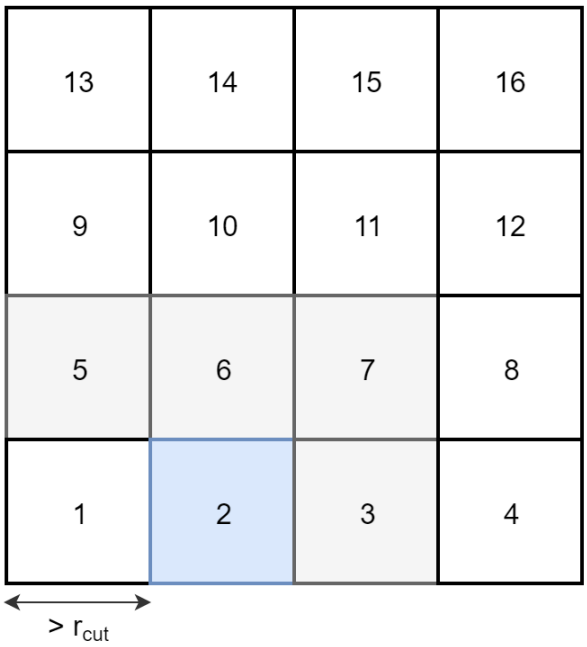

Figure 2.17: A 2 dimensional simulation area discretized into smaller cells of width greater than the pair potential interaction length. Each square has 4 neighbouring squares to calculate particle interactions due to the symmetry of Newtonian mechanics. Neighbouring cells are illustrated for cell 2.

The width of each sector is greater than the potential interaction length. Each particle is therefore only required to search for neighbours in adjacent cells. In molecular dynamics, the pair potential is equivalent in magnitude between pairs ij and ji; as such, *both* interactions can be determined during one pair iteration, therefore each cell is only required to interact with 4 of the 8 nearest neighbours. Care must also be taken to adapt and omit relevant neighbour cells for periodic and reflective boundaries.

The link-cell method then loops through each of the N particles. An array is used to store the single 'head' particle within each discretised cell. Every particle is checked to see which cell it resides in. Before each particle i is set to the head of that given cell, the previous head of cell particle j is stored in a separate 'linked-list' array, at the position of the *displacing* particle i. Finally, all particles within a given cell can be identified by daisy-chaining through the linked list array using the value stored within each element to identify the next, starting at the position acquired by the head of the given cell.

Reducing the number of calculations is just one method for decreasing the time taken to complete a simulation in MD. A prevalent method to decrease computational

time is to simultaneously spread calculations over multiple processor cores, referred to as ‘parallel processing’. Parallel processing can be traced back to the 1970’s [117], using an architecture commonly referred to as ‘pipeline’ processing. This involved several processors simultaneously computing different functions, allowing for data to be passed from one processor to the next [118]. The adoption of parallel processing in computational physics and MD increased following the introduction of commercial machines, such as the CRAY-1 [119], [120].

As processing power increased over the following decades, so did the magnitude of possible MD simulations and the requirement for scalable parallel processing algorithms. Several algorithms were developed where identical functional units could be simultaneously processed under a common control [121]. Some of the most widely adopted methods were published in 1995 by the Sandia National Laboratories [122]. The Sandia research outlined three scalable algorithms for parallel processing; the first assigned each process a fixed subset of atoms, the second assigned each processor a fixed subset of inter-atomic forces to compute, and the third assigned each processor a fixed spatial region.

Parallel algorithms have resulted in large increases in the achievable magnitude of MD simulations, however, their implementation increases the complexity of simulations. As a result, large proportions of modern research is performed using packaged MD software developed in teams. Numerous packages have been developed and successfully applied to hydrodynamics; to name a few, the open source GROMACS package [123] has been used to simulate Couette flow in concentric and eccentric cylinders [124], and ESPResSo [125] has been used to model elastic objects flowing through fluids in the application of bacteria in blood [126].

As the complexity of parallel MD solutions continues to increase with the incorporation of graphical processing units [127], a decision is often made to either utilize complex, optimized software, or utilise relatively simple software that can be self-developed and maintained. The latter approach gives complete control over the simulation, allowing the developer to tailor the code to the specific problem however they see fit. Perhaps somewhat anecdotally, this creation process is also likely to aid the developers’ understanding of the methodology of Molecular Dynamics.

2.3.9 Transport coefficients from Molecular Dynamics

Calculating the Reynolds number of a MD fluid allows for observed phenomena to be characterised to a dimensionless parameter. This theoretically allows any observations to be applied to any given fluid or flow scenario. The shear viscosity of the potential must first be acquired before the Reynolds number can be determined. Equilibrium statistical mechanics provides a theoretical framework in which shear viscosity (or any of the Navier-Stokes transport coefficients) is linked to properties of the force law which governs the interaction of the constituent atoms of a fluid. The relationship is known as a Green-Kubo formula. For the specific case of shear viscosity, the Green-Kubo relationship for an isotropic fluid is given by:

$$\mu = \frac{V}{k_B T} \int_0^\infty \langle \boldsymbol{P}_{xy}(0) \boldsymbol{P}_{yx}(s) \rangle ds \tag{2.116}$$

where $\boldsymbol{P}$ is the viscous stress tensor, V is volume, T is temperature and the term in angle brackets is the equilibrium time correlation function of the stress. The instantaneous stress tensor may be calculated from the time averaged virial which is related to intermolecular forces. The stress-stress autocorrelation function which measures equilibrium fluctuations in the stress must be calculated in a molecular dynamics simulation. Historically the Green-Kubo route to shear viscosity has proven to be problematic in practice, largely due to poor signal to noise ratio in the calculated time correlation function of a given property. A second reason is that the autocorrelation function possesses a long-time tail, making the integral difficult to evaluate due to long computational times [104]. Advances in computational power have however somewhat alleviated the issue of long-time tails, and recent studies have shown that (for certain potentials) Green-Kubo can be a leading method in determining shear viscosity [128].

There is also debate regarding the applicability of the Green-Kubo relations for shear viscosity specifically in 2-dimensional fluids [129]. For these reasons, non-equilibrium molecular dynamics (NEMD) methods are often more practical when calculating shear viscosity.

In direct NEMD, the simulation closely replicates the process as it would occur in nature. In the case of planar Couette flow, particulate walls enclosing the fluid are moved relative to each other to generate a linear velocity profile. The viscous stress is calculated during the simulation and then the shear viscosity may be calculated using

Newton's law of viscosity. There are several problems with this method. The first problem arises in the nature of determining viscosity, shear viscosity is inherently an equilibrium property, therefore viscosity must be calculated at multiple rates of shear and extrapolated to determine the zero-shear value. The second issue arises when attempting to remove the viscous heat generated (which if left unchecked, would cause the fluid temperature to rise indefinitely, preventing a steady state from developing). Using a thermostat embedded in the walls only works at low shear rates, beyond which the heat cannot be removed fast enough [130]. More importantly, with direct NEMD the fluid is inhomogeneous, due to generated density and temperature profiles leading to a thermodynamic state which varies locally throughout the fluid.

Synthetic field NEMD is an alternative to the boundary driven or direct methods of generating non-equilibrium flows. The basic principle is to modify the equations of motion (in some cases this involves abandoning Hamiltonian dynamics) so as to mimic the usual thermal boundary conditions driving the flows. The result is an algorithm which is spatially homogeneous, gives bulk transport coefficients directly, and can be used to study the behaviour of far-from-equilibrium states. A general transport coefficient, L, is then obtained using linear response theory:

$$L = \lim_{F \to 0} \lim_{t \to \infty} \frac{\langle B_t \rangle}{F} \tag{2.117}$$

Where B_t is the conjugate phase variable at time t, dependent upon the external force F. In the case of shear viscosity, the variable B_t is the relevant element of the viscous stress tensor and the generalised force, F is the strain rate. A thermostat (or ergostat) must be used otherwise the limit $t \to \infty$ cannot be taken [104].

An important ingredient of synthetic NEMD algorithms is the use of Lees-Edwards boundary conditions. In this scheme, the usual periodic boundaries are modified to be compatible with planar Couette flow, as illustrated in figure 2.18.

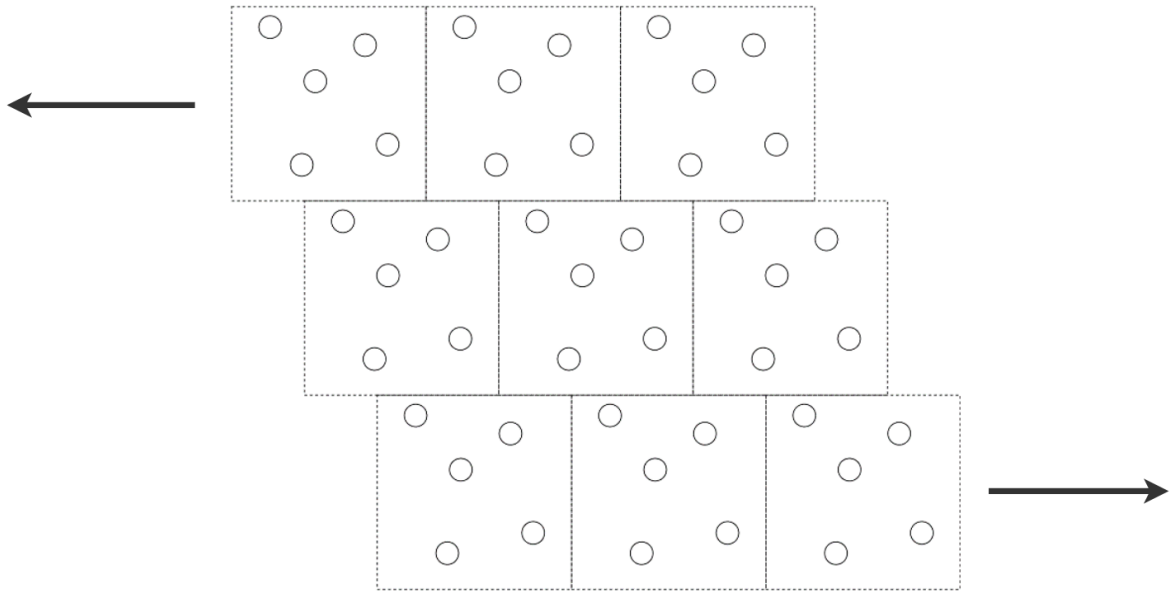

Figure 2.18: The Lee-Edwards periodic boundary conditions. As particles transverse the displaced y-axis boundary, they effectively re-enter the periodic lattice at an offset position, and are also given an offset velocity.

2.3.9.1 The SLLOD algorithm

A modified Hamiltonian for generating planar Couette flow was proposed by Evans *et al* [131]:

$$H = H_0 + \sum_{i=1}^{N} \boldsymbol{q}_i \boldsymbol{p}_i : (\nabla \boldsymbol{v})^T \tag{2.118}$$

where H_0 is the standard Hamiltonian, $\nabla \boldsymbol{v}$ is the strain rate tensor and $\boldsymbol{q}$ and $\boldsymbol{p}$ are the generalised positions and momenta of the fluid atoms. The term involving the summation represents the coupling of the external field (in this case the transpose of the strain rate tensor) to the phase variables given by the dyadic[1], $\boldsymbol{qp}$. It was the presence of this dyadic that lead Hoover to name this algorithm as the DOLLS tensor algorithm after the Kewpee Doll.

The resulting equations of motion derived from the modified DOLLS tensor Hamiltonian are:

[1] Consisting of two parts (position and momenta)

$$\dot{\boldsymbol{r}}_i = \frac{\boldsymbol{p}_i}{m_i} + \boldsymbol{q}_i \cdot \nabla \boldsymbol{u} \tag{2.119}$$

$$\dot{\boldsymbol{p}}_i = \boldsymbol{F}_i - \nabla \boldsymbol{u} \cdot \boldsymbol{p}_i \tag{2.120}$$

When $\nabla \boldsymbol{u}$ has a single, non-diagonal component of velocity, standard planar Couette flow is induced. These equations of motion can be used to drive adiabatic flows. However, for reasons mentioned earlier, a thermostat must be employed to remove the heat produced irreversibly through the conversion of work. A thermostat can be included in the equations of motion as described in section 2.2.4.

Very accurate simulations of planar Couette flow revealed that the DOLLS tensor equations of motion lead to the incorrect non-linear response. A simple remedy proposed by Evans and Morris involved transposing the external field term in the momentum equation [132]. The transposition was the inspiration for the name of this new algorithm – SLLOD. The SLLOD momentum equation of motion is:

$$\dot{\boldsymbol{p}}_\iota = \boldsymbol{F}_i - \boldsymbol{p}_i \cdot \nabla \boldsymbol{u} \tag{2.121}$$

The SLLOD equations, unlike the DOLLS tensor equations, cannot be derived from a Hamiltonian. This lack of a Hamiltonian appears to have no practical consequences and thus the SLLOD algorithm remains the more robust and popular route to the calculation of shear viscosity.

3: Experimental determination of terminal velocity

3.1 Introduction

In section 2.2.2.1, a naïve calculation of terminal velocity for a nuclear waste container sinking through a Newtonian fluid yielded a result 6 orders of magnitude greater than those previously approximated (U.S. Department of Energy, 2013). There are several reasons for this discrepancy, including: assumption of creeping flow, no account taken for the shape of the sinking object and failure to include the effects of a confining boundary. A proper mathematical treatment of the rate of sinking of a confined cylindrical object requires the solution of the full Navier-Stokes equations of hydrodynamics – a formidable undertaking. One of the aims of this thesis is to develop a predictive mathematical model for terminal velocity. The approach taken entails solving a simplified version of the Navier-Stokes equation to obtain a baseline model and then building up the complexity step by step, avoiding adjustable parameters but retaining simplicity and insight. To accomplish this, high quality experimental data is pre-emptively required for validation.

To provide experimental data for validation of the models developed in Chapter 4 this chapter outlines an experimental programme in which terminal velocity is accurately measured for a series of sinking objects – both cylinders and spheres. Results are presented for a set of experiments in which the relevent variables are systematically changed, including sinker length, diameter and density. These results will provide a set of reference data that describes how sinking velocity is independently related to each system variable. This allows for a quantitative and qualitative assessment of how accurately a model replicates the same dependencies.

Additional experiments are also presented in this chapter which investigate and quantify interesting phenomena observed during the sinking of cylinders. These experiments include varying the allowed range of axial tilt during descent and modifying the geometry of the leading cylinder face.

3.2 Methodology

A physical model was constructed comprising of a 6 m long acrylic cylinder (acrylic being chosen for its transparency), vertically mounted, closed at the bottom end, and filled with a fluid (water or glycerine). Metallic cylinders and spheres of various lengths and diameters were then released at the top end of this apparatus and allowed to sink. The time to pass a number of carefully marked rulings was electronically determined and processed with the aid of a computer.

The physical model is highly simplified compared to an actual borehole disposal scenario. In a real DBD situation, the hole would be filled with brine, there would be a geothermal gradient and drill casing would line the inside of the borehole. The simplifications are necessary to ensure that the results will be directly relevant to tractable mathematical models. Inclusion of thermal gradients, concentration gradients and a perforated inner casing are possible, but obtaining analytical solutions of the Navier-Stokes equations would then become impossible, leaving only numerical solutions. Such intricacies are beyond the resources of the present research.

Two different physical apparatus were used: one in which the tube inner diameter was 6.4 cm and one in which it was 1.2 cm. The smaller scale set-up is necessary for testing viscous fluids and very long cylinders, which becomes problematic for reasons explained later in this chapter.

By measuring the time for the sinking objects to pass a series of known marked positions on the tube, it was possible to determine the terminal velocity (a point of mechanical equilibrium) in each case. The dependence of terminal velocity upon κ (the ratio between tube inner diameter and sinker diameter), density and length was then obtained.

3.2.1 Experimental Strategy

For a given tube diameter and fluid, an appreciation of the mechanics of sinking suggests that the key variables affecting the terminal velocity of a sinking (regular) cylinder are likely to be the length, the radius and its density. For a spherical sinker, only radius and density are significant.

A set of sinkers was therefore utilised allowing these variables to be systematically varied, one at a time. A range of five cylinder lengths were available between 5 and 25 cm. Each of these lengths were available with four different diameters in the range of 4.2 to 6.0 cm. These diameters correspond to diameter ratios (the ratio of the diameter of the sinker to the I.D. of the wide bore tubing) between 0.66 to 0.94. This range of values has the added advantage in that it reflects the range of waste package and inner borehole diameter ratios proposed in DBD [7]. All of these cylindrical sinkers were available in both aluminium and steel, giving 2 different densities. In total, 40 different cylindrical samples were obtained for the main group of sinking experiments. Figures 3.1 and 3.2 show the range of lengths and diameters explored.

Figure 3.1: Full range of diameters for cylindrical deployment objects for the large-scale apparatus, including the smallest 4.2 cm diameter sample to the left, to the largest 6.0 cm diameter sample to the right. £1 coin added for comparing scale.

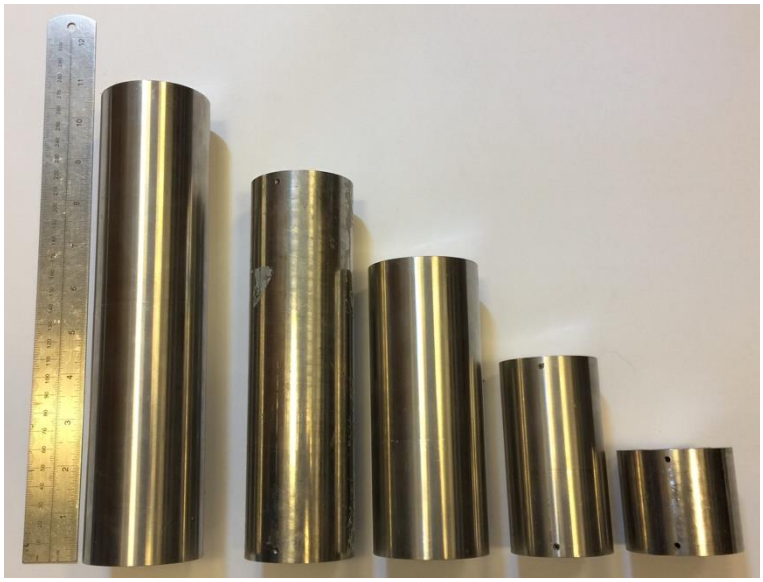

Figure 3.2: Full range of lengths for cylindrical deployment objects for the large-scale apparatus, including the largest 25.0 cm high cylinder to the left, to the shortest 5.0 cm high cylinder on the right. Metal, 30 cm ruler added for scale.

The length and diameter of each cylindrical sample was measured using Vernier callipers such that the measurements had a precision of ± 0.05 mm. The samples were weighed using a digital balance with an accuracy of ± 0.05 g for masses up to 2 kg, and ± 0.5 g for samples over 2 kg. The mass range was 0.2 – 5.6 kg.

Density was calculated from the ratio of mass to volume. For cylindrical samples, the volume was calculated from: $V = \pi D^2 L/4$. Diameter and length were measured at several different points on the cylinders and the mean value recorded in each case. The largest uncertainty in density was therefore 0.3 %.

Steel ball bearings of different diameters were additionally obtained. In addition, some cylinders were constructed with different front face geometries, while other sets of experiments were performed on cylinders employing centralising spacers.

3.2.2 Apparatus Design

The ‘delivery’ tubes were constructed of acrylic – a lightweight, inexpensive plastic which has the advantage of being transparent and easily sourced in convenient lengths and diameters. The tubing was supplied in 2 m lengths (the longest lengths available): the narrow bore tubing had an internal diameter (I.D.) of 12 mm and an outside

diameter (O.D.) of 14 mm. The wider bore tubes had an I.D of 64 mm and O.D. of 70 mm. The outer diameter of these tubes were carefully chosen to closely match the I.D. of larger pieces of available tubing. These larger sections were placed around the 2 m acrylic lengths in order to form joints (see figure 3.3). 2 of these joints were created for each apparatus, making them each have a length of 6 m.

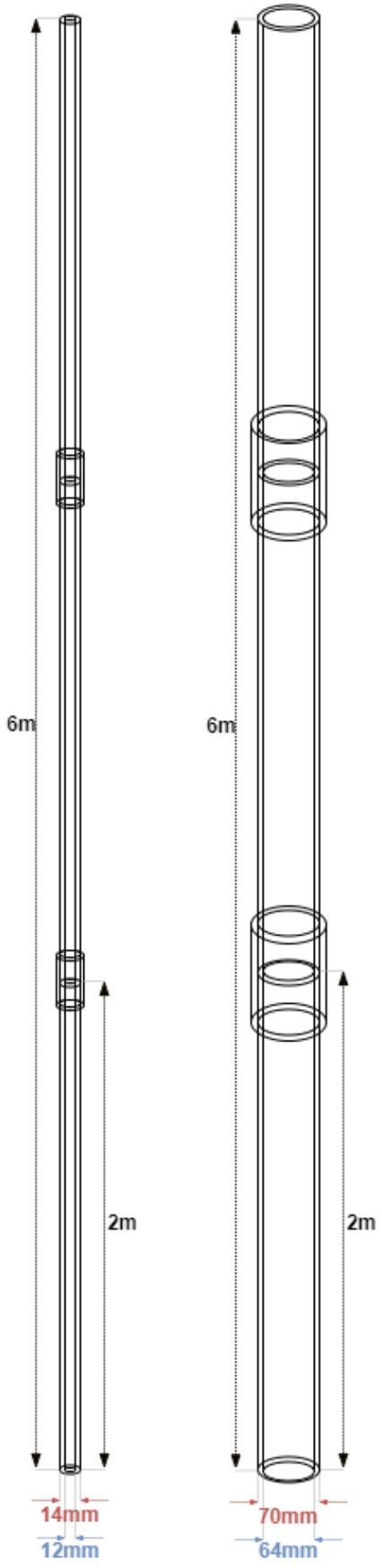

Figure 3.3 Schematic diagram showing narrow and wide bore tubing set-up.

The joints were packed with silicone grease to both aid assembly and provide a good seal. Initial tests using the wide bore apparatus resulted in water leaking from the joints (this is largely due to the greater pressures placed on the joints when the larger sinking objects pass by, and a 2 mm discrepancy between joining tubes). To overcome this problem, grooves 1 mm in depth were machined into the end sections of the tubing and these were fitted with rubber O-rings to yield a tighter joint (Figure. 3.4).

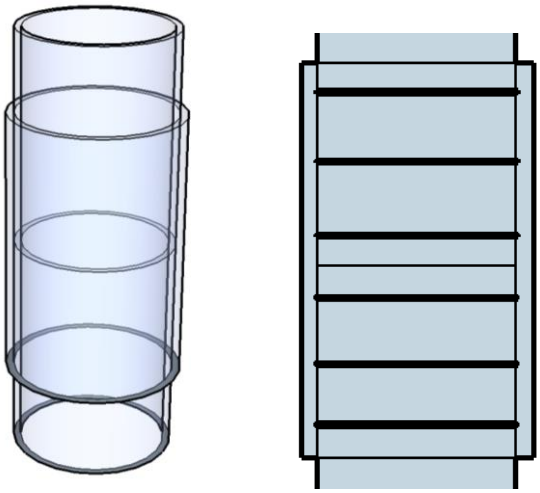

Figure 3.4: Apparatus tubing connection for narrow bore (left) and wide bore (right) apparatus. A length of tubing of similar inner diameter to the main apparatus outer diameter encloses each connection. The large apparatus includes an additional array of o-rings to reinforce the connection.

Both the narrow and wide bore 6 m tubes were mounted vertically in the laboratory using a system of hose clips (narrow bore) and pipe clamps (wide bore). A measuring tape was attached to the side of each tube to aid placement of a series of graduated marks (see later).

The base of each apparatus was closed off using removable plastic screw caps enabling drainage of the fluid and retrieval of the sinking object at the conclusion of an individual experiment. For the wide bore apparatus the screw mechanism is more complex; to drain the larger volume of fluid a tap (standard hose-pipe connection) was fitted to the screw base. A damping mechanism was devised to protect the tap from the impact of a sinker. This damping system comprised a large rubber puck of height 1 cm and diameter 5.5 cm, with a 2 cm diameter hole drilled through its centre. An aluminium puck of similar dimensions was placed immediately below the rubber puck,

and attached to the former using waterproof adhesive. Holes were drilled in the centre of the metal puck radially (figure 3.5) to help distribute fluid pushed through the whole damping device and facilitate the inflow of fluid upon filling the apparatus from the tap mechanism. A scissor jack and tri-stand were used to support the base of the tubing and prevent the screw cap and damping device being forced down by the impact of large sinkers.

Figure 3.5: Damping and draining mechanism used in the wide bore apparatus (see main text for details: a) schematic, b) actual photograph.

An overflow device was fitted to the top of both sets of apparatus to catch any fluid displaced as a sinker is submerged at the start of an experiment. This device comprised a rectangular plastic container with a height of 17 cm and a width of 11 cm. These dimensions were chosen to deal with the worst case scenario of a cylinder having the largest volume and hence displacing the greatest amount of fluid.

With the aid of the tape measure, a total of seven timing gate assemblies were attached to each tube. The first timing gate was placed around 20 cm from the top, this allows for a controlled submersion of each cylinder before release, without triggering the timing sequence. The next 4 were placed at 1 m intervals, so that sinking velocity could be conveniently calculated during experiments, to confirm that cylinders had reached terminal velocity; the fifth timing gate was therefore located 420 cm from the top of the tube. The sixth and seventh timing gates were adjusted between sets of experiments depending on the length of the cylindrical sinkers. On average, these two gates were at distances of 485 and 550 cm from the top of the apparatus. The strategic position of these latter 2 timing gates was chosen to prevent previously deployed sinkers from continuously triggering the final timing gate, therefore allowing more than one sinker to be deployed before the need to remove the screw cap and retrieve them at

the end of an experiment. It also prevented the possibility of bubbles (produced due to turbulent mixing as the sinker reaches the closed end) triggering the seventh and final timing gate prematurely. The timing gate assemblies comprised of a plastic clamp into which 2 holes were drilled. In one hole, an LED was embedded. In the second, facing hole, a photodiode was introduced, again held in place with blu-tack. This pairing of LED and photodiode created a light beam across the tube, which, when interrupted by a passing non-transparent object, would allow current to flow around a relay. Fig 3.6 shows a close-up of the timing gates used in narrow and wide bore tube assemblies while Fig 3.5 shows the relay circuit diagram.

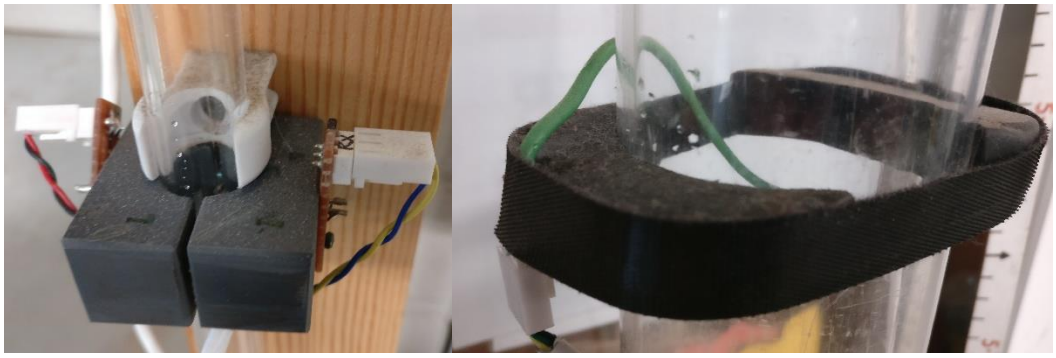

Figure 3.6: Close up images of the smaller bore (left) and larger bore (right) timing gates.

The electric relay circuit was connected to an Arduino which itself was connected to a laptop computer. The computer code used to drive the Arduino is listed in Appendix D.

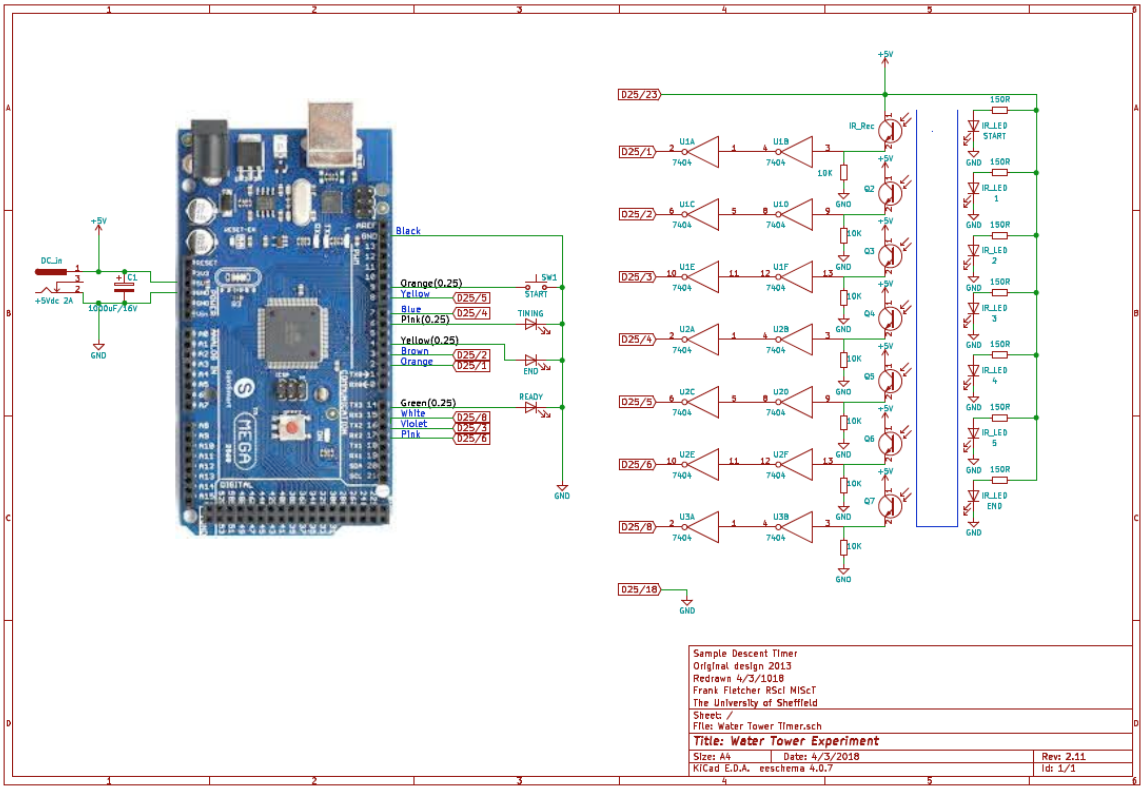

Figure 3.7: circuit diagram showing the electrical connections in the relay circuit used for the timing gates.

3.2.3 Timing gate adaptations for spherical sinkers

For the experiments which used ball bearings as the sinking objects, the timing gates described above were found to be problematic, yielding inconsistent and wildly inaccurate timings. This problem arose when ball bearings with a small radius were deployed – the path of the sinker was not typically straight, meaning that they could pass through a timing gate without crossing the central light beam. Some different timing gate designs were trialled but the most consistent results were obtained with the following device:

1) Two identical, 60 frames per second (fps) cameras were mounted on the wide bore apparatus (all spherical sinking experiments were performed with the wide bore tubing). One was placed at a distance of 1.875 m from the top, the other was placed within 28.2 cm of the closed end of the tube. The distance of 1.875 m was chosen based on the observation that the majority sinking cylinders had reached terminal velocity far before this depth.

2) Three marks (graduations) were made at each camera location, one at the central focal point, and one 3 cm either side of this line.
3) The cameras were synchronised using a 60 fps digital clock so that each was accurate to within 0.02 s of one another.
4) Viewing the camera footage, it was possible to determine the time at which the sinkers passed the central graduated lines.

Figure 3.8 shows a snapshot from the footage taken by the 2nd camera of a sphere passing the markings. The timestamp appears in the lower right portion of the figure.

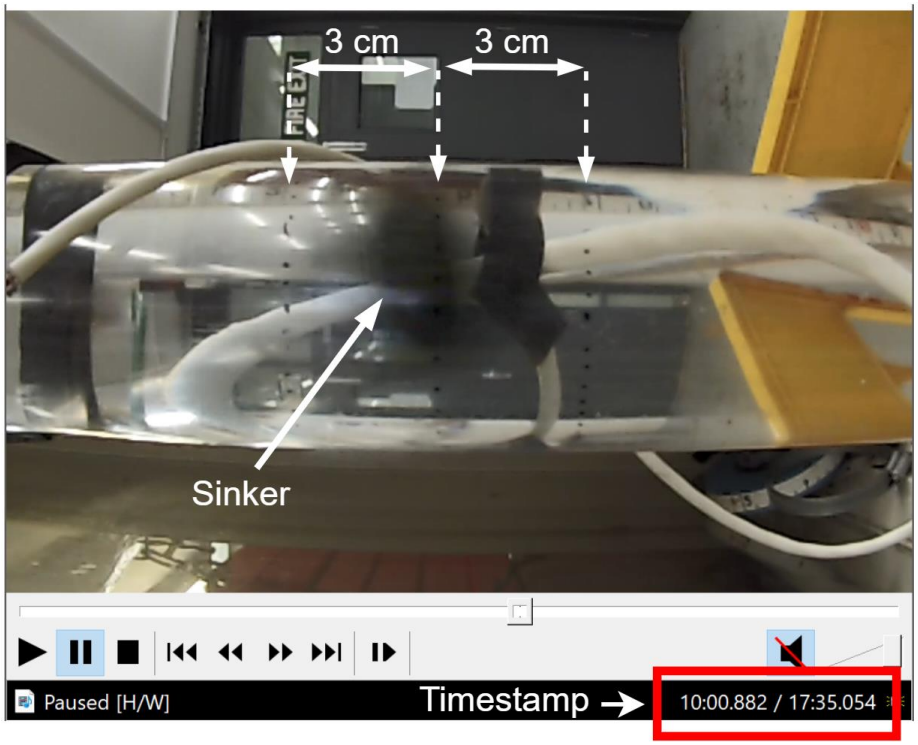

Figure 3.8: A snapshot from the second motion camera in which a sinking ball is seen to descend through the marked scale. The timestamp is shown to a thousandth of a second.

3.3 Determination of terminal velocity

3.3.1 Calculation of terminal velocity of cylindrical objects

The experimental procedure consisted of filling the tube with water and allowing the water to reach room temperature for several hours. The Arduino code was initiated. Then, holding the sinking object so it was just submerged at the top of the tube (taking

care to ensure it was positioned as centrally as possible), it was released. As the sinking object passed through each of the timing gates, the timer recorded the instant that each light beam was broken.

An example of the raw experimental data is shown in Table 3.1 for a test case using a 25 cm long aluminium cylinder with a 4.2 cm diameter (using the wide bore tube), repeated 5 times.

Table 3.1: Table representing the output data from the Arduino for 5 repeated sinking experiments using an aluminium cylinder of 25 cm height and 4.2 cm diameter.

	Time (s)					
Run Number	Gate 2	Gate 3	Gate 4	Gate 5	Gate 6	Gate 7
1	0.855	1.533	2.184	2.844	3.419	3.663
2	0.875	1.561	2.209	2.873	3.450	3.697
3	0.844	1.528	2.180	2.844	3.423	3.670
4	0.856	1.536	2.189	2.853	3.434	3.675
5	0.733	1.413	2.065	2.729	3.305	3.552

Using this data, the sample velocity at each timing gate was calculated using the difference in position and time between that and the previous timing gate. These velocities are depicted in figure 3.9, where it is clear that a plateau is reached after the second gate (first shown velocity). This trend is consistent with the majority of cylinders, with the exception of certain steel 20 & 25 cm length samples. These are terminal by the third timing gate; for the sake of continuity, the terminal velocity of all samples is therefore calculated using third and final timing gate data. Taking measurements using these far-apart timing gates (as opposed to multiple readings from closer timing gates) gives the largest distance possible when calculating velocity, resulting in the lowest possible margin of error (see equation 3.1).

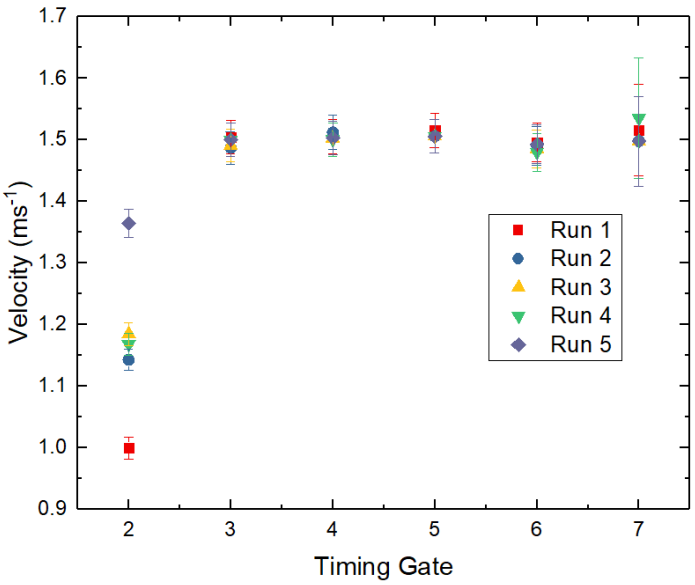

Figure 3.9: Local velocity of an aluminium cylinder of 25 cm in height and 4.2 cm in diameter. Local velocity is calculated using the distance and difference in time between the previous timing gate. Errors are calculated using measurement errors described in equation 3.1.

3.3.2 Estimation of uncertainty

The instantaneous velocities were calculated from a ratio of distance and time. The uncertainty in the velocity, ΔU can therefore be estimated from

$$\frac{\Delta U}{U} = \sqrt{\left(\frac{\Delta d}{d}\right)^2 + \left(\frac{\Delta t}{t}\right)^2} \tag{3.1}$$

Where d is the separation distance and t is time taken to reach a timing gate measured from the previous one. The precision with which the distance could be measured depended on the accuracy with which the tape measure could be read. The measuring tape had a marking discretisation of 0.5 cm, giving a precision of no more than ± 0.25 cm for a single measurement. The distance between any two timing gates requires 2 measurements to be made, giving a 0.5 cm uncertainty in the distance. This uncertainty was then doubled to take account of any slack in the (cloth) measuring tape. A final margin of error of Δd = 1 cm was therefore used for the distance between timing gates. When permanently disrupting a beam path, the time taken for the disruption to be registered is consistently less than 0.01 s. The uncertainty in measuring the time taken

to travel between successive timing gates was therefore taken as the upper bound, i.e. Δt = 0.01s. Inserting the values for the fastest travelling sinker (and therefore the worst case scenario sample in terms of error) into equation 3.1 gave a maximum relative error of 1% in the velocity.

Temperature would have ideally been kept constant to isolate any fluctuations in fluid density and viscosity between experiments. Unfortunately, this was not possible in the available laboratory. Furthermore, the relationship between sinking velocity and viscosity is not precisely known, making temperature fluctuations intractable to a quantifiable error. Temperature is therefore assumed to be room temperature, and not recorded during experiments.

To minimize the effect of unaccounted errors such as temperature, each sinking experiment was repeated. Experiments were repeated a total of 5 times due to time limitations (mostly due to drain and refill times) and a relatively limited spread. A previously recorded reference sinking measurement was repeated several times over the apparatus lifetime to confirm consistency. The reported velocities are always quoted as the arithmetic mean of these values[1]. The uncertainty is taken to be one standard deviation from the mean; the standard deviation of velocity, σ_v, was therefore obtained using

$$\sigma_v = \sqrt{\frac{\sum_{i=1}^{N}(U_i - \bar{U})^2}{N-1}} \tag{3.2}$$

where $\bar{U}$ is the average velocity for a set of repeated experimental values and N is the number of repeat runs (5 in this work). The standard deviation was found to dominate the error calculated using equation 3.1 in almost all cases, therefore that value is used as the uncertainty for the majority of results. When this was not the case, the systematic error calculated using equation 3.1 was used instead.

For the example velocity measurements shown in section 3.3.1, the systematic and random errors were calculated using equations 3.1 & 3.2. The example cylinder is both the longest and narrowest sample, giving it has one of the greatest velocities. This

[1] A median was dismissed due to the relatively low sample size (resulting in a 'jumpy' median) and a lack of significant outliers, making the averaging resistance provided by a median unbeneficial.

results in a relatively large systematic error of 0.008. In comparison, the random error calculated using equation 3.2 gives an error of 0.004. In this case, the systematic error is used to give a velocity of $1.501 \pm 0.008\ ms^{-1}$. For a full table of cylindrical sample data and respective error, see Appendix E.

3.3.3 Calculation of terminal velocity of spherical sinking objects

Using the 2 camera arrangement described in the previous section, the terminal velocity was calculated from the ratio of the known separation of the 2 cameras and the difference in time stamps from frames showing the object passing the central graduation at each camera position. Figure 3.10 shows snapshots from both cameras together with the time stamps. In this example, the ball bearing travelled a distance of 3.843 m and took a time of 18.06 s. The terminal velocity was thus recorded as $0.213\ ms^{-1}$.

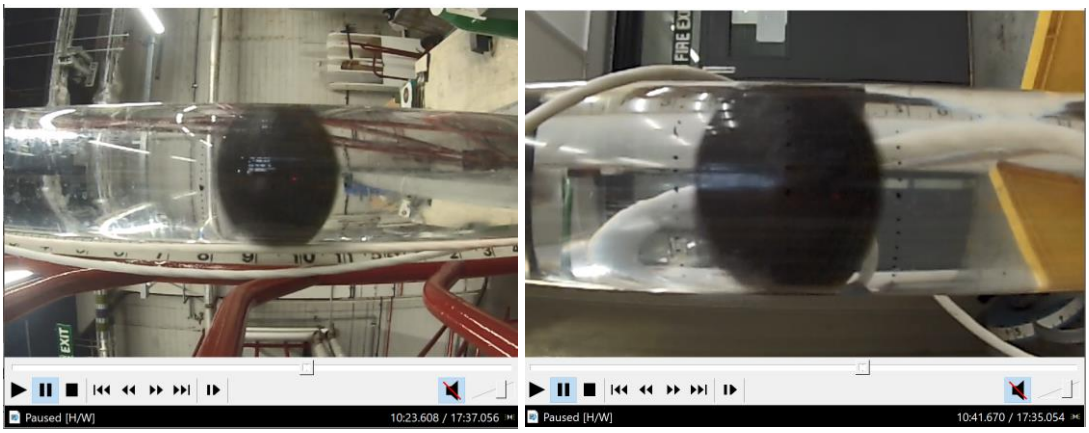

Figure 3.10: A snapshot of the top (left) and bottom (right) cameras showing the same sphere recorded at different positions (and therefore times) of a descent.

The error in the terminal velocity calculation was given as the maximum of the standard deviation of a set of 5 repeat experiments and the error calculated using equation 3.1. The uncertainty in the time measurement in this case is $\Delta t = \pm 0.02$ s. The uncertainty in the distance measurement was an additional Δd of ± 1.5 cm, making a total Δd of ± 2.5 cm. The larger uncertainty in distance (compared with the cylindrical samples) arises from the fact that each frame is 0.02 s long and may not correspond to an image of the object passing the graduation. For an object sinking at 1.5 ms^{-1}, this would result in 3 cm of movement per frame, hence the size of graduations.

3.4 Results for cylinders

Results are presented for sinking experiments involving cylinders, including ones in which the front face was modified to give them an angular profile, ones in which centralising spacers were added and finally a set of experiments involving steel ball-bearings. Unless stated otherwise, all experiments shown in the following sub-section were performed using the wide bore apparatus.

3.4.1 Baseline Results

A broad insight into the importance of cylinder parameters was obtained by comparing a minimal set of sinkers with disparate lengths, densities and diameters. Table 3.2 shows the combinations of these variables explored in four pairs of baseline sinking experiments (labelled A-D).

Table 3.2: length and diameters of the baseline set of sinking experiments representing a combination of large / small length and diameter. Each set (A-D) also consists of a high and low density sinker.

Set	Diameter (cm)	Length (cm)
A	6.0	10
B	6.0	25
C	4.2	10
D	4.2	25

Terminal velocity (U) is given for each of the baseline experiment sinkers in figure 3.11, where several clear observations can be made:

1. The higher density steel samples sink faster than aluminium ones in all cases.
2. The sinker diameter has a greater effect on U than length.
3. Sinker density, length and diameter must *all* contribute to U.

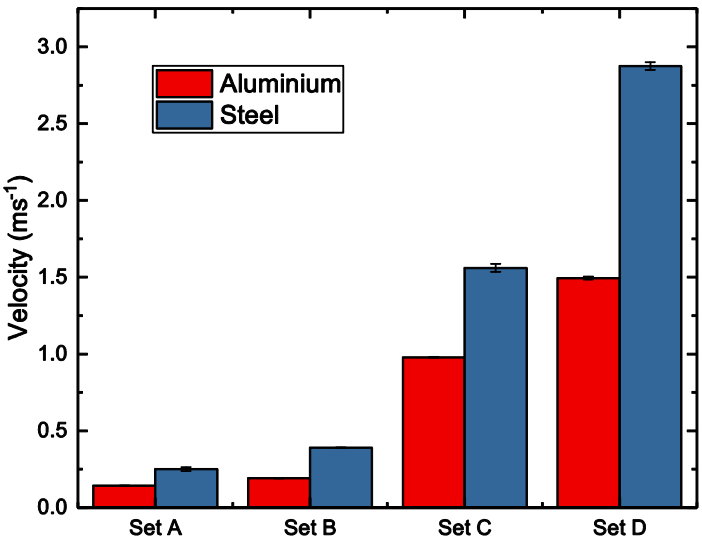

Figure 3.11: *U* for sets of aluminium and steel cylinders. See Table 3.2 for key.

These baseline results were used to plan a more extensive set of sinking experiments, described in the following sections.

3.4.2 Dependence of terminal velocity on sinker diameter

The baseline results of the previous section outlined the importance of diameter in determining *U*. To further explore this effect, 5 sets of experiments were performed using aluminium cylinders of different diameter but the same length; each set used a different length.

The results from these experiments are shown graphically in Figure 3.12. The results clearly show an approximate linear dependence of *U* with the ratio of the sinker diameter to the wide bore tube I.D, κ. *U* decreases with increasing κ regardless of length, approaching zero as $\kappa \rightarrow 1$.

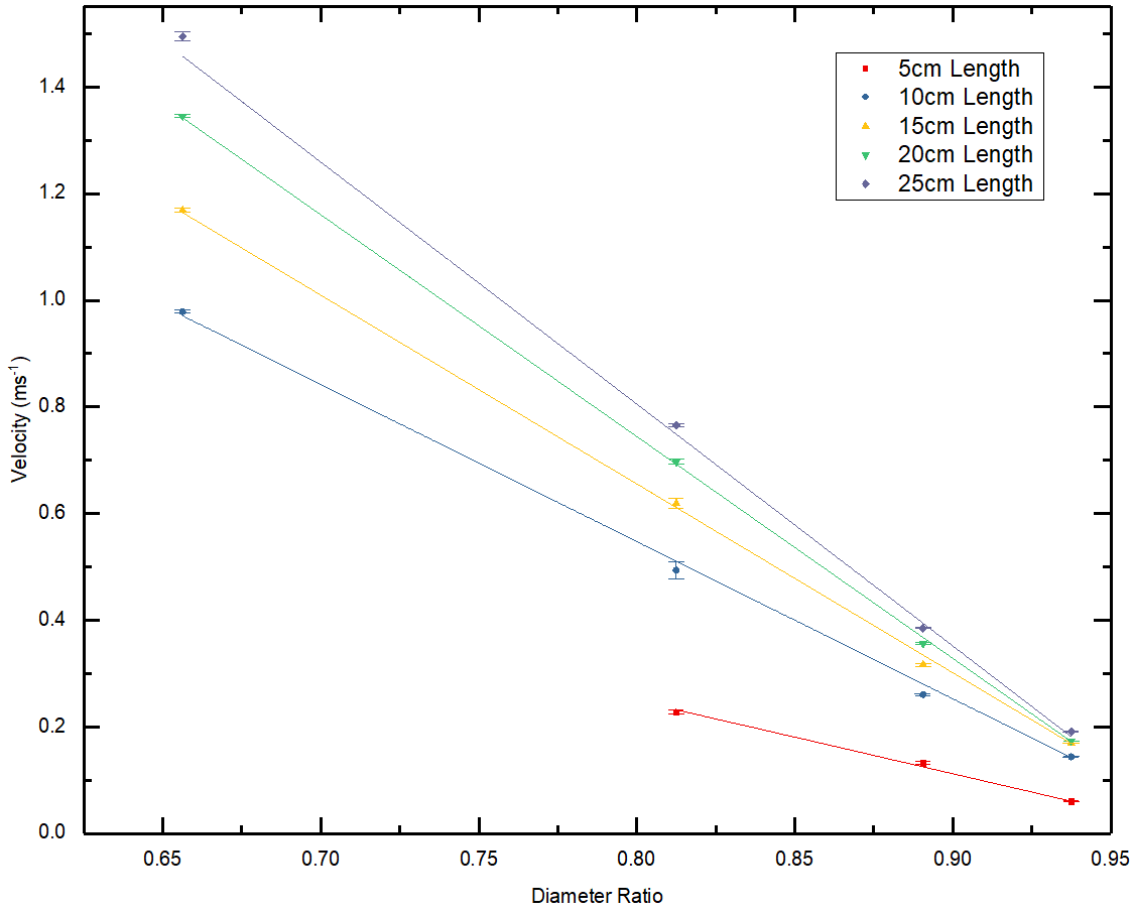

Figure 3.12: *U* as a function of κ for aluminium cylinders of various length. The lines are least squares linear fits to the data. As shown, errors are relatively small in comparison to the variance in data. Error bars are presented for the remaining figures in this chapter, but are often smaller than the marker symbols.

Figure 3.12 shows that this linear decrease with κ applies for all cylinder lengths. However, the gradient *does* depend on length, becoming steeper with increasing length. The data set for the 5 cm length cylinders is noteworthy. The magnitude of *U* is uncharacteristically lower than for the longer samples and the dependence upon κ is also weaker. A possible explanation for this comes from an observation that shorter cylinders were observed to rotate in the axial plane during their descent. This warranted an additional investigation to quantify this effect, which is presented in section 3.4.6.

Figure 3.13 shows a plot of the gradients of the least squares fit lines shown in figure 3.12 (*i.e.* $\frac{\partial U}{\partial \kappa}$), together with data obtained for steel cylinders. Data for the 5 cm sinkers has been omitted due to the reasons given above. The graph shows more clearly how the rate of change of *U* with κ increases as the cylinder length also increases. This

dependency of gradient on length is non-linear and seems to be approaching a plateau – more easily seen with the aluminium data set.

The difference between steel and aluminium samples diminishes for shorter cylinders. To quantify, $\frac{\partial U}{\partial \kappa}$ is about 1.5 times greater for a 10 cm steel cylinder than it is for the same cylinder constructed from aluminium. For cylinders 25 cm in length, the gradient for steel samples is about twice that of aluminium samples.

Mathematically, figure 3.13 suggests that cylinder diameter and length must appear as a product (each raised to some unknown power) in the formula for *U*. Furthermore, the apparent plateau behaviour suggests that the exponent of length is less than unity.

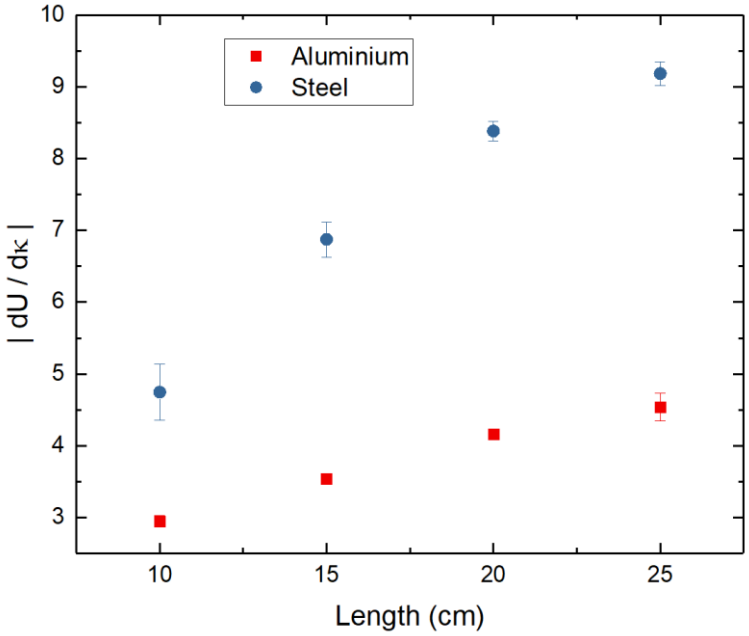

Figure 3.13: The gradient of the velocity-diameter relationship for steel and aluminium sinkers (excluding 5 cm length data set). Error bars reflect the uncertainties in the least squares fits to the data contained in figure 3.12.

Figure 3.14 compares the *U*- κ gradients for wide bore and narrow bore experiments. It is clear from the graph that the same linearity is preserved using the smaller scale apparatus though the magnitude of *U* is much lower. This is evidence that the mechanisms which determine how diameter affects *U* remain the same throughout different scales of experiment magnitude.

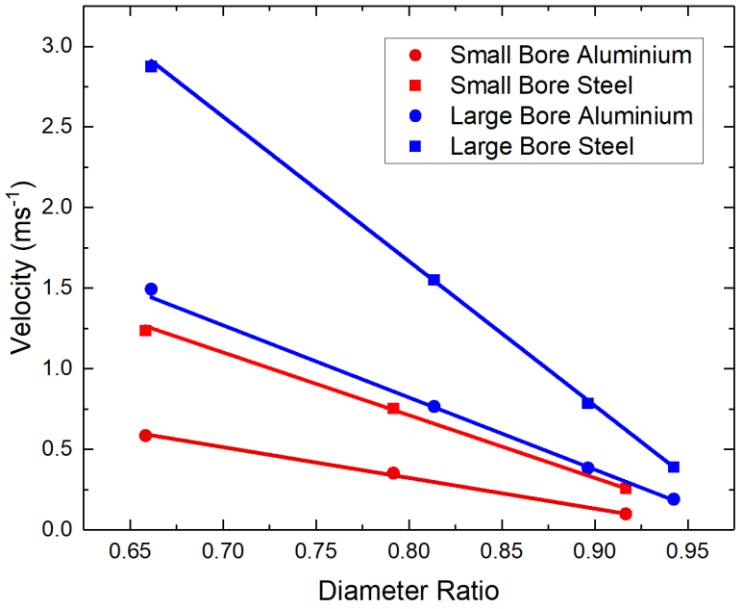

Figure 3.14: *U*-κ relationship for steel and aluminium cylinders in both the large and small bore apparatus. Cylinders are of 4.35 and 25 cm length for small and large scale experiments respectively.

3.4.3 Dependence of terminal velocity on sinker length

The next set of experiments were designed to investigate the effect of length on *U* at fixed κ. Figure 3.15 shows the relationship between length and *U* for aluminium samples at given κ.

The results show that *U* increases monotonically with increasing length. Each data set appears to show asymptotic behaviour at long cylinder lengths. Furthermore, the larger the κ, the lower the length required for an asymptotic *U* to be observed. Figure 3.15 also confirms the hypothesis that κ has a greater effect on *U* than length.

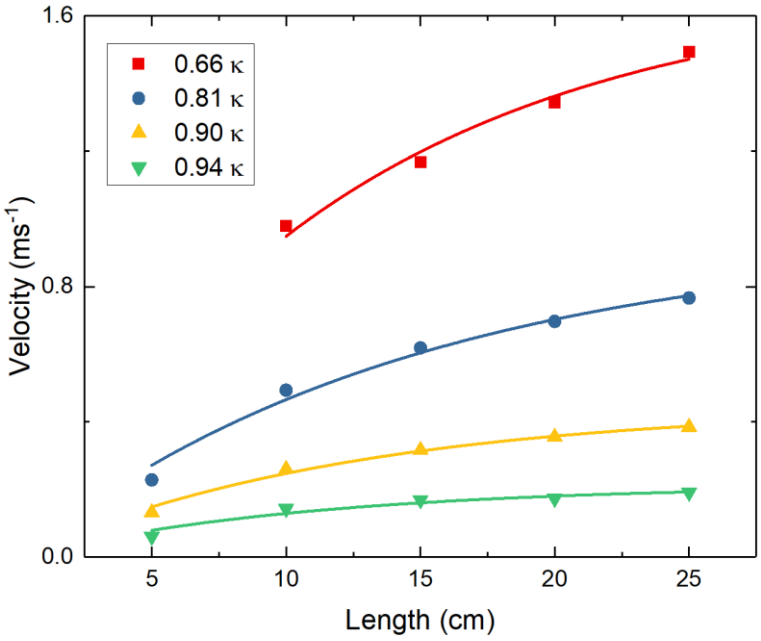

Figure 3.15: *U* plotted as a function of cylinder length. Samples are aluminium, and include a range of κ. Plot symbols are the experimental data, lines are added as a visual guide using fits to $U = \alpha[1 - \exp(-L/\beta)]$, where α and β are arbitrary fitting variables.

To further investigate the hypothesis of an asymptotic *U*, the data set was extended to longer lengths. Due to the practicalities of performing a sinking experiment with a relatively long cylinder, a new sinking experiment, using a steel cylinder with a length of 45.7 cm, was conducted using the *narrow bore* apparatus. The extended set of sinking data (all with $\kappa = 0.79$) for this apparatus is plotted in figure 3.16. The plot appears to confirm the existence of an asymptotic *U* for long cylinders, though there are too few points to say this conclusively. Extending the results to still longer cylinders would require a new, longer apparatus to be constructed – beyond the resources of this study.

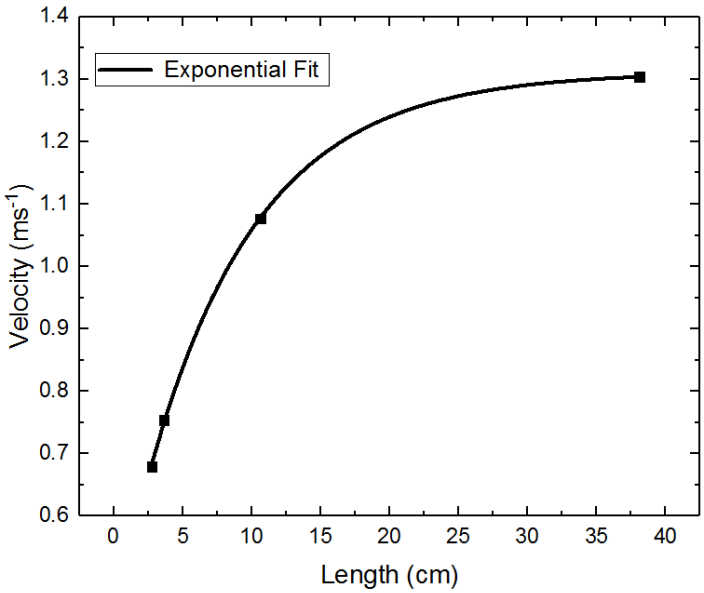

Figure 3.16: Variation of velocity with cylinder length for an extended length range. Experiments were performed using the narrow bore apparatus. Steel samples of 0.79 κ were used.

To explore the effect of density upon the length dependence of *U*, the length to *U* relationship for samples of 0.89 and 0.94 κ are compared between aluminium and steel density counterparts in figure 3.17.

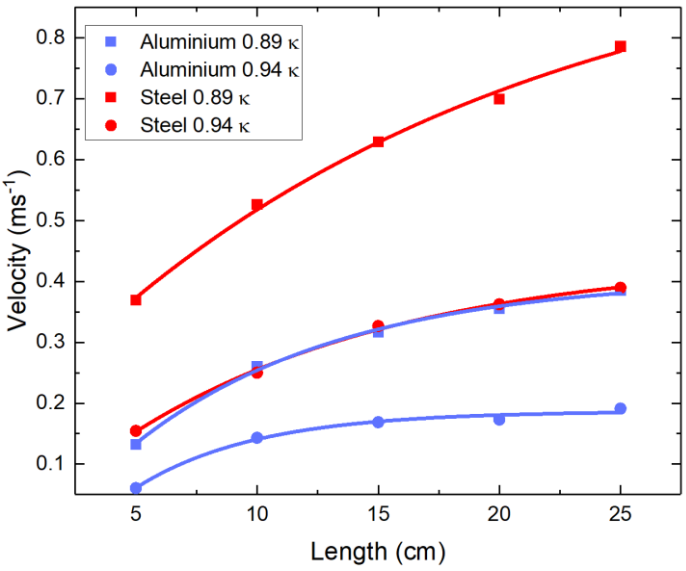

Figure 3.17: Relationship between *U* and length for aluminium and steel cylinders with diameters of 0.89 and 0.94 κ.

From the figure it is clear that higher density results in greater U. However, the change with length as a function of density is subtler. Aluminium samples have a greater increase in U with a change in length than steel ones; a five-fold increase in cylinder length results in at least a factor of two increase in U for steel samples, regardless of diameter. For aluminium samples, this is closer to a factor of three. These results are somewhat skewed by the abnormally low U found for the 5 cm long aluminium cylinders. When these are discounted, an increase in length results in a similar change in U for steel and aluminium cylinders.

Figure 3.17 also shows a greater increase in U as κ decreases for steel cylinders compared to aluminium. In fact, the results for the 0.94 κ aluminium samples are almost indistinguishable from those of the 0.89 κ steel samples. While this is fortuitous, it does indicate that hydrodynamic braking at large κ is enough to overcome the density difference between steel and aluminium. It suggests that κ must appear to a greater magnitude of power than sample density in any U expression.

3.4.4 Dependence of terminal velocity on sinker mass

A change in length gives rise to a change in mass. To isolate the effect of length from mass, the following experiment was performed. Two cylinders with the same diameter (0.66 κ) but different densities were fabricated such that they both had the same mass of 0.555 kg. The resulting lengths of these samples were 14.8 cm and 5.0 cm for aluminium and steel respectively. Both samples were centralised to avoid axial tilt (see section 3.4.6 for further details).

The results from two sinking experiments are displayed in the form of a bar chart in figure 3.18.

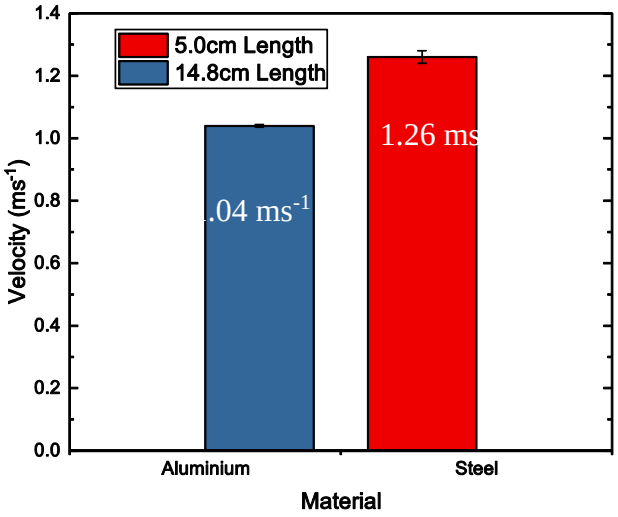

Figure 3.18: *U* of two samples with different density, different length, but the same κ and mass (0.555 kg). The sinkers were centralised using the methods discussed in section 3.4.6.

Figure 3.18 shows a relatively small increase (21 %) in *U* for the denser steel sinker. The far greater length of the aluminium cylinder has increased its *U* such that it almost outweighs the decrease resulting from its comparably lower density compared with the shorter, steel sample.

This shows that length cannot appear in the *U* equation with a higher power than density, since density has a greater effect than length. This is shown in figure 3.18, where a 3-fold increase in length results in just a 17.5% increase in *U*. Alternatively, for the same, 5 cm steel cylinder a 3-fold decrease in *density* results in a 48.4% decrease in *U*).

The dependency of cylinder length upon *U* is compared between the smaller and larger scale apparatus in figure 3.19. The comparison uses steel samples of almost identical density[1] and near consistent κ values of 0.79 and 0.81. This results in a sinker diameter of 0.95 cm for the narrow bore apparatus, and 5.2 cm for the wide bore apparatus. Results show similar qualitative behaviour as a function of sinker length. *U* clearly increases more rapidly with length in the wide bore experiment compared with the narrow bore one.

[1] Different grades of Steel are sourced for each scale experiment, with an average density of 7871 and 7903 kgm^{-3} for small and wide bore apparatuses respectively.

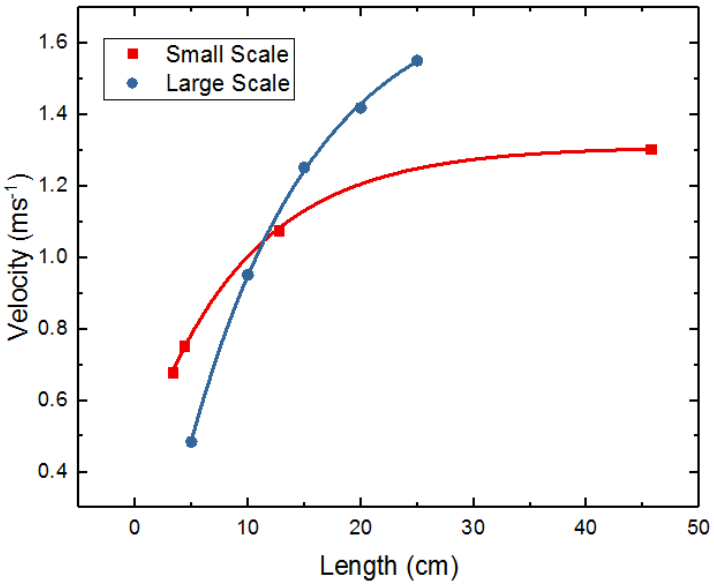

Figure 3.19: *U* plotted against length for narrow and wide bore apparatus. Steel cylinders of 0.79 and 0.81 κ were used for the narrow and wide bore apparatus, respectively.

3.4.5 Axial Tilt

During the experiments described in the previous sections, a possible disparity in results appears to occur for shorter cylinders. This is particularly marked for short, narrow cylinders, to the point that samples 5 cm long with a 4.2 cm diameter (0.66 κ) became lodged in the tube during deployment (this is true for both aluminium and steel cylinders). This behaviour appears to be due to axial tilt (figure 3.20).

Axial tilt is where a cylinder tilts such that its longitudinal axis is rotated. The degree of this available rotation is limited by the length and diameter of each sample, as shorter length and lower diameter samples experience a larger range of axial freedom before coming into contact with the tube. It is of interest to calculate the maximum tilt angle for a cylinder of a given length and diameter to quantify the angles at which jamming may occur.

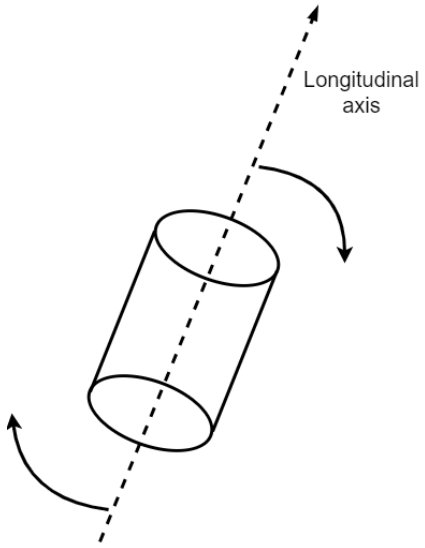

Figure 3.20: Schematic diagram illustrating axial tilt.

For the purpose of this analysis, cylinders are simplified as rectangles with height *h* and width *a*, as shown in figure 3.21.

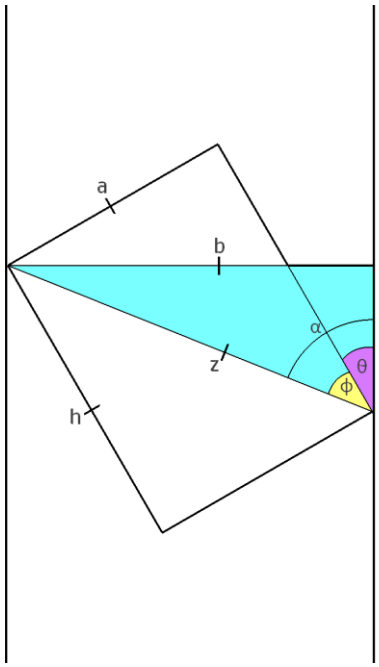

Figure 3.21: Axially rotated cylinder, with an imposed triangle used to calculated the angle of axial rotation, θ.

To calculate the maximum angle of rotation, the rectangle diagonal *z* and the angle φ between rectangle diagonal and height are required. These may be calculated using simple Pythagoras and trigonometry respectively.

$$\varphi = tan^{-1}\left(\frac{a}{h}\right) \tag{3.3}$$

$$z = \sqrt{a^2 + h^2} \tag{3.4}$$

A right angled triangle is constructed using the diameter of the apparatus *b* and the rectangle diagonal *z*, as shown in figure 3.21. Simple trigonometry may then be used to calculate the angle α between rectangle diagonal and apparatus:

$$\alpha = \sin^{-1}\left(\frac{b}{z}\right) \tag{3.5}$$

Finally, the tilt angle is given using:

$$\theta = \alpha - \varphi = \sin^{-1}\left(\frac{b}{\sqrt{a^2 + h^2}}\right) - \ tan^{-1}\left(\frac{a}{h}\right) \tag{3.6}$$

Equation 3.6 is used to calculate the allowed angle of rotation for every cylinder that did *not* get jammed during deployment. The highest of these angles is 16.4°. In comparison, a similar analysis of the cylinders which *did* get jammed resulted in a lowest θ of 38.5° - it can therefore be concluded that the critical θ at which jamming may occur must be between 38.5° and 16.4°.

The limiting tilt angle can be used to determine the necessary cylinder aspect ratio to avoid jamming. Taking the worst-case-scenario of critical tilt angle limit to be 16.4° for 0.5 κ, the diameter-to-length aspect ratio of the cylinder must be least 5:18.

3.4.6 Use of centralising spacers

To quantify the effects of axial rotation on sinker velocity, the rotation must be controlled independently of cylinder geometry. This was achieved by using adjustable centralising spacers arranged as shown in figures 3.22 and 3.23. Centralising spacers consisting of grub screws are fixed to the cylinder. For sinking experiments where the spacers are not required, the screw can be fully inserted.

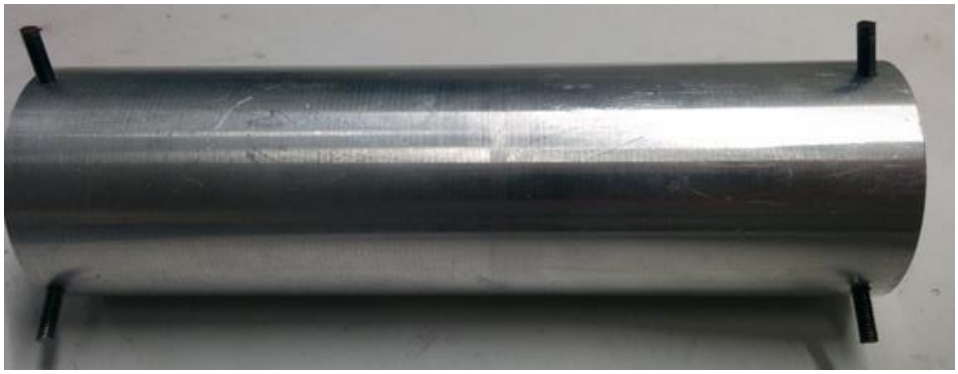

Figure 3.22: Image of a cylinder with extended centralising spacers.

Centralising spacers were integrated into all but the largest diameter samples, where axial rotation is minimal due to the reduced annular clearance. This gave a total of 30 samples with centralising spacers, each with specific pin length to give an identical sum of spacer and sample radius, referred to as 'effective radius' as illustrated in figure 3.23. This allows a consistent degree of axial freedom whilst investigating dimensional variables such as diameter and length. Unless stated otherwise, the effective radius used herein was 30.5 cm, measured using Vernier callipers. κ remains defined as previously - the sample radius divided by tube I.D.; the 'effective radius' should have no effect on clearance.

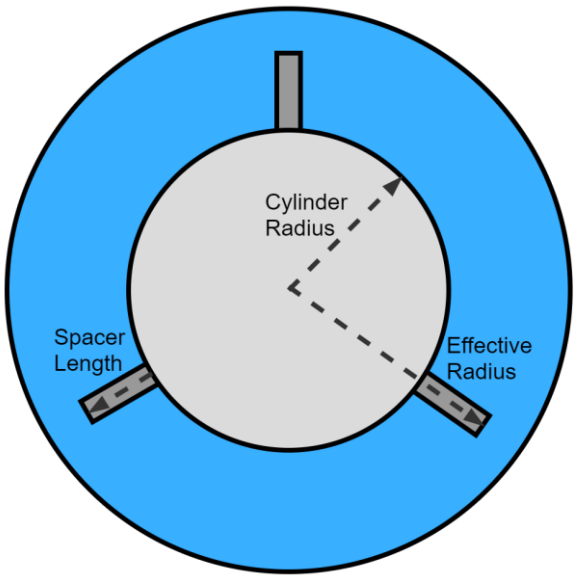

Figure 3.23: Cross-sectional view of a cylindrical sample with centralising spacers, including the labelled original sample radius, length of centralising screws, and the combined effective radius.

Results comparing *U* of centred and conventional cylinders are shown in Figure 3.24. The effect of centralising spacers is to generally lower the *U* compared to the non-central counterparts. An exception is the shortest length (5 cm) cylinders, in which the centralising spacers result in an *increase* in *U*. Another feature of the results displayed in Figure 3.24 is a divergence in *U* between centralised and non-centralised samples with increasing cylinder length.

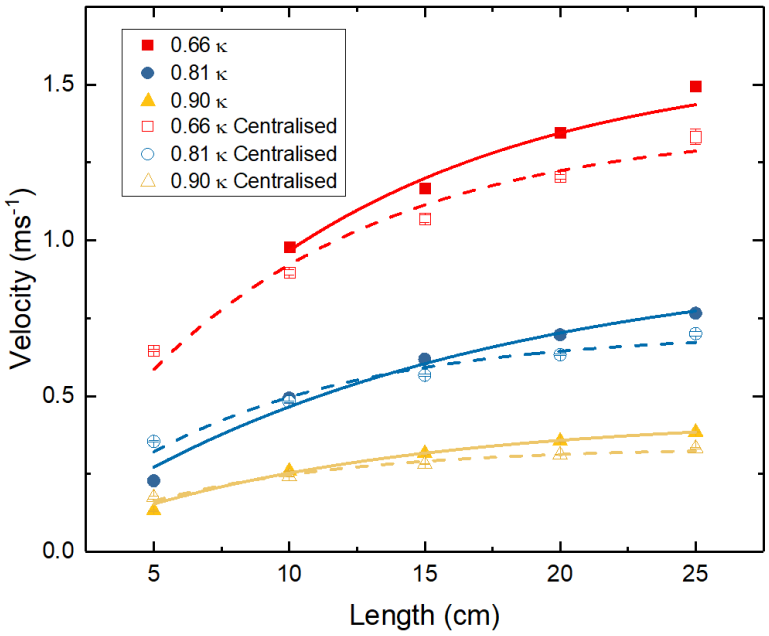

Figure 3.24: *U* comparison between axially centred conventional cylinders as a function of length. Data series are fitted with the exponential-maxima function described previously.

There are several possible explanations for the *decrease* in *U* observed for the majority of centralised cylinders:

(1) The centralising spacers create frictional drag.

(2) The spacers make contact with the tube walls, creating additional friction.

(3) Axial tilt motion can aid the displacement of lateral fluid to behind the cylinder, creating a downward force in a similar manner to aquatic propulsion.

The small size of the spacers effectively rules out reason (1). Reason (2) is a possibility as is reason (3). To investigate (2), an additional experiment was performed in which the effective diameter of the centralised cylinders was lowered by adjusting

the spacer pins. A sinking run was conducted using a 25 cm long cylinder with a diameter of 5.2 cm, with the spacers adjusted so as to give an *effective diameter* of 5.8 cm. The result from this experiment was then compared with the *U* of a non-centralised sample of the same physical dimensions (effective diameter 5.2 cm) and a centralised cylinder, spacers fully extended (effective diameter 6.1 cm). The results are displayed as a bar chart in Figure 3.25.

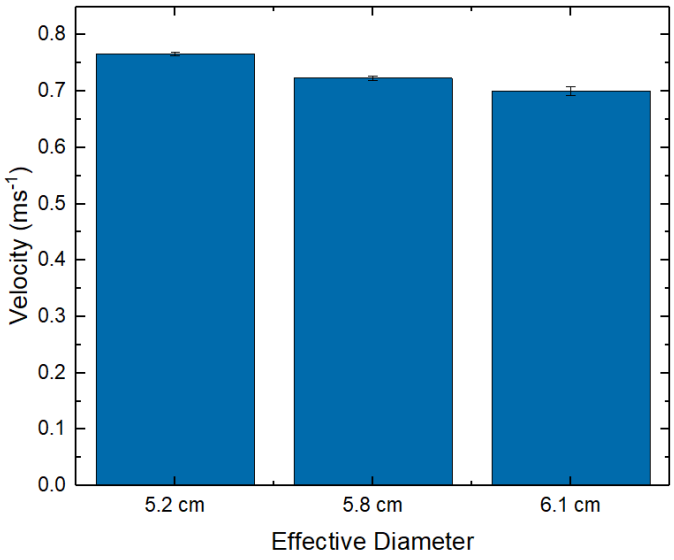

Figure 3.25: *U* of a cylinder with spacers completely inserted, partially inserted and at full width of the cylinder.

The results displayed in figure 3.25 show that a partial extension of the spacers yields a *U* between that of a fully centralised and conventional cylinder (non-centralised). This rules out reason (2) because *U* is still lower than the unpinned sample. However, it does provide support for hypothesis (3) since partial extension of the spacer pins allows for a limited range of axial tilt, but not to the extent that having no pins at all does.

If this hypothesis is correct, one might also expect that a longer length cylinder would displace a larger volume of fluid during tilt, increasing the magnitude of propulsion. This may explain the divergence in velocity with increasing length.

The relationship between *U* and κ for fully centralised and standard (non-centralised) cylinders was next investigated. For these sinking experiments, aluminium samples were used, ranging from 5 cm to 25 cm in length. These results are shown in figures 3.26a-3.26e.

Apart from the 5 cm long samples, the trend is for centralised samples to travel with a lower U than non-centralised ones. This difference diminishes with decreasing clearance (increasing κ). For a given κ, the difference increases slightly with increasing length until about 20 cm, after which length has minimal effect.

The vanishing of U difference with increasing κ adds further support to the tilt propulsion hypothesis, since the tilt magnitude will vanish as clearances become tighter.

The increase in U for centralised 5 cm cylinders may be explained by a limited range of tilt in which propulsion is generated in a beneficial direction. In biological systems the tilt angle is controlled by a self-correcting shape and / or mechanical assistance. The form factor of a cylinder is unlikely to induce a change in tilt direction, therefore a cylinder freefalling through an infinite fluid (and no-longer colliding with a container) would be expected to continuously rotate. In this extreme instance, the fluid displacement would no longer induce propulsion in the longitudinal axis and kinetic energy would simply be lost to fluid friction – if energy is indeed lost to friction in this extreme instance, at a certain degree of rotation the energy losses due to friction must overpower any gains in U through propulsion.

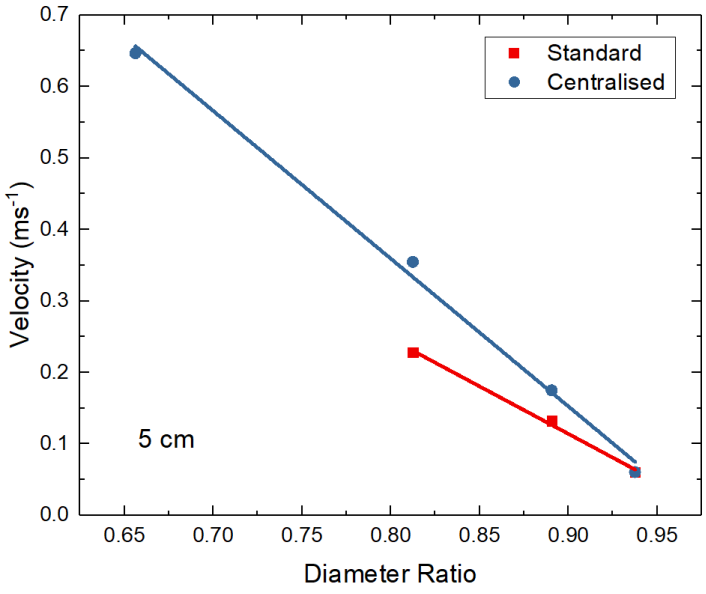

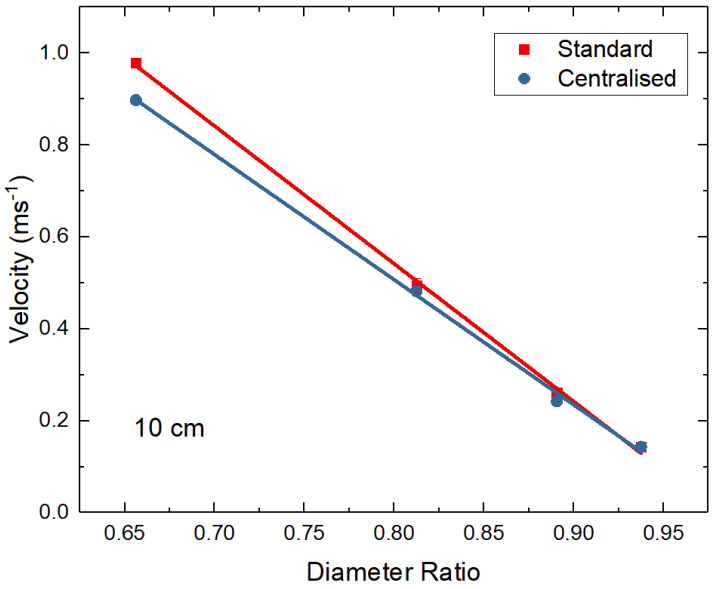
Standard
Centralised
Velocity (ms-1)
1.0
0.8
0.6
0.4
0.2
0.0
10 cm
0.65
0.70
0.75
0.80
0.85
0.90
0.95
Diameter Ratio

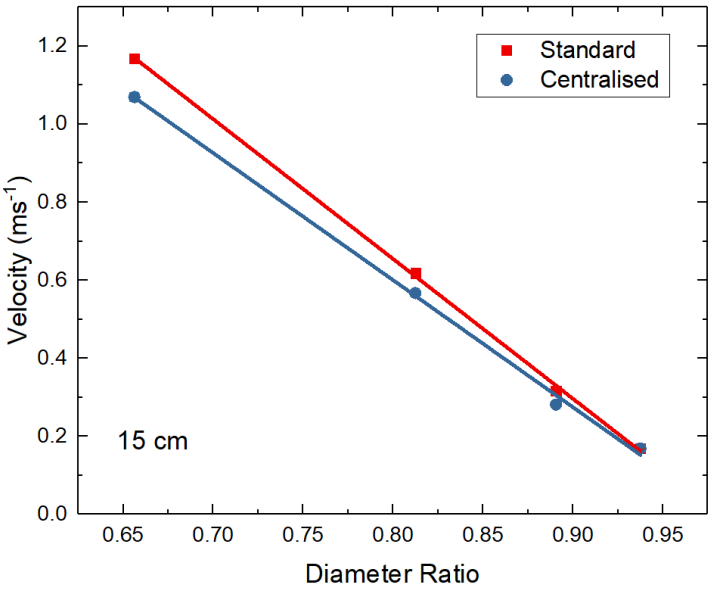
Standard
Centralised
Velocity (ms-1)
1.2
1.0
0.8
0.6
0.4
0.2
0.0
15 cm
0.65
0.70
0.75
0.80
0.85
0.90
0.95
Diameter Ratio

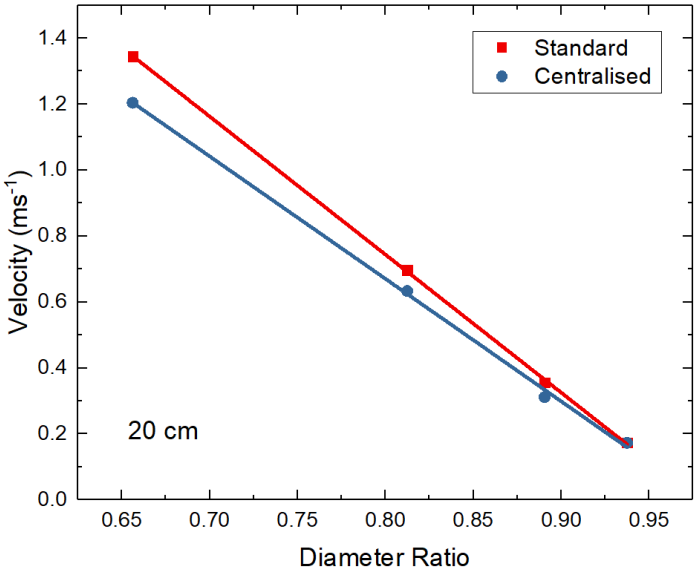

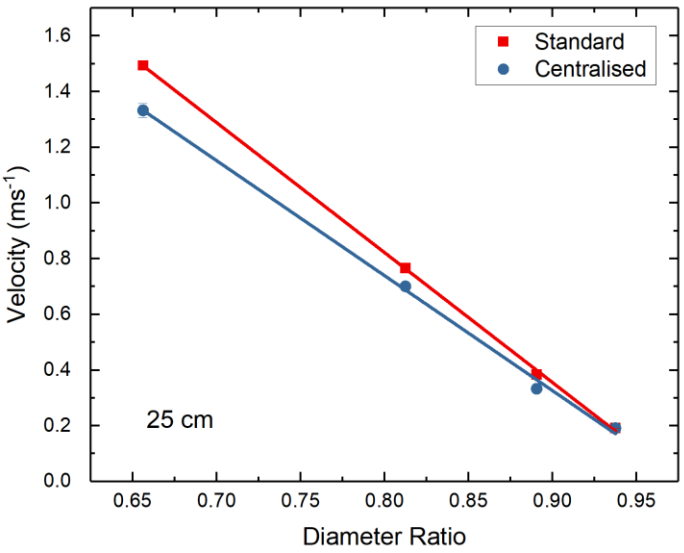

Figures 3.26 (a-e): Comparison of U for centralised samples versus non-centralised samples as a function of κ and cylinder length. All samples were aluminium. Each graph represents a given cylinder length, between 5 cm (figure 3.26 a) and 25 cm (figure 3.26 e).

3.4.7 Investigation of front face geometry

The front face of cylinders was modified in an attempt to quantify the effects of leading face geometry on sinker U.

Aluminium samples of 1.1 cm diameter with a streamlined leading edge were created by machining a smooth cone at the front face. Three samples are used, one with

a conventional cylinder geometry, another with a cone of height twice the diameter (cone A), and another of cone height equal to that of sample diameter (cone B). The length of each cylinder (not including the conical height) were adjusted so that each sinker had a mass of 32.8 g. For pragmatic reasons (cost and speed), these samples were made from aluminium and designed for the narrow bore apparatus.

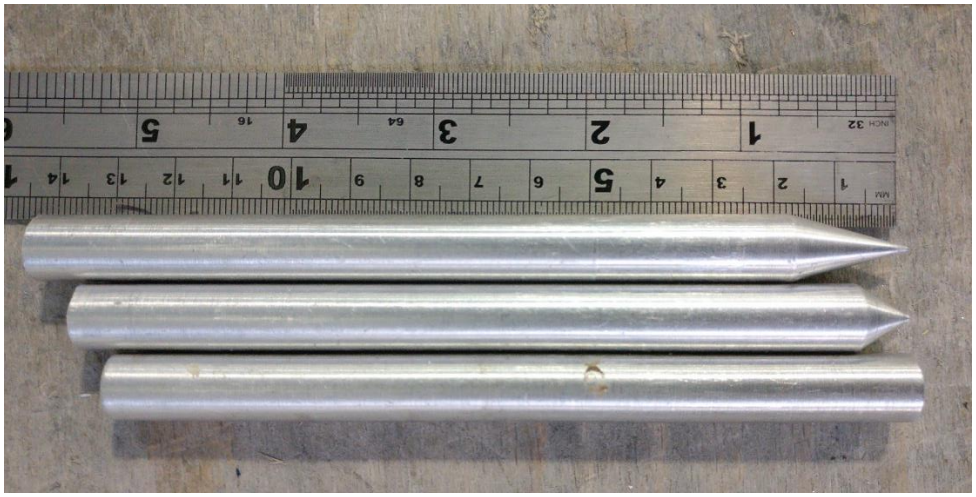

Figure 3.27: The 3 aluminium samples used to investigate the effects of the front face on sinker *U*. Cone A (top) has a cone of height twice its diameter, cone B (centre) has a cone height equal to cylinder width, and finally a generic cylinder of equal diameter (1.1 cm) and mass (32.8 g) is shown at the bottom.

To quantify the effects of the sinker front face, *U* was recorded in an analogous manner to previous samples. Results are shown in figure 3.28, where a streamlined front face is shown to increase *U* by up to 12.6%. The results show that all sharp edged samples attain a higher *U* compared with the conventional cylinder. The sharpest angle cone (cone A) appears to travel at a slightly faster *U* in comparison to the less sharply-angled cone (cone B), suggesting that the angle of cone further streamlines fluid at the leading face. This difference is minimal however, when compared to the difference between cone B and the cylindrical sample. This suggests that simply removing the perpendicular surface to the fluid boundary makes the greatest significance.

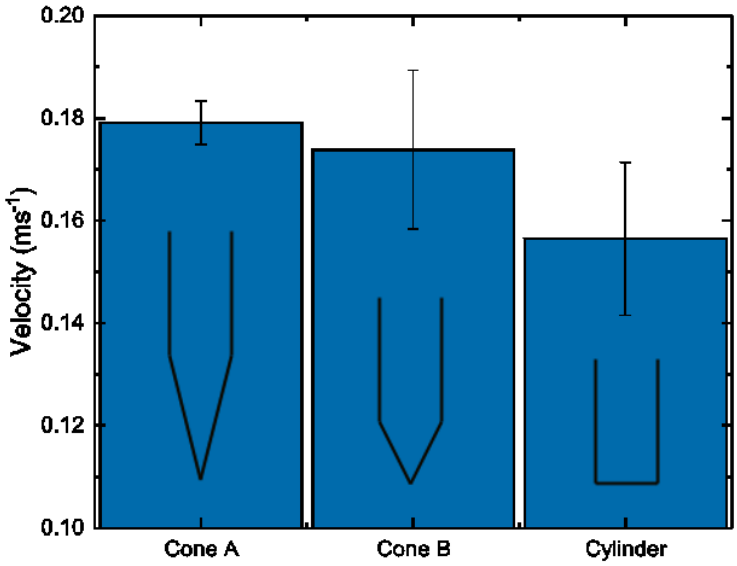

Figure 3.28: *U* for three aluminium cylindrical sinkers of 1.1 cm diameter with different leading face geometries.

3.4.8 Effect of fluid viscosity

The Reynolds number of a fluid characterises the nature of the flow, which can be laminar, turbulent, or a mixture of these. The behaviour of sinkers in alternative flow regimes was investigated by repeating the sinking experiments using a fluid with a considerably higher viscosity than water.

Glycerine was chosen for the experiments due to having a much greater viscosity than water, and being a readily available, low-toxicity, relatively transparent Newtonian fluid. The sourced glycerine is 99.5% concentrate, therefore having a density of 1260 kg m^{-3} and dynamic viscosity of 1.26 Pa s [133]. Results were performed using the narrow bore apparatus to reduce the required volume (and hence cost) of glycerine.

A complete set of *U* results for samples travelling through water and glycerine is shown in table 3.3. It is shown that cylinders travel between 1-2 orders of magnitude slower through glycerine. The Reynolds number of annular flow can be calculated using

$$Re = \frac{2\rho\bar{v}_a R(1-\kappa)}{\mu} \tag{3.7}$$

where $\bar{v}_a$ is the average annular fluid velocity in the axial direction, which can be calculated using sinker *U* [63]. The Reynolds number for annular flow past a cylinder in glycerine is -1 orders of magnitude, or *O*(-1), but *O*(3) in water. It can be concluded that an *O*(4) increase in Reynolds number results in a *O*(2) increase of *U*.

Table 3.3: Dimensions of cylindrical sinkers and their *U* measured in water and glycerine. All results are recorded using the small bore apparatus.

			U(m/s)	
Material	Diameter (cm)	Length (cm)	Water	Glycerine
Aluminium	0.79	4.35	0.586 ± 0.004	0.01 ± 0.01
Aluminium	0.79	12.7	0.86 ± 0.003	0.01 ± 0.01
Brass	0.79	4.35	1.327 ± 0.006	0.07 ± 0.08
Brass	0.79	12.7	1.97 ± 0.04	0.05 ± 0.05
Brass	0.95	4.35	0.77 ± 0.03	0.02 ± 0.02
Inconel	0.994	1.5	0.263 ± 0.003	0.01 ± 0.01
Steel	0.793	4.41	1.237 ± 0.007	0.1 ± 0.1
Steel	0.793	12.88	1.84 ± 0.02	0.07 ± 0.05
Steel	0.952	3.33	0.68 ± 0.002	0.02 ± 0.02
Steel	0.952	4.37	0.754 ± 0.003	0.03 ± 0.03
Steel	0.952	12.75	1.077 ± 0.005	0.03 ± 0.02
Steel	0.952	45.7	1.304 ± 0.003	0.03 ± 0.03

U is shown as a function of diameter in figure 3.29. The *U* dependence upon diameter appears to remain linear. The Reynolds number associated with glycerine means that sinking experiments performed in this fluid were in the laminar (creeping flow) regime, whilst in water the flow regime was turbulent. It can therefore be

concluded (albeit with a large error) that the observed linear *U*-κ relationship is true for both laminar and turbulent flow regimes.

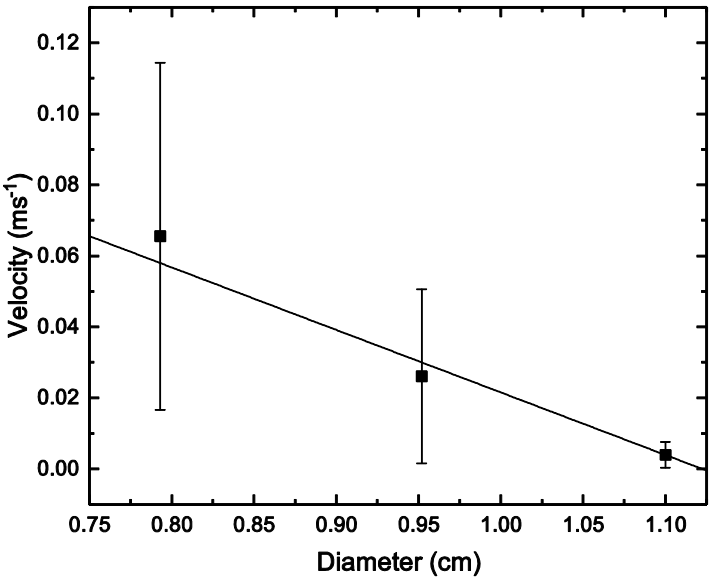

Figure 3.29: *U* of sinkers as a function of diameter in viscous fluid. Cylinders are 12.7 cm high and steel.

The *U*-κ dependence is also an order of magnitude greater than that of equivalent sinkers in water (-0.18 ± 0.03 compared to -4.7 ± 0.7). This is a reasonable observation, as it suggests that hydraulic braking is a function of the internal friction of a fluid.

The margin of error for samples descending through viscous fluids are large, as shown in figure 3.29 and table 3.3. A video analysis of sample deployment revealed that axial rotation is present, as observed in water. Through water, samples appear to *continually* rotate. Through glycerine, samples rotated *intermittently*, at a seemingly random rate. For example, in glycerine, samples are observed to rotate to a position of maximum axial rotation, then proceed to deploy through the apparatus fixed in this position. After a random period of time, samples would then oscillate from one position of maximum axial rotation to another. This significantly effects velocity.

Chen, Lescarboura and Swift postulated that eccentricity would decrease with length, due to an increased resistance to rotation imposed by fluid viscosity on the greater cylinder length [48]. Although there is no reason to disagree with the physics behind the authors' postulate, it has effectively been shown through an alternative

method of increasing this rotation resistance that this can in fact *increase* the observed eccentricity.

Figure 3.30 quantifies the aforementioned tilt effect by showing the local velocity of samples calculated at each timing gate, after velocity (momentarily) stops increasing. It is clear a constant velocity is non-existent, where velocity varies at a seemingly random rate. It would be difficult to account for this effect due to the seemingly random nature of oscillations. One possibility is to repeat the viscous experiments a large number of times, however the time taken to deploy certain cylinders and required volume of glycerine makes this study unobtainable within the available resources. Alternatively, the experiments could be repeated in the larger-bore apparatus, where cylinders could be centralised.

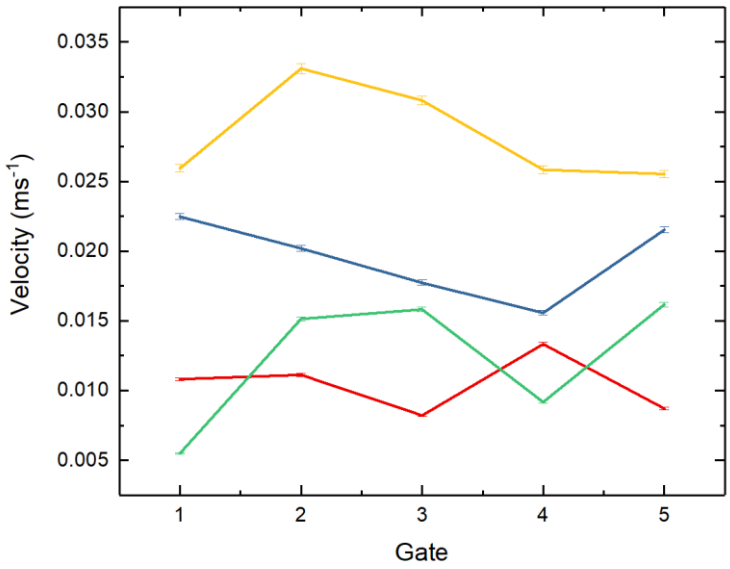

Figure 3.30: The local velocity calculated at each timing gate. Errors are determined using the measurement method (equation 3.1). Each data series represents a *different* sample. Sinking rate does not appear to reach a constant terminal velocity.

Glycerine of course differs in both viscosity and density to water. To investigate the dependencies of these relationships *individually*, additional experimentation outside of the available resources of this project would be required. This could include the repetition of experiments at different temperatures, as the viscosity of glycerine has a greater sensitivity to temperature in comparison to density, providing data sets of similar density yet varied viscosity.

3.5 Sinking experiments with ball-bearings

Sinking experiments were performed using spherical shaped objects (ball bearings) and the wide bore apparatus to determine the *U* dependence on diameter. Spherical samples provide an advantage over cylinders as they are more easily sourced and no machining need take place. Additionally, they differ markedly in their shape, particularly at the leading edge, which is expected to result in lower frictional drag. Spherical samples also provide simplified reference data for comparison with computational modelling, as well as give a link between experiment and theory (Stokes law).

3.5.1 Results

Figure 3.31 shows *U* plotted against diameter. *U* initially increases with increasing radius, passes through a maximum, then decreases. The maximum must correspond to the point at which the confining boundaries become important and hydraulic braking significant. A second order polynomial gives a reasonable fit to the data.

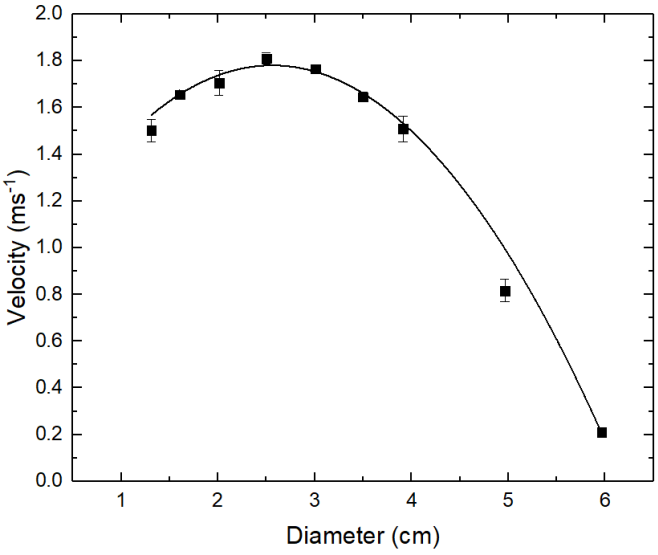

Figure 3.31: *U* relationship with diameter for steel spherical samples. The solid line is a least squares fit to a second order polynomial. The diameter of containing tube is 6.4 cm.

Spherical sinker results were compared with a variety of analytical and empirical solutions as discussed in section 2.2.2.1, including Stokes law (equation 2.47), extended Stokes law (equation 2.51) and the Munroe equation (equation 2.54). Each solution is

calculated using water viscosity and density reference values of 1.002×10^{-3} mPas and 998.2 kgm^{-3} respectively [134], [135]. The average density of samples used was 7850 $kg\ m^{-3}$. Results are shown in figure 3.32 for Stokes law and the Munroe equation. Both solutions are seen to overestimate experimental *U* throughout the diameter spectrum by up to four orders of magnitude. The Reynolds number of the smallest sphere is approximately 2×10^4. As this value is several orders of magnitude greater than the Reynolds number for creeping flow, the overestimation of Stokes law is unsurprising. Despite the overestimation of the Munroe equation, the curvature of the trend appears similar to experiment.

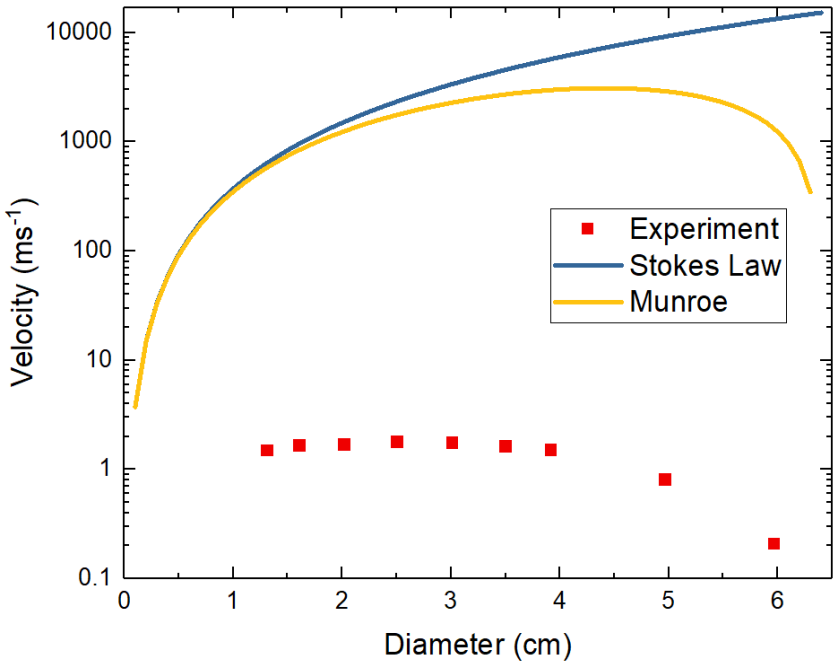

Figure 3.32: Comparison of experiment spherical sinker data to Stokes law (equation 2.47) and the Munroe equation (equation 2.54).

Figure 3.33 shows the high Reynolds number extended Stokes law equation compared to experimental results. The degree of fit is considerably improved, with most experimental data agreeing within an order of magnitude. At lower diameters experimental and extended Stokes law results are in excellent agreement, up to the diameter of 1.6 cm. The accuracy of the extended stokes law equation at low diameters suggests that it is accurate when boundary effects are negligible. This is evidence that for a sinking sphere with a Reynolds number of 10^4, hydraulic braking does not become significant until 0.25 κ. This is important, as previous literature suggests that boundary

effects are significant from 0.15 κ [42]. The contradiction in results suggests that turbulence shifts the point of boundary influence.

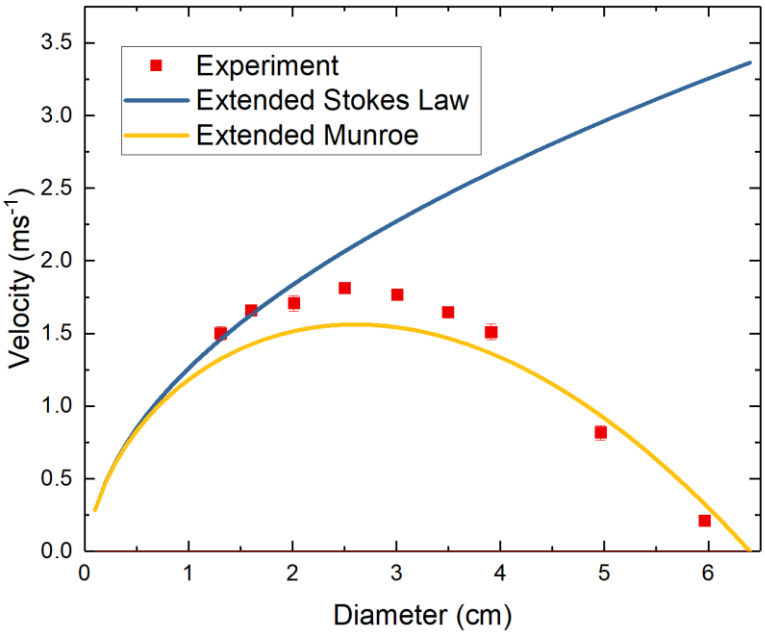

Figure 3.33: Comparison of experiment spherical sinker data to extended Stokes law (equation 2.51) and the extended Munroe equation.

The Munroe equation is simply a correction factor of U calculated through Stokes flow, U_∞. It is therefore suggested that as the extended Stokes formula shows good agreement when boundary effects are negligible, that a combination of the Munroe and extended Stokes law equation would give improved results. This is achieved by using the extended Stokes law to give the reference velocity U_∞. This solution is shown in figure 3.33, denoted as the 'Extended Munroe' data series.

The extended Munroe equation shows a much greater fit in comparison to previous solutions, predicting U within 13.8% accuracy. Results show especially good agreement for the location of the maximum U; a peak analysis applied to the experimental data gives a central peak location at sphere diameter 2.58 cm ($\kappa = 0.403$). In comparison, the peak maximum of the Munroe equation occurs at a diameter of 2.60 cm ($\kappa = 0.406$).

It is of interest to see how applicable these findings are to cylindrical sinkers. This was investigated by comparing U of similar-sized cylinders and spheres. A

cylinder geometry with an aspect ratio of $L\ /\ 2\kappa R = 1$ would give the ideal comparison with a sphere. The closest available approximation of this is a range of cylinders with $L = 5.0$ cm and $2\kappa R$ range between 4.2 and 6.0 cm (0.66 and 0.94 κ). It is well known that the volume of a sphere and cylinder differ significantly even when diameters and lengths are equal. For a cylinder of length and diameter equal to the diameter of a sphere, the cylindrical form factor gives an increased volume of 50%.

Cylinders were centralised (excluding the largest diameter) to reduce the effects of tilt. It may be argued that this is an unfair comparison due to spheres not being centralised; in reality, collisions for spherical samples are unlikely to induce phenomena such as propulsion as previously discussed.

U as a function of diameter for steel cylinders and spheres is shown in figure 3.34. Results show that the *U*-diameter relationship is linear for spheres within the same diameter region this behaviour was observed for cylinders. Spherical and cylindrical samples are in very close agreement with one another, to the extent that each data series is difficult to distinguish. To quantify, the slope of linear least squares fits gave values of 60 ± 2 and 63 ± 1 for cylinders and spheres respectively[1].

This leads to the final question relating to the *U* dependence on diameter: why do spherical and cylindrical samples show such close agreement? It has been shown that cylinders of equal length and diameter to the diameter of a sphere will have a 50% larger volume. The volume per-unit-length is therefore different for a sphere and cylinder. As a result, the net-gravitational force (combined gravity and buoyancy) must also vary differently per unit diameter. The lack of divergence means an additional counter-acting force must be at play.

[1] Omitting the non-centralised, 6.0 cm sinker.

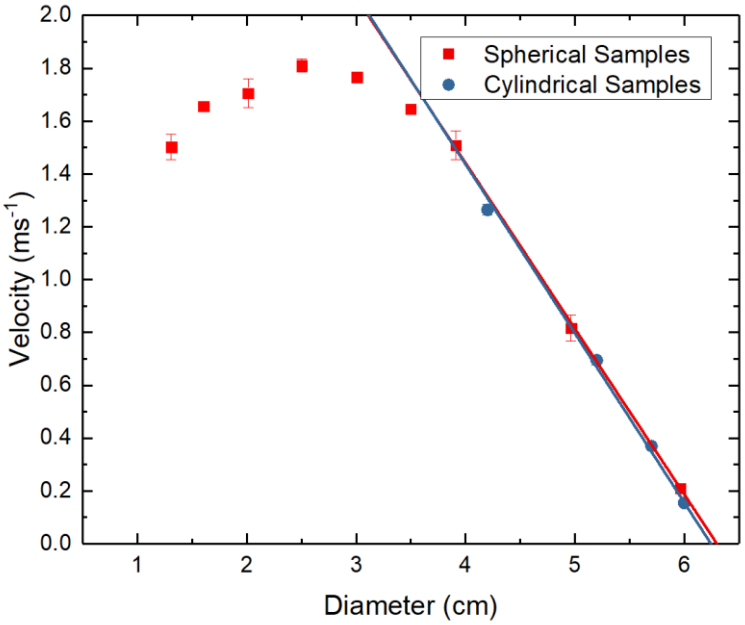

Figure 3.34: Comparison of spherical and cylindrical samples relationship with *U* and diameter.

One hypothesis is that gravitational forces are negligible compared to hydraulic braking. Previous evidence in figures 3.23 and 3.24 suggest this is *not* the case; for a diameter of 4.2 cm, increasing in cylinder volume by 100 % (from 5 to 10 cm) gives rise to an increase in *U* of 43 %. Additional phenomena to hydraulic braking must be at play.

Another explanation is the frictional force applied to samples; cylinders have a larger surface area adjacent to high-velocity fluid flow within the annulus, which would be expected to increase fluid friction. In comparison, an equivalent sphere will have an infinitesimally small region of surface area at this location of maximum fluid velocity. This is unlikely the cause for discrepancy, considering the limited difference in *U* for two samples of the same mass but different length discussed previously.

The most likely phenomenom is the path of fluid past the sinking object. Assuming that the closest moving fluid to a sinker closely follows the sinker surface when flow is laminar, a simple analysis of sphere and cylinder geometry can give the greatest possible flow path. For a sphere, this is simply half of the circumference, therefore for a sphere of volume 1 and radius of 0.62 the greatest flow path is 1.95. For a cylinder, the longest path would be the radius of both faces and the height of the cylinder; for a cylinder with the same volume of 1 and radius of 0.62, this flow path would be 2.07, a 6.15% increase.

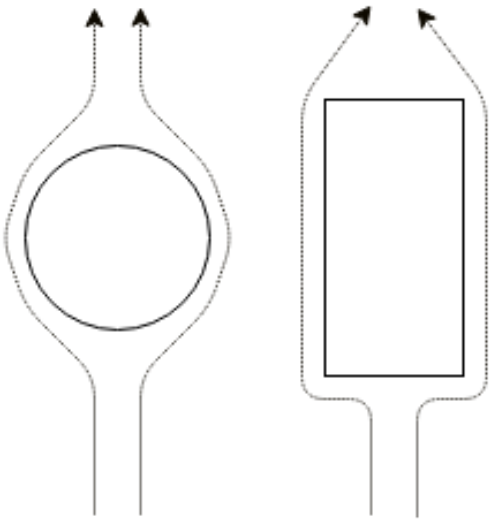

Figure 3.35: Flow patterns for spherical (left) and cylindrical (right) deployment objects. Fluid can be seen to travel around a sphere using a shorter path in comparison to cylinder samples, where fluid must transverse around the edges of the cylinder front face.

An entire velocity distribution of the surrounding fluid is required to quantitatively compare the flow paths of spheres and cylinders. This has not been achieved in its entirety for cylindrical objects (although simplified, partial solutions are the topic of section 4). However, in section 2.2.2.1 it is shown how the Navier-Stokes equations are used to give the velocity distribution of flow past a sphere, and the streamlines of the surrounding fluid. As distance from the object increases, these streamlines gradually dissipate until the fluid returns to its unperturbed streaming state. It would be reasonable to assume that a similar flow pattern would be observed for cylindrical objects, and therefore fluid would travel in a similar pattern to the cylinder geometry at close regions. As a result, a greater proportion of fluid entering the annular gap would be travelling perpendicular to the sinking direction, and a greater amount of energy will be lost redirecting this fluid behind the sinking object. This phenomenom was proven to be a factor of U in section 3.4.7, despite using significantly smaller samples.

3.6 Conclusions

Two scales of apparatus were used to investigate the sinking rate of various cylinders and spherical objects. All objects were observed to quickly reach terminal velocity within 2 meters of sinking.

Spherical sinking objects were more readily available, and were therefore used as a method to investigate a wide range of κ, and linking apparatus accuracy to previous literature. The extended Stokes flow equation (which omits the effects of boundaries) showed excellent agreement to experiments when $\kappa < 0.25$, validating apparatus legitimacy and indicating that boundaries are negligible for lesser values of κ (at the investigated *Re* range).

The Munroe equation was also applied to sphere results, and although the model over predicted *U*, the κ at which maximum *U* occurred was predicted to over 99 % accuracy. The Munroe equation clearly showed a strong qualitative description of the boundary effect; this prompted for an amalgamation of the Munroe and extended Stokes law equations, which proved to be a versatile model of predicting *U* with reasonable accuracy (up to 13.8 % error) over a wide range of κ and *Re*.

When systematically varying the parameters of all cylinders, *U decreased* linearly with κ. Both the cylinder size *and* the mass increase with κ; therefore the rate of increase in friction effects (by reducing annular clearance) outweigh the increase in gravity when increasing diameter (for $\kappa > 0.66$).

Increasing the length of a cylinder resulted in an increase in *U*, seemingly towards a plateau. An investigation attempted to confirm the theory of a plateau maximum by sinking long cylinders of up to 46 cm in length, although an absolute maximum could not be identified.

Results indicated that *U* is proportional to density in a similar fashion to length, with *U* increasing towards a plateau. This further suggests that a maximum *U* exists, and that *any* increase in gravitational force approaches this maximum. The fact that an increase in κ reduces any increase in *U* via length *or* density suggests that this maximum is imposed by an annular throughput limit.

Future work is recommended to confirm or refute the existence of the aforementioned maximum sinking velocities; this would simply entail the sinking of increasingly long and dense cylinders (a progressively expensive investigation).

Increasing *either* the length or density also increases the magnitude of the linear κ-U gradient. It may therefore be concluded that these variables are coupled, and any equation of U must contain κ as a product of length and density to an unknown power.

The magnitude of powers in which these parameters occur could not be experimentally determined, however several limitations were able to be obtained:

1) Length must appear at a lesser power than 1, because increasing length causes U to approach an asymptotic maximum.
2) Density must appear at a lesser power than 1, because increasing density causes U to approach an asymptotic maximum.
3) κ must appear to a greater magnitude of power than density, because decreasing κ by just 6 % was shown to be equivalent to an almost 300 % increase in density.
4) Density must appear to a greater power than length, because denser samples were shown to sink faster than longer samples when mass and κ were kept constant.

Observations during sinking experiments indicated that cylinders would undergo axial rotation during their descent, as identified in previous literature. Furthermore, the slimmest, shortest cylinders would become lodged mid-way down the apparatus, regardless of whether they were aluminium or steel. A geometric analysis of each cylinder's maximum available tilt concluded that they became susceptible to jamming at a diameter-length aspect ratio of less than 5:18. The increments in ratio used to identify this critical aspect ratio were admittedly large; it is therefore suggested that future sinking experiments are performed to gradually reduce the cylinder aspect ratio and identify the critical ratio with better accuracy.

Sinking experiments were repeated with several centralising spacers to reduce the axial tilt, and maintain the same level of tilt regardless of cylinder geometry. The aforementioned trends between U and κ, length or density remained qualitatively consistent using centralised sinkers. All of the 5 cm long cylinders showed a significant increase in U as opposed to un-centralised sinkers, showing that reducing large levels of

tilt increases *U*. Interestingly, an opposite effect was observed for all other cylinders, which exhibited an (albeit minor) decrease in sinking velocity. It was suggested that the most likely explanation is that small levels of tilt displace fluid in a beneficial, propulsive manner. This could be a challenging hypothesis to prove; it is suggested that future work should first attempt to confirm that the observed decrease in *U* is not due to an unforeseen side-effect of the stabilising method (such as spacer 'scraping' or reduced annular volume). This could potentially be achieved by altering the weight distribution of a cylinder to be front-loaded, which should potentially reduce the level of tilt without introducing other side-effects.

Experiments were also performed to quantify the friction associated with the front geometry of cylinders. This was achieved by altering the front face of several cylinders to cones of increasing size, but keeping the mass of each sinker constant. Results showed that streamlining the cylinder increased velocity by up to 12 %, despite experiments being performed at the smaller apparatus scale (front-face surface area was relatively small). This highlights the importance of incorporating the front cylinder face into any mathematical model of *U*.

Fluid viscosity was varied by alternating the fluid to glycerine - a highly viscous fluid. Results showed a decrease in *U* of 1 - 2 orders of magnitude. Previously observed trends between *U* and systematic variables appeared to agree within error, suggesting that previous empirical findings are applicable to systems of various *Re*. However, error bars were admittedly large. These large errors were a result of a disorderly rate of change in tilt, where cylinders would fix to a maximum tilt rotation for seemingly random periods of time, and sink significantly slower when doing so. Further investigations would be required to reduce these errors, such as axially centralising cylinders, or simply performing experiments in slightly less viscous fluids. It should also be noted that viscosity was not *exclusively* varied, as a change in fluid also gives rise to a change in density. Truly isolating viscosity would not be straightforward, one suggestion is to construct an apparatus capable of performing sinking experiments at different temperatures, using a fluid which has a high viscosity sensitivity to temperature, but low density sensitivity to temperature.

A fully analytical solution of the sinking rate of a cylinder in a confined tube is unknown at this point in time. It can be assumed however that sinking rate is

proportional to fluid density and viscosity in the same manner as Stokes law[1]. This gives a sinking velocity proportional to $(\rho_s - \rho_f)/\mu$, where ρ_s is the sinker density, ρ_f the fluid density and μ the fluid viscosity. Inserting values of viscosity and fluid density for temperatures of 15 and 25°c (a 5°c difference from room temperature) into this formula results in a sinking rate difference of up to 13.6%. In reality the variance in temperature was unlikely this severe, as results were performed in the same season. Regardless, this shows that an implementation of temperature control would add further legitimacy to results and should be considered for any future work.

[1] This is relatively likely, considering that the fluid density and viscosity contributions to teminal velocity are acquired entirely from the bouyancy and weight components of the force balance equation in Stokes law. A sinking cylinder will experience the forces of bouyancy and weight in a comparable manner.

4: Analytical Solutions for Cylinder Terminal Velocity

4.1 Introduction

The Navier-Stokes equations were solved for flow past a stationary sphere in section 2.2.2.1, yielding an expression for terminal velocity of a sinking spherical object. This is one of only a handful of cases which permit an analytical solution of the Navier-Stokes equations. Even this example could only be solved exactly under the assumption of so-called creeping flow conditions, where the Reynolds number is small, enabling the advective term to be ignored.

No general analytical solution exists for a cylindrical object sinking under similar flow conditions whether in an infinite medium or confined by a column or pipe. Nevertheless, it is instructive to attempt to build a model capable of predicting the qualitative dependence of terminal velocity upon length, radius, density and annular clearance.

The approach taken is pedagogical; a model will be built incrementally, beginning with an analytical solution of a simple, related flow problem. The model will be tested for its shortcomings before additional physics are added, and the process repeated. Each additional change will be simple and contain useful insight. Empirical correction factors are avoided so that the model retains simple, tractable relationships between key parameters, and remains modular for subsequent improvement.

The main aim is not to obtain quantitative agreement with the experiment - that is beyond the resources of the present research, though close agreement is desirable. The goal is rather to yield the correct functional dependencies on key parameters using a model which may be subsequently improved.

4.2 Model A

The baseline model considers a solid tube moving with constant speed U through a wider diameter cylinder filled with a viscous fluid, as shown in figure 4.1. The moving tube has a radius κR whilst the larger tube has a radius of R. κ is a dimensionless quantity ranging from 0 to 1.

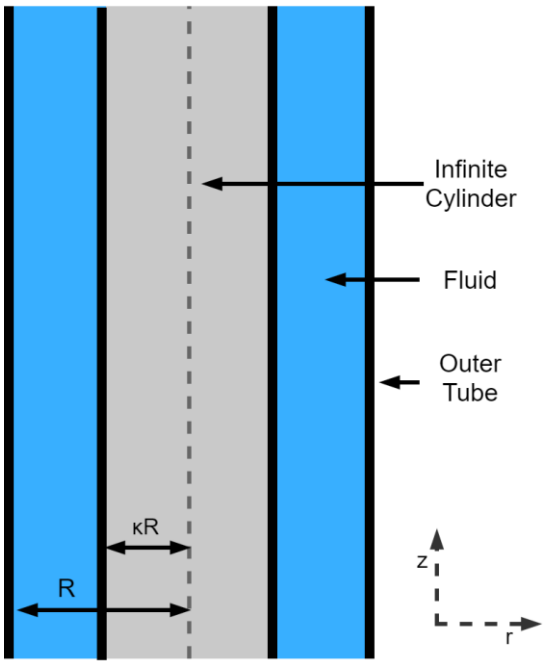

Figure 4.1: Schematic diagram of an infinite concentric cylinder with radius κR within a tube of radius R, moving with constant speed U in the positive z direction.

The motion of the inner tube results in Couette flow. At steady state, the incompressible Navier-Stokes momentum equation in cylindrical-polar co-ordinates becomes:

$$\frac{\partial}{\partial r}\left(r\frac{\partial v_z(r)}{\partial r}\right) = 0 \tag{4.1}$$

where the advective term has been discarded, which is true only for low Reynolds number flow. The pressure is assumed to be constant at all points along the fluid.

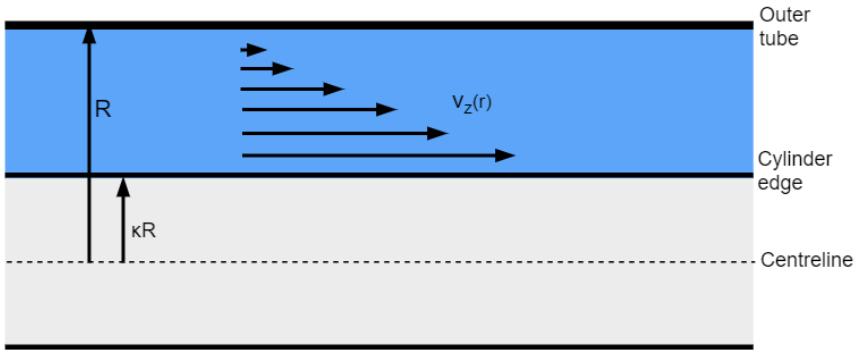

Figure 4.2: Fluid velocity profile between a co-moving concentric cylinder and fixed outer tube.

Equation 4.1 can be solved with the boundary conditions:

$$v_z(r) = U \; at \; r = \kappa R \tag{4.2}$$

$$v_z(r) = 0 \; at \; r = R \tag{4.3}$$

giving:

$$v_z(r) = U \frac{ln\left(\frac{r}{R}\right)}{ln(\kappa)} \tag{4.4}$$

For a given clearance (measured here by κ) and cylinder speed, equation 4.4 predicts a logarithmic dependence of velocity on radial position as shown by figure 4.3.

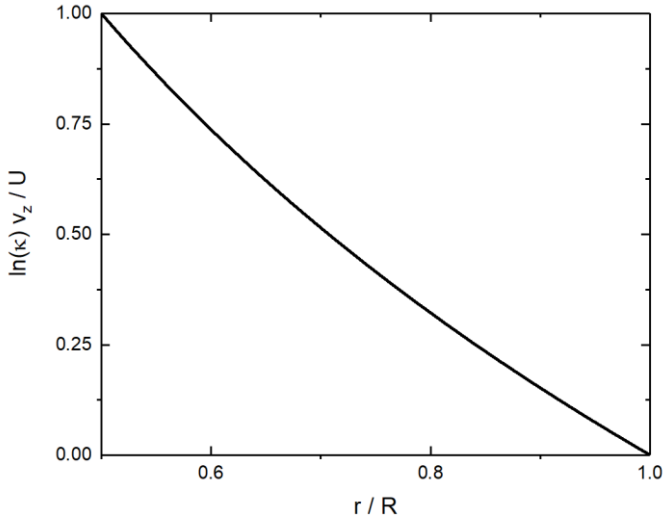

Figure 4.3: Variation of non-dimensionalised fluid velocity $v_z(r)$ as a function of radial position.

The velocity distribution obtained in equation 4.4 is the starting point for deriving a number of other useful quantities. The average velocity, for example, is given by:

$$\langle v_z \rangle = \frac{\int_0^{2\pi}\int_{\kappa R}^{R} v_z r d\theta dr}{\int_0^{2\pi}\int_{\kappa R}^{R} r d\theta dr} \tag{4.5}$$

$$= \frac{2U}{R^2(1-\kappa^2)\ln(\kappa)} \int_{\kappa R}^{R} r ln\left(\frac{r}{R}\right) dr$$

$$= \frac{2U}{\ln(\kappa)(1-\kappa^2)} \int_{\kappa}^{1} \bar{r} ln(\bar{r}) d\bar{r}$$

where $\bar{r} = {}^{r}/_{R}$ is the non-dimensionalised radial position. Performing the integral on the right hand side of equation 4.5 gives:

$$\langle v_z \rangle = \frac{-U}{2\ln(\kappa)(1-\kappa^2)} [(1-\kappa^2) + 2\kappa^2 \ln(\kappa)] \tag{4.6}$$

The average annular velocity $\langle v_z \rangle$ may now be used to determine the volumetric flow rate Q (speed across annular area) using:

$$Q = \langle v_z \rangle \pi R^2 (1-\kappa^2) \tag{4.7}$$

The mass flow rate W follows trivially from $W = \rho Q$. The frictional force on the surface of inner cylinder can be calculated with the radial fluid velocity distribution using:

$$F = \int_0^{2\pi} \int_0^{L} \mu \left.\frac{\partial v_z}{\partial r}\right|_{r=\kappa R} \kappa R \, d\theta dz \tag{4.8}$$

where L is the length of a finite patch of surface along the cylinder. Differentiating the velocity distribution in equation 4.4 with respect to r gives:

$$\frac{\partial v_z}{\partial r} = \frac{U}{r ln\kappa} \tag{4.9}$$

Substituting equation 4.9 into equation 4.8 gives:

$$F = \frac{2\pi\mu U}{ln\kappa} \int_0^{L} dz = \frac{2\pi\mu UL}{ln\kappa} \tag{4.10}$$

With the magnitude of the drag force determined, it is now possible to obtain an expression for the terminal velocity U for a fictitious version of the sinking cylinder of which end effects are ignored. This is achieved by imposing the condition of mechanical equilibrium. For the cylinder sinking in a gravitational field this gives:

$$F_w + F_B + F_D = 0 \tag{4.11}$$

where F_w, F_B, and F_D are the z-components of the forces of weight, buoyancy drag respectively. The buoyance and weight is simply given by:

$$F_B = -\rho_f \pi R^2 \kappa^2 L g \tag{4.12}$$

$$F_w = \rho_s \pi R^2 \kappa^2 L g \tag{4.13}$$

Inserting equation 4.10, 4.12 and 4.13 into 4.11 finally gives:

$$U = \frac{-\kappa^2 R^2 g(\rho_s - \rho_f) ln(\kappa)}{2\mu} \tag{4.14}$$

Which is the terminal velocity of a sinking cylinder, as given using model A. It is clear from equation 4.14 that for model A, terminal velocity depends linearly on the density difference, is independent of length, but depends of the radius ratio κ as $\kappa^2 \ln(\kappa)$, as shown in figure 4.4 where the non-dimensionalised terminal velocity $\widetilde{U} = \frac{2\mu U}{R^2 g(\rho_s - \rho_f)}$.

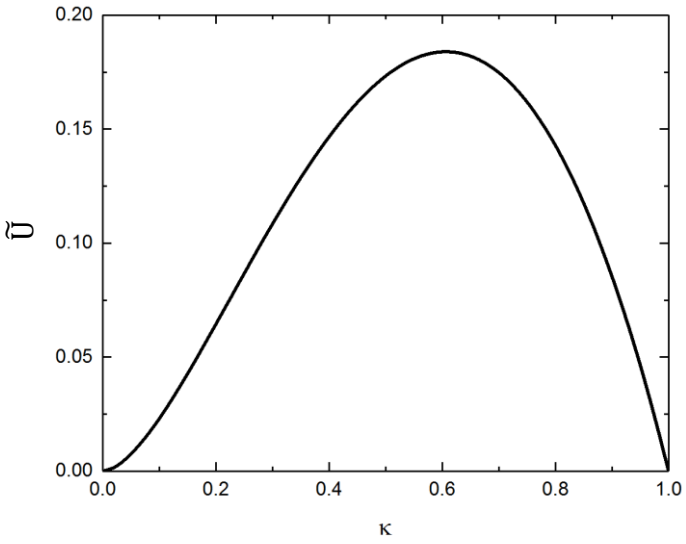

Figure 4.4: The non-dimensionalised terminal velocity, $\widetilde{U}$ as a function of diameter ratio κ.

The non-dimensionalised velocity first increases with increasing κ, then passes through a maximum before decaying at high values of κ. The initial increase in velocity is due to the resultant downward force (weight minus buoyancy) dominating the frictional drag. At small clearances, drag then dominates causing the decrease seen in figure 4.4. The location of the maximum can be found by differentiating the dimensionless terminal velocity, where:

$$\frac{\partial}{\partial \kappa}[\kappa^2 \ln(\kappa)] = \kappa[1 + 2\ln(\kappa)] = 0 \tag{4.15}$$

which has the solutions:

$$\kappa = 0 \tag{4.16a}$$

$$\kappa = e^{-\frac{1}{2}} \tag{4.16b}$$

Clearly $\kappa = 0$ can not be the maximum, therefore the remaining, physically meaningful solution is $\kappa = e^{-1/2}$, which gives a maximum at $\kappa = 0.607$. Figure 4.5 shows a plot of actual terminal velocity calculated from model A using parameters relevant to a steel sinker. This reference examples uses a fluid viscosity μ of 1.002 m Pa s and fluid density ρ_f of 998.2 kg m^{-3} [134], [135], and a sinker density ρ_s of 7903 kg m^{-3} which is calculated using an average of all (calculated) steel sample densities. The bore radius R is consistent with experiment, at 3.2 cm. The maximum terminal velocity of this example sinker is approximately 6×10^3 m s^{-1}, which is 3 orders of magnitude greater than comparable data obtained by experiment in section 3.4. This is not only true for the maxima – when comparing model A with experiment data (κ ranges between 0.66 and 0.94) model A continues to over predict terminal velocity by 3 orders of magnitude. Furthermore, the location of the Maxima in model A results in a highly non-linear κ-U relationship within the 0.66 – 0.94 κ region, again contradicting experiments.

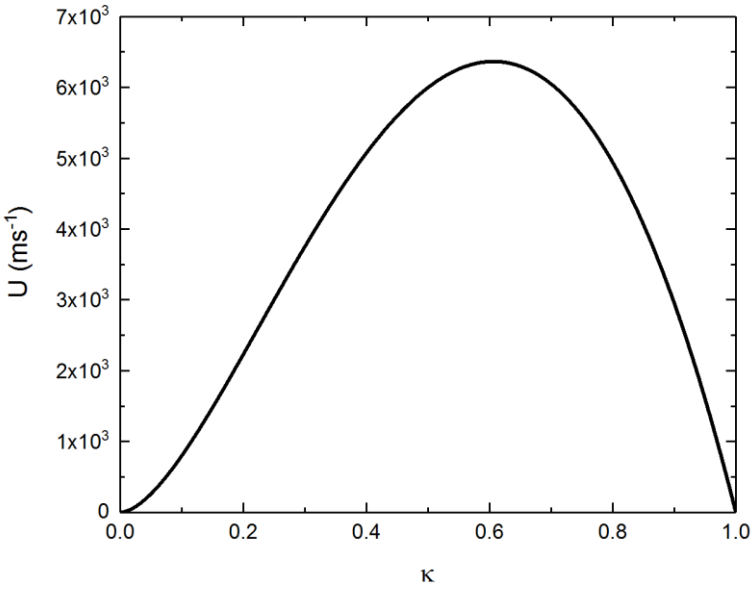

Figure 4.5: The terminal velocity of the reference cylinder calculated using model A, as a function of diameter ratio κ.

4.3 Model B – Introduction of a Pressure Gradient

A major omission in model A was the neglect of any pressure gradients. As a cylindrical sinker advances, fluid will be pushed away from the leading face and squeezed vertically upwards (in opposite direction to the cylinders' direction of travel) through the annular gap, as shown in figure 4.6. The Navier-Stokes equation to be solved in this case is:

$$\frac{1}{r}\frac{\partial}{\partial r}\left(r\frac{\partial v_z}{\partial r}\right) = \frac{1}{\mu}\frac{dP}{dz} \tag{4.17}$$

where the right hand side now contains the pressure gradient dP/dz. Equation 4.17 can now be solved within the annular region using the same boundary conditions as used to derive model A (equations 4.2 & 4.3). Again, this assumes that the cylinder is infinite and end effects are ignored. The solution is:

$$v_z(r) = \frac{U ln\left(\frac{r}{R}\right)}{\ln(\kappa)} + \frac{1}{4\mu}\frac{dP}{dz}\left[r^2 - R^2 - \frac{ln\left(\frac{r}{R}\right)}{ln(\kappa)}R^2(\kappa^2 - 1)\right] \tag{4.18}$$

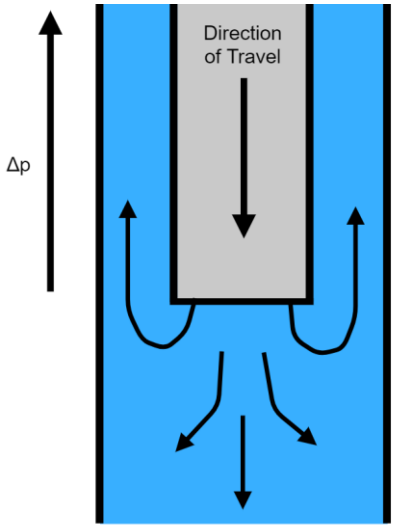

Figure 4.6: Schematic diagram showing the displacement of water from the front of the cylinder to the annular region.

It is instructive to plot a non-dimensionalised form of equation 4.18. Using the following dimensionless variables: $\tilde{v}_z = v_z/U$, $\tilde{r} = r/R$ and $A = R^2/4U\mu \cdot dP/dz$, equation 4.18 becomes:

$$\tilde{v}_z = A\left[\tilde{r}^2 - 1 + \frac{(1-\kappa^2)\ln(\tilde{r})}{\ln(\kappa)}\right] + \frac{\ln(\tilde{r})}{\ln(\kappa)} \tag{4.19}$$

Figure 4.7 shows a plot of the dimensionless velocity against scaled radial distance for various values of A, for a fixed value of κ (0.9).

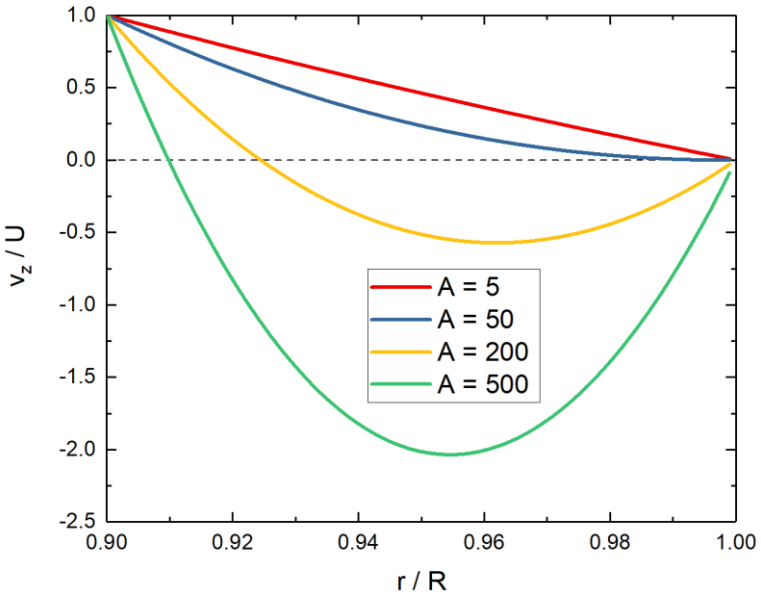

Figure 4.7: The dimensionless velocity plot as a function of dimensionless radius for various values of *A*.

At low values of dimensionless variable A (proportional to the pressure gradient) the velocity remains positive across the annular gap. However, for $A = 200$ and $A = 500$, it is negative for large regions, indicating back-flow.

Equation 4.18 is used to give the average velocity in the annular region in an analogous manner to model A (equation 4.5); this gives:

$$\langle v_z \rangle = \frac{-U}{2\ln(\kappa)}\left[1 + \frac{2\kappa^2\ln(\kappa)}{(1-\kappa^2)}\right] - \frac{R^2}{8\mu}\frac{dP}{dZ}\left[(1+\kappa^2) + \frac{(1-\kappa^2)}{\ln(\kappa)}\right] \qquad (4.20)$$

The pressure gradient $dP\ /\ dz$ must be removed from equation 4.18 to give a closed solution for the velocity distribution. This is accomplished using the postulate of mass continuity. The quantity of fluid (volume) displaced by the leading face of the moving cylinder per unit of time is:

$$Q = \pi R^2 \kappa^2 U \qquad (4.21)$$

Since this displaced fluid must be forced *back* through the annular gap (due to closed end boundary conditions), the throughput must also be given by equation 4.7. Equations 4.21 and 4.7 may therefore be equated together (see Appendix F for detailed algebra) to give:

$$\frac{dP}{dz} = \frac{4\mu}{R^2}\left[\frac{-U}{(1+\kappa^2)\ln(\kappa) + (1-\kappa^2)}\right] \tag{4.22}$$

It is instructive to examine how this pressure gradient depends on clearance (as measured by κ). Defining a dimensionless pressure gradient $\Delta\tilde{P}$ by $\frac{R^2 dP\,/\,dz}{4\mu U}$, this variation can be sketched as shown in figure 4.8.

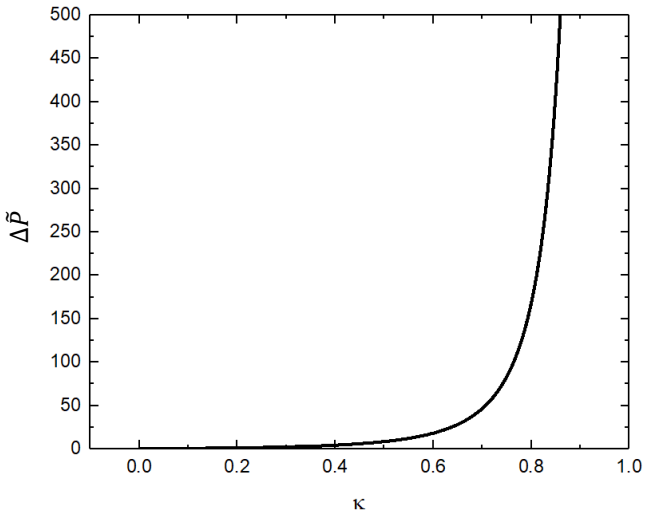

Figure 4.8: The dimensionless pressure gradient shown as a function of κ.

The plot shows the dramatic rise of the pressure gradient at small clearances (high values of κ).

With the pressure gradient known, equation 4.22 may be substituted into equation 4.18 to give:

$$v_z(r) = U\left(\frac{ln\left(\frac{r}{R}\right)}{\ln(\kappa)} - \left[\frac{\left({}^{r}/_{R}\right)^2 - 1 - \frac{ln\left(\frac{r}{R}\right)(\kappa^2-1)}{\ln(\kappa)}}{ln(\kappa)(1+\kappa^2) + (1-\kappa^2)}\right]\right) \tag{4.23}$$

which is the closed-expression analytical form of the velocity profile. Figure 4.8 shows a plot of the non-dimensional velocity against scaled radial position for several values of κ. For each κ the fluid velocity begins positive at the surface of the sinker, but changes sign and goes towards a minimum, indicating back flow. After the minimum, the velocity goes to the boundary value of zero. The magnitude of backflow increases significantly for tighter annular clearances (high κ).

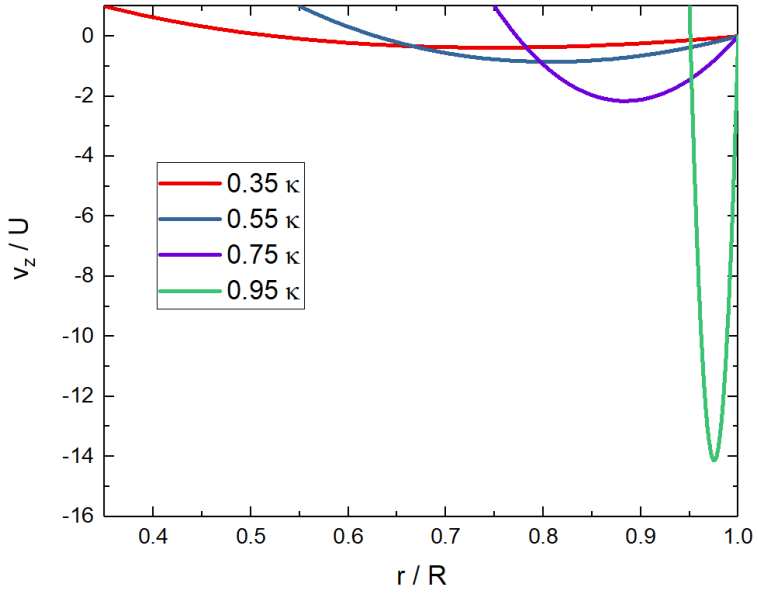

Figure 4.9: The relative velocity distribution (v_z/U) in the annular region as a function of radial position for κ values of 0.35, 0.55, 0.75 and 0.95.

Now considering a *finite* cylinder sinking through stationary fluid, the friction applied to the annular surface of a cylinder of given length L is determined using the velocity distribution given in equation 4.23. Substituting equation 4.23 into equation 4.8 therefore gives:

$$F_D = 2\pi\mu UL\left[\frac{(1-\kappa^2)}{(1+\kappa^2)\ln(\kappa)+(1-\kappa^2)}\right] \tag{4.24}$$

The dimensionless friction $\tilde{F}_D$ can therefore be given as

$$\tilde{F}_D = \frac{F_D}{\mu LU} = \frac{2\pi(1-\kappa^2)}{(1+\kappa^2)\ln(\kappa)+(1-\kappa^2)} \tag{4.25}$$

and is plotted as a function of κ in figure 4.10 below.

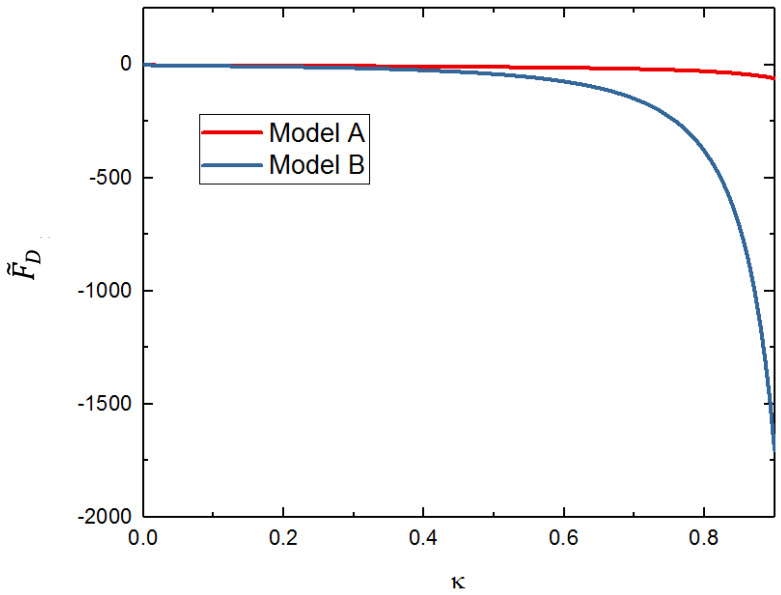

Figure 4.10: Non-dimensional frictional drag force as a function of diameter ratio κ. Model A is the red line, whilst model B is the blue line.

The most obvious point to note is the sign; $\tilde{F}_D$ acts in the opposite direction to the movement of the cylinder. This is the case for both models A and B. The magnitude has a weak κ dependence for low to intermediate values of κ, but then shows a steep drop beyond $\kappa \approx 0.6$. This is the so-called hydrodynamic braking affect. A similar effect is present for model A, but the divergent behaviour occurs at a much higher range of κ (approximately 0.95).

With the frictional drag force known it is now possible to determine an expression for the terminal velocity of a *finite* cylinder by substituting equation 4.25 into the previously determined force balance, equation 4.11.

$$U = \frac{-\kappa^2 R^2 g(\rho_s - \rho_f)}{2\mu}\left[\frac{(1+\kappa^2)\ln(\kappa) + (1-\kappa^2)}{(1-\kappa^2)}\right] \tag{4.26}$$

It should be noted that this terminal velocity is consistent with the basic solution of Bird *et al* that was developed for the falling cylinder viscometer [38], [47]. The functional dependence of the terminal velocity upon κ is displayed in figure 4.11 below.

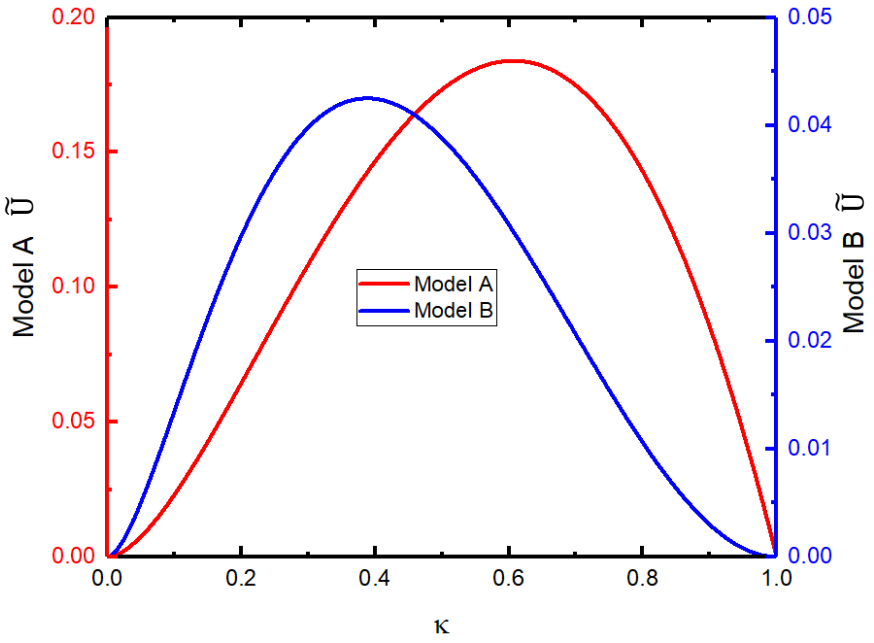

Figure 4.11: Dimensionless terminal velocity of model A and model B, plotted as a Y-Y plot as a function of diameter ratio κ. The red line represents model A, whilst the blue line represents model B.

The velocity once again shows a maximum, but compared to model A, the maximum is located at a lower value of κ. Maximising the velocity and solving numerically, the velocity maximum occurs at $\kappa = 0.3882$. The region of κ explored experimentally has become somewhat increasingly linear thanks to this shift in maxima towards a lower value of κ, however, substantial non-linearity remains.

Substituting in the values for the reference steel sinker gives the velocity distribution shown in figure 4.12. The velocity of model B is significantly lower than the prediction of model A, however, model B still over predicts the terminal velocity by almost 3 orders of magnitude compared to the experiment results. This indicates that important physics remain missing from the model.

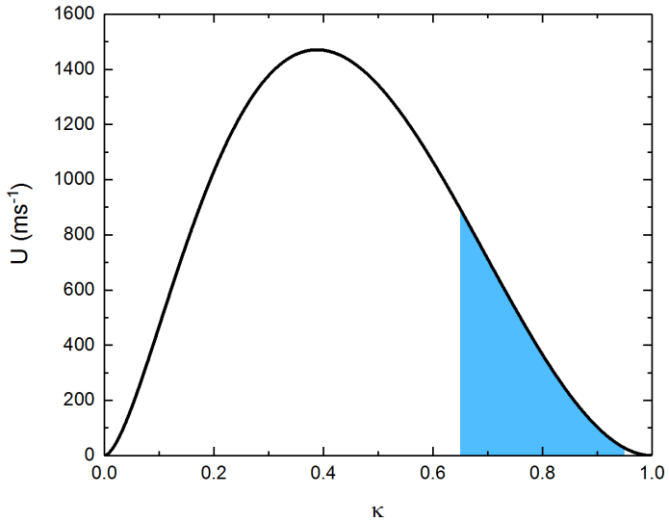

Figure 4.12: The terminal velocity for the reference cylinder as predicted by model B, plotted against diameter ratio κ. Highlighted in blue is the κ region of interest to experiment.

4.4 Model C – Accounting for the Additional Retarding Force

The fact that the cylinder will push fluid ahead of it back through the annular space was taken into account when deriving model B, this resulted in a pressure gradient. The force required to push this mass of fluid through the gap was not accounted for however. Such a force clearly arises due to the high pressure at the front face of the cylinder.

Model C is constructed from model B, retaining the same velocity distribution, but now incorporating the additional opposing force F_F into the force balance, which reads

$$F_G + F_B + F_D + F_F = 0 \tag{4.27}$$

Figure 4.13 shows 3 regions of interest along the length of the cylinder.

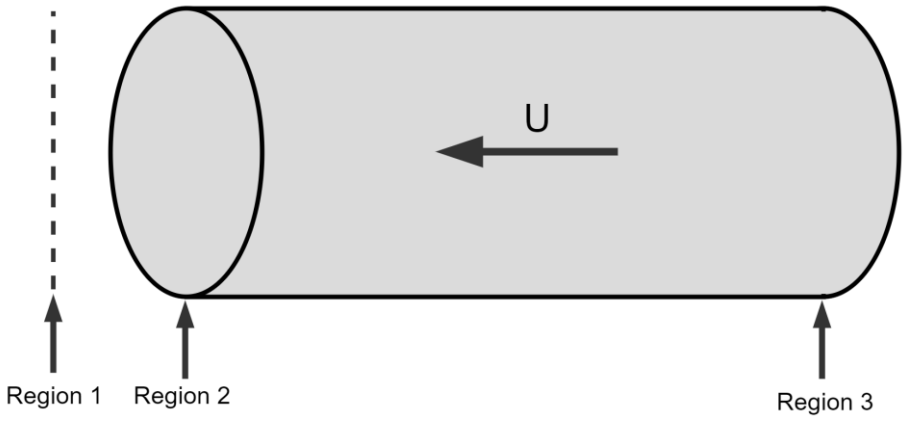

Figure 4.13: Schematic diagram showing 3 regions of interest used to obtain an expression for force at the front face. The first is a fictitious region in which the momentum is postulated to be zero; this is used later in the derivation of model D. The second region is the entrance to the annulus; this pressure must have a corresponding frictional force applied to the cylinder front face. Region 3 is the annulus exit.

Ignoring end effects, the pressure gradient along the annular gap must be given by:

$$\frac{dP}{dz} = \frac{P_2 - P_3}{L} \tag{4.28}$$

where P_2 and P_3 are the pressures at regions 2 and 3 respectively (as shown in figure 4.13). It is assumed that the pressure at region 3 is negligible. The pressure gradient may therefore be approximated as:

$$\frac{dP}{dz} \cong \frac{P_2}{L} \tag{4.29}$$

The total friction applied to the cylinder at region 2 is equal to the pressure in region 2 multiplied by the area of the front face, therefore:

$$F_F = \pi\kappa^2 R^2 L \frac{dP}{dz} \tag{4.30}$$

Inserting the pressure gradient, equation 4.22 into equation 4.30 gives:

$$F_F = 4\mu\pi\kappa^2 L \left[\frac{-U}{(1+K^2)lnK + (1-K^2)}\right] \tag{4.31}$$

Now that all the forces have been obtained, they are substituted into the force balance, equation 4.27 to give:

$$U = \frac{-R^2\kappa^2 g(\rho_s - \rho_f)}{2\mu}\left(\frac{(1+\kappa^2)\ln(\kappa) + (1-\kappa^2)}{1+\kappa^2}\right) \tag{4.32}$$

The dimensionless terminal velocity is shown in figure 4.14 as a function of κ.

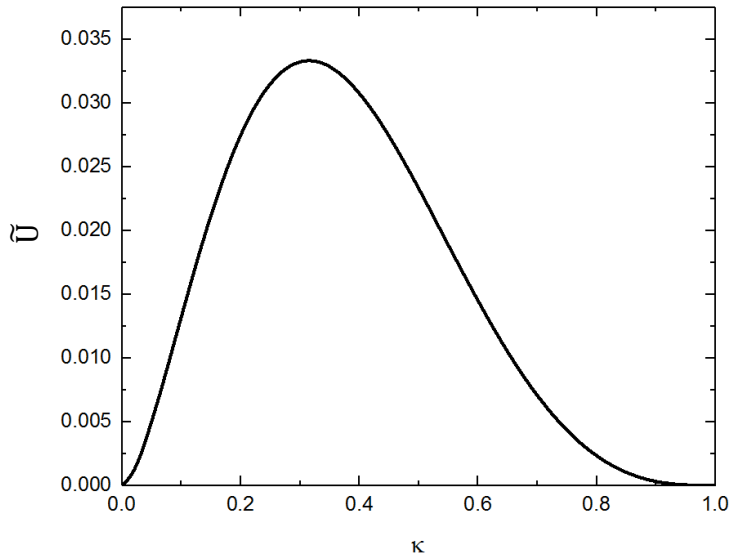

Figure 4.14: Dimensionless terminal velocity as a function of diameter ratio κ, as given by model C.

The trend in figure 4.14 is qualitatively similar to the equivalent model B plot (figure 4.11). The location of the maxima in model C is at $\kappa = 0.3150$ (determined numerically), significantly lower than that of model B. The models are compared *quantitatively* in figure 4.15, using the values of the baseline sinker.

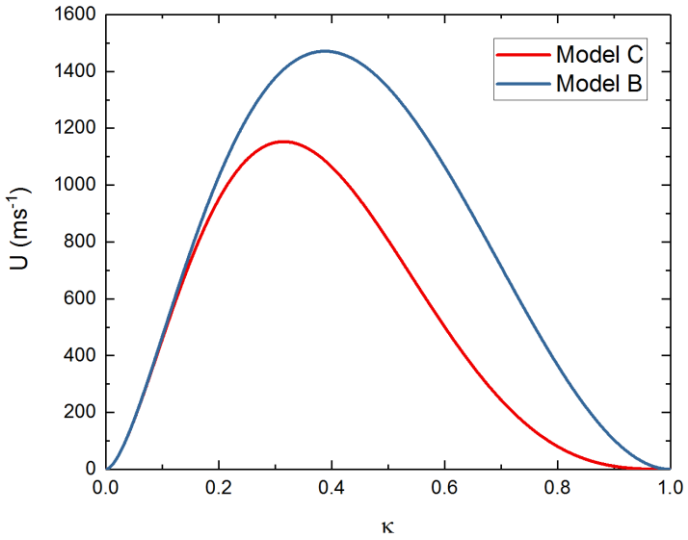

Figure 4.15: Terminal velocity of the reference cylinder as a function of diameter ratio κ, as given by models B and C.

It can be seen from figure 4.15 that the maximum velocity magnitude has significantly decreased in model C. Furthermore, in the diameter regime of interest to experiment ($0.66 < \kappa < 0.94$), the value of terminal velocity is reduced by around a factor of 2 in comparison to model B.

Model C is clearly still incorrect; there is no length dependence for terminal velocity, and the magnitude is still 2 orders of magnitude too high compared to experiments.

4.5 Model D – Improved Model of Front Face Pressure

Model D improves upon model C, by taking a more detailed derivation of the pressure within region 2 at the leading face of the cylinder. First, a mass balance is performed between regions 1 and 2 (see figure 4.13). This is effected by equating the fluid displaced from the cylinder and the average flow into the annular region:

$$\pi R^2 \kappa^2 \rho_f U - \langle v_z \rangle \pi R^2 (1 - \kappa^2) \rho_f = 0 \tag{4.33}$$

which can be rearranged to give:

$$\langle v_z \rangle = \frac{\kappa^2}{(1-\kappa^2)} U \tag{4.34}$$

A momentum balance over the same region results in the following:

$$(P_1 - P_2)\pi R^2(1-\kappa^2) - \rho_f \langle v_z \rangle^2 \pi R^2 (1-\kappa^2) = 0 \tag{4.35}$$

which can be rearranged to give:

$$P_1 = P_2 + \rho_f \langle v_z \rangle^2 \tag{4.36}$$

Substituting equation 4.34 into 4.36 gives:

$$P_1 = P_2 + \frac{\rho_f \kappa^4 U^2}{(1-\kappa^2)^2} \tag{4.37}$$

However, in model C it is shown that $P_2 \cong L\frac{dP}{dz}$ (equation 4.29). Using this to eliminate P_2 from equation 4.37 yields:

$$P_1 = \frac{4L\mu}{R^2}\left[\frac{-U}{(1+\kappa^2)\ln(\kappa) + (1-\kappa^2)}\right] + \frac{\rho_f \kappa^4 U^2}{(1-\kappa^2)^2} \tag{4.38}$$

Equation 4.38 can be used to give a more accurate expression for the force associated with pressure at the front face:

$$\mathrm{F_F} = \pi R^2 \kappa^2 \mathrm{P_1} = 4\mathrm{L}\mu\pi\kappa^2\left[\frac{-\mathrm{U}}{(1+\kappa^2)\ln(\kappa) + (1-\kappa^2)}\right] + \frac{\rho_f \pi \kappa^6 R^2 U^2}{(1-\kappa^2)^2} \tag{4.39}$$

Substituting equation 4.39 into the force balance (equation 4.27) yields an implicit expression for terminal velocity:

$$0 = U^2 \frac{\rho_f \kappa^6 R^2}{\mu L (1-\kappa^2)^2} + U\left(\frac{-2(1+\kappa^2)}{(1+\kappa^2)\ln(\kappa) + (1-\kappa^2)}\right) - \frac{\kappa^2 R^2 g}{\mu}(\rho_s - \rho_f) \tag{4.40}$$

which is of the general form:

$$0 = \alpha U^2 + \beta U + \gamma \tag{4.41}$$

where:

$$\alpha = \frac{R^2 \rho_f \kappa^6}{\mu L (1-\kappa^2)^2} \tag{4.42}$$

$$\beta = \frac{-2(1+\kappa^2)}{(1+\kappa^2)\ln(\kappa) + (1-\kappa^2)} \tag{4.43}$$

$$\gamma = \frac{-R^2 \kappa^2 g(\rho_s - \rho_f)}{\mu} \tag{4.44}$$

The solution can be obtained immediately using

$$U = \frac{-\beta + \sqrt{\beta^2 - 4\alpha\gamma}}{2\alpha} \tag{4.45}$$

The first thing of note is that terminal velocity is now a function of length, unlike models A - C. For an *infinitely* long cylinder, the α term can be considered negligible ($\alpha \propto \frac{1}{L}$), resulting in a solution to terminal velocity exact to that of model C (equation 4.32).

By fixing the diameter ratio to 0.9, terminal velocity is plotted as a function of length. This is shown in figure 4.16, where terminal velocity increases asymptotically with length. It is also shown in figure 4.16 that for at a diameter ratio of 0.9 and length of 25 cm, the terminal velocity is approximately 1 ms^{-1} for the reference cylinder.

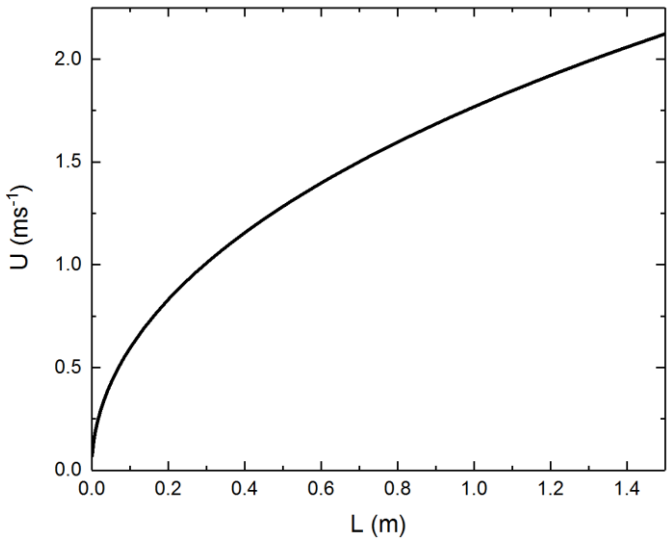

Figure 4.16: Terminal velocity given by model D as a function of cylinder length L for the reference cylinder at a fixed κ value of 0.9.

The diameter ratio dependence of model D is also shown in figure 4.17 for the reference cylinder, where length is now fixed at 25 cm. Figure 4.17 shows that model D has a much lower peak velocity in comparison to model C (280 ms^{-1} as opposed to 1150 ms^{-1}). The location of the peak velocity also shifts further to the left in comparison to model C, appearing at a diameter ratio of approximately $\kappa = 0.1$.

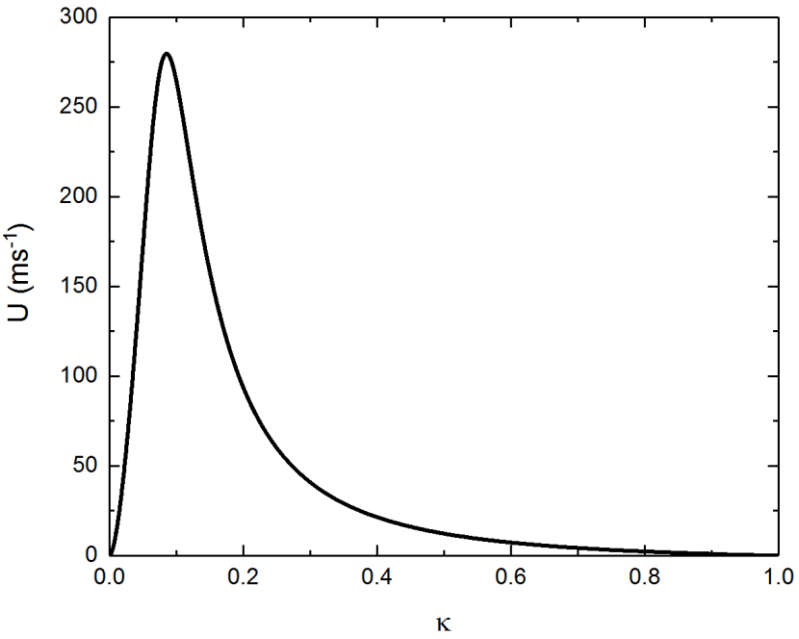

Figure 4.17: Terminal Velocity given by model D as a function of κ for the reference cylinder at a fixed length of 25 cm.

The nature of trends shown indicate that model D captures the essential physics and shows a strong hydraulic braking effect across a large range of diameter ratios.

4.6 Comparison of Best Model with Experiment Results

Experimental data gathered in the previous chapter is used to quantify the accuracy of the most developed analytical solution, model D. Due to experimental density values being calculated using mass and volume, same material samples may have marginal differences in calculated density (<1%), yet are considered equivalent, as these errors will be due to slight inaccuracies in volume (form factor, radius and length measurements). An average density of each material is therefore used as input for model D, at 2709 and 7903 kg m^{-3} for aluminium and steel respectively. Unless otherwise specified, results from the large-bore apparatus are used for comparison. Both centralised and conventional cylinders are used when most applicable.

4.6.1 Length

Experimental data was compared with model D for steel and aluminium samples (two different diameters) to examine how well model D predicts the length dependence of terminal velocity. Figures 4.18a and 4.18b show the results of this comparison.

Since model D assumes the sinker does not tilt or rotate as it moves through the fluid, the centralised samples offer the fairest comparison. Figure 4.18 shows that while model D gives the correct qualitative behaviour with length, quantitatively it over predicts terminal velocity by around a factor of 2 in the worst cases (largest clearances). For the smallest clearances, the comparison is significantly improved for both steel and aluminium samples. In all cases, the model *over predicts* the terminal velocity, suggesting the deficiencies are found in omitted or undervalued frictional terms.

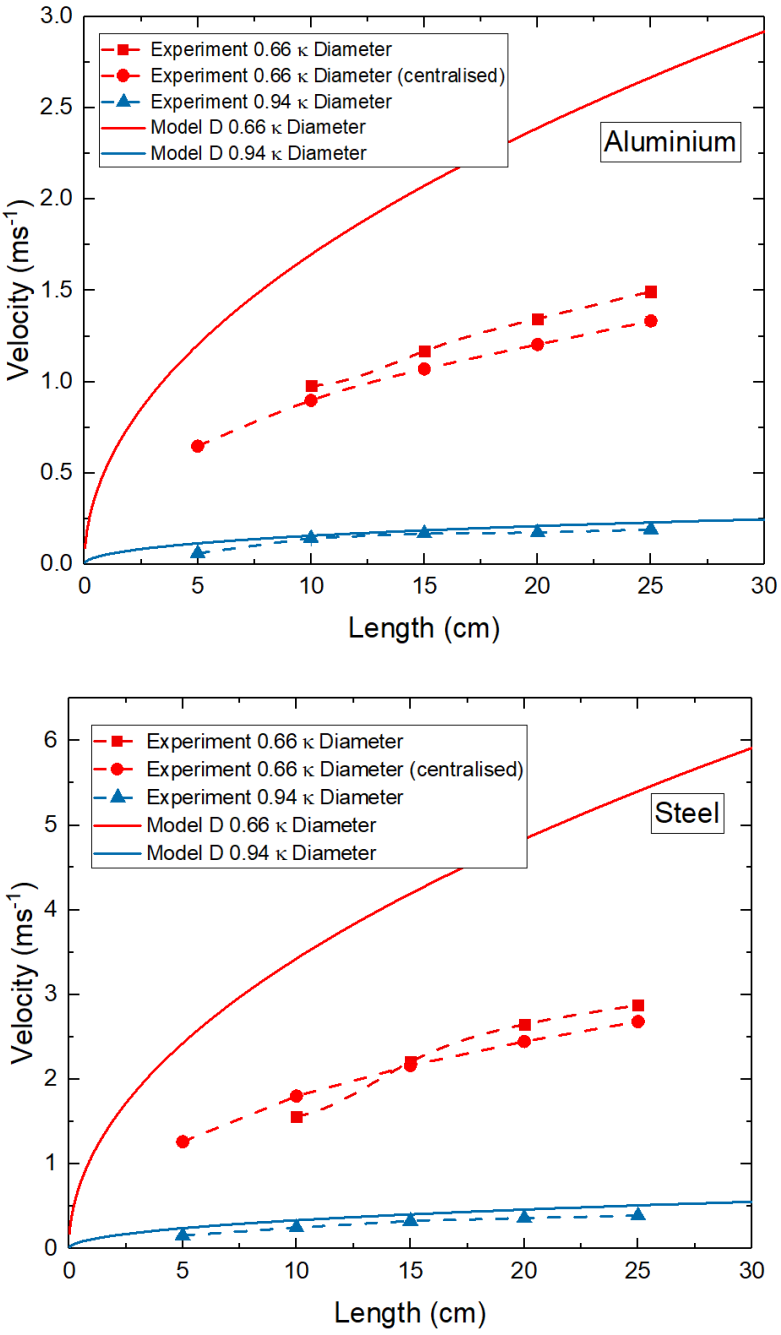

Figures 4.18 (a & b): Model D and experiment terminal velocities plotted as a function of cylinder length. The larger diameter series samples were not centralised. Figure 4.18a is for aluminium samples, figure 4.18b is for steel. Dashed lines fitted to experiment values are for visual aid only.

The quality of fit between model D and experiment data is more specifically quantified using a regression analysis. The regression analysis results in a coefficient of determination, which describes the quality of fit using a coefficient of determination between 0 (poor) and 1 (good). Table 4.1 shows that there is statistically little

resemblance between model D and all experiment data as a function of length. This is unsurprising considering the consistent over prediction of terminal velocity. It can however be concluded that model D more accurately accounts for the functional dependency of length as density is decreased and κ increased.

Table 4.1: The coefficient of determination for model D as a function of length individually compared to all experiment data sets with a fixed κ and density.

κ	Aluminium	Steel
0.66	-10.85	-19.16
0.81	-2.32	-5.37
0.90	-4.95	-2.28
0.94	0.22	0.14

4.6.2 Diameter

The ability of model D to predict the correct diameter dependency is next investigated, Figure 4.19 shows experimental data for aluminium and steel samples. The data sets are for 10 cm and 25 cm long cylinders with κ ranging from 0.66 to 0.94.

Quantitatively, model D over estimates sinking velocity in all cases, with the maximum discrepancy being around a factor of 2 for the smallest diameter ratios (largest clearance). The discrepancy diminishes for high diameter ratios (smallest clearances). Qualitatively, model D predicts a non-linear dependence on diameter whilst the experimental data conforms to a linear variation with κ.

Trends are similar for aluminium and steel though the sinker velocities are higher for the latter.

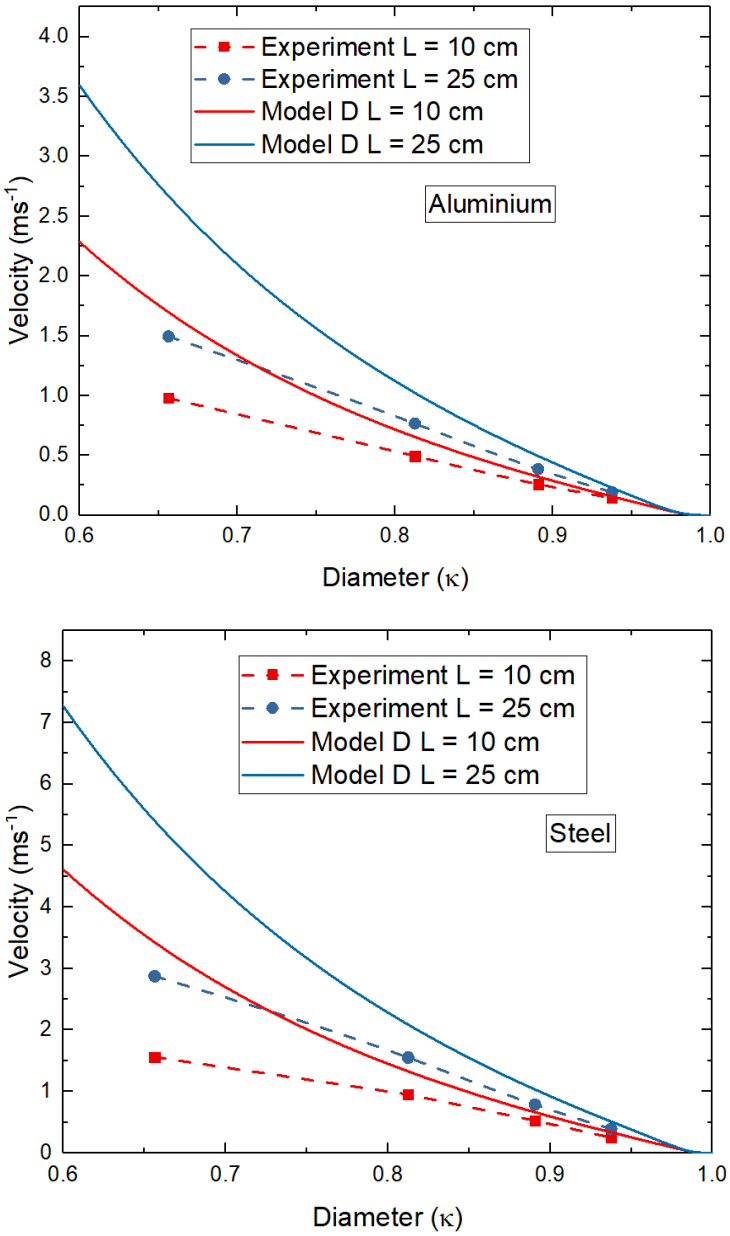

Figures 4.19 (a & b): Terminal velocity plotted as a function of the ratio between sinker and container diameters. Solid lines are predictions of model D, plot symbols are experimental data. Figure 4.19a is aluminium, whilst 4.19b is steel. Dashed lines are for visual guidance only.

Table 4.2 shows the coefficients of determination between model D and experiment data as a function of κ. Once again the regression analysis indicates that there is minimal resemblance between model D and the trend of experiment data, reflecting the lack of linearity consistent over prediction of terminal velocity in model D.

Table 4.2: The coefficient of determination for model D as a function of κ, individually compared to all experiment data sets with a fixed length and density.

L	Aluminium	Steel
5	-0.58	-0.36
10	0.44	-0.82
15	0.19	-1.24
20	0.14	0.15
25	-0.47	0.17

4.6.3 Density

Due to a limited number of samples having different density, only 2 experiment points are available to plot; one set for cylinders with diameter 4.2 cm and another with 6.0 cm diameter. Figure 4.19 shows a plot of terminal velocity versus $\rho_s - \rho_f$ together with the predictions of model D. The experimental results have been 'extended' by adding the origin as a third point (it is obvious that when $\rho_s - \rho_f = 0$, the cylinder would be neutrally buoyant and therefore stationary).

Figure 4.20 shows that model D captures the correct qualitative dependence of terminal velocity upon density, which is $\approx \sqrt{\rho_s - \rho_f}$. The model consistently over predicts the experiment results but is quantitatively quite good for wider cylinders ($\kappa = 0.94$).

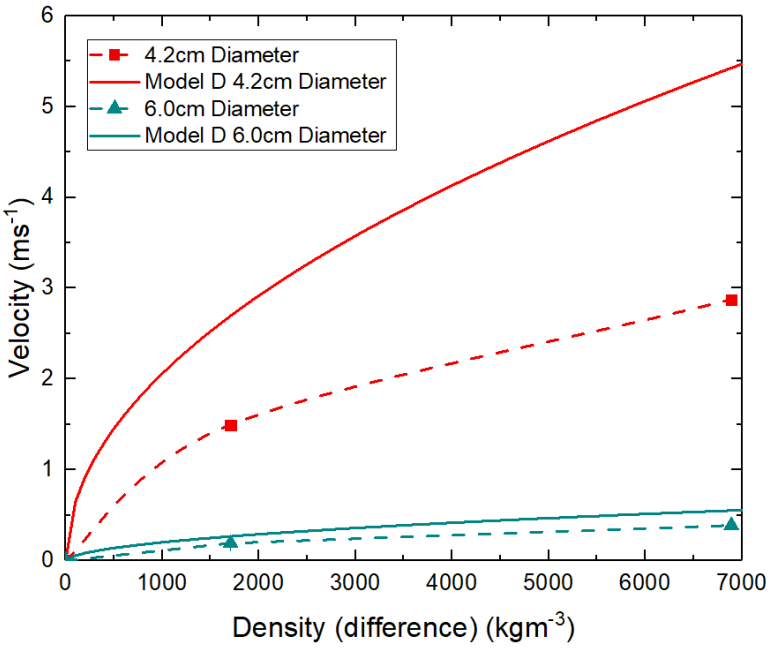

Figure 4.20: Comparison of model D predictions and experiment data for the terminal velocity of a sinking cylinder through a column of fluid. The length of the cylinders are 25 cm. Velocity is expressed as a function of the difference in density between sample and fluid.

A maximum velocity appears to occur for increases in fluid velocity through *either* an increase in length or density. This suggests that this is imposed by hydraulic braking effects being a function of fluid through-flow within the annulus. It is expected that the approach to a maximum happens at a faster rate for length, due to the coupled increase in buoyancy force.

4.6.4 Viscosity

Figure 4.21 compared model D and experiment terminal velocity for two different fluids. Both trends are for the same, 12.7 cm long steel samples. The trends of each series suggest that model terminal velocity *under* predicts experiment for the higher viscosity glycerine, as opposed to the over prediction shown for water.

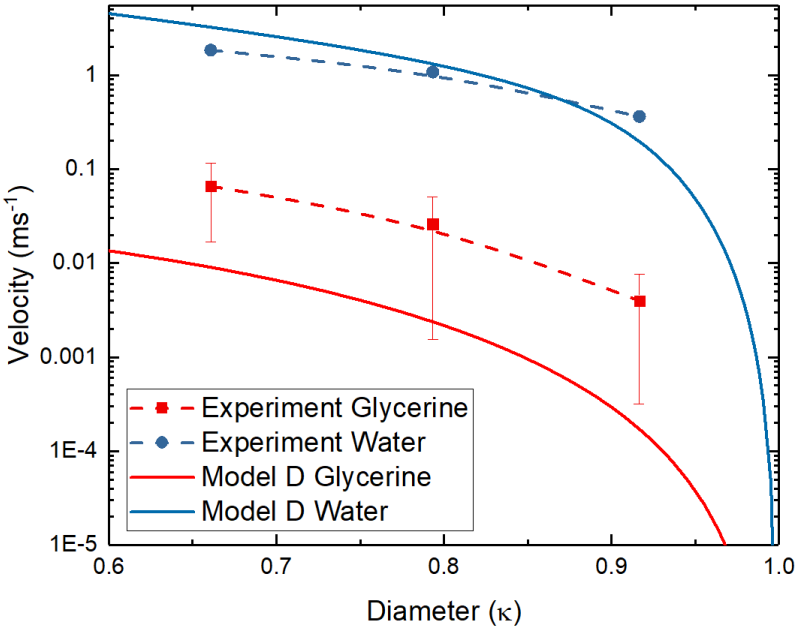

Figure 4.21: Comparison of terminal velocity as a function of fluid viscosity for both model D and experiment results. Samples are steel, with a length of 12.7 cm.

The tilt of cylinders is believed to be the cause of the large errors in glycerine sinking, as discussed in section 3.4.8. This is due to cylinders sinking slower when tilted. If this eccentric behaviour is indeed the source of discrepancy, model D would be expected to *significantly* over predict experimental results, due to it being a concentric model. It is therefore unexpected that the opposite of this behaviour is shown in figure 4.21. Moreso, tilt has been shown to decrease as κ increases, yet model D becomes *less* accurate at larger κ ranges (small clearances).

4.6.5 Scale

Model D is now compared over the two scales used during experimentation. These results are shown in figure 4.22. Centralized cylinders are not available for the smaller scale, therefore non-centralised sinkers are used throughout. The comparison uses cylinders of 10 cm length for the large apparatus, and 4.35 cm length for the small apparatus - this results in a similar degree of axial freedom.

In figure 4.22, the accuracy of the model appears similar across both apparatus scales. Model and experiment velocity converge to similar levels of accuracy at large κ

(small clearance), yet velocity is over predicted by a *greater* margin at lower diameters for the large scale apparatus (up to a factor of 2).

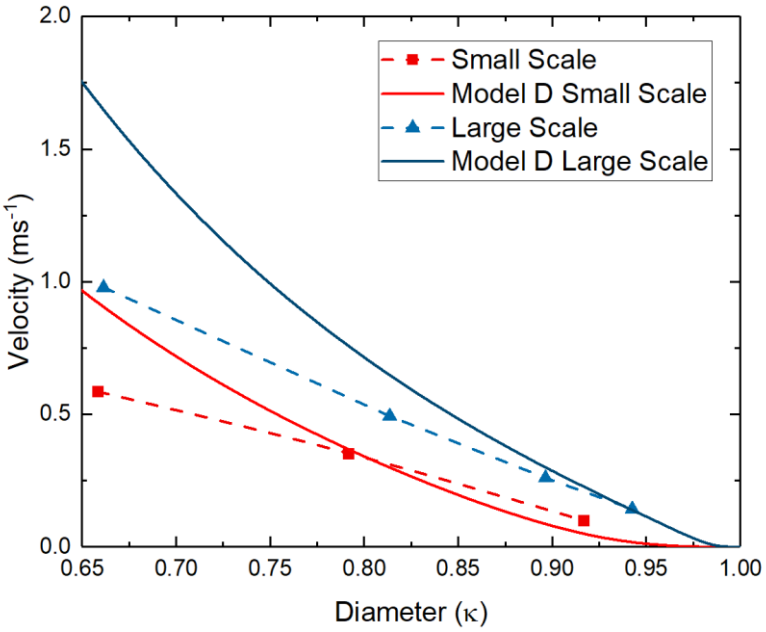

Figure 4.22: Comparison of model D and experiment velocity as a function of diameter, over both scales. The large scale apparatus uses 10.0 cm samples, whilst the small scale 4.35 cm.

The model is compared with experiment data as a function of length over the two apparatus scales in figure 4.23. The diameter ratios used are 0.81 and 0.79 for large and small apparatus respectively. The trend predicted using model D appears to qualitatively follow that of experiment for *both* scales. The accuracy of model D significantly differs between the investigated scales; for the larger scale, the model over predicts terminal velocity by up to a third[1]. In contrast, the small scale apparatus over predicts this velocity by up to a factor of two, although this will be exacerbated by the greater range of investigation at the smaller scale.

[1] Excluding the 5 cm sample due to tilt. The 5 cm *centralized* sample is within the aforementioned range, at 31%.

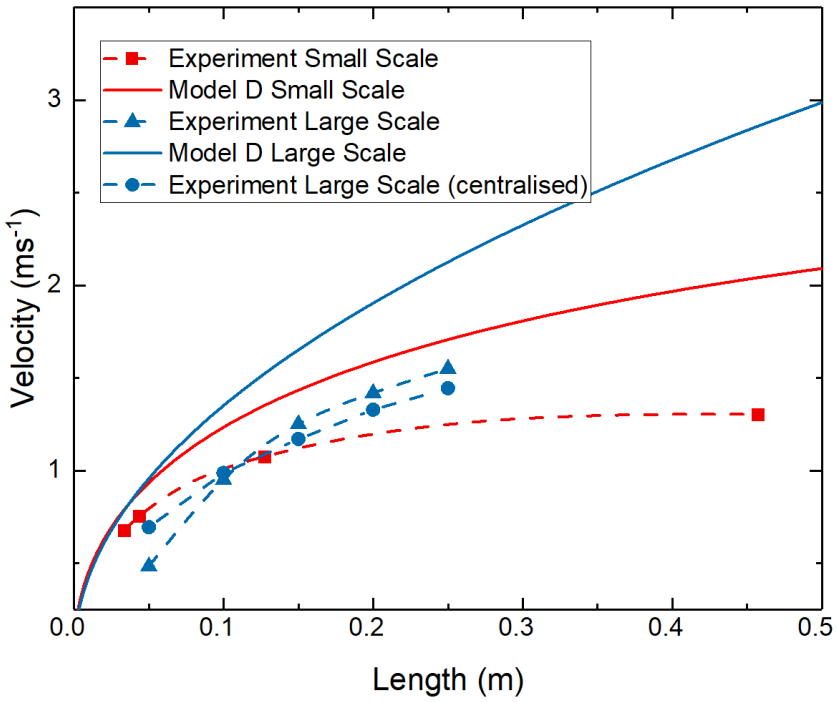

Figure 4.23: Comparison of model D and experiment velocity. Terminal velocity is investigated for multiple container scales, as a function of diameter.

4.7 Conclusions

A model of a cylinder sinking through a confined tube was constructed by incrementally incorporating analytically defined frictional forces. The first iteration of the model accounted for the friction imposed onto the cylinder surface as a result of the velocity gradient within the annular gap. This velocity gradient was defined using a simplified version of the Navier-Stokes equations which omit advective flows. The model predicted a terminal velocity 3 orders of magnitude greater than experiments, depended linearly on density, and was independent of cylinder length.

The second iteration of the model introduced a pressure gradient into the Navier-Stokes equations that was representative of the displacement of fluid from the front face into the annulus. This slightly lowered the maximum sinking velocity, but significantly lowered sinking velocity throughout the range of κ relevant to experiments.

The third iteration of the model determined the frictional forces applied to the front face as a result of the pressure at this region. This had a similar effect on the

sinking velocity as model B: slightly lowering the absolute maximum and significantly lowering velocity at the κ region relative to experiments.

The fourth and final iteration of the model improves upon the frictional force at the front face by accounting for the cost of changing the direction of the fluid. The solution becomes implicit, although an immediate solution can be obtained via the quadratic formula. The model is the first to describe sinking velocity as a function of length, and correctly predicts an asymptotic relationship for both length and density. Quantitatively, sinking velocity is accurately predicted for large values of κ, but is over predicted by a factor of 2 at lesser values of κ. This reflects the poor qualitative dependency between sinking velocity and κ.

A regression analysis was used to statistically determine the quality of fit between the best model and experiments. The regression analysis showed that the model became a marginally better fit to experiments as κ increased, but as a whole proved that the model poorly described the results of experiments. This is a reflection of the models consistent over prediction of sinking velocity, and should not detract from the models strong qualitative description of sinking velocity dependence to length and density.

The over prediction of the analytical model can be seen to exacerbate as the velocity of reference data increases (be through a decrease in κ, increase in length, or increase in density). This implies a dependence with Reynolds number, and that the laminar flow assumptions made in regards to boundary conditions and annular velocity distribution are insufficient.

The discrepancy of results may also be due to the experiment not being an exact reflection of the analytical model. This would likely be due to eccentricity; it is well documented that even the slightest amounts of eccentricity have a significant effect on sinking velocity [48]. Eccentricity was observed during experiments, even after attempts were made to centralize samples and stabilize tilt, yet the analytical model assumes perfect concentricity.

It is reasonable to conclude that the analytical model is undervaluing friction forces and further improvements are necessary. Phenomena at the trailing face of the cylinder could potentially improve upon the accuracy of the model; an elongated trail, or pressure at the annulus exit that lessens the annular pressure gradient would likely

reduce sinking velocity. The method of accounting for flow paths at the front face may also potentially be improved upon, as the current solution is somewhat crude.

One possible avenue of future work is to investigate whether experiment results could be presented in a non-dimensionalised format, similar to those presented throughout this chapter. This would allow for further analyses between the analytical model and experiments, potentially providing additional statistical insight into the deficiencies of the analytical model.

It could be argued that the complexity of the model has increased to an extent that keeping future iterations analytical are neither advantageous or feasible. An empirical correction factor could potentially be a more practical solution. Considering that model accuracy decreases as a function of Reynolds number, the most logical form of correction factor would be an empirical description of turbulence, likely as a function of Reynolds number, similar to the extended Stokes law shown in equation 2.52.

5: Calculation of Shear Viscosity

5.1 Introduction

In chapter 4 an analytical model was constructed to describe the sinking rate of a cylinder. The model correctly described the functional dependencies for length and density, but increasingly over predicted sinking velocity as diameter decreased. There is clearly scope to improve upon the current model. Detailed insight into the behaviour of fluid during finite-boundary sinking is therefore required to better understand and identify the necessary areas of improvement.

Molecular dynamics (MD) is a convenient method of investigating fluid flow. The solving of the equations of motion at a particle level removes the need to solve the Navier-Stokes equations, and the absence of a mesh allows for the straightforward implementation of moving objects (such as sinkers). MD will therefore be used to obtain detailed fluid information that is troublesome to obtain in experiments, such as local pressure, density and velocity vectors. It is important to obtain the shear viscosity of the pair potential used in these simulations for two reasons:

1) To enable an estimate of the Reynolds number of flows in MD simulations. This characterizes turbulence and allows for comparisons between different length scales.
2) To parametrise the viscous stress tensor in continuum modelling of flow past a stationary object or sinking simulations (a suggestion for future work).

This chapter will therefore apply the methods of non-equilibrium molecular dynamics (NEMD) as described in section 2.3.9 to determine shear viscosity of the soft-repulsive force potential (equation 2.81) that is used in MD simulations. Following a suitable collection of viscosity data, a model is derived that describes viscosity as a function of fluid density and temperature.

5.2 Methodology

The SLLOD method was used to determine the shear viscosity of fluids described by the soft-repulsive potential ($\varepsilon = 100$). In this section the relevant simulation parameters (such as the magnitude of timestep, number of timesteps to equilibrate, number of

timesteps to simulate and number of particles) are justified for the execution of SLLOD simulations.

An equilibrated fluid was prepared at a given density and temperature by running an isokinetic molecular dynamics simulation starting from a square lattice. Initial simulations were conducted using 729 particles, which was sufficient to determine the optimum timestep for the equilibration phase, but this was later increased (see later).

The time step of the simulation was chosen as the largest value which did not result in significant drift in total energy during an equilibrium simulation. The threshold of accuracy is chosen to be consistent with other applications of the soft-repulsive potential found in literature - *i.e.* five significant figures [108]. Time step accuracy was investigated by running constant energy (NVE) molecular dynamics simulation of 729 particles for a reduced time, $\tau = 5{,}000$ (i.e. 500,000 steps for a time step of 0.01). The maximum divergence from initial total energy at each investigated time step is shown in figure 5.1, where a time step of 0.001 can be seen to maintain an accuracy between 6-7 significant figures. A time step of 0.001 was therefore selected and this value was used in all simulations described in this chapter.

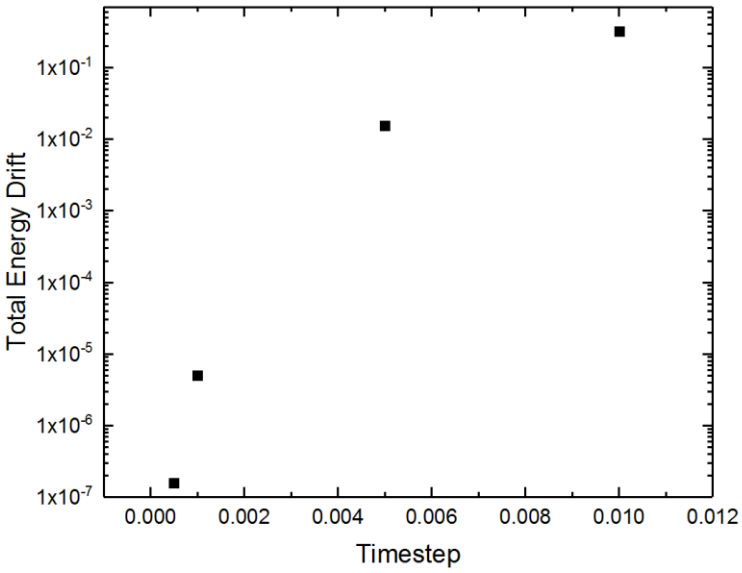

Figure 5.1: The total energy drift for simulations of 729 soft-repulsive potential particles after a reduced time, $\tau = 5{,}000$.

Isokinetic SLLOD dynamics were switched on starting with well-equilibrated fluids. For a given strain rate, the simulation was run until a non-equilibrium steady state was achieved. This was determined by examining the variation of total energy with time.

The steady state was deemed to be reached when there was no upward/downward drift in the mean energy (energy is not conserved away from equilibrium but fluctuates about a mean value). The lower the strain rate, the longer it takes for the simulation to approach steady state. To avoid determining the time required to reach steady state for each specific strain rate, the time taken to reach steady state for the *lowest* strain rate was used throughout. In practice, a simulation with strain rate of 0.01 appears to reach steady state after $\sim 5 \times 10^3$ iterations, as shown in figure 5.2 for $\rho = 1$ and $T = 1$. To be sure that this number of steps would work for all thermodynamic states (higher densities require longer), this time was extended to 5×10^5 time steps.

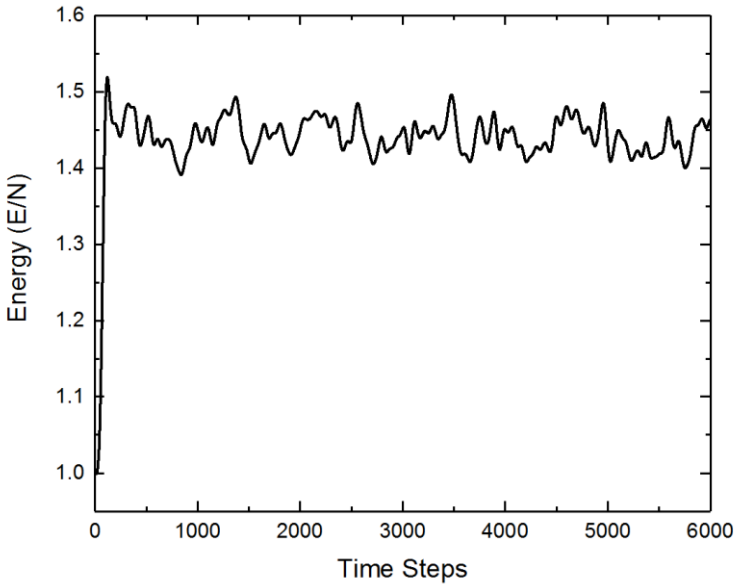

Figure 5.2: Instantaneous total energy from a SLLOD simulation with an applied shear rate of 0.01.

Once steady state was attained production runs of 6 million steps (see later) were conducted over which the values of properties such as the stress tensor elements were averaged. The (strain rate dependent) shear viscosity was calculated from the relationship:

$$\mu(\gamma) = \frac{-\langle P_{xy} \rangle}{\gamma} \tag{5.1}$$

where γ is the applied strain rate and P_{xy} is the xy element of the pressure tensor. It is well known that transport properties calculated from molecular simulations have a number dependence [136], [137]. To ascertain how large this is for two dimensional

soft sphere fluids, several runs were conducted at a strain rate of 0.1, time step of 0.001, run time of 6 million steps using different systems sizes ranging from 625 to 1521 ($\rho = 1$ and $T = 1$). The viscosity was calculated in each case and plotted as a function of 1 / N.

Results are shown in figure 5.3, where viscosity can be seen to converge (within error) when $\frac{1}{N} < 0.0012$. A system size of 1156 particles ($\frac{1}{N} = 8.65 \times 10^{-4}$) was therefore chosen due to being comfortably within the limits of viscosity convergence, and having a relatively low margin of error.

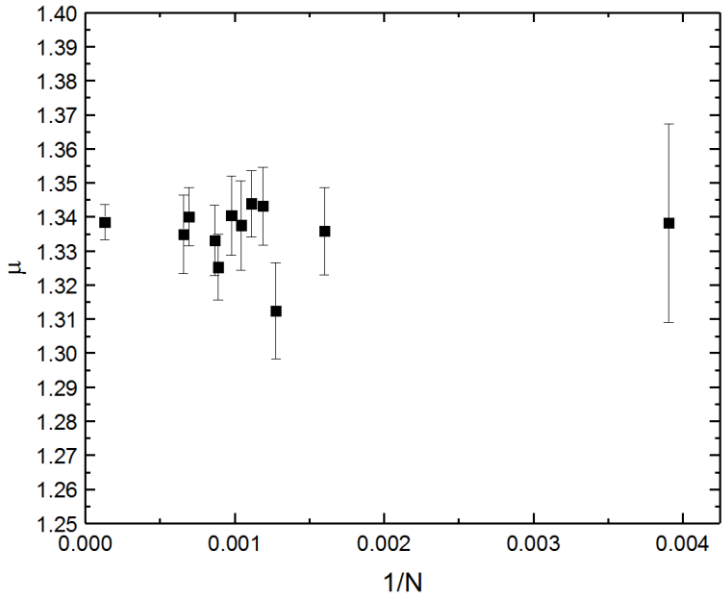

Figure 5.3: Shear viscosity as a function of the reciprocal number of particles. Each ensemble is iterated using a time step of 0.001 over 5 million steps, for a shear of 0.1.

To determine the optimum production run length (with due regard for the uncertainty in calculated shear viscosity), a very long simulation was conducted and the viscosity calculated after various stages. According to Gaussian error analysis, the relative error in the shear stress (and hence the viscosity) $\propto \sqrt{timesteps}$.

Shear viscosity is shown as a function of production runtime in figure 5.4. The viscosity appears to converge after 6×10^6 with an uncertainty of about 4 %. This was deemed to be an acceptable error – reducing this to 1 % for instance would require about 20 times longer simulation time, making it impractical in this project. The production run length was therefore chosen to be 6 million steps in all cases.

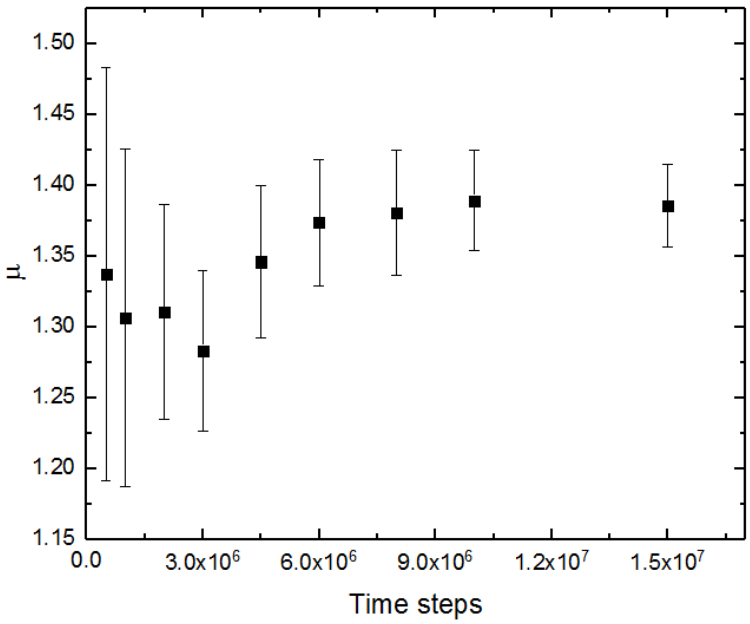

Figure 5.4: Shear viscosity as a function of production phase timesteps. Simulations use a total of 1156 particles and 5×10^5 number of equilibrium iterations with an applied shear rate of 0.02.

5.3 Results

The shear viscosity was calculated over a range of strain rates for series of densities between 0.8 and 1.4 and a fixed temperature of 1. The range of shear rates included a limited logarithmic selection of 0.100, 0.219, 0.468 and 1.000, a somewhat linear range equidistant between the logarithmic shears at 0.130, 0.180, 0.260, 0.300, 0.343, 0.645 and 0.822, and a limited range of shears below the suspected signal to noise limit of 0.030, 0.050 and 0.070. The highest strain rate used was unity – beyond strain rates of unity, thermostatting becomes problematic [138].

These results are shown in figure 5.5. It is clear from the results that the soft sphere fluid is non-Newtonian across the full range of densities, displaying shear thinning behaviour. Only the zero shear rate viscosity is required. The zero shear rate viscosity must be obtained by extrapolating the shear-dependent viscosity. Unfortunately, there is no agreed upon expression for the limiting shear rate dependence of viscosity in either 2 or 3 dimensions. Kawasaki and Gunton claimed that the relationship in 2-dimensions is logarithmic [139]. If correct, this would lead to a divergent viscosity at the origin. In this work, a pragmatic approach has been taken. An

empirical expression due to Cross [140] is often used by rheologists for fitting the non-Newtonian viscosity of real fluids.

The cross-fit function takes the form

$$\frac{\mu(\gamma) - \mu_\infty}{\mu(0) - \mu_\infty} = \frac{1}{(1 + (K\gamma)^m)} \tag{5.2}$$

where μ_∞ is the maximum viscosity, $\mu(0)$ the zero shear viscosity, and K and m adjustable constants - the former having dimensions of time. Treating $\mu(0)$ and μ_∞ likewise as adjustable constants gives a 4-parameter equation. Non-linear least squares methods were used to fit equation 5.2 to each set of viscosity-shear rate data. The best fit curves are displayed in figure 5.5. The fits were weighted by the error bars in the shear viscosity.

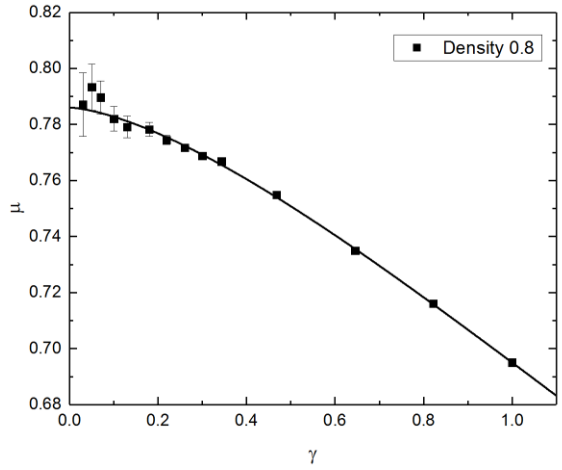
Density 0.8
μ
γ

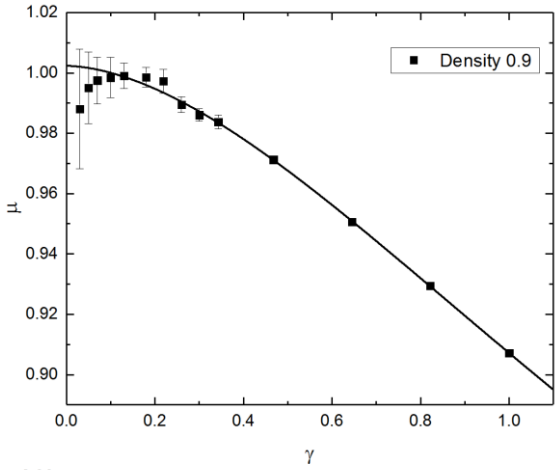
Density 0.9
μ
γ

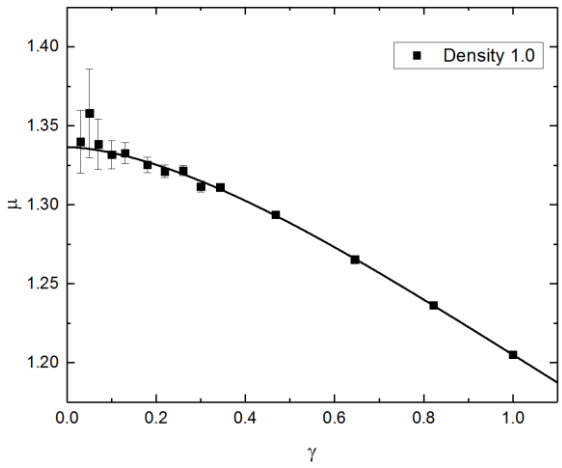
Density 1.0
μ
γ

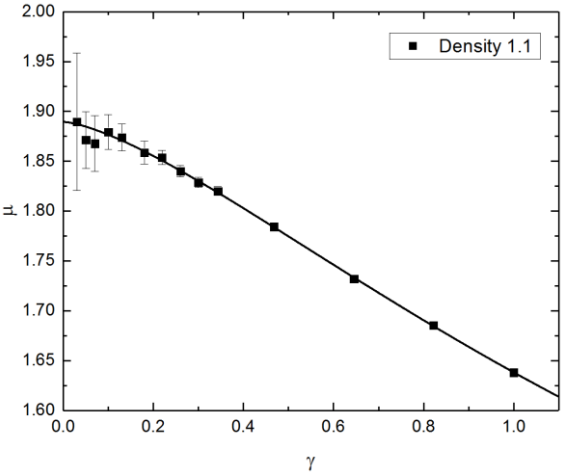
Density 1.1
μ
γ

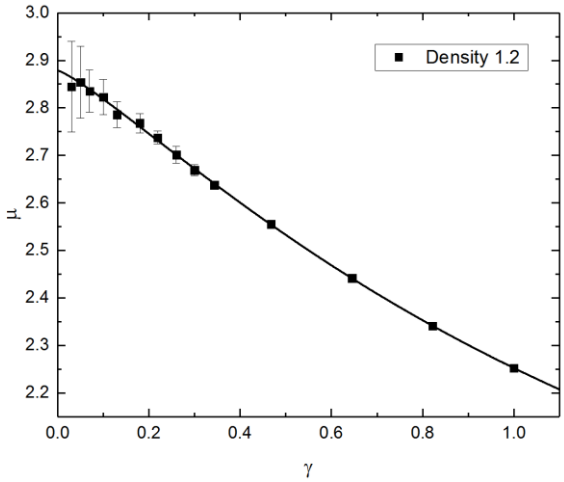
Density 1.2
μ
γ

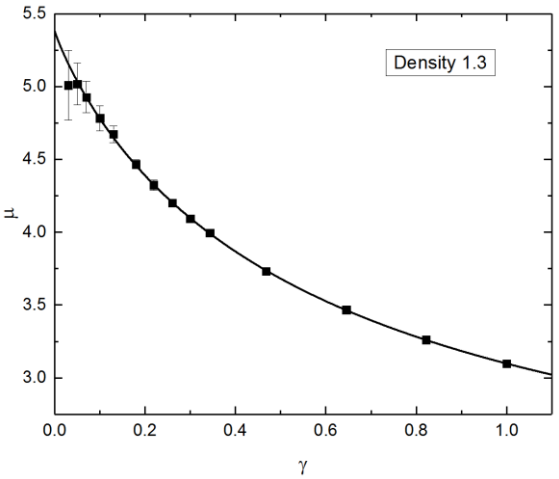
Density 1.3
μ
γ

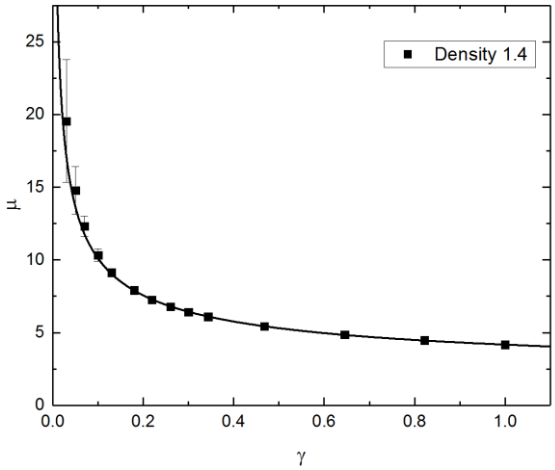

Figures 5.5 (a-g): Shear viscosity as a function of strain for a range of densities from 0.8 (figure 5.5a) to 1.4 (figure 5.5h). Lines are non-linear least squares fits to the Cross equation.

The 4-parameter Cross equation fits all the data sets quite well. The shape of the fit changes with density – up to $\rho = 1.2$, the curves are convex. Beyond $\rho = 1.2$, the curve changes to concave in shape. At $\rho = 1.3$ the curve fit extrapolates to the origin but overshoots the data points. At $\rho = 1.4$ the viscosity rises very steeply as the origin is approached, which appears to agree with Kawasaki's logarithmic behaviour. These high density trends are likely due to the soft sphere fluid freezing at this state point. This is illustrated in the particle plot shown in figure 5.6, where repeating triangular unit-cells begin to resemble segments of a solid lattice. The extrapolated zero shear viscosities are collectively shown in Table 5.1.

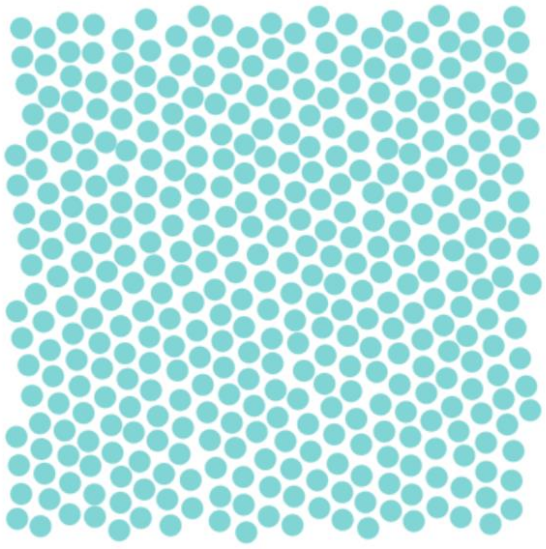

Figure 5.6: Particle plot of the soft-repulsive fluid with $T = 1$ and $\rho = 1.5$.

Viscosity is investigated over a narrower range of temperatures in comparison to density, these results are shown in figure 5.7.

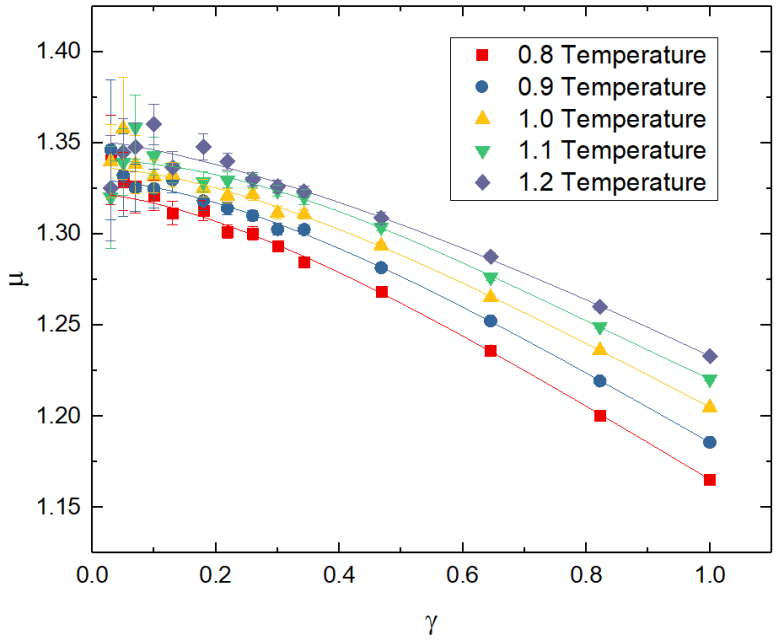

Figure 5.7: Shear viscosity as a function of applied strain rate for a range of temperature simulations.

The zero strain viscosity gradually increases in magnitude as a function of temperature. Each data series also follows a similar trend across the observed range of temperatures.

Table 5.1: The extrapolated viscosity from figures 5.5, 5.7 and 5.8, in addition to other viscosity measurements taken at an extended divergence from the reference fluid state.

Temperature	Density	Viscosity
1.0	0.8	0.786 ± 0.003
1.0	0.9	1.002 ± 0.002
1.0	1.0	1.337 ± 0.003
1.0	1.1	1.889 ± 0.006
1.0	1.2	2.88 ± 0.01
1.0	1.3	5.38 ± 0.07
1.0	1.4	200 ± 1000
0.8	1.0	1.322 ± 0.004
0.9	1.0	1.330 ± 0.003
1.1	1.0	1.340 ± 0.003
1.2	1.0	1.351 ± 0.007
0.8	0.8	0.744 ± 0.003
0.8	1.3	0.820 ± 0.004
1.2	0.8	14 ± 3
1.2	1.3	4.28 ± 0.03
0.9	0.9	0.987 ± 0.003
0.9	1.1	1.903 ± 0.006
1.1	0.9	1.020 ± 0.005
1.1	1.1	1.863 ± 0.007

Additional fluid simulations that differ in *both* temperature and density were also performed to quantify the coupling effects of density and temperature on shear viscosity. These are shown in figure 5.8, in addition to selected previous data.

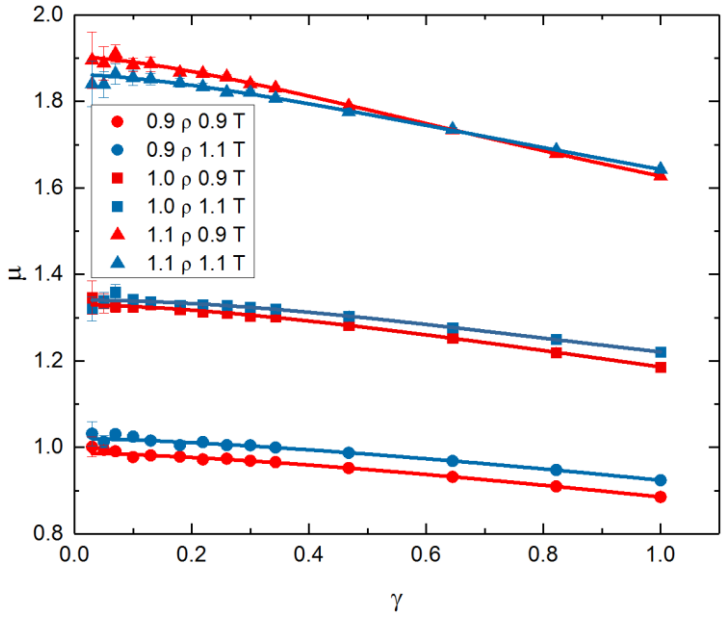

Figure 5.8: Viscosity as a function shear rate for three sets of densities and two alternate temperature fluids.

Figure 5.8 shows three pairs of alternate temperatures at a fixed density. It can be seen that, in contrast to figure 5.7, viscosity does *not* consistently increase with temperature. This is due to the coupling of density. One explanation would be the approach of the solid phase at high densities; as the fluid density increases and begins to solidify, additional heat in the fluid resists the change in phase and decreases the viscosity. Additional simulations at a density of 1.3 support this theory, as shown in table 5.1.

5.4 Development of a Shear Viscosity Function

It is constructive to provide an equation which gives a smoothly varying value of viscosity as a function of fluid density and temperature. This allows for a convenient method of determining any viscosity within the measured range as well as giving a suitable description of viscosity for any future continuum work. The approach to developing such a function is as follows:

1) Sets of extrapolated viscosities at a fixed temperature and different densities were fitted by a power series in the density *deviations* from the reference density of $\rho = 1$.

2) Sets of extrapolated viscosities at a fixed density and different temperatures were fitted by a different power series in deviations of temperature about the reference temperature of $T = 1$.
3) The two 1-dimensional fitting functions were then combined using extrapolated viscosities at deviations in both the reference temperature and density ($\rho = 1$, $T = 1$). This was fitted with a conjugate density and temperature power series, which includes the 1-dimensional fitting coefficients as fixed parameters.

Figure 5.9 shows the extrapolated viscosity as an exclusive function of divergence in density from the reference value.

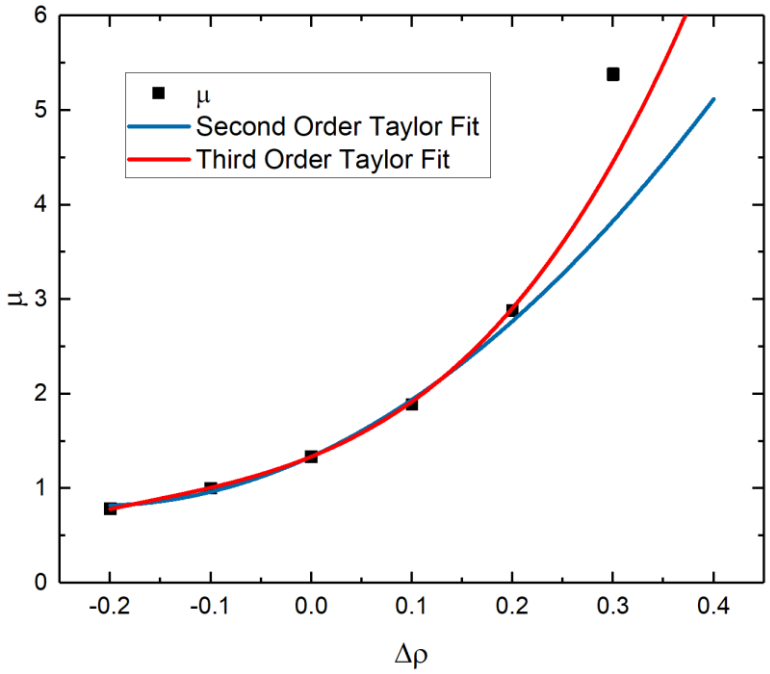

Figure 5.9: Extrapolated viscosity as a function of density divergence, at $T = 1$. An additional data point at $\rho = 1.4$ ($\Delta\rho = 0.4$) is included in the fitting, but has minimal influence upon the trend due to its large error. Error values are a similar size to markers.

Both 2nd and 3rd order error-weighted power fits were applied using the reference state viscosity ($\mu = 1.337$) as a fixed parameter. The 2nd order power series showed a poor level of fit. Although the 3rd order fit does not converge, the fit is acceptable. This gives viscosity as a function of density to be:

$$\mu = 1.337 + 4.292\Delta\rho + 12.68\Delta\rho^2 + 25.51\Delta\rho^3 \qquad (5.3)$$

The fixed density coefficients are determined in a similar fashion to those of fixed temperature, as shown in figure 5.10.

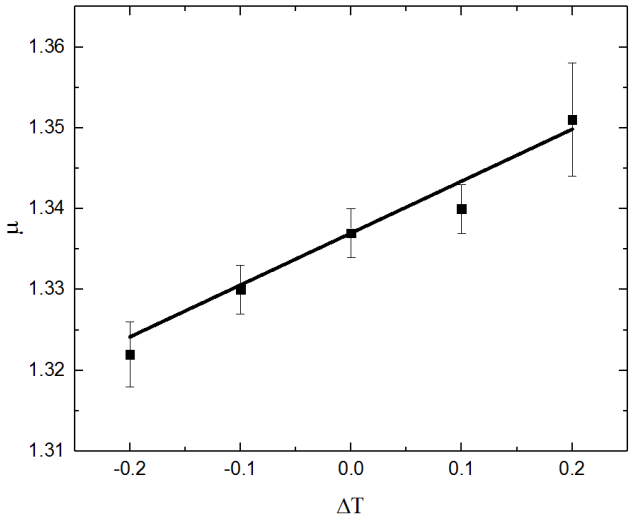

Figure 5.10: Extrapolated viscosity as a function of divergence in temperature from the reference state for unity density.

Viscosity appears to vary linearly with deviations from the reference temperature. The magnitude of this relationship is significantly smaller in comparison to divergences in density. A linear, first-order power series is therefore applied to the temperature exclusive viscosity dependence, where:

$$\mu = 1.337 + 6.423 \times 10^{-2}\Delta T \tag{5.4}$$

The previously determined fitting coefficients were used as fixed parameters in a power series surface fit to determine the conjugate density-temperature coefficients. Results were fitted to all extrapolated viscosity data shown in table 5.1. The extrapolated viscosities at divergences of 0.8 and 1.3 density showed poor levels of fit when including up to 4th order power series terms. Such divergences in both density and temperature were therefore excluded from the fit, and are considered beyond the accuracy of the final viscosity function. The power series surface fit for the remaining viscosity data is shown in figure 5.11.

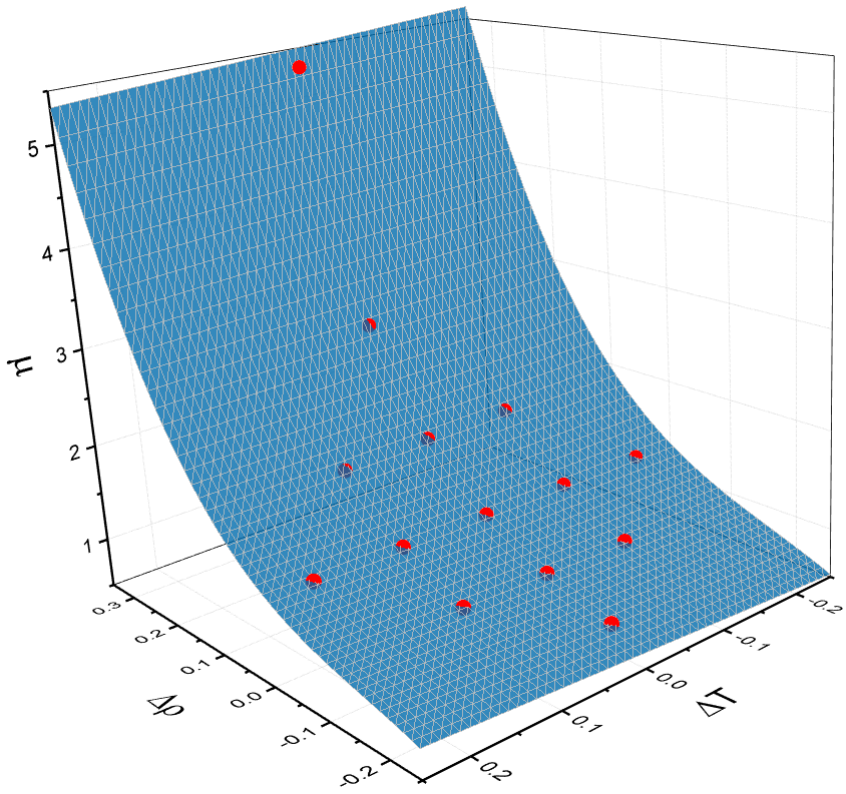

Figure 5.11: The surface plot of the conjugate density-temperature power series fitting function, fitted to deviations in both density and temperature from the reference state.

A first order power series fit showed reasonable accuracy for the small deviations in both density and temperature from the reference state. Higher order terms were discarded due to giving rise to un-physical behaviour (such as random oscillations) at the expense of a marginal increase in convergence. The first order conjugate coefficient completes the shear viscosity function, where:

$$\mu = 1.337 + 6.423 \times 10^{-2}\Delta T + 4.292\Delta\rho + 12.68\Delta\rho^2 + 25.51\Delta\rho^3 - 1.825\Delta\rho\Delta T \qquad (5.5)$$

6: Molecular Dynamics Simulation of Sinking Objects

6.1 Introduction

The focus of this chapter is the study of the sinking of a solid object through a viscous fluid using molecular dynamics. The aims are as follows:

(1) To gain insight into the pressure, stress and velocity distributions in the vicinity of the sinking object in order to better understand the phenomena governing sinking rates and guide future numerical sinking rate solutions.
(2) To generate pseudo-experimental data for use in continuum mechanics simulations of sinking, which will provide reference data for any attempts to expand simulations beyond the mesoscale.
(3) Corroborate laboratory experiments with simulation data.

Two different approaches were employed. In the first approach, a large disc is allowed to sink under the influence of a gravitational field through a fluid. In the second approach, the disc remains stationary while fluid moves past it at a fixed streaming velocity. The first approach resembles the sinking experiments but the frame of reference of the second approach leads to simpler interpretation of the results.

6.2 Sinking Disc Simulations

6.2.1 Methodology

A two-dimensional disc is allowed to sink using a gravitational field through a fluid comprised of particles interacting through the soft-repulsive pair potential ($\epsilon = 100$, $\sigma = 1$). The first stage of the model involved the generation of an equilibrated fluid. The initial condition comprised a rectangular column of particles in which the unit cell had the symmetry of a square lattice. Each of these particles was given a random initial velocity between -0.5 and +0.5, which was scaled to the desired temperature using the *ad-hoc* thermostat. The mass of the particles was unity. The bottom boundary (*x*-axis) condition was elastic, as were the lateral boundaries.

Newton's equations of motion were then solved using a 4th order Runge-Kutta algorithm with a timestep of $\Delta t = 0.001$. The momenta were re-scaled using the *ad-hoc* thermostat (see section 2.3.4.1) in order to maintain the average temperature to the target value. The simulation was run for a number of timesteps sufficient to remove all trace of the starting lattice and in which properties began to fluctuate about their mean values – an indication that equilibrium had been established.

The sinker, in this case a large disc, was positioned near the top of the column of fluid but in such a way that the top of the disc was located at the top of the top of the container. Once the density (ρ_s) and radius (R) of the sinker were specified, its mass (M_s) could be calculated using $\rho_s \pi R^2$. Once the disc was in position beneath the surface of the fluid, any fluid particles occupying the area inside its circumference were deleted from the simulation, as shown in figure 6.1.

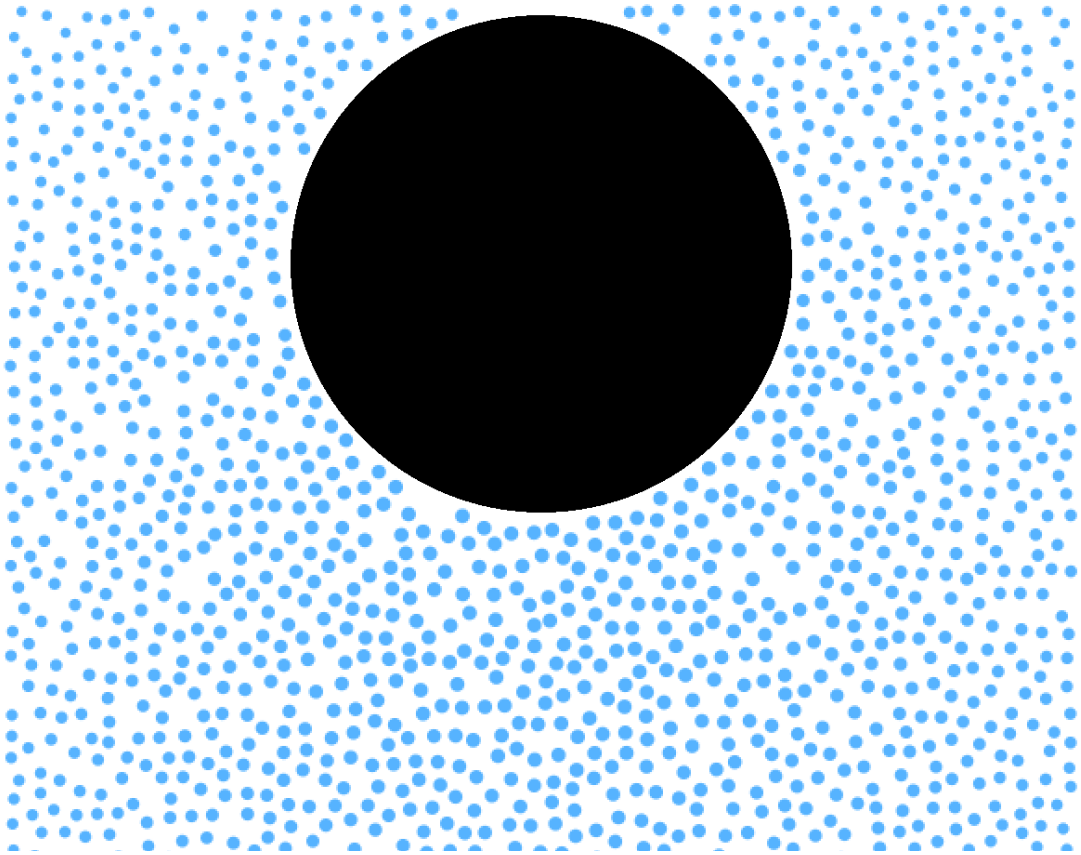

Figure 6.1: Particle plot near the beginning of a sinking disc simulation, with the sinking disc placed at the top of the simulation area.

The disc interacts with the fluid using an offset version of the soft-repulsive potential. The magnitude of the offset is effectively the radius of the disc, this is achieved by simply using a modified pair separation when computing the pair potential such that:

$$\delta r = r - R < \sigma \tag{6.1}$$

The force on a fluid particle resulting from its interaction with the sinker can be obtained from differentiating the extended potential, giving:

$$\boldsymbol{F}_i = 8\varepsilon\left(\frac{\delta r}{\sigma^2}\right)\left[1 - \left(\frac{\delta r}{\sigma}\right)^2\right]^3 \frac{\boldsymbol{r}_{ij}}{r} \tag{6.2}$$

from which it can be seen that the force is zero at the point of contact between a fluid particle and the sinker and has its greatest value at $\delta r/\sigma = \sqrt{1/7}$. The force on the sinker resulting from a neighbouring fluid particle is obtained from equation 6.2 by reversing the sign.

In addition to the above force, a gravitational force is added to the total force acting on the sinking disc. The equation of motion for the momentum of the sinker is therefore:

$$\dot{\boldsymbol{p}}_s = \boldsymbol{F}_s^{sr} - M_s g\tilde{\boldsymbol{y}} \tag{6.3}$$

where the s subscript refers to the sinker, g is the strength of gravity and $\tilde{\boldsymbol{y}}$ is a unit vector in the positive y direction. The gravitational force has not been applied to the fluid particles; including such a force results in strong density gradients being established in the simulation which would be unphysical at this length scale.

The strength of the gravitational field is given as an arbitrary value of g = 0.1. This value was chosen on the basis of exploratory simulations. Using values much greater lead to the sinker travelling faster than the speed of sound. Too low a value lead to the sinker either not sinking at all, or sinking too slowly. The trajectory of the sinker was obtained from its motion equations using the same RK4 integration scheme used for the fluid atoms with a time step of 0.001.

6.2.1.1 Scoping Studies

The density and temperature of the fluid determine both its behaviour and more importantly, its state. The aim was to find a fluid density and temperature that allows a sinking object to reach a steady velocity, whilst also being representative of a reasonably incompressible fluid.

It is useful to observe the instantaneous velocity for a sinking disc in fluids of different densities. Equilibrated starting configurations were prepared using fluids with densities of 0.8, 1.0 and 1.2, and at unit temperature. Sinking simulations were then performed using discs with a radius of 6.5 and a density of 3.0. The results from these simulations are shown in figure 6.2.

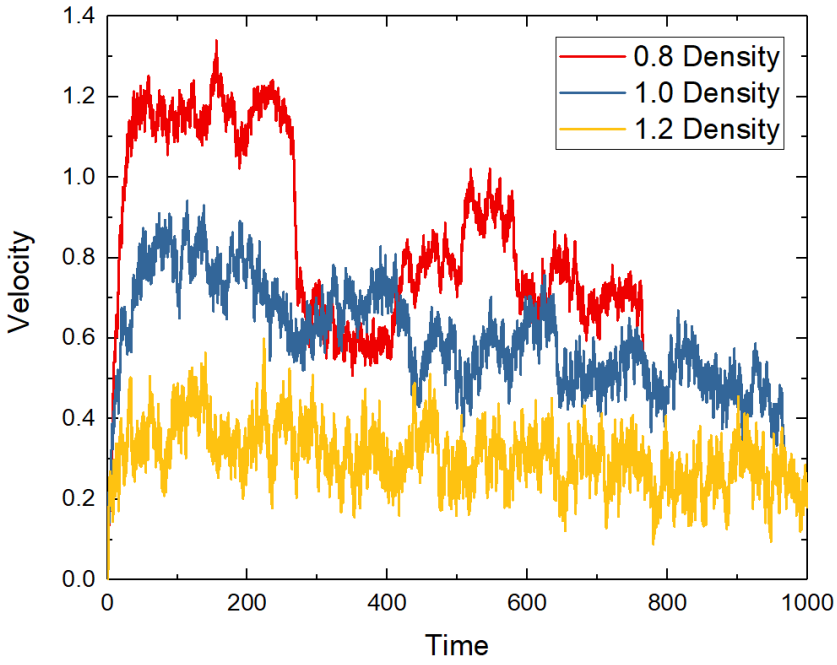

Figure 6.2: Instantaneous sinker velocity as a function of time, for fluid densities of 0.8, 1.0 and 1.2. Readings are taken every 10 time steps, or 0.01 reduced time units. Ball density of 3.0 and radius of 6.5, fluid width of 20 and height of 600, with temperature of 1.

It is clear in figure 6.2 that the instantaneous velocity trends from high (time, t = 50) to low (t = 250) at a density of 0.8, despite the large quantity of thermal noise. This is due to the fluid initially compressing before the fluid density beneath the sinker reaches an equilibrium, causing the sinker to finally travel at a terminal velocity. In reality, this equilibration will consist of fluid 'waves' between the sinker and bottom boundary,

resulting in several peaks as shown. This is clearly evidence of an undesired, highly compressible fluid.

Increasing the density from 0.8 clearly decreases the compressibility, as illustrated by the reduction in velocity peaks for densities of 1.0 and 1.2. The 1.2 density series is noisier than the 1.0 density series which we attribute to partial solidification of the fluid at higher densities. Figure 6.3 shows snapshots of the fluid particles directly beneath the sinking disc at the three different densities. The $\rho = 1.2$ configuration clearly shows long range order indicative of a solid-like structure. Based on these results, fluids of $\rho = 0.8$ and 1.2 were ruled out and sinking experiments were confined to densities at or close to unity.

Temperature was the next variable to be explored. Starting configurations were prepared with the fluid density $\rho = 1.0$, but temperature set to values ranging from $T = 0.25$ to $T = 1.25$. Sinking experiments were then performed in each case. For these simulations, the distance of the sinking disc from the base boundary were recorded as a function of time. Figure 6.4 shows these results.

It is clear that as temperature decreases, the time taken for the sinker to reach the bottom increases. Furthermore, a hump can be seen in the trajectory of lowest temperature centred on a time of ~ 300.

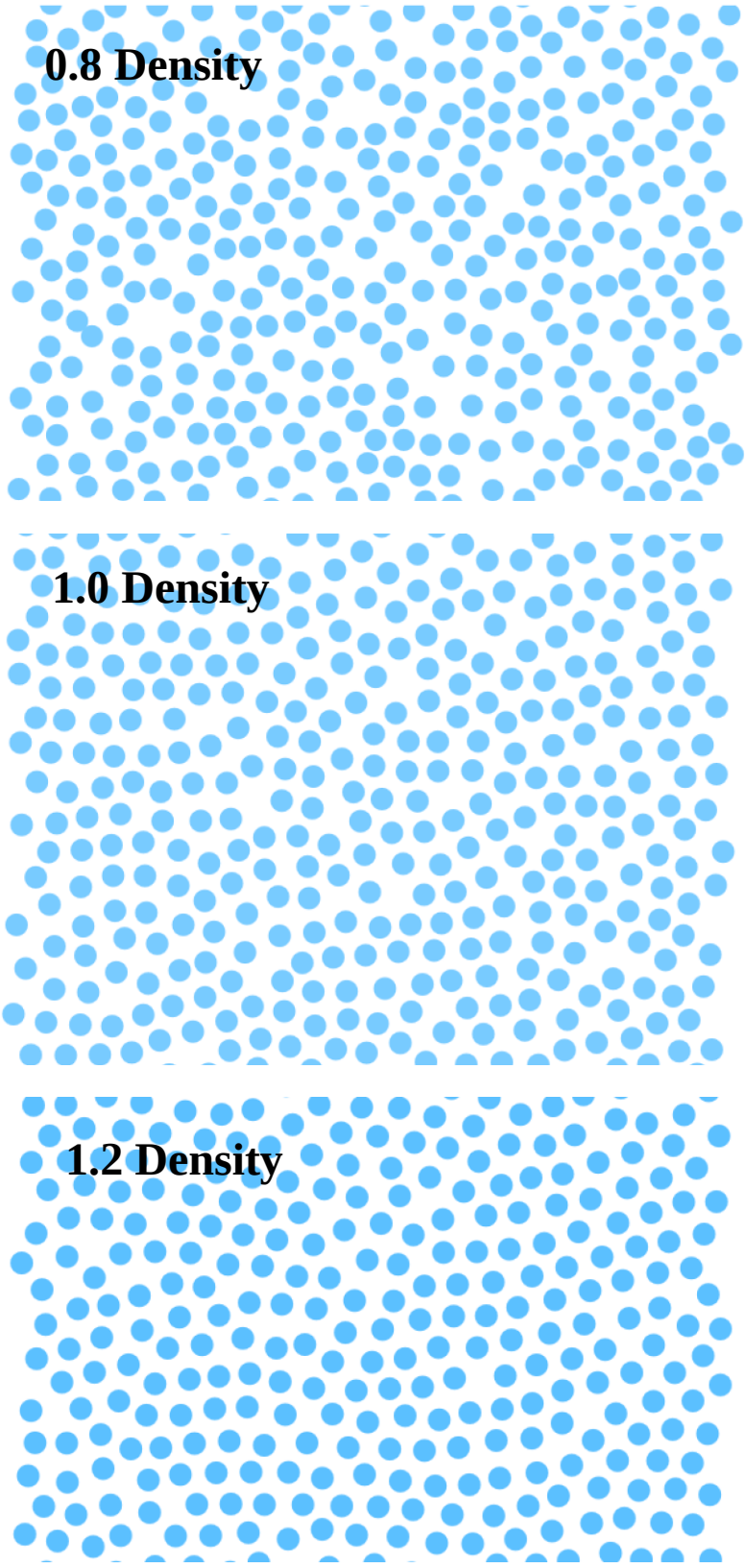

Figure 6.3: The fluid configuration beneath a sinking disc of radius 6.5 within a 20 particle width lattice for fluids of density 0.8 (figure 6.3a, top) 1.0 (figure 6.3b, middle) and 1.2 (figure 6.3c, bottom).

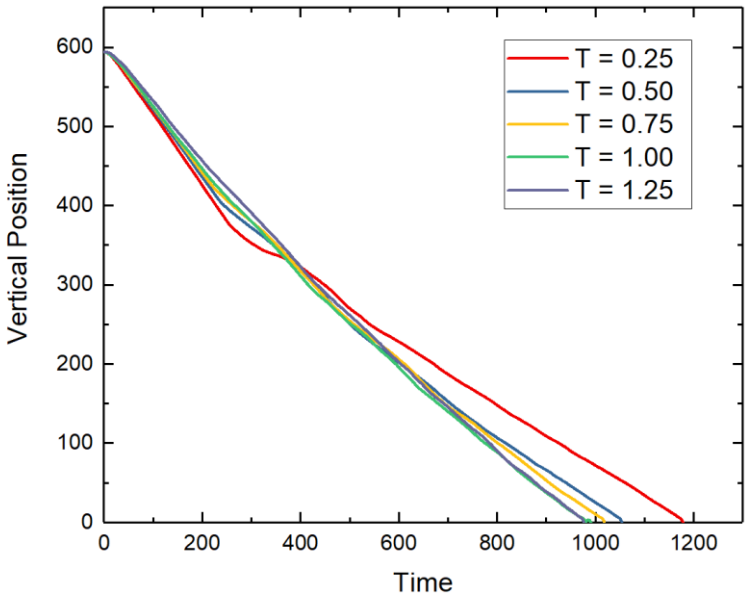

Figure 6.4: Sinker distance from base, as a function of elapsed sinking duration.

A higher temperature is therefore desirable to have a greater chance of the sinker reaching terminal velocity before it hits the bottom of the simulation box (longer simulation cells greatly add to the computational cost[1]). Since the curves shown in figure 6.4 are largely indistinguishable from each other beyond $T = 1$, a range of temperatures close to unity was selected for future sinking simulations.

The majority of simulations are performed close to the reference state used to derive the continuum equation of state, $\rho = 0.95$ and $T = 1.05$ respectively.

6.2.1.2 Calculation of Sinking Velocity

The velocity of the sinking disc is an important variable to calculate. The velocity obtained from the equations of motion proved to be too noisy for practical purposes due to thermal fluctuations, as shown in figure 6.2. This noise could essentially be reduced

[1] The computational costs refer to the necessary computing power to complete simulations. During this study the computational resources were limited; any increase in computational costs therefore resulted in a longer time to complete simulations. The computational costs were therefore directly limited by the corresponding timeframe of this research.

by reducing the magnitude of disc-particle collisions - this could be achieved through either:

1) Increasing the ratio of sinker to fluid density
2) Decreasing the relative fluid particle size

The sinker to fluid density ratio is already a systematic variable in this investigation, and is coupled to the gravitational force on the sinker. To keep the density of the fluid constant, fluid particle mass must be decreased and the number of particles increased, limiting this solution to the available processing power. Due to the computational time constraints on this project an alternative method of determining sinking velocity was imposed. The velocity of the sinker was obtained indirectly by first plotting the vertical separation of the centre of the disc to the bottom boundary, and then extracting the velocity from the slope of a linear least squares fit to the linear portion of the data. Figure 6.5 shows raw experimental data from a typical sinking 'experiment'. The early portion of the plot is non-linear and therefore ignored. The final part was ignored as it is in the region where the ball would interact with the bottom boundary.

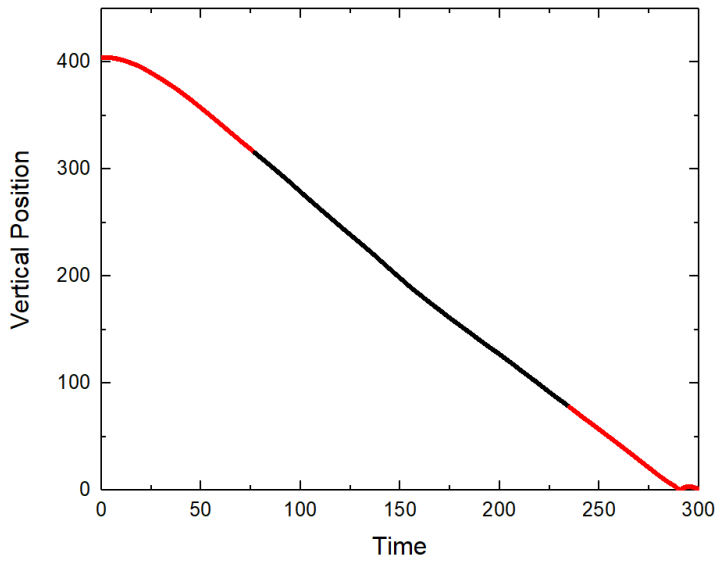

Figure 6.5: The separation between disc and fluid base as a function of time for a sinking disc of 0.14 κ in a column of fluid with width 84.2. The red zones indicate excluded data where velocity is non-terminal due to end-effects.

6.2.2 Disc Density

The density of discs was systematically varied in order to understand the relationship between density and sinking velocity in a finite boundary system. Simulations were performed using a constant κ of 0.65 (ratio of the diameter of the disc to the width of the simulation box), in a column of fluid with density 1.0, temperature 1.0, with a height of 600 units and a width of 20 units. These results are shown in figure 6.6.

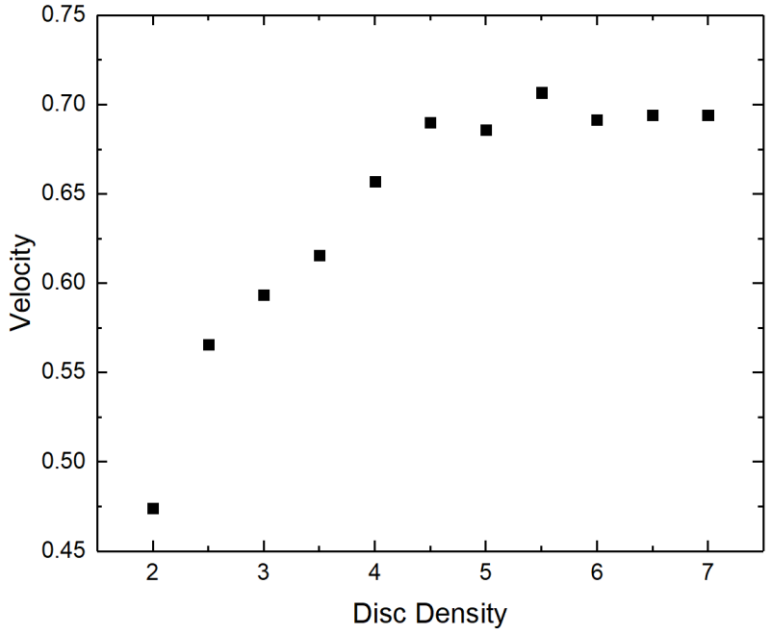

Figure 6.6: Sinking (terminal) velocity as a function of sinker density for a disc with 0.65 κ. Error bars are of similar size to the marker box.

The terminal velocity can be seen to increase with increasing sinker density up to a disc density of around 4.0, after which it appears to plateau towards a maximum. Not only is this in agreement to the analytical model in section 4, but this also supports the hypotheses made in chapter 3 regarding an asymptotic velocity when increasing the density (or length) of a given cylinder - a difficult trend to prove experimentally due to the increasingly dense (and expensive) range of materials required.

It is noteworthy that the plateau in velocity shown in figure 6.6 is not approached smoothly, despite the very small margins of error. This is believed to be due to the compression of fluid as density is increased, a phenomenon also shown at lower fluid densities (see figure 6.2). This can be visualised by plotting the sinker height (above the bottom boundary) as a function of time, as shown in figure 6.7. It is clear to

see that as density increases, greater fluctuations in velocity appear as the fluid compresses. A low sinker density of $\rho = 2.5$ is therefore used in the majority of later simulations in an attempt to avoid this behaviour.

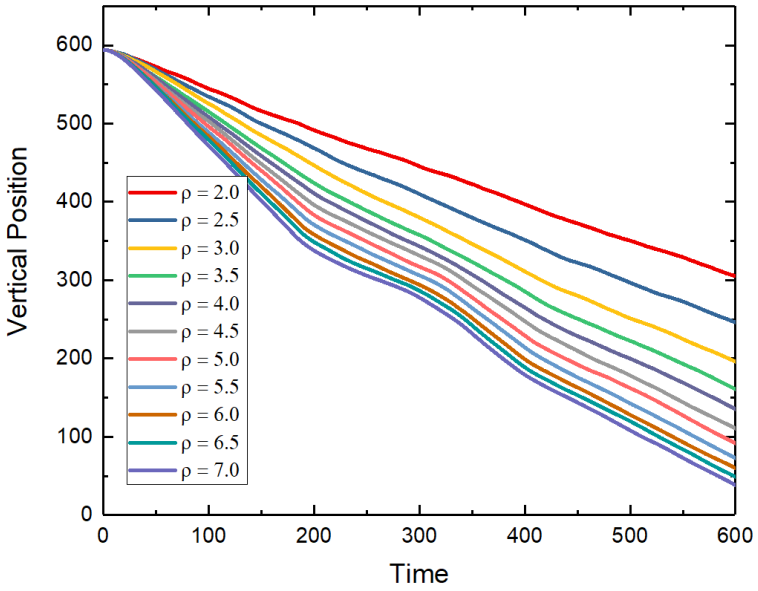

Figure 6.7: Vertical distance from sinking discs to the base of the simulation as a function of time. Each series is representative of a different sinking density between 2.0 to 7.0.

6.2.3 Disc Diameter

Several discs with different diameters were allowed to sink through a column of fluid in order to determine the relationship between sinking velocity and diameter. Results are shown in figure 6.8 using a fluid of $\rho = 0.95$, $T = 1.05$, with a height of 450 units and a width of 56.4 units.

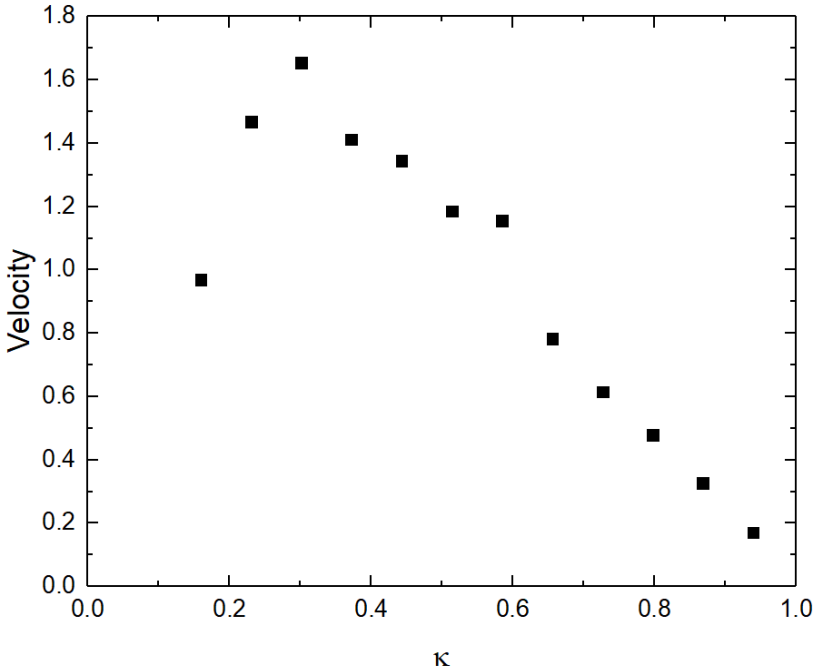

Figure 6.8: The terminal velocity of sinking discs each with a different diameter. The abscissa is diameter ratio, κ.

Terminal velocity first increases with κ, until approaching a maximum at approximately 0.3 κ, then descends to zero. In this broad sense, this velocity behaviour qualitatively agrees with observations during experiments of the sinking spheres and all analytical solutions. Quantitatively, this maximum occurs 74% below sinking sphere experiments and 300% above the analytical model D. This peak maximum is in relatively close agreement to experiments considering the difference in dimensions. Furthermore, literature documents that the restrictive 'wall effects' become more important as scale decreases [141], which would explain why a peak would occur at a lesser κ for particle based simulations.

The linear decrease of velocity with respect to κ when $\kappa > 0.6$ in simulations also corroborates the sinking sphere *and* cylinder experiments in section 3, and suggests that this linear relationship may hold true for a wider range of κ (up to $\sim$0.4).

6.2.4 Disc Trajectory

By viewing snapshots (and later movies) of the sinking simulations, it became clear that the sinking object followed a tortuous path on its way to the bottom of the simulation box. Figure 6.9 shows a typical snapshot, showing the asymmetry in the disc's position.

The trajectory of discs can be studied in greater detail by fitting the x and y co-ordinates of the sinker at every 10 time steps to a spline function. This is shown in figure 6.10 for a range of κ discs of constant density sinking through a fluid of 450 units in height and 56.4 units in width. For lower values of κ the discs can be seen to have considerable lateral movement, drifting up to 15 units in the x direction, despite external forces applied exclusively to the y axis. In figures 6.10(b) and 6.10(c) the magnitude of lateral movement can be seen to steadily decrease as κ increases, even when the range of lateral motion is normalised to account for the sinker radius (as the disc size increases, there is less room for lateral movement). At increasingly large values of κ this lateral movement begins to increase, as illustrated in figure 6.10(d). The magnitude of lateral movement can therefore be seen to follow a similar trend in κ compared to terminal velocity.

The fact that this behaviour was observed in a 'perfect' computational setting is supporting evidence that the trajectory phenomena observed during experiments in chapter 3 were not due to any inconsistencies, such as deviations in the release of the sample, or minute misalignments of the apparatus.

It was discussed in significant detail throughout section 3 (in particular section 3.5.5) how cylinders would axially rotate during descent, despite efforts for a controlled, submerged and centralised initial release. This observation of significant lateral movement during simulations is therefore supporting evidence that such movement patterns are an inherent component of narrow-clearance sinking, especially considering that discs are initially set *exactly* central within the container before descent.

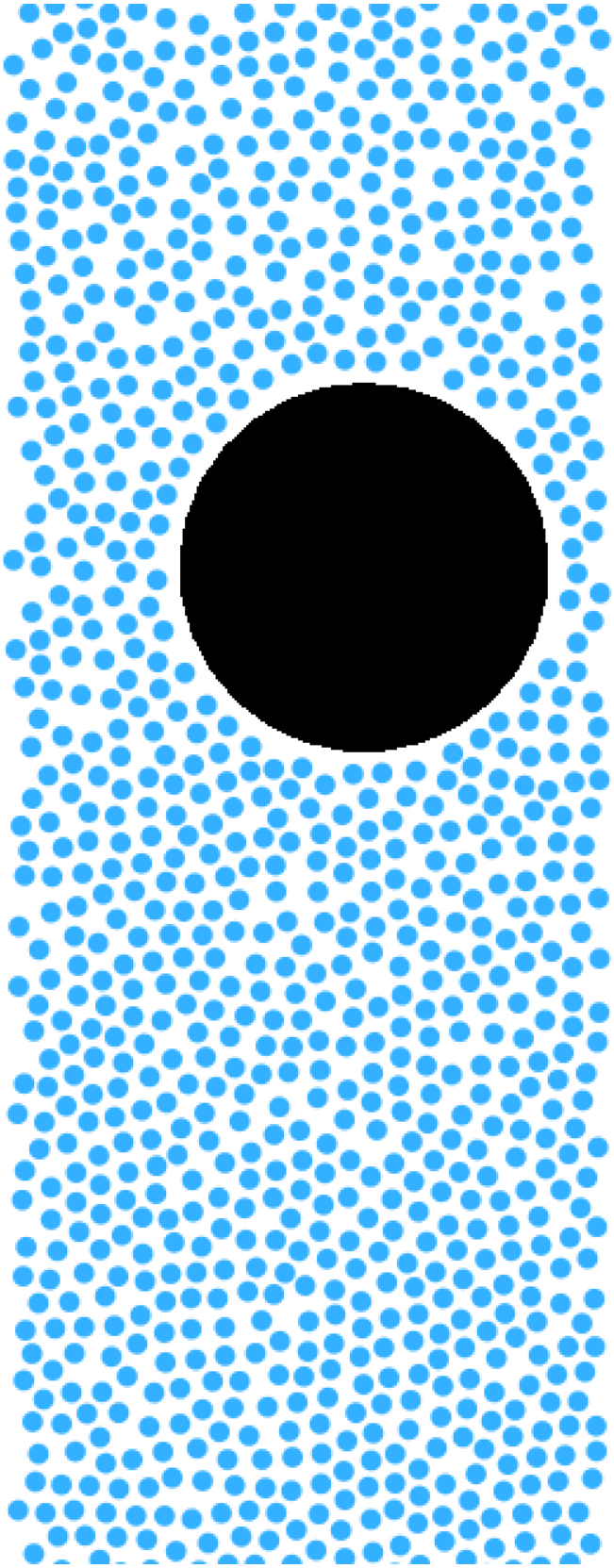

Figure 6.9: Particle plot from a sinking simulation showing the non-central disc and surrounding fluid particles.

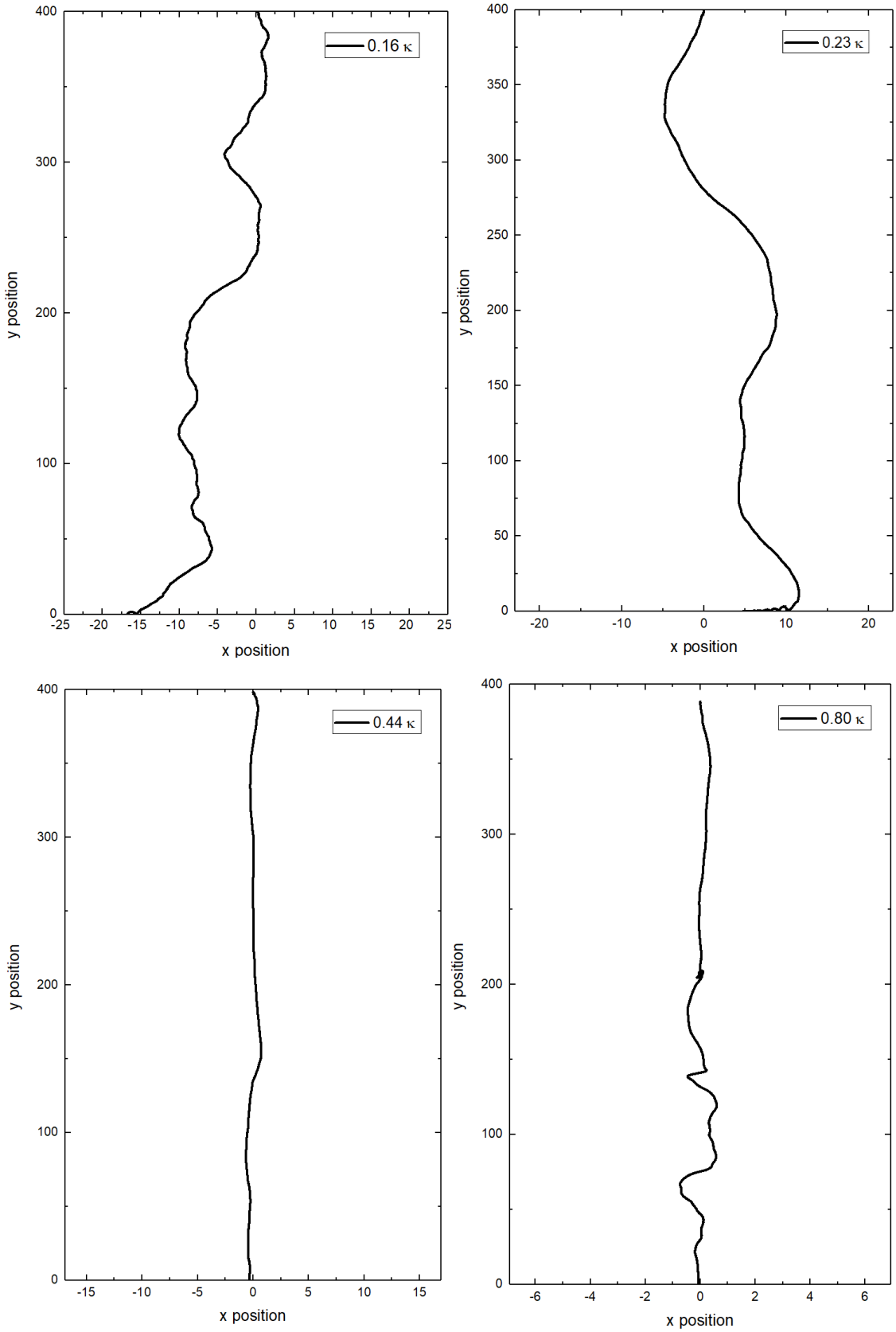

Figures 6.10 (a-d): The trajectory of 4 discs sinking through a fluid of $\rho = 0.95$ and $T = 1.05$. The trajectory is illustrated using a spline fitted to the x and y co-ordinates of the sinker at every 10 time steps. The column of fluid is 450 dimensionless units in

height and 56.4 units wide; the x axis of each figure is normalised so that the visible region corresponds to the entire region of travel before the disc comes into contact with the container.

6.2.5 Container Width

The only practical method of systematically varying κ during experiments was to modify the radius of the sinking object. A drawback of this approach is that terminal velocity is not *exclusively* investigated as a function of clearance, as sinker density and 'volume' (area in 2D) are also a function of object radius. In contrast, the size of the apparatus can easily be modified in a simulation, within the constraints of computational time. A disc of constant radius was therefore allowed to sink within a range of fluid column widths to investigate the relationship with sinking time and κ. These simulations were performed using a fluid of height 450 units, T = 1.05, ρ = 0.95, and with a sinking disc of radius 12 and density = 2.5.

Figure 6.11 shows terminal velocity as a function of absolute fluid container width. Velocity increases as the container increases and boundary effects become negligible. As the container size increases, the trend appears to go an asymptotic limit, where the effects of a boundary become negligible.

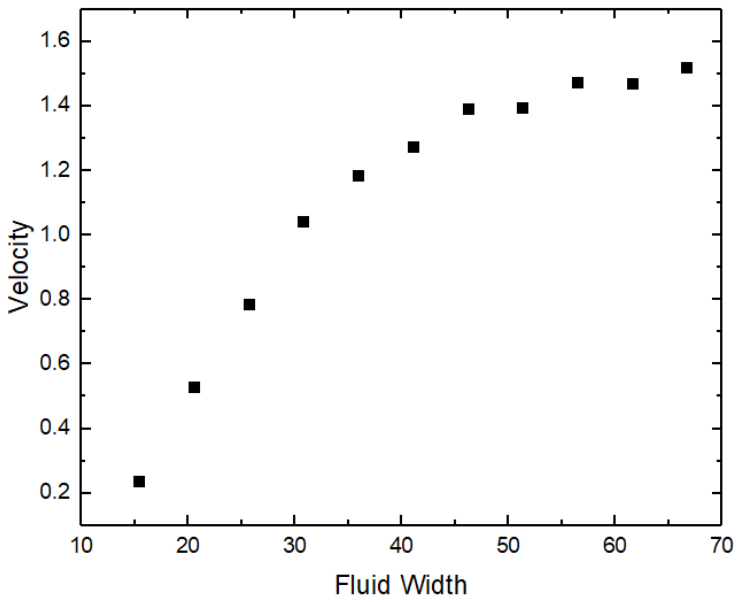

Figure 6.11: Terminal sinking velocity as a function of container width for a fixed sized disc

Figure 6.12 shows the same relationship as a function of κ. Results show that velocity appears to be linearly proportional to the sinking velocity throughout the entire range of κ. This suggests that the linear velocity-κ relationship observed when varying sinker *diameter* (figure 6.8) is a result of the effects of clearance dominating other forces, such as gravity. This is the strongest evidence thus far that frictional force associated with hydrodynamic braking is not only linear, but the dominant force at $\kappa > 0.6$.

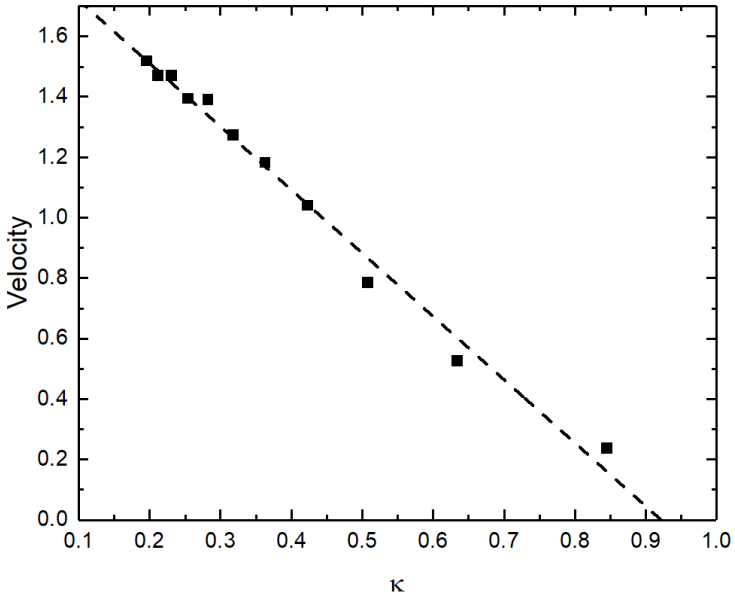

Figure 6.12: Terminal sinking velocity of a fixed sized disc within a varying container width as a function of the disc-container ratio (κ).

The fact that the velocity of the disc continuously increases with container size also shows that hydrodynamic braking is still in effect at the lowest investigated κ of 0.2. This contradicts the findings in section 3.5, which indicated that wall effects became significant at approximately $\kappa = 0.25$. This could simply be explained by the weakened effect of hydrodynamic braking associated with an alternative frame of reference [141].

6.2.6 Simulation Scale

The influence of the container width can also be investigated *independent* of clearance. This was achieved by increasing the size of the experiment and scaling the disc radius accordingly, such that κ is kept constant regardless of the container width. Results are shown in figure 6.13 using a fluid of height = 450, T = 1.05, ρ = 0.95.

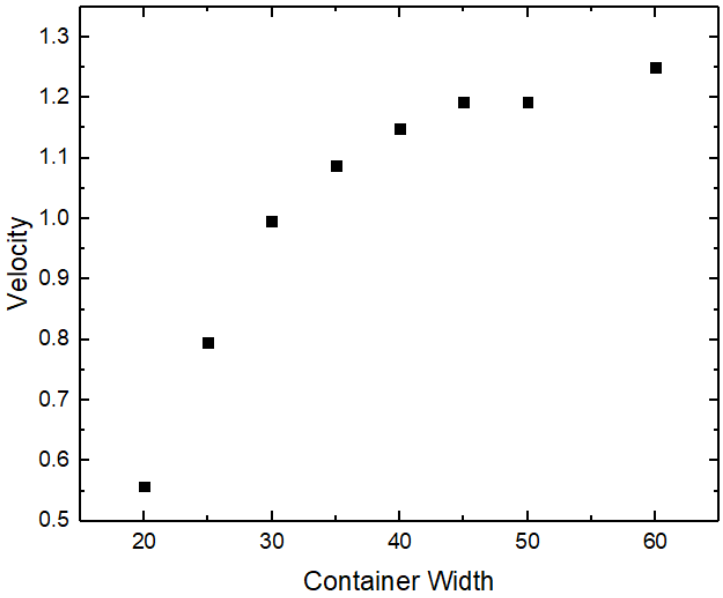

Figure 6.13: The velocity of a disc as a function of container size. The disc radius is adjusted such that κ is kept constant.

The sinking velocity of the disc can clearly be seen to increase with the size of the container, possibly towards an asymptotic maximum. One explanation for this approach to a maximum could be the area of fluid being displaced: the volume of displaced fluid and annular gap should increase at the same rate, however, during displacement the average fluid path length *towards* the annular gap will only increase with scale.

More fundamentally, results show that scale is an important factor in determining the terminal velocity of sinkers and is unlikely to have a simple linear dependency upon terminal velocity. Scale would therefore need to be thoroughly investigated before incorporating any results into an empirical model capable of accurately predicting sinking rates (a largely omitted variable from experiments).

6.3 Stationary Disc Simulations

The sinking disc experiments provided a useful method to investigate the functional dependencies between sinking rate and system variables in a similar manner to experiments. However, it is beneficial to gain a more in depth understanding of the phenomena that govern sinking rates. This is not only insightful from a hydrodynamics

perspective, but also allows for informed guidance into the future iterations of a predictive sinking velocity model.

The calculation of fluid properties is problematic for a disc sinking through a column of fluid. The time averaged field properties of the fluid in the Eulerian frame of reference are perturbed by the moving disc. Furthermore, the lateral movement of the sinker makes the calculation of fluid properties in the Lagrangian reference frame (originating from the sinker) problematic. A convenient solution is to shift the frame of reference, fixing the sinker in position and applying a flow of fluid past the object. The simulations in the following sections were performed using a modified source code originally provided by Karl Travis [142].

6.3.1 Methodology

The fluid flow across a stationary disc is implemented using two boundary conditions at either end of a fluid container, as illustrated in figure 6.14. A column of particles are repeatedly added to the left of the simulation with the desired streaming velocity v_x. This streaming velocity is fixed constant throughout the region $x < \sigma$ (the green region in figure 6.14). A new column of particles is added to the simulation after a period of time $t = \frac{\sigma}{v_x}$. The position of these newly added particles is equal to the left-most column of particles in the simulation, horizontally displaced by $-\sigma$.

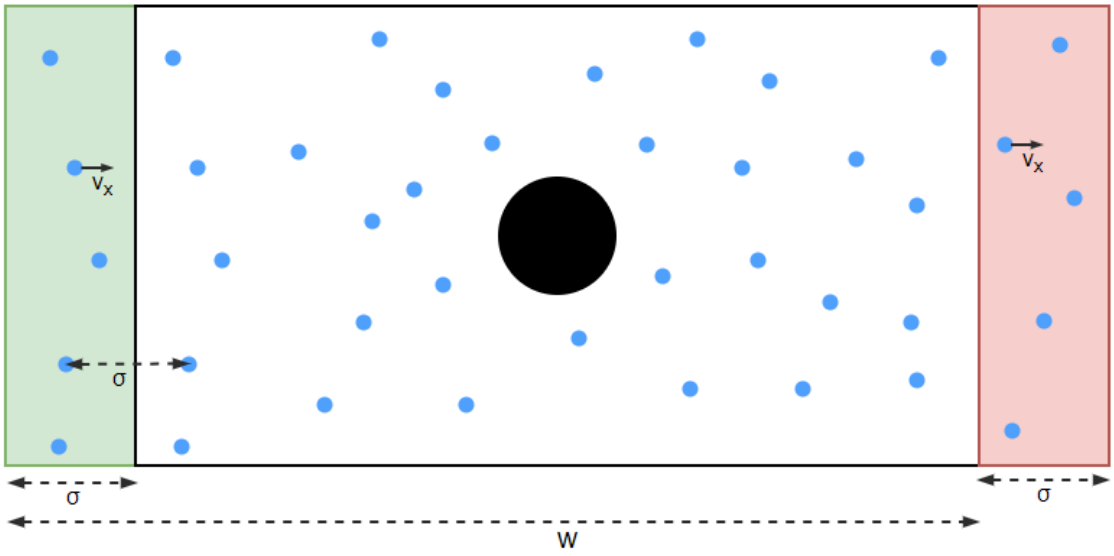

Figure 6.14: Schematic diagram of the stationary disc simulation, including the boundary regions in which particles are added and removed, as shown by the green and red zones respectively.

When a fluid particle reaches the position $x = w$ (see figure 6.14), the x velocity is once again fixed to v_x and cannot be modified through particle interactions. Finally, particles are removed from the simulation when they reach the position $x = w + \sigma$. These boundary conditions do not inherently enforce mass conservation, as particles are continuously added to the simulation at the same rate, and leave the simulation as and when they reach the right hand side boundary. That being said, the number of particles should equilibrate (as later discussed in section 6.3.2).

Previous simulations were performed at a timestep that provided a high level of precision so as to accurately determine continuum coefficients. However, simulations must be performed for long time periods when the streaming velocity is low. A greater magnitude of timestep is therefore necessary to ensure an equilibrium. The accuracy of timesteps was justified by repeating a set of simulations from the previous sinking disc section over a range of time steps. This was performed using a 56.43 wide and 400 high column of fluid where ρ = 0.95, T = 1.05 and a disc density of 2.5. The results shown in table 6.1 indicate minimal variance with the sinking velocity at different timesteps, with no notable trend.

Table 6.1: The velocity of two discs sinking through a column of fluid at multiple timesteps.

Timestep	κ	Velocity	Divergence (%)
0.001	0.37	1.40377	N/A
0.001	0.58	1.04204	N/A
0.002	0.37	1.42227	1.32
0.002	0.58	1.02246	1.88
0.005	0.37	1.4091	0.38
0.005	0.58	1.0403	0.17
0.01	0.37	1.38406	1.40
0.01	0.58	1.03191	0.97

A timestep of 0.005 is used despite results showing that a timestep of up to 0.01 is reasonably accurate. This is to allow headroom to investigate systems with higher particle velocities within this section (a faster velocity will increase the magnitude of errors). The fourth order Runge-Kutta method is used to integrate the simulation over time.

The equations of motion are calculated using MD methods equivalent to those in section 6.1, however, for analytical purposes *only* the local properties were calculated as smoothed particle applied mechanics (SPAM) averages. In SPAM these averages are used to calculate the influence of surrounding field properties for each particle given location, but can equally be used to provide a weighted average of any property via local properties and a separation distance. This method is described below:

1) The simulation cell was subdivided using a number of equally spaced lines placed perpendicular to the direction of fluid flow.
2) The local mass density at the x-position of each line was calculated from a weighted sum of particle masses:

$$\rho(x = x_i) = \sum_{j=1}^{N} m_j w\left(\left|x_i - x_j\right|\right) \tag{6.4}$$

where *w* is the Lucy 1-D weight function:

$$w_{1D} = \frac{5}{4\Pi}\left(1 + 3\frac{r}{\Pi}\right)\left(1 - \frac{r}{\Pi}\right)^3 \tag{6.5}$$

and Π is the smoothing length, whilst x_i is the x-position of a lateral averaging point and x_j the x-position of a local particle. A smoothing length of 3 was used throughout these averages.

3) The instantaneous properties were smoothed by sub-averaging over blocks of time. Unless specifically stated otherwise, this was at a rate of every 10 steps in 1000 iterations, performed after a simulation time of 7×10^6 iterations.

The above procedure for mass density was adapted to calculate all other quantities of interest including pressure, temperature and stress. For pressure, the virial contribution was computed by assigning half of its value to each atom of an interacting pair. The streaming velocity was obtained from the instantaneous ratio of the mass flux to the mass density. This streaming velocity was subsequently used to subtract the convective contribution to the momentum flux prior to calculation of the pressure, as well as the convective part from the kinetic energy prior to calculation of the temperature.

For radial profiles, the simulation cell was divided into a number of concentric circles centred on the stationary disc. The 1-dimensional SPAM averaging process was employed for the properties as previously described.

For the velocity vector plots, particle velocities were resolved onto a 2 dimensional rectangular spatial grid using a 2-dimensional Lucy weight function.

All of the following simulations were performed within a fluid of 100 height and 200 width, with an initial density of 1. Fluid particles were initiated with a random velocity between - 0.5 to + 0.5, and initially scaled using an *ad-hoc* thermostat to give a fluid temperature of 0.5. A reflective boundary condition is imposed along the *x* axes for the majority of simulations. The exception is for the smallest discs of 0.21 κ, which are used as a reference to flow past an 'infinite' boundary system; these therefore use periodic boundaries.

To investigate the influence of finite boundary systems upon fluid properties and flow regimes for flow past a disc, a range of simulations were performed at different clearances and streaming velocities. This was achieved by systematically varying κ between 0.21 to 0.91, and v_x between 0.25 to 3.0. A limited number of simulations were also performed at lower streaming velocities of 0.1.

6.3.2 Steady State

The x component of the mass flux across the simulation is used to determine whether a steady state has been reached. Figure 6.15 shows the mass flux as a function of x position for each extreme value of κ (0.21 and 0.91).

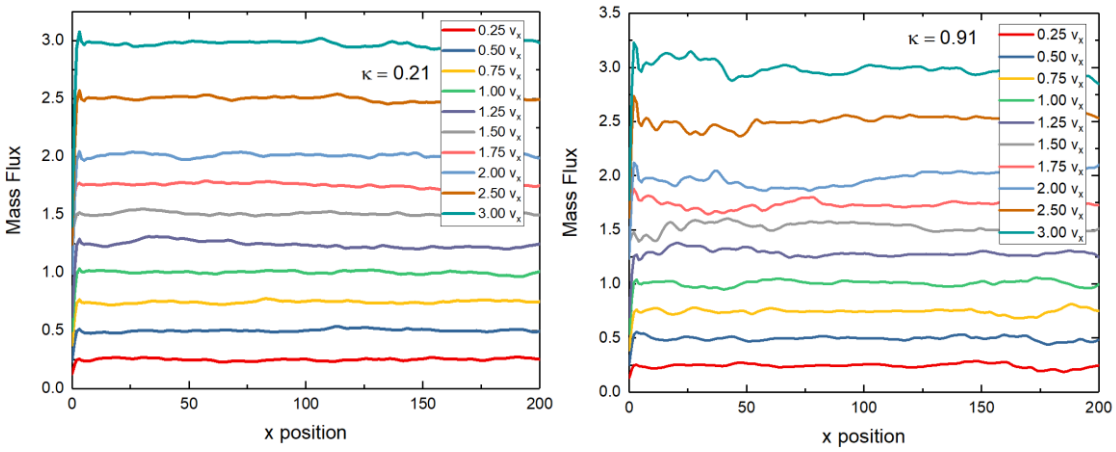

Figures 6.15 (a & b): The *x*-component of the mass-flux as a function of *x* position in the simulation. Figure 6.15a is the mass flux for various streaming velocities for the smallest disc (0.21 κ), whereas figure 6.15b is for the largest disc (0.91 κ).

For a disc of 0.21 κ the mass flux is consistent across the simulation for the majority of streaming velocities. At 0.91 κ the momentum flux appears considerably more noisy, increasing in noise substantially at streaming velocities greater than v_x = 1.0. Despite this noise there appears to be no notable drift from a higher to lower value of flux.

Another method of determining whether a fluid is at steady state is to observe the momentum flux at various points in time. As fluid travels past a disc with limited clearance, pressure increases in front of the disc until the total mass flux across the disc is equal to the total streaming mass flux. If the fluid is at a steady state, the momentum flux should be relatively constant throughout the simulation. Results are shown in figure 6.16 for the disc with the least clearance ($\kappa = 0.91$), and streaming velocities of 0.25 to 3.00.

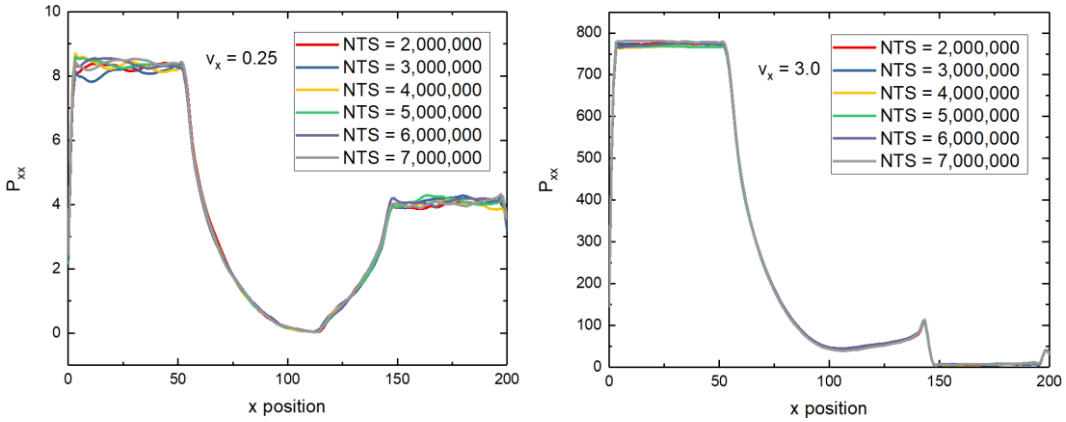

Figures 6.16 (a & b): P_{xx} as a function of x position, for multiple points throughout the same simulation. The disc has a κ of 0.91, whilst figure 6.16a represents a streaming velocity of 0.25 and figure 6.16b a streaming velocity of 3.0.

Momentum flux clearly does not vary at different points in time during the simulation. All simulations are therefore deemed to be at steady state.

6.3.3 Flow Regimes

6.3.3.1 Thermal Noise and Wake

At low streaming velocities and small values of κ the time averaged velocity profiles failed to show clear laminar flow. This is illustrated in figure 6.17 for 0.31 κ and 0.25 v_x, where velocity clearly varies chaotically. This is evidence of thermal (or intrinsic) noise, an inherent noise in all atomistic simulations resulting from local thermal fluctuations [143]. Thermal noise may be reduced by averaging at the rate of $\sim {}^{1}/_{\sqrt{N}}$, where N is the number of particles [144]; it is therefore suggested that these simulations be repeated in future at greater scales to determine the existence of 2-dimensional laminar flow in MD.

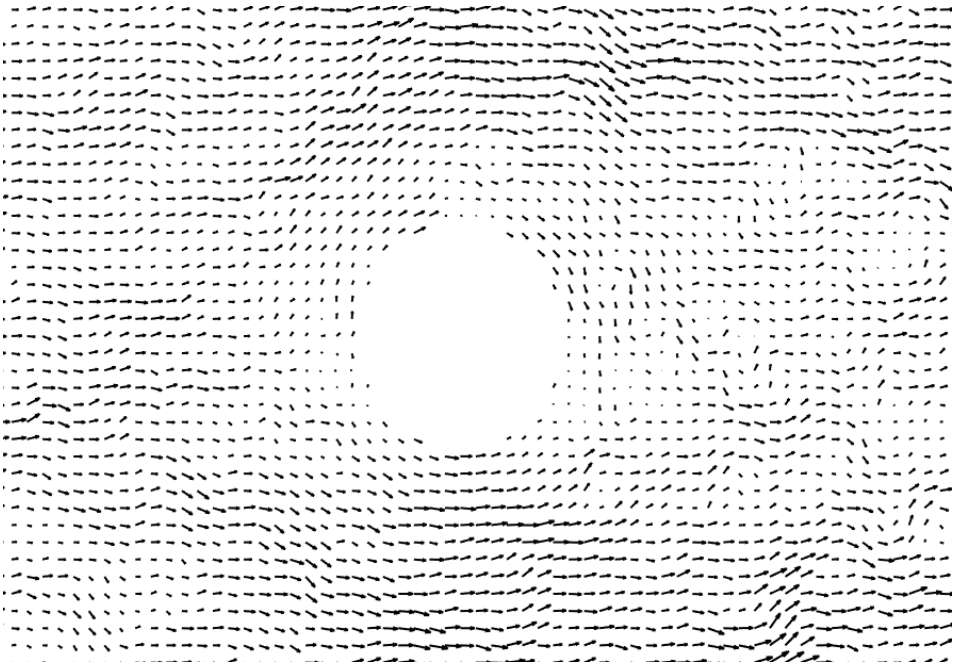

Figure 6.17: Vector profile of flow past a disc of 0.31 κ and $v_x = 0.25$.

Increasing the streaming velocity across a disc of 0.31 κ to 0.5 v_x removed the majority of noise, as shown in figure 6.18. An *increase* in velocity giving rise to *less* fluid fluctuations is further evidence that the previous instabilities were simply due to thermal noise (as opposed to turbulence). This is due to turbulence increasing with streaming velocity.

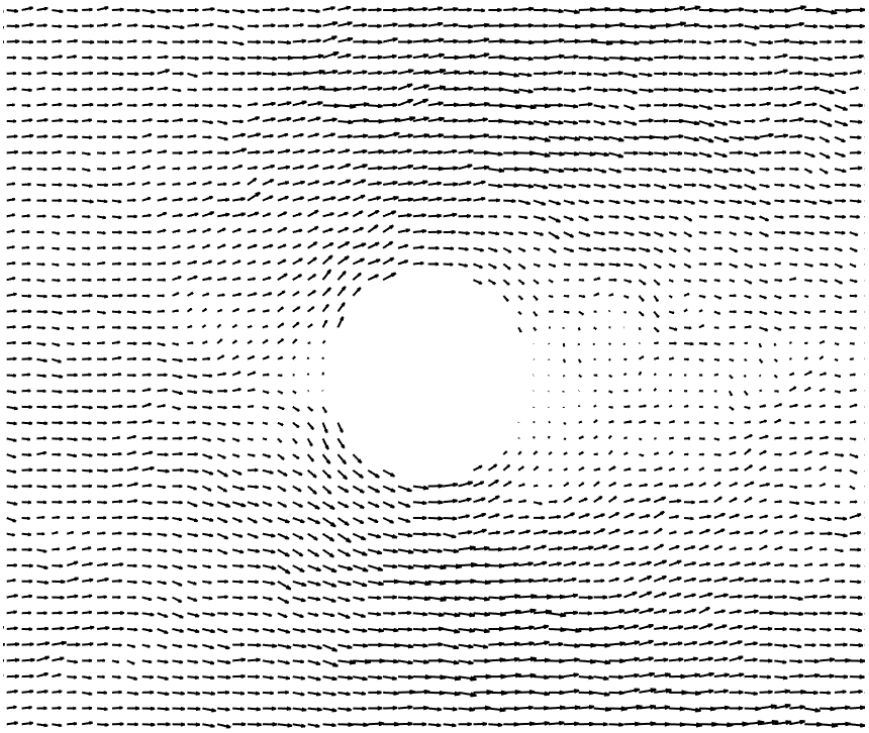

Figure 6.18: Vector profile of flow past a disc where 0.31 κ and 0.5 v_x.

A wake can be observed to the right of the disc in figure 6.18. For flow past a disc, theory predicts a uniform flow pattern at either side in creeping flow regimes [145]. The wake therefore suggests that a streaming velocity of 0.5 is *not* within the creeping flow regime, despite this being the lowest observed streaming velocity free from thermal noise. It may only be stated that either:

1) Creeping flow does not exist in 2-dimensions.
2) Due to thermal noise creeping flow is not obtainable in MD.
3) A larger / longer MD simulation is required to observe creeping flow.
4) Continuum theory is incorrect, and some level of wake is present within the creeping flow regime.

Flow past a fixed cylinder within an *unconfined* boundary has been the subject of both experiment and computational studies [146], [147]. The wake observed in figure 6.18 is synonymous with observations from infinite boundary experiments; Taneda [148] and later Coutanceau and Bouard [149] observed wakes experimentally at Re $\geq$ 3.64, as shown in figure 6.19. A key observation of figure 6.19 in comparison to 6.18 is the distinguishable vortices *within* each half of the wake at *Re* $\geq$ 13.05, which is *not* observable at the scale of the presented simulations. It is possible that this is simply due

to the resolution of simulations performed, and separated vortices would be observable if using a greater number of particles. Further simulations would be required to confirm this hypothesis.

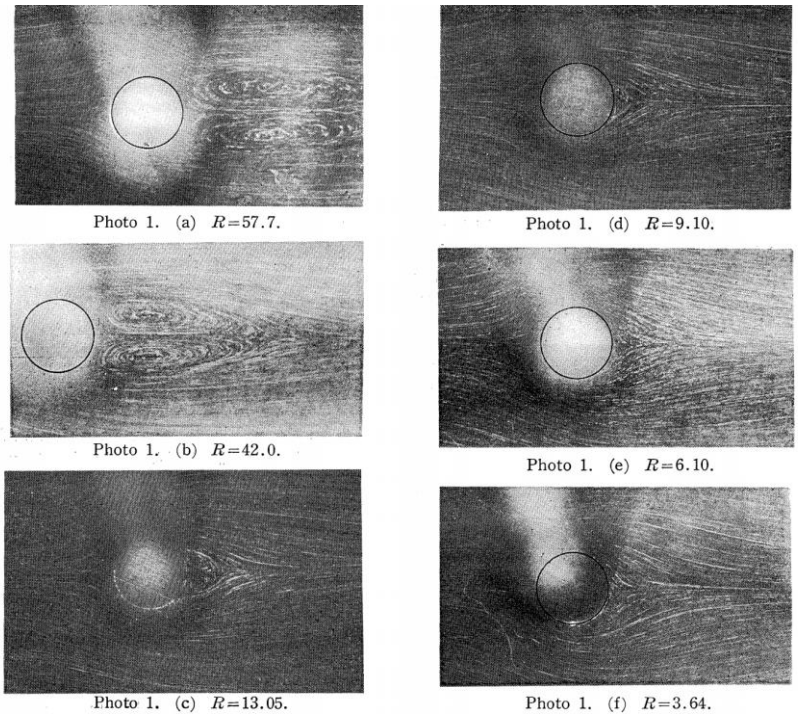

Figure 6.19: Still images of flow past a cylinder captured during experiments. Image taken from external source [148].

Increasing the size of the disc increases the size of the wake. This is visualised in figure 6.20 by normalising the vector plot (such that the length of all arrows are uniform) of two discs of 0.31 and 0.61 κ, with a streaming velocity of 0.5. The observed increase in wake magnitude as a result of increasing κ is an important observation. This shows that increasing the disc size in a *confined* boundary system has the same effect as increasing the streaming velocity in an *infinite* boundary system (as illustrated in figure 6.19). These observations can be explained by the greater change in direction as flow circumvents the larger sized disc, and a larger *local* velocity as a result of the same volume of fluid travelling through a smaller clearance.

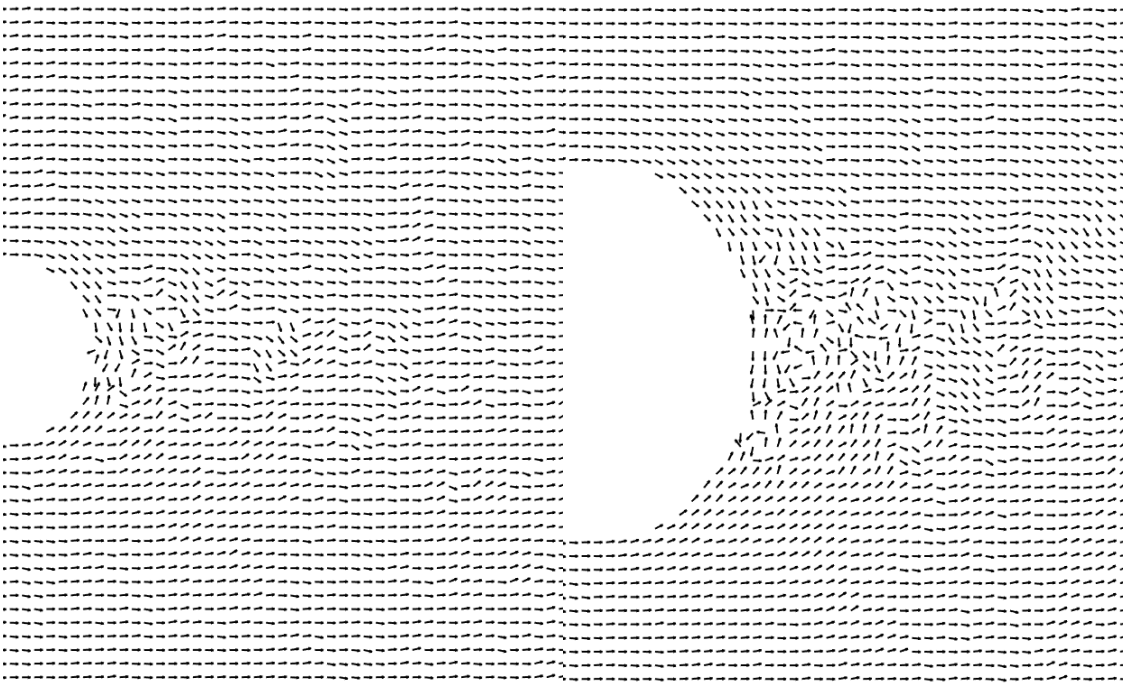

Figures 6.20 (a & b): Normalised vector profiles of flow past a 0.31 κ disc (left) and 0.62 κ disc (right) with 0.5 v_x. The wake at the right of the disc appears larger for the disc of 0.62 κ.

The magnitude of wake can be further quantified by the fluid density as a function of x position, as shown in figure 6.21.

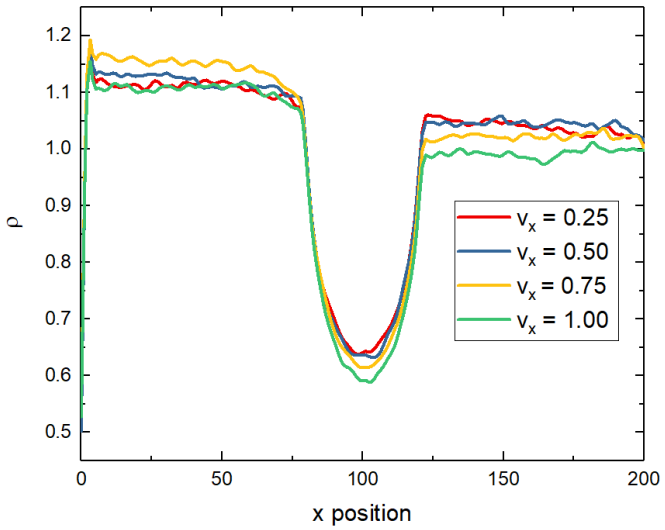

Figure 6.21: Density as a function of position for the 0.31 κ disc at several streaming velocities.

It can be seen that a rise in streaming velocity results in a *lower* density at the region to the right of the disc, a common indication of turbulent eddies [89]. This is corroborating evidence that the magnitude of wake can be increased by an increase in streaming velocity as well as an increase in κ.

It should also be noted that for very large discs there is evidence of a vortex at the front of the disc, as illustrated in figure 6.22. The flow to the right of the disc also suggests the presence of a wake, although the thermal noise is high.

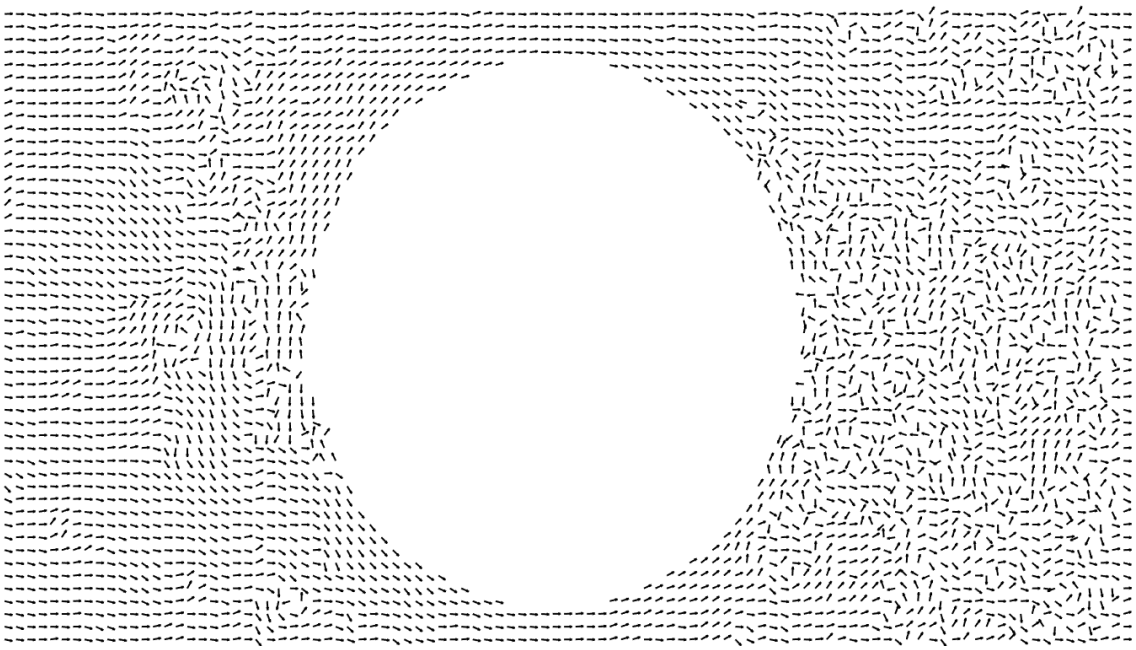

Figure 6.22: Normalised vector plot of flow past a disc of 0.91 κ, with 0.1 v_x. An eddy can be observed to the left of the disc, whereas high amounts of thermal noise is observed to the right.

6.3.3.2 Oscillatory wake and Von Karman Vortices

Continuing to increase the streaming velocity gives rise to an oscillatory wake. For a disc of 0.31 κ, this begins to occur at 2.0 v_x (see figure 6.23a) and in greater clarity at 2.5 v_x (see figure 6.23b).

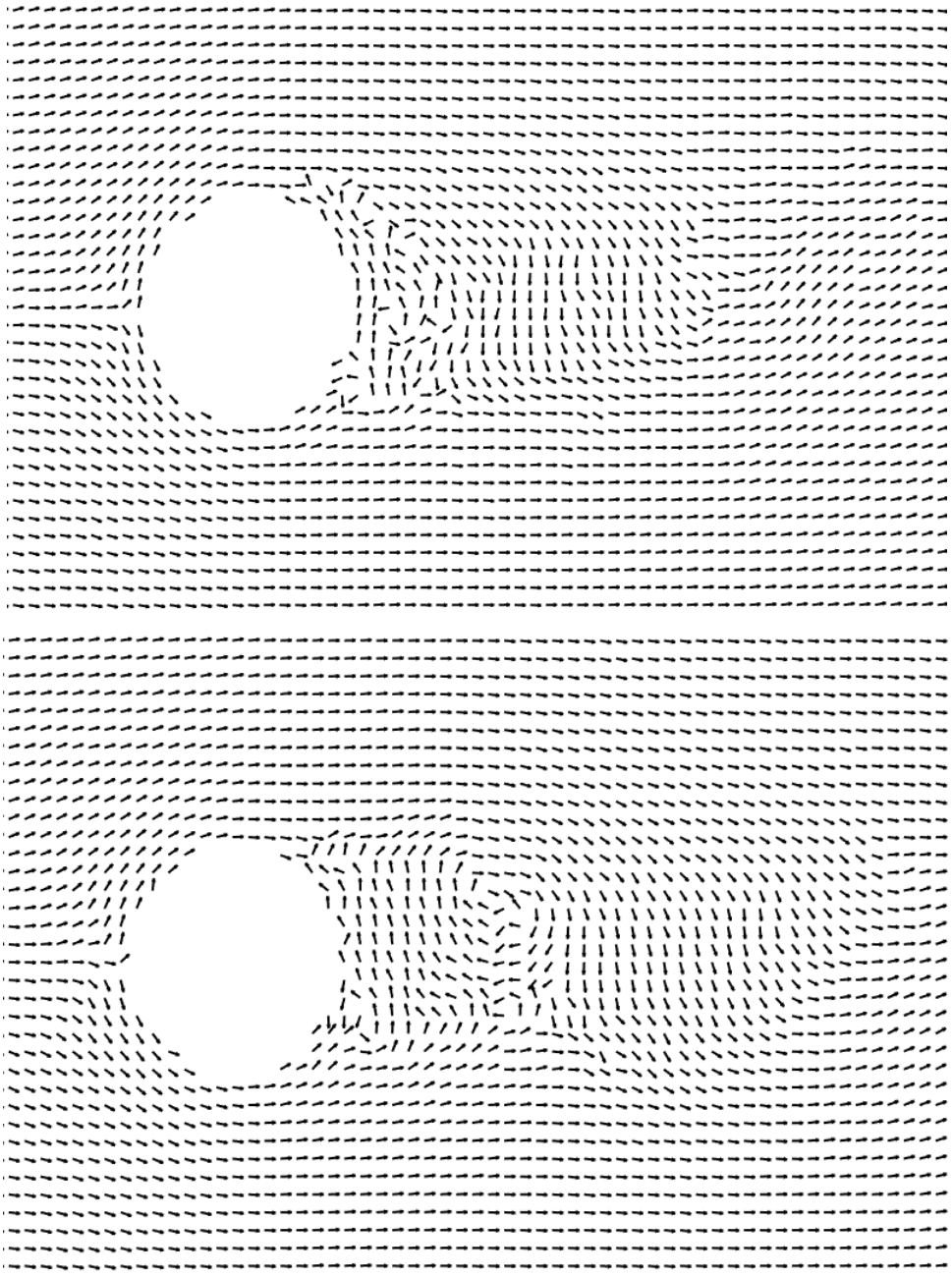

Figures 6.23 (a & b): Normalised vector profile for flow past a disc of 0.31 κ and a streaming velocity of 2.0 v_x (top) and 2.5 v_x (bottom).

These alternating flow patterns are in agreement with the previous simulations of Rapaport [86], and are often referred to as wake symmetry instabilities, or oscillatory wakes, where each half of the wake oscillates in magnitude over time. Oscillatory wakes have been observed in experiments at Re $>$ 30 [150], including those obtained by Gerrard shown in figure 6.24 [151].

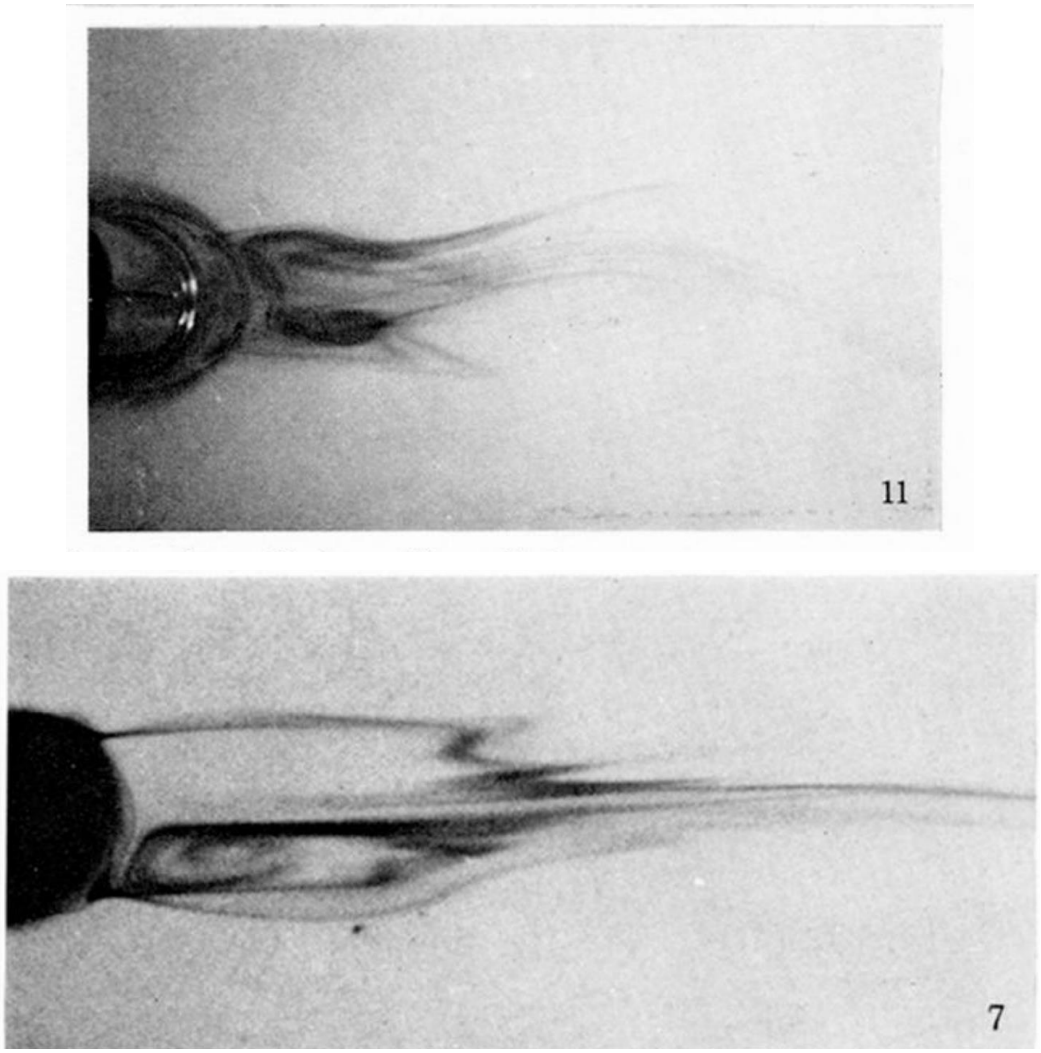

Figures 6.24 (a & b): Experiment images of wake non-symmetry, observed at Re = 44.4 (top) and Re = 52.5 (bottom). Images taken from external source [151].

Reducing the clearance causes the wake instabilities to be observed at lower streaming velocities. For a disc of 0.61 κ an alternating wake is visible from 1.25 v_x, a streaming velocity 37.5% lesser than those used to observe similar flow regimes at 0.31 κ. Furthermore, a slight increase in streaming velocity to 1.5 results in distinct vortices observed beyond the cylinder, as illustrated in figure 6.25. These distinct eddies are referred to as Von Karman vortices [152], and have been observed experimentally and computationally at Re > 100 [153], [154]. An example of Von Karmen vortices observed during experiments carried out by Williamson [155] are shown in figure 6.26 for comparative purposes.

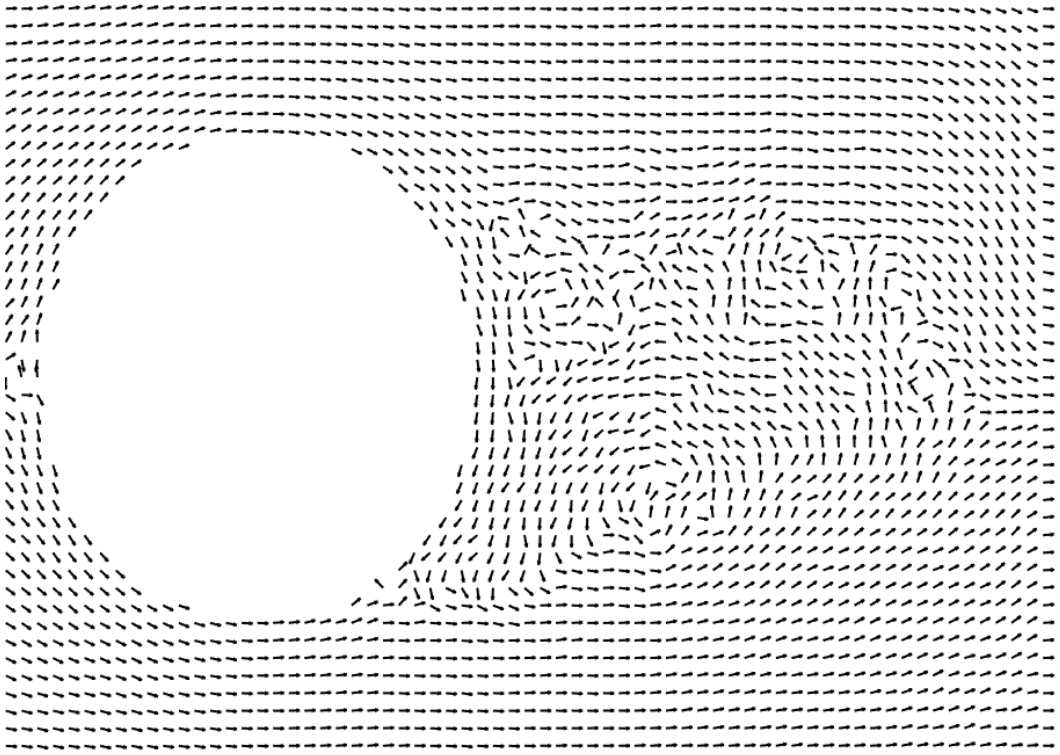

Figure 6.25: A normalised vector profile of v_x = 1.5 flow past a disc of 0.61 κ.

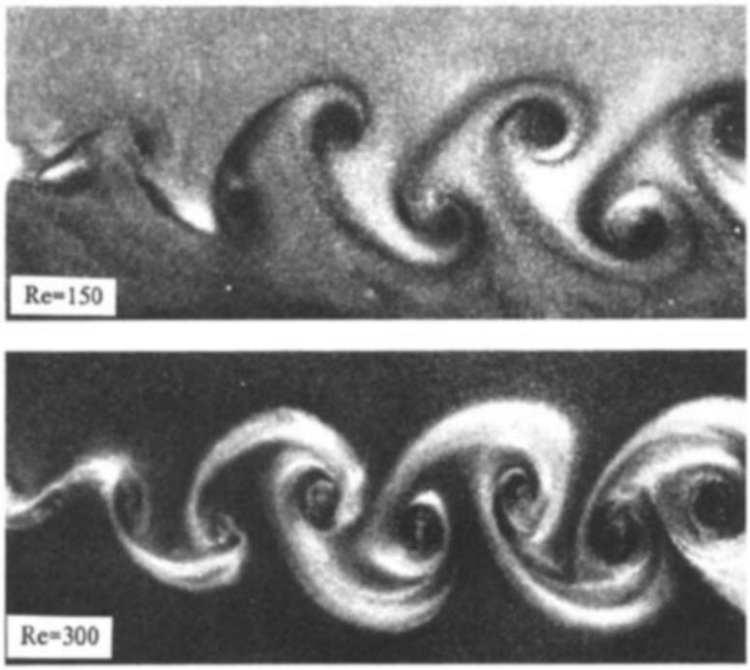

Figure 6.26: Von Karmen vortices observed experimentally at Re = 150 (top) and Re = 300 (bottom). Image taken from external source [155].

Alternating wake regimes can also be illustrated by comparing v_θ as a function of the radial distance from the disc at different points in time throughout the simulation. This is shown in figure 6.27 for a $0.61\ \kappa$ disc with a streaming velocity of 1.5.

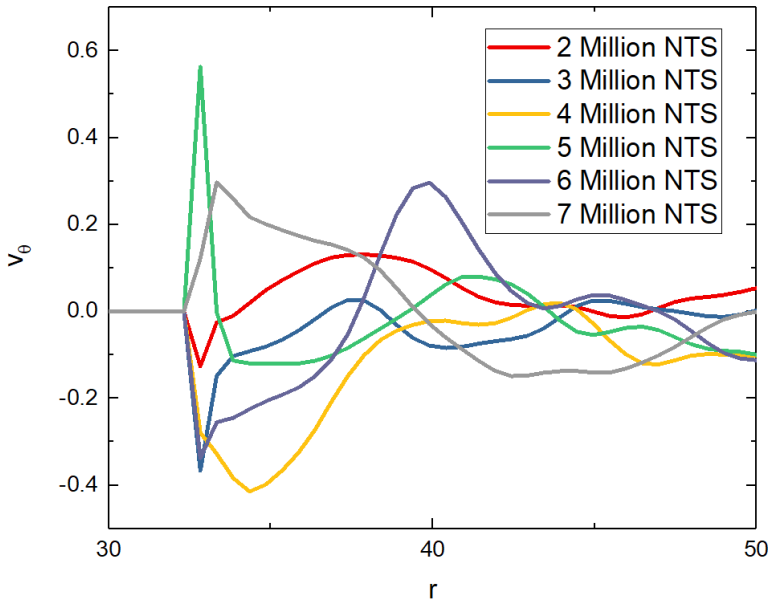

Figure 6.27: v_θ as a function of radial distance from the centre of a 0.61 κ disc, at several points in time throughout a simulation.

The polarity of v_θ can be seen to clearly alternate as a function of both radial position and time in the simulation. This corresponds to the changing positions and directions of the Von Karman vortices observed at the wake.

6.3.3.3 Wake Separation

As the flow past the disc increases in magnitude Von Karman vortices dissipate and separate wakes are observed. This was shown for a $0.61\ \kappa$ disc with a streaming velocity of 2 in figure 6.28. Fixed-position vortices are present at the end of each of these wakes, although the velocity profiles are considerably noisy. This is better illustrated by performing a longer velocity profile average (1,000,000 time steps), as shown in figure 6.28b.

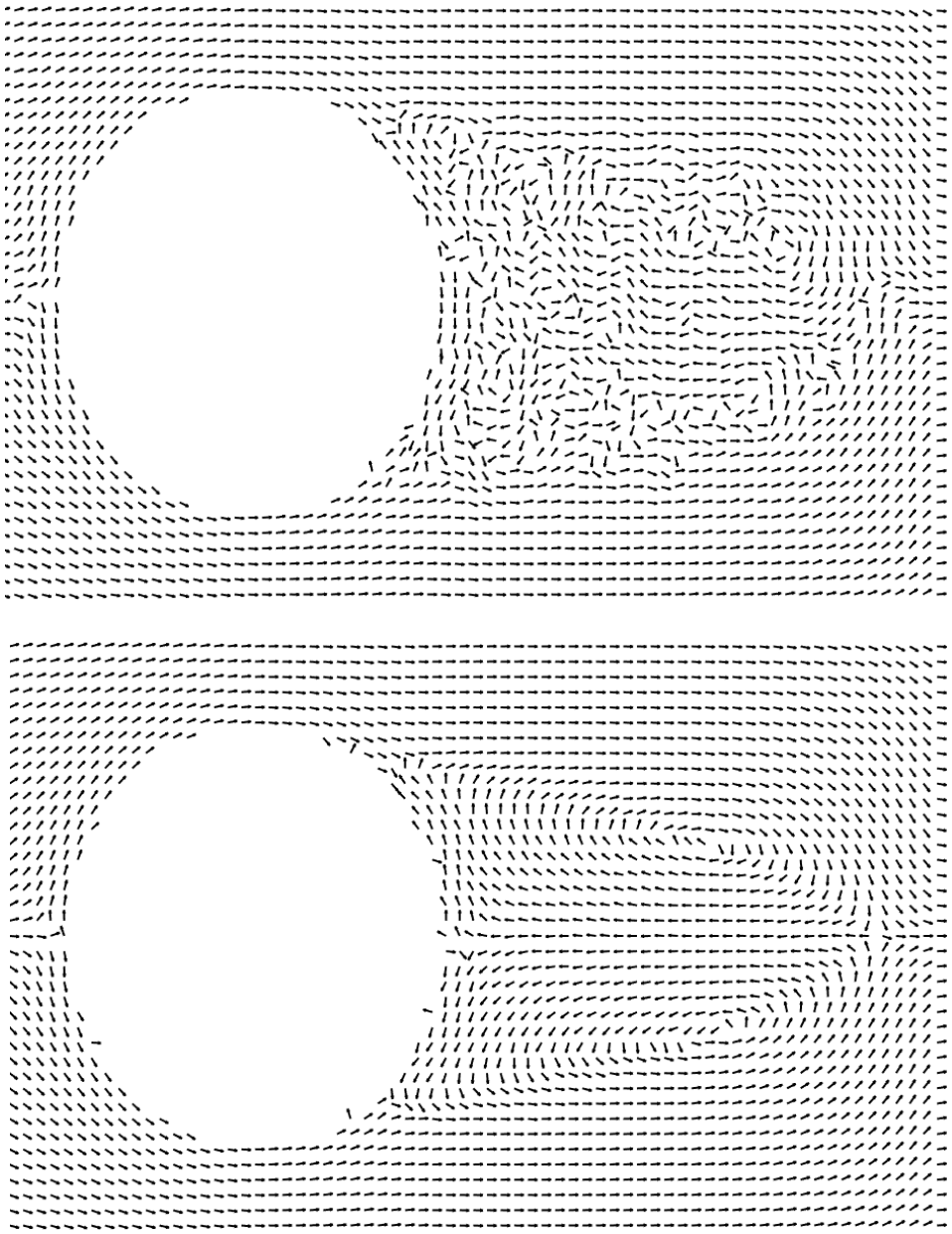

Figures 6.28 (a & b): Normalised vector profiles for a short-term, conventional average performed over a time of 1,000 time steps (top) and a longer averaging performed over 1,000,000 time steps (bottom). The disc has a diameter ratio of 0.61 and the streaming velocity is 2.

The conventional velocity profiles taken over a 1,000 step average (figure 6.28a) appear to show relatively chaotic flow patterns, indicative of turbulent flow. However, at longer time averages (figure 6.28b) flow patterns resemble regimes discussed in section 6.3.3.1, where fixed separated wake vortices (see figure 6.19) are characteristic of less turbulence than oscillatory wakes and von Karmen vortices. This would suggest a

decrease in turbulence, despite an *increase* in streaming velocity. Plausible explanations for this behaviour include:

1) Extreme fluid densities are required to create the pressure difference necessary to maintain a high flow rate through a tight clearance. At such large densities the viscosity may dramatically increase, reducing turbulence.
2) The exit boundary condition does not allow fluid to freely exit the simulation, but instead enforces the fluid to leave at the given streaming velocity. High streaming velocities and small clearances will result in fast-moving currents above and below the cylinder. If these currents reach the exit boundary before dispersing, the exit boundary will redirect this fast-moving current and 'compress' the wake region. This is visualised in figure 6.30.

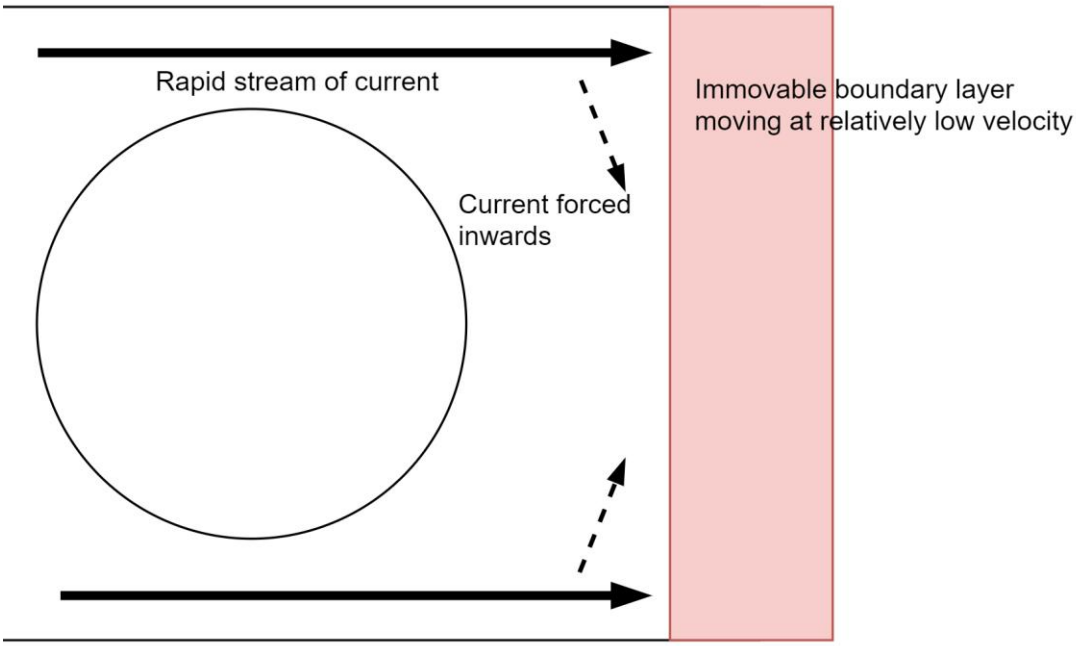

Figure 6.29: Visualisation of the postulated wake compression effect at high streaming velocity and low clearance. Rapid currents come into contact with the fixed-rate boundary system before they have dissipated throughout the fluid. This causes a central shift in fluid direction.

Explanation 1 is dependent on the fluid compressibility, and therefore the pair potential used in simulations. Further simulations would be required to quantify the fluid compressibility and the resulting effect on the observed flow regimes.

Explanation 2 is a result of the limited distance between the disc and exit boundary. Future studies could isolate these effects by expanding the region between disc and boundary, or by re-designing the boundary behaviour.

As κ increases wake separation is observed at lesser streaming velocities; for a disc of 0.91 κ wake separation is observed at just 0.25 v_x, an *eight-fold* decrease in the streaming velocities necessary to observe the same behaviour at 0.61 κ.

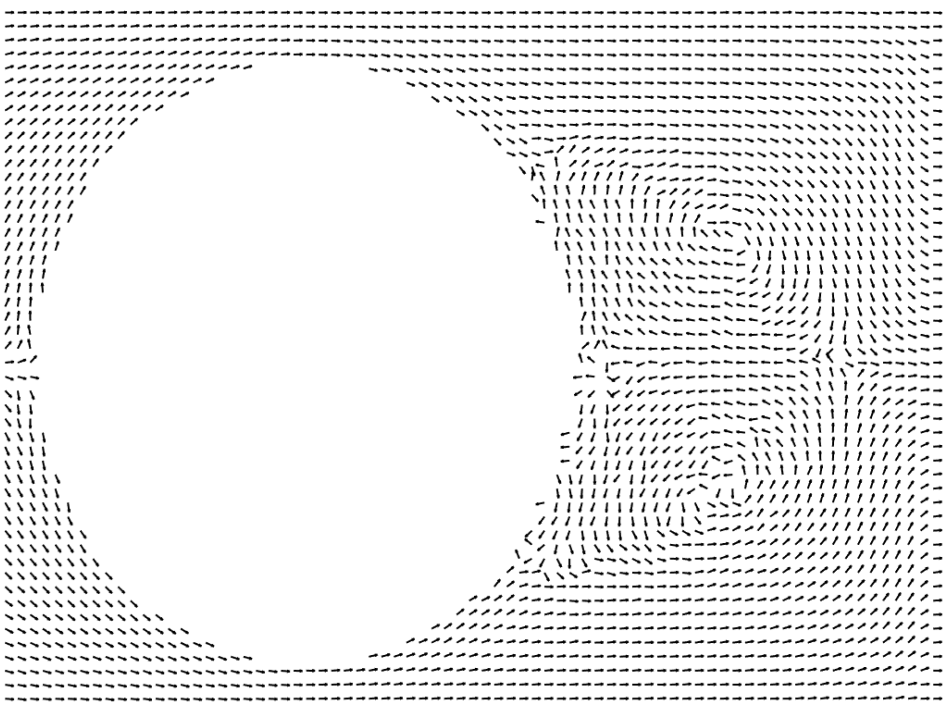

Figure 6.30: Wake separation illustrated using a normalised vector plot of flow past a 0.91 κ disc with a streaming velocity of 0.25. Velocity profile averaged over 1,000,000 time steps.

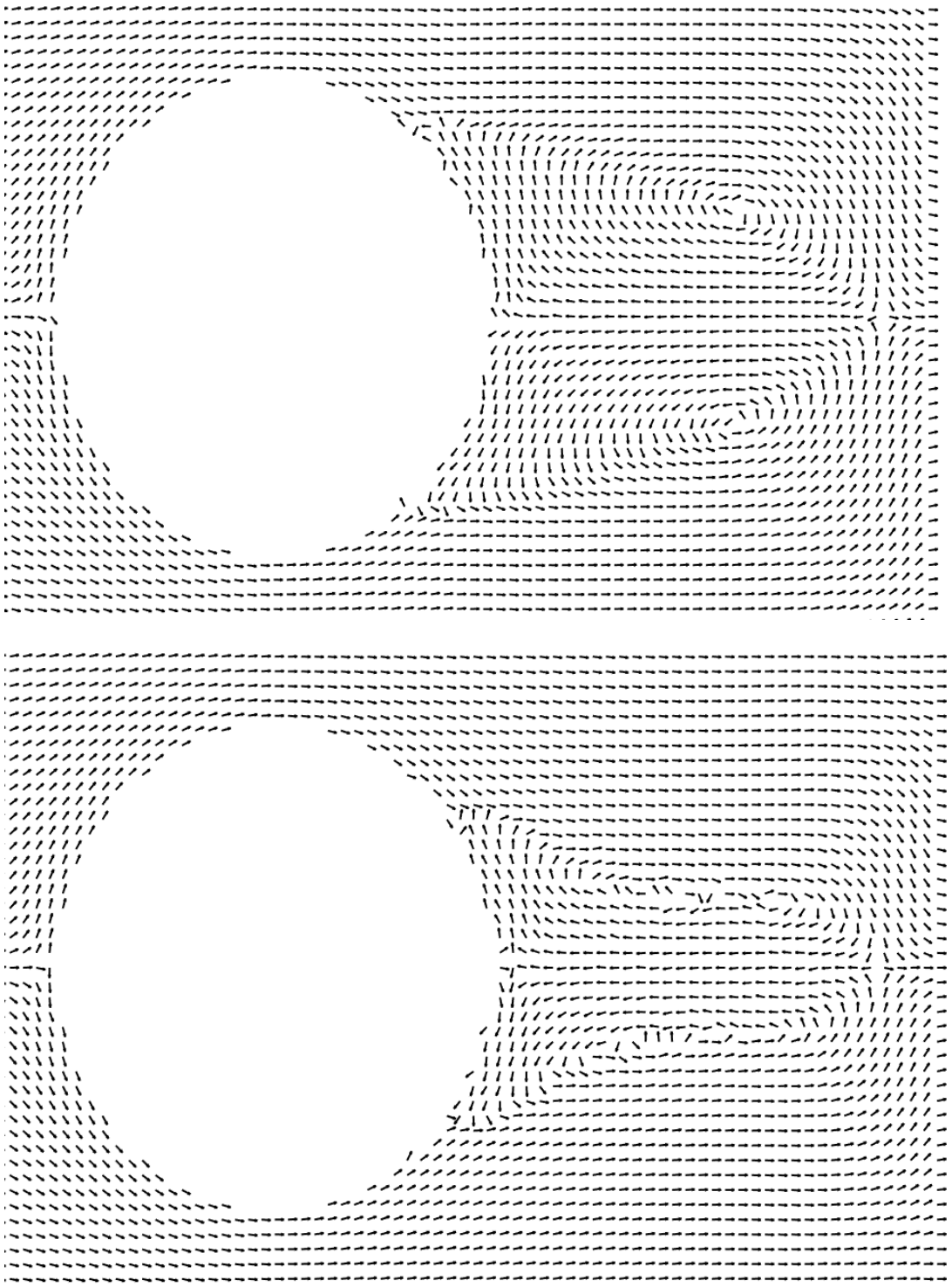

Figures 6.31 (a & b): Normalised vector profile showing wake compression due to an increase in streaming velocity. The disc has 0.71 κ and the streaming velocity is 1.75 (top) and 3 (bottom). Vector profiles taken over a longer (1,000,000 timesteps) average.

Further increasing the streaming velocity *reduces* the width of the wake, once again indicating a reduction in turbulence. This can be seen for a $0.71\ \kappa$ disc and streaming velocities of 1.75 and 3.00 respectively in figure 6.31.

The wake-separation regime can be conveniently visualised using a colour-map of density, as shown in figure 6.32 for a $0.71\ \kappa$ disc. A relatively high density region can be seen in-between the two vortex streams, where flow travels back towards the disc.

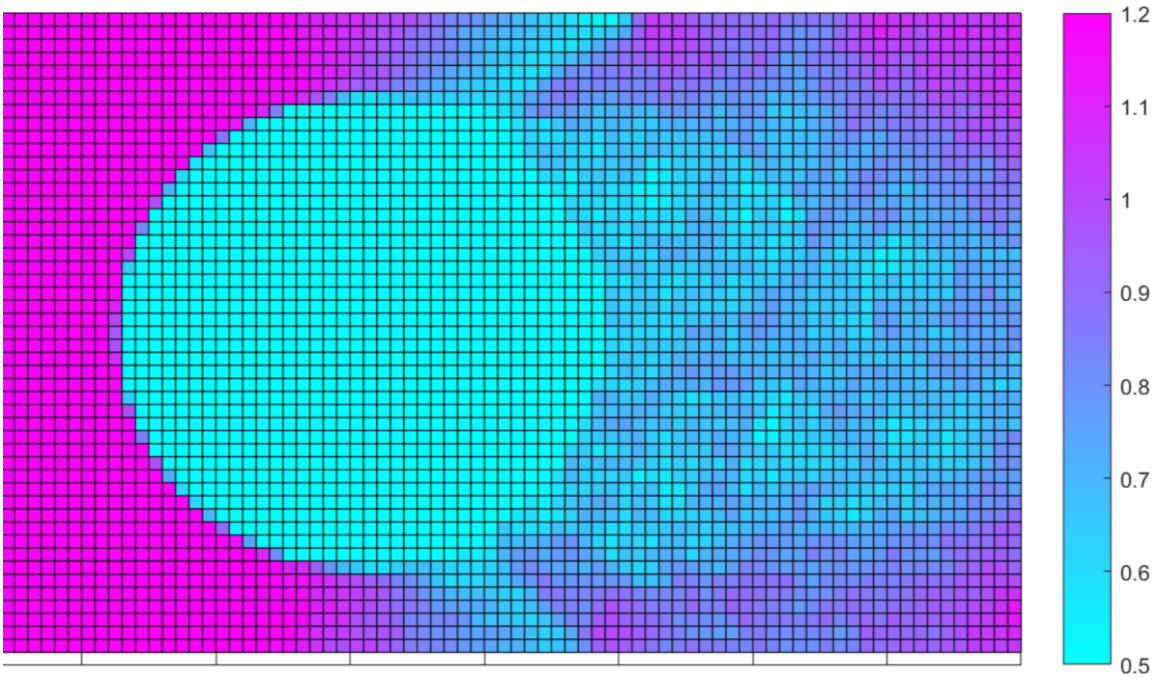

Figure 6.32: Local averaged density visualised using a colour map grid, for a disc of $0.71\ \kappa$ and $1.75\ v_x$. The density shown is restricted to a minimum and maximum of 0.5 and 1.2 (actual maximum density $\sim$1.5).

6.3.3.4 Reverse Slip

An interesting observation occurred exclusively for the largest disc of $0.91\ \kappa$ and high streaming velocities involving the rotation of a thin layer of fluid at the disc boundary.

Figure 6.33 shows a streaming velocity of 1.5 past a disc of $0.91\ \kappa$. A thin layer of fluid can be seen to circulate the entirety of the disc. This non-interrupted circulation means that a layer of fluid is effectively travelling *back* through the annular gap, despite the tremendous magnitude of fluid travelling in the opposing direction.

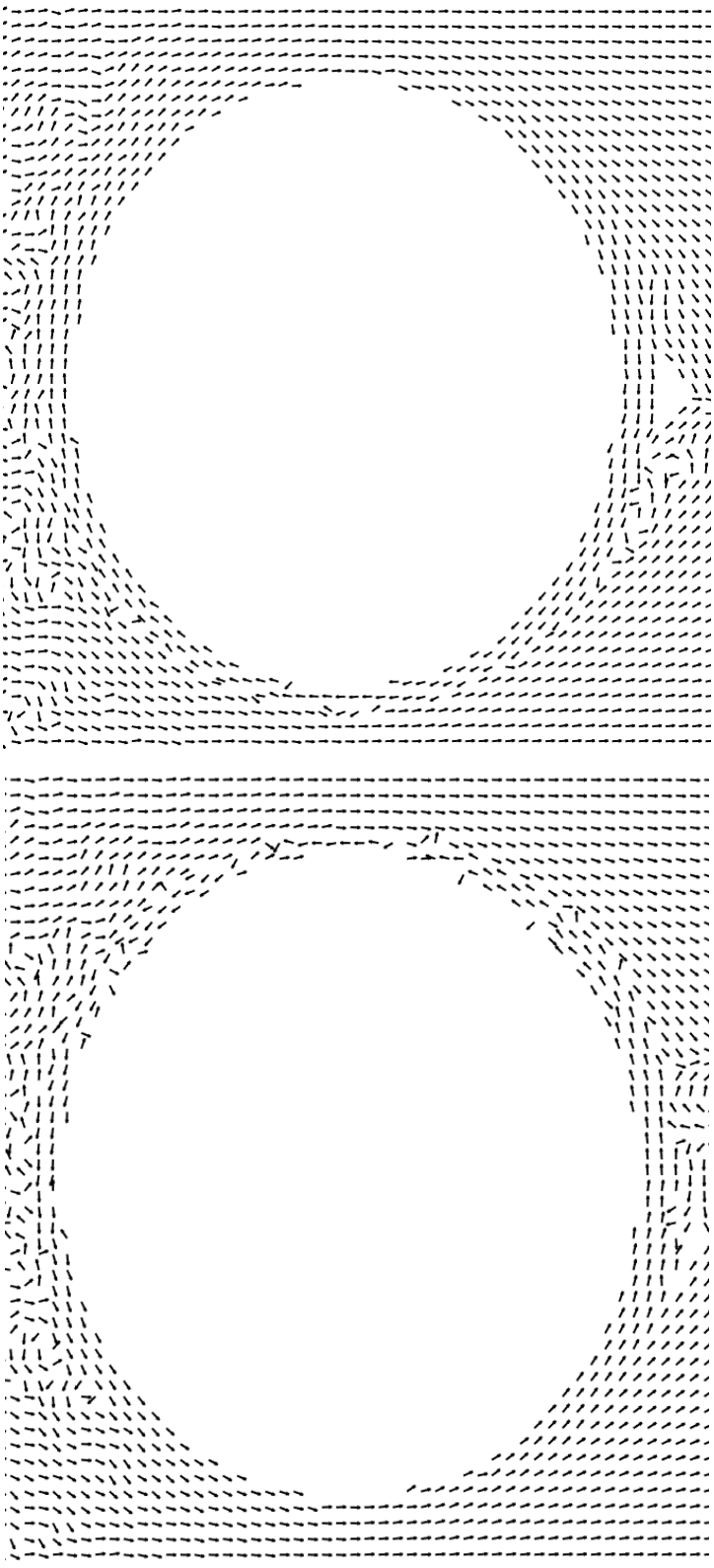

Figures 6.33 (a & b): Normalised vector velocity profiles for flow past a 0.91 κ disc with a streaming velocity of 1.5. Figure 6.34a is taken at 6 million time steps and figure 6.34b at 7 million time steps. The slip layer direction can be seen to alternate in direction.

The region of reverse slip was shown to oscillate in direction throughout the simulations, which is illustrated when comparing the vector profiles in 6.33a and 6.33b. This was confirmed by analysing the angular velocity profiles, which can clearly be seen to oscillate in polarity throughout simulations (see figure 6.34).

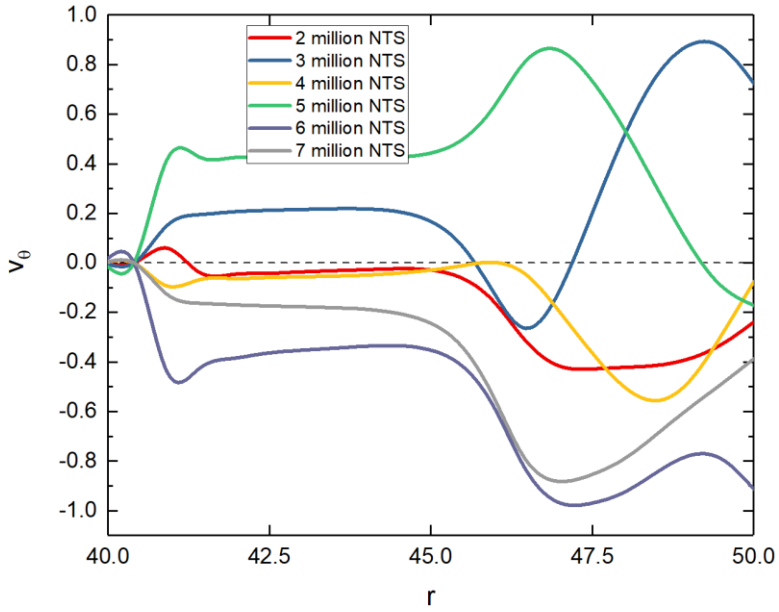

Figure 6.34: v_θ at several points in time for a streaming velocity of 1.75 past a disc of 0.91 κ.

The angular velocity profiles also indicate a miniature peak corresponding to the position of the reverse slip. This miniature peak clearly represents the observed slip layer due to an opposite polarity to v_θ at other distances from the disc. At the time of writing no known observations of this reverse slip phenomena have been observed for flow past a stationary sphere. Further research would be required to determine whether this phenomenon can be found in nature, or whether this is simply a characteristic of the implemented pair potential.

6.3.4 Fluid Density

It has been shown how either increasing the streaming velocity or decreasing the clearance between disc and container (increasing κ) can give rise to various regimes of

turbulent flow. This is believed to be due to the fluid velocity through the restricted gap increasing.

A high pressure is necessary in front of the disc to maintain a large fluid velocity through the gap. This results in an inhomogeneous fluid, illustrated by the difference in density across the simulations shown in figure 6.35. The fluid clearly becomes increasingly inhomogeneous when streaming velocity increases (see figure 6.35a) or when clearance decreases (see figure 6.35b).

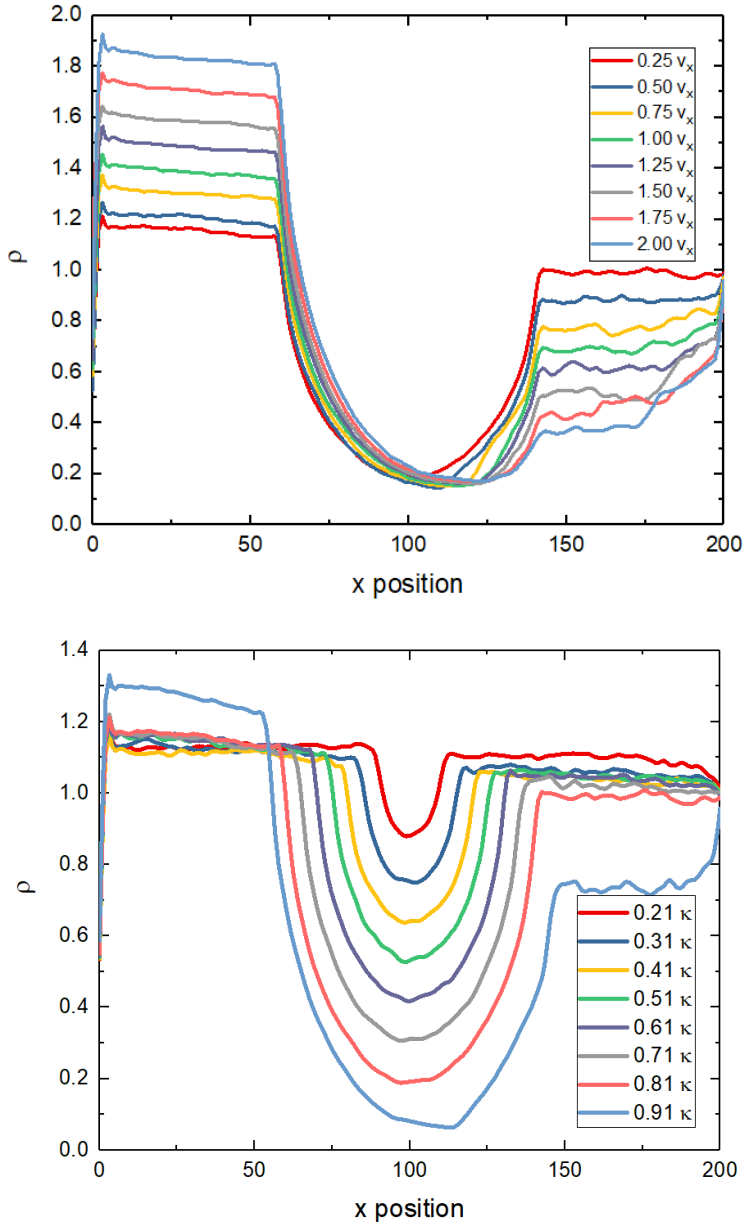

Figures 6.35 (a & b): Density as a function of *x* position within the simulation box. This is shown for various v_x and a fixed sized disc of 0.81 κ (top) and for various κ and a fixed v_x of 0.25 (bottom).

6.3.5 Reynolds Number

The conventional method of characterising flow regimes is the Reynolds number. There are 2 characteristic Reynolds numbers when considering flow past a confined object: the flow associated with the object, and the flow associated within the restricted gap. For a disc, this 'gap' is somewhat ambiguous, due to curvature. Regardless, a drastic increase in velocity must occur at this region.

In its most generic form, the Reynolds number is given by:

$$Re = \frac{v\rho D_h}{\mu} \tag{6.6}$$

where D_h is the hydraulic diameter. For the Reynolds number of flow past the disc, Re_d, the hydraulic diameter is given by κh (where h is the height of the container) and the velocity is simply the streaming velocity.

The SLLOD simulations from the previous section were used to determine viscosity via equation 5.5. The conjugate $\Delta\rho\Delta T$ term is omitted due to a rise in unphysical behaviour at large deviations from the reference density and temperature. This should still provide a reasonable viscosity for estimating *Re*.

Finally, the fluid density is given using $N \,/\, (A_c - A_d)$, where A_c and A_d are the areas of container and disc respectively. The Reynolds number calculated using equation 6.6 is shown in figure 6.36. The following observations can be made from figure 6.36:

1) At $\kappa \geq 0.61$, *Re* increases with v_x.
2) At $\kappa \geq 0.61$, *R*e increases with κ.
3) At $\kappa = 0.81$ and $v_x < 1.5$, *Re* increases with v_x.
4) At $\kappa = 0.81$ and $v_x < 1.5$, *Re* decreases with v_x.

Observations 1, 2 and 3 are to be expected - an increase in effective velocity through the annular gap resulting in an increase in *Re*. On the other hand, observation 4 disagrees with literature as an increase in velocity is correlating to a lesser *Re*. However, this does support the theory that observations such as wake separation (see section 6.3.3.3) are a

result of the *Re* number decreasing, possibly due to an increase in viscosity with density.

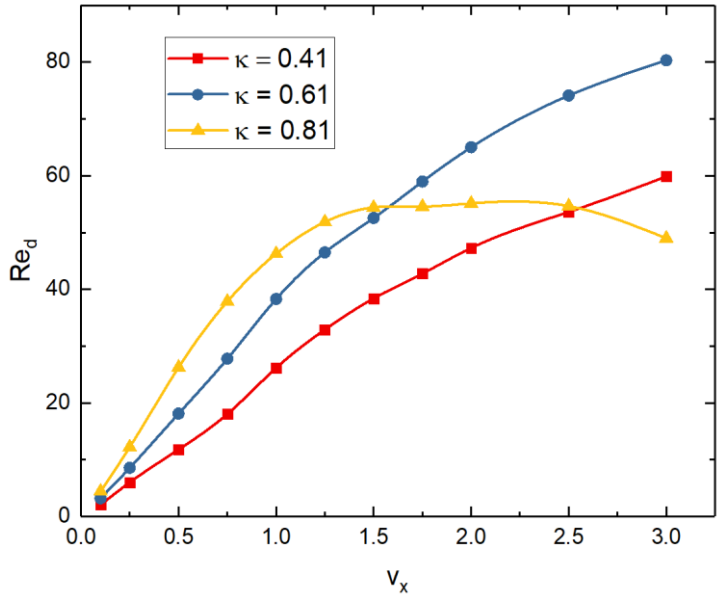

Figure 6.36: Disc associated Reynolds number as a function of streaming velocity for κ values 0.41, 0.61 and 0.81.

The somewhat ambiguous 'gap Reynolds number' Re_g is determined in an attempt to improve upon the unphysical behaviour shown in figure 6.36. D_h is now given using the smallest clearance, $h(1-\kappa)$. Assuming that the streaming velocity is constant, the velocity in the gap can be given by $v_x \,/\, (1-\kappa)$.

Re_g is shown for various discs and velocities in figure 6.37. The magnitude of Re_g is much greater than that of Re_d, by up to an order of magnitude. The Reynolds number once again is shown to increase with the streaming velocity for both 0.41 and 0.61 κ. However, an increase in κ now gives rise to a decrease in Reynolds number for *each* of the observed discs.

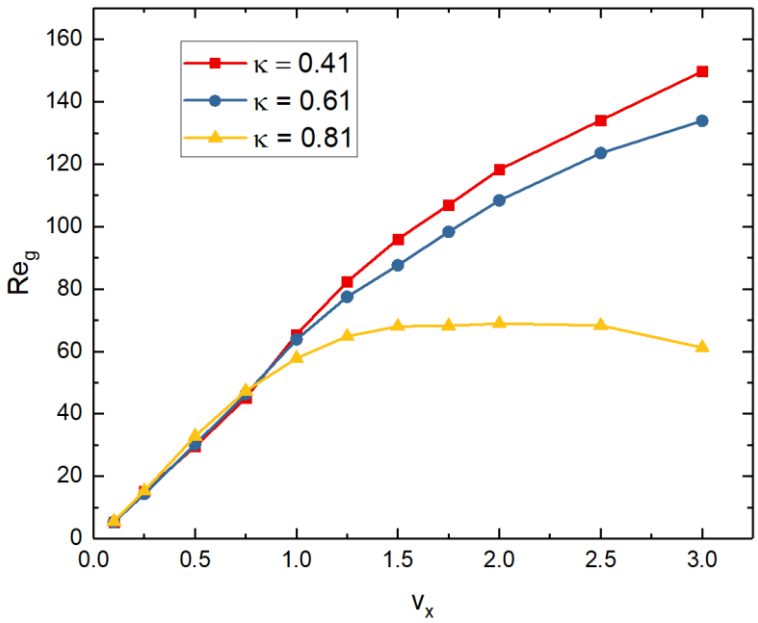

Figure 6.37: Disc associated Reynolds number as a function of streaming velocity for κ values 0.41, 0.61 and 0.81.

Neither the disc nor gap Reynolds numbers appear to be adequate at characterizing the flow regime. One possible explanation is the inhomogeneity of the fluid. For example, it has been shown that density varies throughout the simulation at high κ (see figure 6.35), which would cause the local viscosity to vary significantly.

It remains to be seen whether these discrepancies can be improved by an alternate handling of D_h, better calculation of fluid properties (such as density and viscosity), or if there is a fundamental flaw in determining the Reynolds number at either the molecular scale, 2-dimensional frames of reference, or for highly inhomogeneous fluids.

6.3.6 Pressure

When the streaming velocity increases or clearance decreases, the rate of flow through the disc-container gap must increase. This requires an increased pressure *difference* either side of the disc,

The difference in pressure was quantified by averaging the local pressure either side of the disc using a sum of x profile averages (see equation 6.4) of P_{xx} and P_{yy}, over a region 20 units wide, and 5 units from either side of the disc. This is to ignore

anomalies where the smooth averages overlap the disc. The averaging regions are illustrated in figure 6.38.

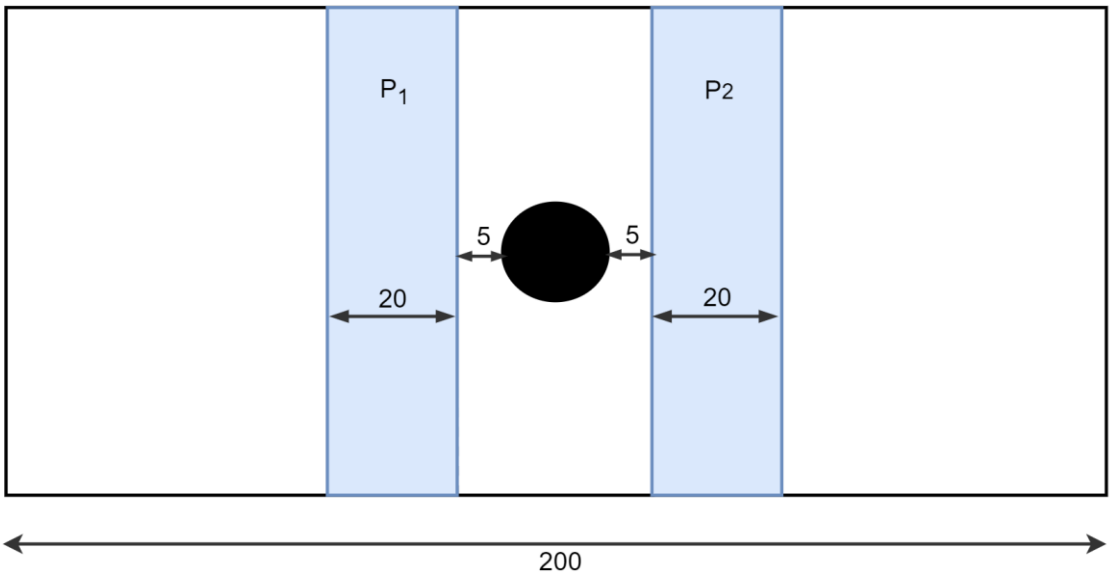

Figure 6.38: The regions used to calculate local averages in pressure before and after the disc. Figure not to scale.

The pressure drop as a function of streaming velocity is shown in figure 6.39a. An increase in v_x or κ results in a greater difference in pressure which is necessary to drive the increased velocity within the gap. It is also clear that this relationship is non-linear - as the pressure difference increases the resulting magnitude of fluid throughput decreases.

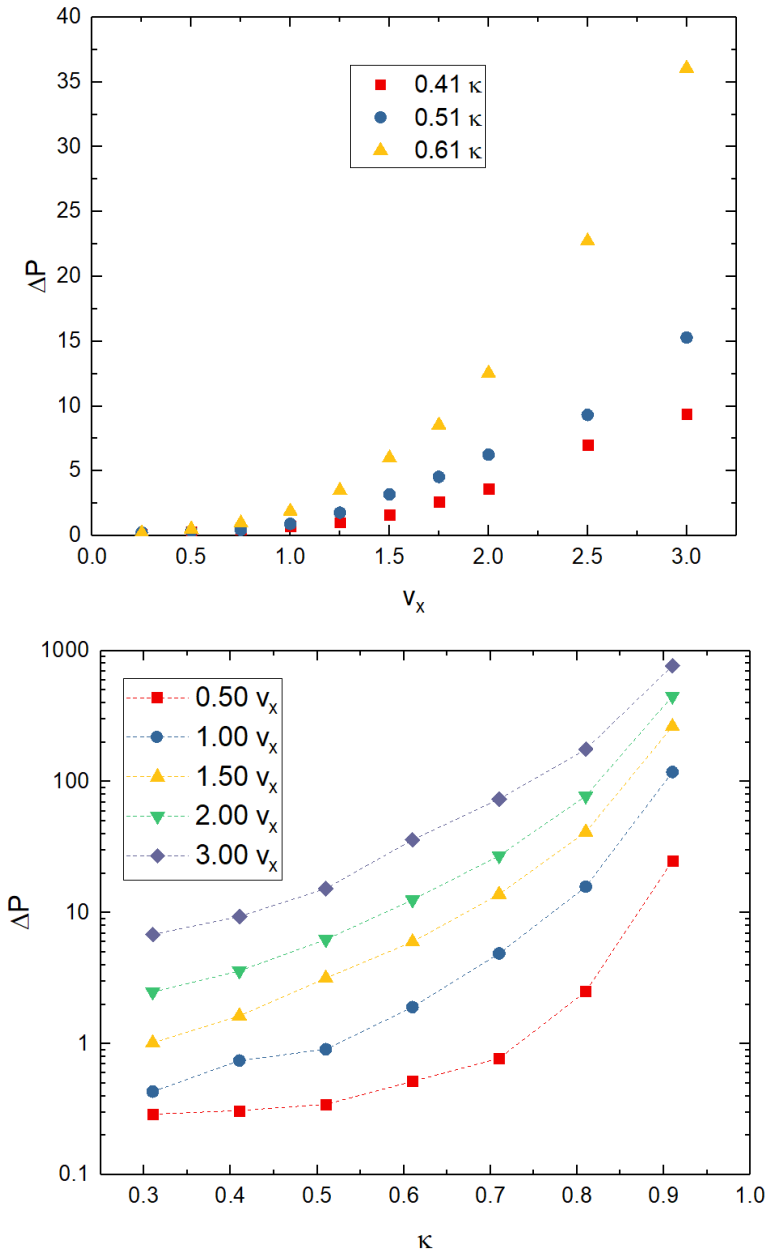

Figure 6.39 (a & b): Pressure loss as a function of streaming velocity for discs with a κ range of 0.41 – 0.61 (top) and as a function of κ for streaming velocities between 0.5 and 3.0 (bottom).

Figure 6.40b visualizes the non-linear pressure relationship in terms of κ, where an increase from 0.31 to 0.41 κ results in approximately a 10 % increase in pressure difference to maintain any given streaming velocity. In contrast, an increase from 0.81 to 0.91 κ requires an order of magnitude increase in pressure difference. This highlights how important small changes in κ are as κ approaches unity.

6.3.7 Radial Velocity

The angular velocity trends were discussed in detail throughout the description of various flow regimes (see section 6.3.3). The radial velocity can also give insight into the behaviour of the fluid. In spherical co-ordinates, the radial velocity is essentially a measure of fluid moving towards or away from the disc.

The radial velocity v_r is calculated independently at both the left and right hand sides of the disc, as shown in figure 6.40. The left and right radial averages of v_r are shown to dramatically diverge, with v_r being greater in magnitude to the right of the disc. This is a disagreement with the theory of laminar flow, which predicts uniform velocity profiles either side of the disc [35].

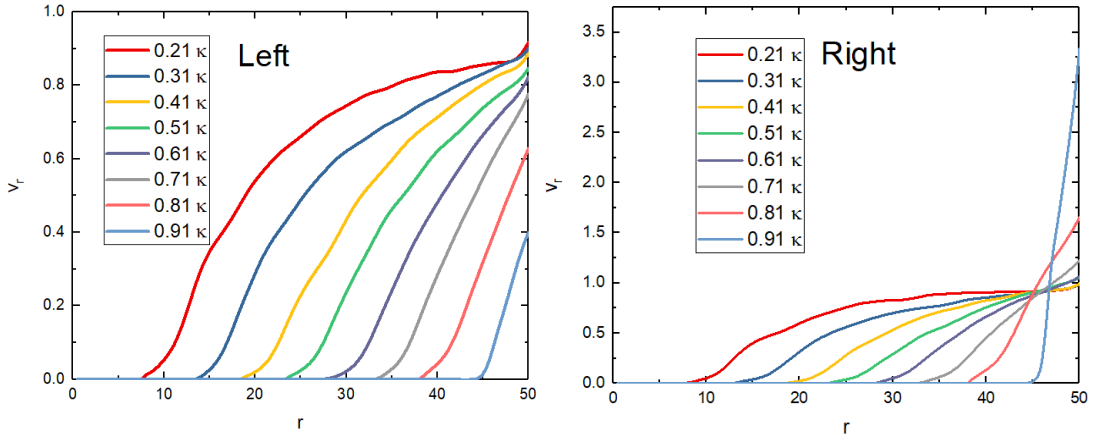

Figure 6.40 (a & b): Radial velocity component as a function of radial distance from the centre of the disc. Streaming velocity is fixed to 1.5.

As the disc radius increases so does the time taken for v_r to reach a steady state of $\sim 0.9\ v_x$. This is logical, as the larger the disc, the greater the *angular* velocity must be to circumvent the disc. For large discs of $\kappa > 0.7$ the radial velocity to the right of the disc increases significantly (see figure 6.40b) as velocity rapidly disperses at the right of the disc and the post-disc runway (relatively) decreases. This is in agreement with the observations in 6.3.3.3, where the fluid leaving the gap travels away from the disc at a high velocity past a well-established wake.

6.4 Conclusions

The computational study of objects sinking through fluids with finite boundaries was performed in two distinct frames of reference: a disc sinking through a column of particles under gravity, and fluid flowing past a fixed disc. The first of these approaches is more analogous to the sinking experiments performed in section 3, and provided several important corroborating results:

1) The sinking disc did *not* follow a straight-line descent, despite being placed exactly central within the container. This suggests that the observed rotations during experiments were not a result of small imperfections or misalignments, but inherent behaviour of finite-boundary sinking.
2) Velocity increased towards a plateau with respect to disc density. This is supporting evidence of the previously hypothesised maximum sinking velocity for a given κ, as suggested in chapter 3.
3) Sinking velocity as a function of κ results in a peak velocity at a similar κ value to ball bearing experiments (0.3 κ and 0.4 κ respectively). Furthermore, velocity decreased linearly when $\kappa > 0.6$, corroborating the observed behaviour in *both* cylinder and ball bearing sinking experiments.

Velocity as a function of κ was also investigated by fixing the disc size and systematically varying the size of the container. This keeps the gravitational forces constant and isolates the hydrodynamic braking forces. A continuously linear velocity-κ relationship was observed, which is strongly supportive evidence that the linearity observed during experiments (when $\kappa > 0.6$) is a result of hydrodynamic braking.

Sinking simulations were performed over a variety of scales (a difficult set of experiments to perform in the laboratory). Results showed that scale is an important factor in sinking velocity, with the sinking velocity increasing (potentially asymptotically) with scale. This is a logical avenue for future research, where simulations could be used to determine the exact functional dependency with scale and identify any coupling effects with other system variables. This could provide valuable pseudo-experiment data which is impractical to obtain in the laboratory.

Another suggestion for future work would be to vary volume and density concurrently at a specific rate that keeps mass constant. This would be an insightful set

of sinking simulations which isolate surface area as a systematic variable, assuming the fluid is kept infinite. This would take advantage of being able to apply gravity exclusively to the sinker and remove buoyancy varying with volume (an impossible experiment in the laboratory).

Sinkers were shown to exhibit significant lateral movement in this study, but a more rigorous analysis of lateral distance travelled could expand upon this. For example, the total distance travelled could be measured and any functional dependencies between lateral movement and system variables could be quantified.

The frame of reference could also be better aligned with experiments. The logical next step would be to perform simulations in 3 dimensions - a relatively trivial operation mathematically, but one that requires a significant increase in computational power. This would ultimately require a codebase optimised for parallel processing[i1] - which was out of the scope of this project. The sinking object could also be made to more accurately represent experiment sinkers, perhaps by interlinking repulsive particles to the shape of a cuboid or cylinder.

Further simulations were performed in the frame of reference of flow past a fixed disc. This made for a more convenient method when determining fluid properties. Simulations were performed for the flow past a fixed disc within a finite boundary, systematically varying both the flow rate and disc size. All simulations were shown to reach a steady state, although the necessary pressure difference across the disc was shown to be non-linear with disc size. This was quantified by an increase in κ from 0.31 to 0.41 requiring a 10 % increase in pressure, yet an increase in κ from 0.81 to 0.91 requiring an order of magnitude increase. The highly non-linear nature of this pressure difference highlights its diminishing returns with annulus throughput, which corroborates the observations of a sinking velocity plateau as a function of sinker length and density made in chapter 3. Furthermore, this is in agreement with the similar asymptotic trends between sinking velocity and length or density shown by the analytical model in chapter 4.

[1] This does not necessarily imply upgrading the current bespoke codebase to utilise parallel processing. Several existing packages are available which already utilise parallel processing. The advantages of a bespoke software may no longer outweigh the complexity of implementing parallel processing algorithms.

A vector analysis of fluid velocity was used to identify several flow regimes. At very low streaming velocities eddies were observed throughout the simulation, possibly due to thermal noise. A wake was shown at the lowest streaming velocity where noise was *not* observed – indicative of non-laminar flow. It is suggested that simulations are repeated at much larger scales, such as those obtainable using parallel processing methods, in order to identify whether laminar flow is obtainable using MD methods.

The wake seen at low streaming velocities was shown to increase in magnitude synonymously through *either* increasing the magnitude of streaming velocity or size of the disc. The wake became unstable at greater streaming velocities, where each side of the wake could be seen to oscillate in magnitude. The phenomenom was observed from streaming velocities of 2 for a disc of 0.31 κ; increasing the disc size to 0.61 κ caused for wake oscillations to be observed at a streaming velocity of just 1.25, a 37 % reduction. Furthermore, a streaming velocity of 1.5 past the 0.61 κ disc gave rise to von Karmen vortex shedding, another well-known turbulent flow regime. This clearly shows that reducing the clearance in annular flow regimes causes for an increase in turbulence in an equivalent manner to increasing the velocity of annular flow.

At very large values of κ and streaming velocities fixed separated wakes were observed as opposed to shedding vortices. Interestingly, this shift in flow regime is an indication of a *decrease* in turbulence, as opposed to an increase. Similarly, several analysies of the Reynolds number (using both the simulation and clearance width as the hydraulic diameter) seemed to indicate that the Reynolds number could decrease at large κ or streaming velocity. However, the fluid was shown to be *highly* inhomogenious either side of the disc, and the reductions in Reynolds number are likely due to the extremely high density (and thus viscosity) at the front of the disc, which is necessary to maintain a large pressure difference. Further simulations using a less compressable potential are recommended to allow for a better Reynolds number analysis.

Another explanation for the fixed vortex wakes is the small area between disc and exit boundary for very large discs. It is hypothesised that fluid is forced towards the wake due to the fixed-velocity exit boundary, restricting vortex shedding. Additional simulations using a larger area between disc and exit boundary are suggested to investigate this phenomenom. Alternatively, a change in the behaviour of the exit boundary alone may be sufficient in the removal of any inward velocity streams.

7: Closing Remarks

Several methods were employed to gain insight into the sinking rate of waste packages in deep borehole disposal. A scaled-down, simplified apparatus was used to perform investigative experiments into the influence of various parameters on the terminal velocity of a cylinder sinking through a finite column of fluid. The Navier-Stokes equations were used to develop a tractable model capable of predicting the terminal velocity of cylinders sinking through a finite column of fluid. Finally, molecular dynamics simulations were used to obtain pseudo-experiment results using a sinking disc, and further flow information using a fixed disc within a streaming fluid.

Spheres were used during experiments to provide a link between apparatus and literature. It was shown that the sinking velocity obtained using experiments closely agreed with the Reynolds number extended Stokes law equation for sinker-diameter ratios (κ) of less than 0.25, showing agreement between apparatus and theory. Furthermore, the extended Reynolds number Stokes law equation was combined with the Munroe equation to provide a reasonably accurate sinking velocity (within 14 %) for all sinking spheres. It was later shown that spheres and cylinders of the same density and radius exhibited extremely similar sinking velocities; the combined Munroe equation could therefore be applied as a simple yet versatile method of predicting the sinking rate or Reynolds number of waste packages in DBD over a wide range of κ. The Munroe equation also conveniently over predicted sinking rate, making it a suitable model when determining the maximum potential impact a waste package must withstand.

Sinking experiments were performed for a variety of 'cylinders' with different degrees of cones at the leading face to determine the frictional losses undergone at the leading face. It was shown that streamlining the cylinder would increase the sinking rate by up to 12 %, despite using cylinders of only 1 cm in diameter. This highlights the importance in including front-face frictional forces into any sinking velocity predictive model.

The experiments, sinking disc simulations and the analytical model all showed that increasing diameter consistently caused a decrease in sinking velocity at diameters relevant to DBD ($\kappa > 0.65$). Furthermore, experiments showed that a 6% decrease in κ would give an equivalent increase in sinking velocity to tripling the sinker density.

Should the free-fall sinking rate of a full-scale DBD canister be too low (such that deployment becomes un-economical) or too high (such that safety concerns arise), altering the diameter of the container would therefore be the most impactful method in tailoring the sinking rate accordingly.

The relationship between κ and velocity was also shown to be linear at $\kappa > 0.65$. This was demonstrated for experiments using both cylinders and spheres, as well as in sinking disc simulations. Furthermore, sinking disc simulations were performed using a varied container size to investigate the κ-velocity relationship (keeping sinker mass and surface area constant), which showed the relationship to be linear throughout the entire range of κ. This is evidence that the restrictive forces associated with a tight clearance, or hydrodynamic breaking, have a linear dependency on κ, therefore the linearity observed during experiments is a result of dominant hydrodynamic breaking forces. This linear regime is fortuitous, as this would relatively simplify any empirical models of predicting DBD sinking rates should they be desired; determining how scale, density difference and cylinder length affect the κ-velocity gradient should give a capable model.

Increasing the length or density of cylinders during experiments showed an increase in sinking velocity, seemingly towards a plateau. Although this plateau could not be reached using the cylinders available in experiments, the analytical model demonstrated similar behaviour with both length and density, whilst the sinking disc simulations demonstrated a clear plateau with density. Increasing length or density increases the mass, and therefore the gravitational force, it may therefore be concluded that hydrodynamic braking forces increase with throughput. The fixed disc simulations exhibited analogous behaviour, as the required pressure difference across the disc increased exponentially with the streaming velocity magnitude.

Experiments performed at different apparatus scales showed that scale was an important factor in determining sinking velocity, with sinkers of similar κ having greater sinking velocity in a larger scale apparatus. Sinking velocity was also shown to be a function of scale in the analytical model, with sinking velocity also increasing with scale. Sinking disc simulations provided a more convenient method of investigating scale. Results confirmed that sinking velocity increased with scale, seemingly towards a plateau. This scale relationship would be fortuitous should a plateau be reached close to

the scales associated with experiments, as this would make experiment data a close approximation of full-scale DBD.

As discussed, the analytical model was shown to give good qualitative descriptions of velocity dependence on length and density (compared to both experiment and simulation data). However, the accuracy of the analytical model varied with diameter. For example, at 0.66 κ the model over predicted sinking velocity by a factor of 2, yet at 0.94 κ sinking velocity was marginally over predicted. The accuracy of the model decreases as sinking velocity increases; this would theoretically increase turbulence, which may explain the discrepancy with the analytical model. Regardless of its accuracy, the over-estimating nature of the analytical model would make it a suitable method for predicting an upper-bound sinking velocity. However, the aforementioned modified Munroe equation may provide a more suitable method if waste package diameter and length are low.

Several experiments and simulations provided further insight into finite-boundary sinking. It became apparent throughout experiments that cylinders would undergo significant axial rotation, despite a carefully controlled sinker release. Interestingly, isolating this tilt increased sinking velocity when tilt was large, yet decreased sinking velocity when tilt was low. Furthermore, sinking disc simulations ensured that sinkers would be perfectly central before release, yet all discs demonstrated lateral movement during descent. Oscillatory flow patterns were also observed in stationary disc simulations at the wake of discs, indicating that stresses would be unevenly applied to the sinker. These observations show that eccentricity is inherent to finite boundary sinking and must be controlled accordingly for a safe deployment of waste packages in DBD.

Stationary disc simulations were used to observe flow parameters in greater detail. A creeping flow regime was not observable at low streaming velocities, instead, turbulent flow regimes including elongated wakes, alternating wakes and von Karmen vortex streets were shown. These turbulent flow regimes were proven to occur at lower streaming velocities as κ increased. This is evidence that turbulence is highly likely to occur in finite boundary systems where κ is large, especially at the wake of the sinking object.

The insight obtained may be used to guide future efforts in the creation of an accurate sinking model for DBD. The analytical predictive model presented in this study could potentially be improved upon to become sufficiently accurate, as the model already shows good qualitative agreement between sinking velocity and several system variables. Suggested avenues for improvement would be the inclusion of a trailing face, which has been proven to contain significant eddy flows through stationary disc simulations. This could potentially give the necessary reduction in sinking velocity by giving a rear face pressure and decrease the annular pressure gradient, or by artificially lengthening the cylinder via an elongated wake.

Stationary disc simulations also showed that turbulence is inherent in finite boundary flows. This suggests that the advective terms of the Navier-Stokes equations would be required to accurately describe the fluid. Despite these terms being omitted in the current analytical model, the solution is relatively complex. Further derivatives would make a solution difficult (if possible) to obtain. Alternative methods may therefore be advantageous in future studies; for example, an empirical correction factor used in conjunction to the present analytical model may give an accurate and simple solution.

The Navier-Stokes equations may also be determined using computational methods to estimate partial derivatives (as opposed to solving them analytically). Capable methods include finite volume simulations with Reynolds-Averaged Navier Stokes (RANS) models to account for turbulence. However, simulations in the Lagrangian frame of reference (such as smoothed particle applied mechanics) would potentially provide a more comparable solution to sinking objects. The disadvantage of a computational approach is the requirement to simulate each unique configuration (diameter, length, density, scale) of waste package to obtain a sinking velocity. Not only would this be cumbersome, but insight into how sinking velocity functionally depends on various parameters would be difficult to ascertain (although several of these dependencies has been widely described throughout this study). Simulation data could, however, be used to construct an empirical solution, alleviating the aforementioned constraints. This approach may also take advantage of the linear sinking velocity-κ relationship observed in this study; simply determining how length, density and scale affect the sinking velocity-κ gradient should provide a sufficient predictive model. The

experiment data presented in this study could also be used to construct such a model, but would require additional data in regards to scale.

Further research would also be beneficial to several specific sections of this study. For experiments, sinking velocity as a function of length and density appeared to plateau, however an absolute maximum could not be identified at the range of sinkers used. A simple set of additional experiments which use a more expansive range of sinker lengths and densities could be used to confirm or refute the existence of plateaus with these system variables.

Additional experiments which systematically vary the Reynolds number would also be highly constructive. For example, varying the fluid would be a convenient method of controlling the Reynolds number without the need to alter the apparatus scale. This could provide a valuable assessment of the applicability of experiment data to larger length scales, such as DBD.

Experiments isolating cylinder tilt were inconclusive as to why certain sinkers decreased in sinking velocity, whilst others increased as tilt was restricted. Many of the proposed hypotheses are ambitious to prove, although several could be disregarded through an alternative method of stabilization. For example, further experiments using a varied weight distribution of cylinders could be used to control tilt, as front-loaded cylinders should reduce the magnitude of tilt without altering the sinker geometry.

The sinking disc simulations would also benefit from future study. These should primarily focus upon making the frame of reference more analogous to real world sinking. An obvious method would be to perform simulations in 3-dimensions. Although this would mathematically be a trivial change, the computational cost would increase significantly and require optimized parallel processing methods to obtain results within reasonable time frames. Ideally the sinker would also better represent a cylinder. This could be achieved by applying both an attractive and repulsive potential to a separate set of particles such that they behave as a solid. Any geometry sinker could be obtained using this method as long as the particles are initialised accordingly. Lastly, simulations indicated large amounts of fluid compressibility - a phenomenon unlikely to occur at larger scales. Future simulations using various potentials and potential coefficients could be used to identify an alternative force potential which is less susceptible to compressibility.

Other avenues for expanding upon sinking disc simulations would be to quantify lateral movement and determine any coupling with sinker parameters. This would allow for an informed selection of sinker parameters which reduce unwanted lateral movement or tilt. Sinker density could also be modified with radius, keeping the total mass of the sinker constant. If the sinker container is also modified such that κ is kept constant, these simulations will exclusively quantify friction losses associated with the sinker surface area (such as flow path losses and surface friction). These simulations would be almost impossible to perform in a laboratory due to buoyancy being an uncontrollable parameter, whereas simulations may remove buoyancy by exclusively applying gravity to the sinker.

As with the sinking disc simulations, stationary disc simulations would equally benefit from being made similar to real world sinking, be that through a less compressible potential, modifying the sinker shape or increasing dimensions. Sinking disc simulations were unable to identify laminar flow regimes although this may have been due to thermal noise. Further simulations using a larger number of particles would allow for more spatial averaging, which would reduce thermal noise and potentially investigate laminar flow regimes by increasing the simulation scale and spatial averaging.

Separated wakes at large κ and streaming velocity are indicative of a decrease in turbulence with κ and an anomaly to other flow regime observations. It is hypothesised that this behaviour is due to the nearby exit boundary, therefore further simulations using wider containers should confirm or refute this hypothesis. Alternatively, the behaviour of the exit boundary could be modified so as to reduce wake interference. This could be achieved by exclusively locking the x velocity component at the exit boundary, or by removing the exit boundary velocity lock entirely.

References

[1] Department for Business Energy & Industrial Strategy and NDA, *Radioactive Wastes in the UK*. DBEIS & NDA, 2017.

[2] Department for Business Energy & Industrial Strategy and NDA, *Radioactive Wastes in the UK: UK Radioactive Waste Inventory Report*. 2017.

[3] Department for Business Energy & Industrial Strategy and NDA, *Radioactive Wastes in the UK: Radioactive Wastes and Materials not Reported in the 2016 Waste Inventory*. 2017.

[4] IAEA, *Nuclear Power Reactors In The World*, 36th ed. IAEA, 2016.

[5] Department of Energy & Climate Change, "Implementing Geological Disposal A Framework for the long-term management of higher activity radioactive waste," 2014.

[6] F. Gibb, K. Travis, and K. Hesketh, "Deep borehole disposal of higher burn up spent nuclear fuels," *Mineral. Mag.*, vol. 76, no. 08, pp. 3003–3017, Dec. 2012.

[7] J. Beswick, F. Gibb, and P. Travis, "Deep borehole disposal of nuclear waste: engineering challenges," *Proc. Inst. Civ. Eng. - Energy*, vol. 167, no. 2, pp. 47–66, May 2014.

[8] F. Gibb, "A new scheme for the very deep geological disposal of high-level radioactive waste," *J. Geol. Soc. London.*, vol. 157, no. 1, pp. 27–36, Jan. 2000.

[9] F. G. F. Gibb, N. A. McTaggart, K. P. Travis, D. Burley, and K. W. Hesketh, "High-density support matrices: Key to the deep borehole disposal of spent nuclear fuel," *J. Nucl. Mater.*, vol. 374, no. 3, pp. 370–377, Mar. 2008.

[10] F. Gibb, K. Travis, N. McTaggart, D. Burley, and K. Hesketh, "Modeling Temperature Distribution Around Very Deep Borehole Disposals of HLW," *Nucl. Technol.*, vol. 163, no. 1, pp. 62–73, 2008.

[11] B. Arnold *et al.*, "Deep Borehole Disposal Research: Demonstration Site Selection Guidelines, Borehole Seals Design, and RD&D Needs," 2013.

[12] B. Arnold, P. Brady, S. Bauer, C. Herrick, S. Pye, and J. Finger, "Reference Design and Operations for Deep Borehole Disposal of High-Level Radioactive

Waste," 2011.

[13] K. Travis and F. Gibb, "Deep Borehole Disposal Research: What have we learned from numerical modeling and what can we learn?," *MRS Proc.*, vol. 1744, pp. 193–203, 2015.

[14] 3KQ, "Public dialogue on geological disposal and working with communities," 2016.

[15] M. Apted and J. Ahn, *Geological repository systems for safe disposal of spent nuclear fuels and radioactive waste*, 2nd ed. Woodhead Publishing, 2017.

[16] W. Cornwall, "Deep sleep," *Science (80-.).*, vol. 349, no. 6244, pp. 132–5, 2016.

[17] R. Murray and K. Holbert, *Nuclear energy : an introduction to the concepts, systems, and applications of nuclear processes*, 7th ed. Butterworth-Heinemann, 2014.

[18] F. Gibb and K. Travis, "Sealing Deep Borehole Disposals of Radioactive Waste by "Rock Welding"," in *High-Level Radioactive Waste Management*, 2015, pp. 401–406.

[19] F. Gibb, K. Taylor, and B. Burakov, "The 'granite encapsulation' route to the safe disposal of Pu and other actinides," *J. Nucl. Mater.*, vol. 374, no. 3, pp. 364–369, 2008.

[20] N. Collier, H. Balboa, N. Milestone, and K. Travis, "Inorganic anions as retarders for deep borehole disposal grouts," *Adv. Cem. Res.*, vol. 29, no. 8, pp. 347–357, 2017.

[21] J. Beswick, "Status of Technology for Deep Borehole Disposal," 2008.

[22] E. Bates, "A drop-in-concept for deep borehole canister emplacement," Massachusetts Institute of Technology, 2011.

[23] "Drilling Operations 1984 Vol. 3," 1985.

[24] E. Tadmor, R. Miller, and R. Elliott, *Continuum mechanics and thermodynamics : from fundamental concepts to governing equations*. Cambridge University Press, 2012.

[25] S. Flügge, *Principles of Classical Mechanics and Field Theory / Prinzipien der Klassischen Mechanik und Feldtheorie*. Springer Berlin Heidelberg, 1960.

[26] B. Castelli, *Della misura dell'acque correnti castelli*. Bologna: Per gli HH del Dozza, 1628.

[27] D. Bernoulli, *Hydrodynamica*. 1738.

[28] L. Euler, "Principes généraux du mouvement des fluides," in *Mémoires de l'Academie des Sciences de Berlin*, 1757, pp. 274–315.

[29] I. Newton, *Philosophiæ naturalis principia mathematica*. 1687.

[30] A. Cauchy, "Recherches sur l'équilibre et le mouvement intérieur des corps solides ou fluides, élastiques ou non élastiques," *Bull. la Société philomatique*, pp. 9–13, 1823.

[31] J. Fourier, *Théorie analytique de la chaleur*. Paris, F. Didot, 1822.

[32] A. Fick, "Ueber Diffusion," *Ann. der Phys. und Chemie*, vol. 170, no. 1, pp. 59–86, 1855.

[33] R. Mauri, *Non-Equilibrium Thermodynamics in Multiphase Flows*. Dordrecht: Springer Netherlands, 2013.

[34] L. Landau and E. Lifshitz, *Fluid Mechanics*, 2nd ed. Pergamon Press, 1959.

[35] H. Lamb, *Hydrodynamics*. Cambridge University Press, 1895.

[36] G. Stokes, "On the effect of the internal friction of fluids on the motion of pendulums," 1850.

[37] D. Bland, *Solutions of Laplace's Equation*. Springer Netherlands, 1961.

[38] R. Bird, W. Stewart, and E. Lightfoot, *Transport phenomena*, Second. J. Wiley, 2002.

[39] G. Batchelor, "An Introduction to Fluid Dynamics," 1967.

[40] B. Lautrup, *Physics of Continuous Matter: Exotic and Everyday Phenomena in the Macroscopic World*. Institute of Physics, 2005.

[41] O. Reynolds, "An Experimental Investigation of the Circumstances Which Determine Whether the Motion of Water Shall Be Direct or Sinuous, and of the Law of Resistance in Parallel Channels," 1883.

[42] R. Mott, "Some Aspects of Fluid Flow," in *London Arnold*, 1950, p. 242.

[43] V. Fidleris and R. Whitmore, "Experimental determination of the wall effect for

spheres falling axially in cylindrical vessels," *Br. J. Appl. Phys.*, vol. 12, no. 9, pp. 490–494, 1961.

[44] A. Francis, "Wall Effect in Falling Ball Method for Viscosity," *Physics (College. Park. Md).*, vol. 4, no. 11, pp. 403–406, 1933.

[45] H. Munroe, "The English versus the continental system of jigging-is close sizing advantageous?," *Trans. Am. Inst. Mining, Metall. Pet. Eng.*, vol. 17, pp. 637–659, 1888.

[46] C. Ataíde, F. Pereira, and M. Barrozo, "Wall effects on the terminal velocity of spherical particles in Newtonian and non-Newtonian fluids," *Brazilian J. Chem. Eng.*, vol. 16, no. 4, pp. 387–394, 1999.

[47] J. Lohrenz, G. Swift, and F. Kurata, "An experimentally verified theoretical study of the falling cylinder viscometer," *AIChE J.*, vol. 6, no. 4, pp. 547–550, 1960.

[48] M. Chen, J. Lescarboura, and G. Swift, "The effect of eccentricity on the terminal velocity of the cylinder in a falling cylinder viscometer," *AIChE J.*, vol. 14, no. 1, pp. 123–127, 1968.

[49] E. Ashare, R. Bird, and J. Lescarboura, "Falling cylinder viscometer for non-Newtonian fluids," *AIChE J.*, vol. 11, no. 5, pp. 910–916, 1965.

[50] S. Matsuhisa and R. Bird, "Analytical and numerical solutions for laminar flow of the non-Newtonian Ellis fluid," *AIChE J.*, vol. 11, no. 4, pp. 588–595, 1965.

[51] W. Ostwald, "Ueber die rechnerische Darstellung des Strukturgebietes der Viskosität," *Kolloid-Zeitschrift*, vol. 47, no. 2, pp. 176–187, 1929.

[52] F. Eichstadt and G. Swift, "Theoretical analysis of the falling cylinder viscometer for power law and bingham plastic fluids," *AIChE J.*, vol. 12, no. 6, pp. 1179–1183, 1966.

[53] N. Park and T. Irvine, "Falling cylinder viscometer end correction factor," *Rev. Sci. Instrum.*, vol. 66, no. 7, pp. 3982–3984, 1995.

[54] H. Brenner, "Effect of finite boundaries on the Stokes resistance of an arbitrary particle," *J. Fluid Mech.*, vol. 12, pp. 35–48, 1962.

[55] N. Park and T. Irvine, "The falling needle viscometer a new technique for

viscosity measurements," *Wärme- und Stoffübertragung*, vol. 18, no. 4, pp. 201–206, 1984.

[56] A. Quarmby, "An experimental study of turbulent flow through concentric annuli," *Int. J. Mech. Sci.*, vol. 9, no. 4, pp. 205–221, 1967.

[57] A. Quarmby, "An analysis of turbulent flow in concentric annuli," *Appl. Sci. Res.*, vol. 19, no. 1, pp. 250–273, 1968.

[58] R. Deissler, "Analysis of Turbulent Heat Transfer, Mass Transfer, and Friction in Smooth Tubes at High Prandtl and Schmidt Numbers," 1954.

[59] S. Goldstein, *Modern Developments In Fluid Dynamics*. Oxford At The Olarendon Press, 1938.

[60] Y. Lee and S. Park, "Developing turbulent flow in concentric annuli: An analytical and experimental study," *Wärme- und Stoffübertragung*, vol. 4, no. 3, pp. 156–166, 1971.

[61] H. Reichardt, "Vollständige Darstellung der turbulenten Geschwindigkeitsverteilung in glatten Leitungen," *ZAMM - Zeitschrift für Angew. Math. und Mech.*, vol. 31, no. 7, pp. 208–219, 1951.

[62] I. Sud and J. Chaddock, "Drag Calculations for Vehicles in Very Long Tubes from Turbulent Flow Theory," *ASME J. Fluids Eng.*, vol. 103, pp. 361–366, 1981.

[63] D. Kotlow and F. White, "An Analysis of Developing Turbulent Flow Between a Moving Cylinder and a Concentric Tube," 1967.

[64] C. COLEBROOK, "Turbulent flow in pipes, with particular reference to the transition region between the smooth and rough pipe laws," *J. Inst. Civ. Eng.*, vol. 11, no. 4, pp. 133–156, 1939.

[65] P. Bridgman, *Dimensional Analysis*. Kessinger Publishing, 1922.

[66] P. Neofytou, "A 3rd order upwind finite volume method for generalised Newtonian fluid flows," *Adv. Eng. Softw.*, vol. 36, no. 10, pp. 664–680, 2005.

[67] G. Mompean and M. Deville, "Unsteady finite volume simulation of Oldroyd-B fluid through a three-dimensional planar contraction," *J. Nonnewton. Fluid Mech.*, vol. 72, no. 2–3, pp. 253–279, 1997.

[68] I. Demirdžić and M. Perić, “Finite volume method for prediction of fluid flow in arbitrarily shaped domains with moving boundaries,” *Int. J. Numer. Methods Fluids*, vol. 10, no. 7, pp. 771–790, 1990.

[69] F. Moukalled, L. Mangani, and M. Darwish, *The finite volume method in computational fluid dynamics : an advanced introduction with OpenFOAM® and Matlab®*. Springer, 2015.

[70] H. Versteeg and W. Malalasekera, *An introduction to computational fluid dynamics : the finite volume method*. Pearson Education Ltd, 2007.

[71] L. Prandtl, “Bericht fiber Untersuchungen zur ausgebildeten Turbulent,” *Zeitschrift fiir Angew. Math. und Mech.*, vol. 5, no. 2, pp. 136–139, 1925.

[72] A. Kasmi and C. Masson, “An extended k–ε model for turbulent flow through horizontal-axis wind turbines,” *J. Wind Eng. Ind. Aerodyn.*, vol. 96, no. 1, pp. 103–122, 2008.

[73] M. Lateb, C. Masson, T. Stathopoulos, and C. Bédard, “Comparison of various types of k–ε models for pollutant emissions around a two-building configuration,” *J. Wind Eng. Ind. Aerodyn.*, vol. 115, pp. 9–21, 2013.

[74] Z. Khan and J. Joshi, “Comparison of k–ε, RSM and LES models for the prediction of flow pattern in jet loop reactor,” *Chem. Eng. Sci.*, vol. 127, pp. 323–333, 2015.

[75] R. Lukes, J. Hart, J. Potts, and S. Haake, “A CFD Analysis of Flow Around a Disc,” *Procedia Eng.*, vol. 72, pp. 685–690, 2014.

[76] J. Smagorinsky, “General circulation experiments with the primitive equations,” *Mon. Weather Rev.*, vol. 91, no. 3, pp. 99–164, 1963.

[77] J. Fröhlich and D. Terzi, “Hybrid LES/RANS methods for the simulation of turbulent flows,” *Prog. Aerosp. Sci.*, vol. 44, no. 5, pp. 349–377, 2008.

[78] B. Rajani, A. Kandasamy, and S. Majumdar, “LES of Flow past Circular Cylinder at Re = 3900.,” *J. Appl. Fluid Mech.*, vol. 9, no. 3, pp. 1421–1435, 2016.

[79] S. Murakami, S. Iizuka, and R. Ooka, “Cfd analysis of turbulent flow past square cylinder using dynamic les,” *J. Fluids Struct.*, vol. 13, no. 7–8, pp. 1097–1112,

1999.

[80] S. Orszag and G. Patterson, “Numerical Simulation of Three-Dimensional Homogeneous Isotropic Turbulence,” *Phys. Rev. Lett.*, vol. 28, no. 2, pp. 76–79, 1972.

[81] P. Moin and K. Mahesh, “Direct Numerical Simulation: A Tool In Turbulence Research,” *Annu. Rev. Fluid Mech.*, vol. 30, no. 1, pp. 539–578, 1998.

[82] G. Liu and M. Liu, *Smoothed particle hydrodynamics : a meshfree particle method*. World Scientific, 2003.

[83] A. Puhl, M. Mansour, and M. Mareschal, “Quantitative comparison of molecular dynamics with hydrodynamics in Rayleigh-Bénard convection.,” *Phys. Rev. A, Gen. Phys.*, vol. 40, no. 4, pp. 1999–2012, 1989.

[84] J. Given and E. Clementi, “Molecular dynamics and Rayleigh–Benard convection,” *J. Chem. Phys.*, vol. 90, no. 12, pp. 7376–7383, 1989.

[85] D. Hirshfeld and D. Rapaport, “Molecular Dynamics Simulation of Taylor-Couette Vortex Formation,” *Phys. Rev. Lett.*, vol. 80, no. 24, pp. 5337–5340, 1998.

[86] D. Rapaport, “Microscale hydrodynamics: Discrete-particle simulation of evolving flow patterns,” *Phys. Rev. A*, vol. 36, no. 7, pp. 3288–3299, 1987.

[87] D. Rapaport and E. Clementi, “Eddy Formation in Obstructed Fluid Flow: A Molecular-Dynamics Study,” *Phys. Rev. Lett.*, vol. 57, no. 6, pp. 695–698, 1986.

[88] J. Weeks, D. Chandler, and H. Andersen, “Role of Repulsive Forces in Determining the Equilibrium Structure of Simple Liquids,” *J. Chem. Phys.*, vol. 54, no. 12, pp. 5237–5247, 1971.

[89] S. Cui and D. Evans, “Molecular Dynamics Simulation of Two Dimensional Flow Past a Plate,” *Mol. Simul.*, vol. 9, no. 3, pp. 179–192, 1992.

[90] T. Ishiwata, T. Murakami, S. Yukawa, and N. Ito, “Particle Dynamics Simulations of The Navier–stokes Flow with Hard Disks,” *Int. J. Mod. Phys. C*, vol. 15, no. 10, pp. 1413–1424, 2004.

[91] A. Satoh, “Molecular dynamics simulation of a subsonic flow of a rarefied gas past a sphere,” *Adv. Powder Technol.*, vol. 4, no. 1, pp. 59–70, 1993.

[92] S. Volz and G. Chen, “Molecular-dynamics simulation of thermal conductivity of silicon crystals,” *Phys. Rev. B*, vol. 61, no. 4, pp. 2651–2656, 2000.

[93] D. Heyes, “Transport coefficients of Lennard-Jones fluids: A molecular-dynamics and effective-hard-sphere treatment,” *Phys. Rev. B*, vol. 37, no. 10, pp. 5677–5696, 1988.

[94] J. Hardy, O. de Pazzis, and Y. Pomeau, “Molecular dynamics of a classical lattice gas: Transport properties and time correlation functions,” *Phys. Rev. A*, vol. 13, no. 5, pp. 1949–1961, 1976.

[95] J. Lagrange, *Mécanique analytique*. 1788.

[96] B. William Rowan Hamilton, “On a General Method in Dynamics,” 1834.

[97] M. Allen and D. Tildesley, *Computer simulation of liquids*. Clarendon Press, 1987.

[98] J. Sengers, R. Kayser, C. Peters, and H. White, *Equations of state for fluids and fluid mixtures*. Elsevier, 2000.

[99] B. Alder and T. Wainwright, “Phase Transition for a Hard Sphere System,” *J. Chem. Phys.*, vol. 27, no. 5, pp. 1208–1209, 1957.

[100] B. Alder and T. Wainwright, “Studies in Molecular Dynamics. I. General Method,” *J. Chem. Phys.*, vol. 31, no. 2, pp. 459–466, 1959.

[101] A. Rahman, “Correlations in the Motion of Atoms in Liquid Argon,” *Phys. Rev.*, vol. 136, no. 2A, pp. 405–411, 1964.

[102] W. Hoover, A. Ladd, and B. Moran, “High-Strain-Rate Plastic Flow Studied via Nonequilibrium Molecular Dynamics,” *Phys. Rev. Lett.*, vol. 48, no. 26, pp. 1818–1820, 1982.

[103] D. Evans, “Computer ‘“experiment”’ for nonlinear thermodynamics of Couette flow,” *J. Chem. Phys.*, vol. 78, no. 6, pp. 3297–3302, 1983.

[104] D. Evans and G. Morriss, *Statistical mechanics of nonequilibrium liquids*, Second. Cambridge University Press, 2008.

[105] S. Nosé, “A molecular dynamics method for simulations in the canonical ensemble,” *Mol. Phys.*, vol. 52, no. 2, pp. 255–268, 1984.

[106] W. Hoover, “Canonical dynamics: Equilibrium phase-space distributions,” *Phys. Rev. A*, vol. 31, no. 3, pp. 1695–1697, 1985.

[107] C. Gray, K. Gubbins, and C. Joslin, *Theory of molecular fluids*. Oxford University Press, 1984.

[108] W. Hoover, *Smooth Particle Applied Mechanics*, vol. 25. World Scientific, 2006.

[109] L. Euler, *Institutionum calculi integralis*. imp. Acad. imp. Saènt., 1768.

[110] L. Verlet, “Computer "Experiments" on Classical Fluids. I. Thermodynamical Properties of Lennard-Jones Molecules,” *Phys. Rev.*, vol. 159, no. 1, pp. 98–103, 1967.

[111] B. Leimkuhler, S. Reich, K. Zentrum, and R. Skeel, “Integration methods for molecular dynamics,” 1995.

[112] C. Runge, “Mathematische Annalen,” vol. 46, pp. 167–178, 1895.

[113] W. Kutta, “Beitrag zur näherungsweisen Integration totaler Differentialgleichungen,” *Z. Math. Phys.*, vol. 46, pp. 434–453, 1901.

[114] W. G. Hoover and C. G. Hoover, “THREE LECTURES: NEMD, SPAM, and SHOCKWAVES,” 2010.

[115] W. G. Hoover, T. G. Pierce, C. G. Hoover, J. O. Shugart, C. M. Stein, and A. L. Edwards, “Molecular dynamics, smoothed-particle applied mechanics, and irreversibility,” *Comput. Math. with Appl.*, vol. 28, no. 10–12, pp. 155–174, 1994.

[116] A. Newell and J. Shaw, “Programming the logic theory machine,” in *Papers presented at the February 26-28, 1957, western joint computer conference: Techniques for reliability*, 1957, pp. 230–240.

[117] C. Purcell, “The control data STAR-IOO-Performance measurements,” in *National Computer Conference*, 1974, pp. 385–387.

[118] M. Pinches, D. Tildesley, and W. Smith, “Large Scale Molecular Dynamics on Parallel Computers using the Link-cell Algorithm,” *Mol. Simul.*, vol. 6, no. 1–3, pp. 51–87, 1991.

[119] D. Brown, H. Minoux, and B. Maigret, “A domain decomposition parallel processing algorithm for molecular dynamics simulations of systems of arbitrary

connectivity," *Comput. Phys. Commun.*, vol. 103, no. 2–3, pp. 170–186, 1997.

[120] D. C. Rapaport, "Multi-million particle molecular dynamics: II. Design considerations for distributed processing," *Comput. Phys. Commun.*, vol. 62, no. 2–3, pp. 217–228, 1991.

[121] P. Lombdahl and D. Beazley, "State of the art parallel computing," *Los Alamos Sci.*, vol. 22, pp. 44–57, 1994.

[122] S. Plimpton, "Fast Parallel Algorithms for Short-Range Molecular Dynamics," *J. Comput. Phys.*, vol. 117, no. 1, pp. 1–19, 1995.

[123] H. Berendsen, D. van der Spoel, and R. van Drunen, "GROMACS: A message-passing parallel molecular dynamics implementation," *Comput. Phys. Commun.*, vol. 91, no. 1–3, pp. 43–56, 1995.

[124] I. Götze, H. Noguchi, and G. Gompper, "Relevance of angular momentum conservation in mesoscale hydrodynamics simulations," *Phys. Rev. E*, vol. 76, no. 4, p. 046705, 2007.

[125] P. Giannozzi *et al.*, "Quantum ESPRESSO: a modular and open-source software project for quantum simulations of materials," *Condens. Matter*, vol. 21, no. 39, pp. 1–19, 2009.

[126] I. Cimrák, M. Gusenbauer, and I. Jančigová, "An ESPResSo implementation of elastic objects immersed in a fluid," *Comput. Phys. Commun.*, vol. 185, no. 3, pp. 900–907, 2014.

[127] A. Ruymgaart, A. Cardenas, and R. Elber, "MOIL-opt: Energy-Conserving Molecular Dynamics on a GPU/CPU System," *J. Chem. Theory Comput.*, vol. 7, no. 10, pp. 3072–3082, 2011.

[128] J. Milner, "Modelling Melt Viscosity for Nuclear Waste Glass," The University of Sheffield, 2014.

[129] D. Evans and G. Morriss, "Nonequilibrium Molecular-Dynamics Simulation of Couette Flow in Two-Dimensional Fluids," *Phys. Rev. Lett.*, vol. 51, no. 19, pp. 1776–1779, 1983.

[130] S. Liem, D. Brown, and J. Clarke, "Investigation of the homogeneous-shear nonequilibrium-molecular-dynamics method," *Phys. Rev. A*, vol. 45, no. 6, pp.

3706–3713, 1992.

[131] D. Evans, W. Hoover, B. Failor, B. Moran, and A. Ladd, “Nonequilibrium molecular dynamics via Gauss’s principle of least constraint,” *Phys. Rev. A*, vol. 28, no. 2, pp. 1016–1021, 1983.

[132] D. Evans and G. Morriss, “Nonlinear-response theory for steady planar Couette flow,” *Phys. Rev. A*, vol. 30, no. 3, pp. 1528–1530, 1984.

[133] *Physical properties of glycerine and its solutions.* New York: Glycerine Producers’ Association, 1963.

[134] L. Korson, W. Drost-Hansen, and F. Millero, “Viscosity of water at various temperatures,” *J. Phys. Chem.*, vol. 73, no. 1, pp. 34–39, 1969.

[135] J. Patterson and E. Morris, “Measurement of Absolute Water Density, 1 °C to 40 °C,” *Metrologia*, vol. 31, no. 4, pp. 277–288, 1994.

[136] D. Evans, E. Cohen, and G. Morriss, “Viscosity of a simple fluid from its maximal Lyapunov exponents,” *Phys. Rev. A*, vol. 42, no. 10, pp. 5990–5997, 1990.

[137] J. SUN and S. SUNDARESAN, “A constitutive model with microstructure evolution for flow of rate-independent granular materials,” *J. Fluid Mech.*, vol. 682, pp. 590–616, 2011.

[138] K. Travis and C. Braga, “Configurational temperature and pressure molecular dynamics: review of current methodology and applications to the shear flow of a simple fluid,” *Mol. Phys.*, vol. 104, no. 22–24, pp. 3735–3749, 2006.

[139] K. Kawasaki and J. Gunton, “Theory of Nonlinear Transport Processes: Nonlinear Shear Viscosity and Normal Stress Effects,” *Phys. Rev. A*, vol. 8, no. 4, pp. 2048–2064, 1973.

[140] K. Travis, Searles D, and D. Evans, “Strain rate dependent properties of a simple fluid,” *Mol. Phys.*, vol. 95, no. 2, pp. 195–202, 1998.

[141] R. Di Felice, “A relationship for the wall effect on the settling velocity of a sphere at any flow regime,” *Int. J. Multiph. Flow*, vol. 22, no. 3, pp. 527–533, 1996.

[142] K. Travis, “Private Communications.” 2017.

[143] D. Rapaport, *The Art of Molecular Dynamics Simulation*. Cambridge University Press, 2004.

[144] F. Rizzi *et al.*, "Uncertainty Quantification in MD Simulations. Part I: Forward Propagation," *Multiscale Model. Simul.*, vol. 10, no. 4, pp. 1428–1459, Jan. 2012.

[145] H. Schlichting, *Boundary Layer Theory*. McGraw-Hill Book Company, 1960.

[146] C. Christov, R. Marinova, and T. Marinov, "Does the stationary viscous flow around a circular cylinder exist for large Reynolds numbers? A numerical solution via variational imbedding," *J. Comput. Appl. Math.*, vol. 226, no. 2, pp. 205–217, 2009.

[147] A. Khalili and B. Liu, "Stokes' paradox: creeping flow past a two-dimensional cylinder in an infinite domain," *J. Fluid Mech.*, vol. 817, pp. 374–387, 2017.

[148] S. Taneda, "Experimental Investigation of the Wakes behind Cylinders and Plates at Low Reynolds Numbers," *J. Phys. Soc. Japan*, vol. 11, no. 3, pp. 302–307, 1956.

[149] M. Coutanceau and R. Bouard, "Experimental determination of the main features of the viscous flow in the wake of a circular cylinder in uniform translation. Part 1. Steady flow," *J. Fluid Mech.*, vol. 79, no. 02, p. 231, 1977.

[150] V. Patel, "Symmetry of the flow around a circular cylinder," *J. Comput. Phys.*, vol. 71, no. 1, pp. 65–99, 1987.

[151] J. Gerrard, "The Wakes of Cylindrical Bluff Bodies at Low Reynolds Number," *Philos. Trans. R. Soc. A Math. Phys. Eng. Sci.*, vol. 288, no. 1354, pp. 351–382, 1978.

[152] T. von Kármán, "Ueber den Mechanismus des Widerstandes, den ein bewegter Körper in einer Flüssigkeit erfährt," *Nachrichten von der Gesellschaft der Wissenschaften zu Göttingen, Math. Klasse*, vol. 1911, pp. 509–517.

[153] P. Bearman, "On vortex street wakes," *J. Fluid Mech.*, vol. 28, no. 04, p. 625, 1967.

[154] M. Breuer, "A CHALLENGING TEST CASE FOR LARGE EDDY SIMULATION: HIGH REYNOLDS NUMBER CIRCULAR CYLINDER FLOW," *First Symposium on Turbulence and Shear Flow Phenomena*. Begel

House Inc., 1999.

[155] C. Williamson, “Vortex Dynamics in the Cylinder Wake,” *Annu. Rev. Fluid Mech.*, vol. 28, no. 1, pp. 477–539, 1996.

[156] J. Wendt, J. Anderson, and Von Karman Institute for Fluid Dynamics., *Computational fluid dynamics : an introduction*. Springer, 2008.

[157] S. Groot and P. Mazur, *Non-equilibrium thermodynamics*. Dover.

[158] W. Thomson, *Introduction to transport phenomena*. Prentice Hall, 1999.

[159] R. Berker, *Integration des équations du mouvement d’un fluide visqueux incompressible. Handbuch der Physik*. Berlin: Springer-Verlag, 1963.

[160] A. Kolmogorov, “Three approaches to the quantitative definition of information,” *Int. J. Comput. Math.*, vol. 2, no. 1–4, pp. 157–168, 1968.

Appendix A: Basic Continuum Mechanics

A.1 Conservation of Mass

In this section the conservation of mass through a given volume is described. It is first assumed that the given volume *V* is a perfect cuboid, as shown in figure A.1. The net change of mass $\frac{\partial M}{\partial t}$ must be equal to the rate of mass entering less the rate of mass leaving the cell, as mass may not be generated within[1].

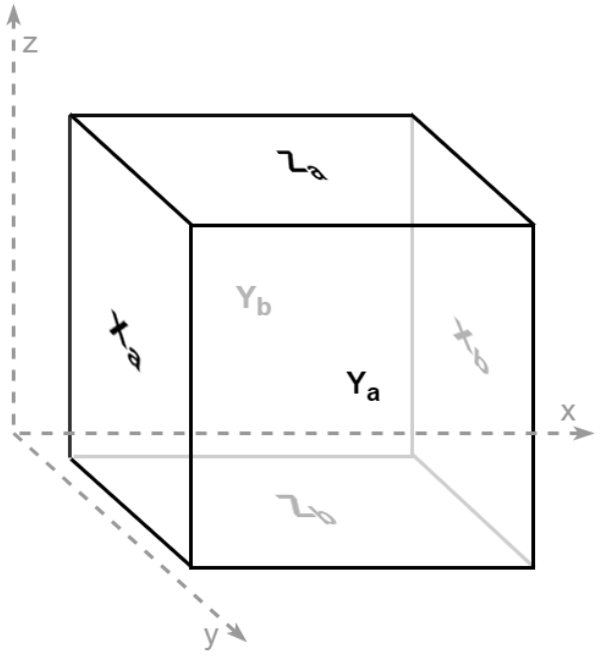

Figure A.1: Three dimensional cubic cell volume, with *a* and *b* labelled faces in the *X*, *Y* and *Z* directions. The width, height and depth of the cell are Δx, Δy and Δz.

The mass flow at a given position in the cubic cell is the product of density and fluid velocity at that position. The flow rate across face X_a is therefore equal to $\Delta y \Delta z \rho v_{xa}$, where v_{xa} is the velocity at face X_a in the *x* direction. Mass flow in the *x* direction is therefore equal to $\Delta y \Delta z \rho v_{xa} - \Delta y \Delta z \rho v_{xb}$. The same principle is applied to the remaining directions, giving:

[1] Excluding any relativistic effects.

$$\frac{\partial M}{\partial t} = \Delta x \Delta y \Delta z \frac{\partial \rho}{\partial t} \tag{A.1}$$
$$= \Delta y \Delta z[\rho v_{xa} - \rho v_{xb}] + \Delta z \Delta x[\rho v_{ya} - \rho v_{yb}]$$
$$+ \Delta x \Delta y[\rho v_{za} - \rho v_{zb}]$$

Dividing both sides of equation A.1 by $\Delta x \Delta y \Delta z$ and taking the limit as Δx, Δy and Δz shrink to zero gives the equation of continuity [156], where bold text denotes a vector:

$$\frac{\partial \rho}{\partial t} = -\left(\frac{\partial}{\partial x}\rho v_x + \frac{\partial}{\partial y}\rho v_y + \frac{\partial}{\partial z}\rho v_z\right) = -\nabla \cdot \rho \boldsymbol{v} \tag{A.2}$$

The previous derivation used a cubic control volume. Exactly the same equation can be obtained for an arbitrary volume, *V*. This is achieved by defining the mass through a volume integral,

$$M = \int_V \rho d\boldsymbol{r} \tag{A.3}$$

where $d\boldsymbol{r}$ is an element of volume. The rate of increase of mass dM/dt is therefore given by

$$\frac{dM}{dt} = \int_V \frac{\partial}{\partial t}\rho d\boldsymbol{r} \tag{A.4}$$

Since mass may not be created or destroyed, the mass of *V* can only change through the flow of material across the boundaries of the volume element. The mass flux is equal to ρ**v**, giving

$$\frac{dM}{dt} = -\int_S \rho \boldsymbol{v} d\boldsymbol{S} \tag{A.5}$$

where the minus sign reflects $d\boldsymbol{S}$ being an element of surface with normal directed outwards [104]. The divergence theorem can be used to convert the surface integral into a volume integral, such that

$$-\int_{S} \rho \boldsymbol{v} d\boldsymbol{S} = -\int_{V} \boldsymbol{\nabla} \cdot \rho \boldsymbol{v} d\boldsymbol{r} \tag{A.6}$$

Equation A.6 may be combined with equation A.4 to give

$$\frac{dM}{dt} = -\int_{V} \boldsymbol{\nabla} \cdot \rho \boldsymbol{v} d\boldsymbol{r} \tag{A.7}$$

The two equations describing the rate of change of mass, equations A.4 and A.7 are equated together. The volumes are arbitrary, therefore the integrands must be equal. This gives the final form of the mass continuity equation in the fixed point Eulerian frame, equation A.8, which is in agreement with equation A.2.

$$\frac{\partial \rho}{\partial t} = -\boldsymbol{\nabla} \cdot \rho \boldsymbol{v} \tag{A.8}$$

An expression for the mass continuity may also be obtained for a co-moving, Lagrangian frame of reference, using the Eulerian-Lagrangian field variable relationship,

$$\frac{dA}{dt} = \frac{\partial A}{\partial t} + \boldsymbol{v} \cdot (\boldsymbol{\nabla} A) \tag{A.9}$$

where A is an arbitrary function of position and time. In this context, d/dt is commonly referred to as a ‘material derivative’. Setting density as the arbitrary variable in equation A.9 and inserting into equation A.8 gives

$$\frac{d\rho}{dt} = \boldsymbol{v} \cdot (\boldsymbol{\nabla} \rho) - \boldsymbol{\nabla} \cdot \rho \boldsymbol{v} \tag{A.10}$$

The chain rule is used to expand second term on the right hand side of equation A.10:

$$\boldsymbol{\nabla} \cdot \rho \boldsymbol{v} = \rho (\boldsymbol{\nabla} \cdot \boldsymbol{v}) + \boldsymbol{v} \cdot \boldsymbol{\nabla} \rho \tag{A.11}$$

This can be used to simplify equation A.10, giving:

$$\frac{d\rho}{dt} = -\rho(\boldsymbol{\nabla} \cdot \boldsymbol{v}) \tag{A.12}$$

This is the Lagrangian form of the mass continuity equation. The Lagrangian form of the conservation laws will be used extensively in the later work using the smooth-particle applied mechanics method.

A.2 Conservation of Momentum

In a similar manner to section A.1.1, the rate of change of momentum in *any* volume of fluid *V* is considered. For the total momentum *p* contained within the volume, the rate of change in momentum is given by

$$\frac{dp}{dt} = \int_V \frac{\partial \rho \boldsymbol{v}}{\partial t} d\boldsymbol{r} \tag{A.13}$$

The total momentum can change either by convection, or by pressure exerted across the surface of the volume by surrounding matter (the stress component). Newton's 2nd law of motion states that force must be proportional to the rate of change of momentum. Forces acting across the unit surface therefore induce the conductive flow of momentum. Force can consequently be related to pressure as shown in equation A.14, where $\boldsymbol{P}$ is the pressure tensor. This is a second rank tensor, requiring nine scalars in three dimensions to define it (though these may not all be independent).

$$d\boldsymbol{F} = -\boldsymbol{P} \cdot d\boldsymbol{S} \tag{A.14}$$

The stress momentum is given by integrating force, such that

$$\frac{dp_{stress}}{dt} = -\int_S \boldsymbol{P} \cdot d\boldsymbol{S} \tag{A.15}$$

The convective momentum contribution can be expressed as

$$\frac{dp_{conv}}{dt} = -\int_S \rho \boldsymbol{v} \boldsymbol{v} d\boldsymbol{S} \tag{A.16}$$

Equations A.15 and A.16 may then be added together to give the total rate of change of momentum, and the divergence theorem can be used to convert the surface integrals to volume integrals.

$$\frac{dG}{dt} = \int_V \frac{\partial \rho \boldsymbol{v}}{\partial t} d\boldsymbol{r} = -\int_V \boldsymbol{\nabla} \cdot [\rho \boldsymbol{v}\boldsymbol{v} + \boldsymbol{P}] d\boldsymbol{r} \tag{A.17}$$

Since volume is arbitrary, equation A.17 can be rewritten as:

$$\frac{\partial \rho \boldsymbol{v}}{\partial t} = -\boldsymbol{\nabla}(\rho \boldsymbol{v}\boldsymbol{v} + \boldsymbol{P}) \tag{A.18}$$

which is the momentum conservation law in the Eulerian frame of reference. The momentum conservation law may also be derived in Lagrangian terms. This requires the use of a total and streaming derivative relationship, similar to equation A.9 but generalised for an arbitrary *vector* field, $\boldsymbol{A}$.

$$\frac{d\boldsymbol{A}}{dt} = \frac{\partial \boldsymbol{A}}{\partial t} + \boldsymbol{v} \cdot (\boldsymbol{\nabla A}) \tag{A.19}$$

Using the chain rule to expand the left hand side of equation A.18 gives

$$\boldsymbol{v}\frac{\partial \rho}{\partial t} + \rho \frac{\partial \boldsymbol{v}}{\partial t} = -\boldsymbol{\nabla}(\rho \boldsymbol{v}\boldsymbol{v} + \boldsymbol{P}) \tag{A.20}$$

Inserting the velocity vector as the arbitrary vector into equation A.18 and re-arranging gives

$$\rho \frac{\partial \boldsymbol{v}}{\partial t} = \rho \frac{d\boldsymbol{v}}{dt} - \rho \boldsymbol{v} \cdot (\boldsymbol{\nabla v}) \tag{A.21}$$

Equation A.21 may be substituted into equation A.20 to give

$$\rho \frac{d\boldsymbol{v}}{dt} = -\boldsymbol{v}\frac{\partial \rho}{\partial t} - \boldsymbol{\nabla} \cdot \rho \boldsymbol{v}\boldsymbol{v} - \boldsymbol{\nabla} \cdot \boldsymbol{P} + \rho \boldsymbol{v} \cdot (\boldsymbol{\nabla v}) \tag{A.22}$$

The mass continuity equation, equation A.8 is substituted into the first term on the right hand side of equation A.22, to give

$$\rho \frac{d\boldsymbol{v}}{dt} = \boldsymbol{v}(\boldsymbol{\nabla} \cdot \rho \boldsymbol{v}) - \boldsymbol{\nabla} \cdot \rho \boldsymbol{v}\boldsymbol{v} - \boldsymbol{\nabla} \cdot \boldsymbol{P} + \rho \boldsymbol{v} \cdot (\boldsymbol{\nabla} \boldsymbol{v}) \tag{A.23}$$

The following vector identity:

$$\boldsymbol{\nabla} \cdot \rho \boldsymbol{v}\boldsymbol{v} = \boldsymbol{v}(\boldsymbol{\nabla} \cdot \rho \boldsymbol{v}) + \rho \boldsymbol{v} \cdot (\boldsymbol{\nabla} \boldsymbol{v}) \tag{A.24}$$

may be used to reduce equation A.23 to give:

$$\rho \frac{d\boldsymbol{v}}{dt} = -\boldsymbol{\nabla} \cdot \boldsymbol{P} \tag{A.25}$$

This is the Lagrangian (and simplest) form of the momentum continuity equation.

A.3 Conservation of Energy

The total energy density ρe, where e is the energy per unit mass, is comprised of two parts. The first is the kinetic energy associated with the motion of fluid elements, whilst the second is the thermodynamic internal energy per unit mass, u:

$$\rho e = \rho \frac{\boldsymbol{v}^2}{2} + \rho u \tag{A.26}$$

The main interest is to derive an equation for the conservation of internal energy, however, the total energy must first be derived. If E is the total energy within the volume V, then

$$\frac{dE}{dt} = -\int_V \frac{\partial \rho e}{\partial t} \, \partial \boldsymbol{r} \tag{A.27}$$

Three mechanisms exist which may modify the total energy of the volume: convection through the surface, diffusion across the surface, and the work done by stresses applied to the surface [104]. This is shown in equation A.28, where $\boldsymbol{J}_Q$ is the heat flux vector (the co-moving flux of heat energy).

$$\frac{dE}{dt} = -\int_S \left[\rho e \boldsymbol{v} + \boldsymbol{J}_Q\right] d\boldsymbol{S} - \int_S [\boldsymbol{P} ds]\, \boldsymbol{v} d\boldsymbol{S} \tag{A.28}$$

The divergence theorem is used to simplify equation A.28 to give:

$$\frac{dE}{dt} = -\int_V \nabla \cdot \left[\rho e \boldsymbol{v} + \boldsymbol{J}_Q - \boldsymbol{P}\boldsymbol{v}\right] d\boldsymbol{r} \tag{A.29}$$

Equations A.28 and A.29 are combined and the arbitrariness of volume is applied to give:

$$\frac{\partial \rho e}{\partial t} = -\nabla \cdot \left[\rho e \boldsymbol{v} + \boldsymbol{J}_Q - \boldsymbol{P}\boldsymbol{v}\right] \tag{A.30}$$

which is the energy conservation law in the fixed Eulerian frame of reference. To express the energy conservation law in a Lagrangian frame of reference, the left hand is first expanded using the chain rule:

$$\rho \frac{\partial e}{\partial t} + e \frac{\partial \rho}{\partial t} = -\nabla \cdot \left[\rho e \boldsymbol{v} + \boldsymbol{J}_Q - \boldsymbol{P}\boldsymbol{v}\right] \tag{A.31}$$

The specific energy per unit mass is inserted into the partial derivative relationship, equation A.9 as the arbitrary variable. The resulting equation is substituted in place of $e\frac{\partial \rho}{\partial t}$ in equation A.31, giving:

$$\rho \frac{\partial e}{\partial t} = \rho \boldsymbol{v} \cdot (\boldsymbol{\nabla} e) + e \boldsymbol{\nabla} \cdot \rho \boldsymbol{v} - \boldsymbol{\nabla} \cdot \left[\rho e \boldsymbol{v} + \boldsymbol{J}_Q - \boldsymbol{P}\boldsymbol{v}\right] \tag{A.32}$$

$$\rho \frac{\partial e}{\partial t} = \rho \boldsymbol{v} \cdot (\boldsymbol{\nabla} e) + e \boldsymbol{v} \cdot \boldsymbol{\nabla} \rho + \rho e \boldsymbol{\nabla} \cdot \boldsymbol{v} - \boldsymbol{\nabla} \cdot \left[\rho e \boldsymbol{v} + \boldsymbol{J}_Q - \boldsymbol{P}\boldsymbol{v}\right] \tag{A.33}$$

Equation A.33 is simplified using the vector identity:

$$\boldsymbol{\nabla} \cdot \rho e \boldsymbol{v} = \rho \boldsymbol{v} \cdot (\boldsymbol{\nabla} e) + e \boldsymbol{v} \cdot \boldsymbol{\nabla} \rho + \rho e \boldsymbol{\nabla} \cdot \boldsymbol{v} \tag{A.34}$$

This gives the energy continuity equation in the Lagrangian frame of reference:

$$\rho \frac{\partial e}{\partial t} = -\boldsymbol{\nabla} \cdot [\boldsymbol{J}_Q - \boldsymbol{P}\boldsymbol{v}] \tag{A.35}$$

Furthermore, from equation A.26 the rate of change in thermodynamic internal energy can be given by:

$$\rho \frac{dU}{dt} = \rho \frac{de}{dt} - \rho \frac{d}{dt}\left(\frac{\boldsymbol{v}^2}{2}\right) \tag{A.36}$$

The second term on the right hand side of equation A.36 may be expressed as

$$\rho \frac{d}{dt}\left(\frac{\boldsymbol{v}^2}{2}\right) = \rho \boldsymbol{v} \cdot \frac{d\boldsymbol{v}}{dt} \tag{A.37}$$

The momentum continuity equation, equation A.25, may be rearranged such that

$$\frac{d\boldsymbol{v}}{dt} = -\frac{\boldsymbol{\nabla} \cdot \boldsymbol{P}}{\rho} \tag{A.38}$$

Equation A.38 is substituted into equation A.37 to give

$$\rho \frac{d}{dt}\left(\frac{\boldsymbol{v}^2}{2}\right) = -\boldsymbol{v} \cdot (\boldsymbol{\nabla} \cdot \boldsymbol{P}) = -\boldsymbol{v} \cdot (\boldsymbol{\nabla} : \boldsymbol{P}) \tag{A.39}$$

Equations A.35 and A.39 are substituted into equation A.36 to give

$$\rho \frac{du}{dt} = -\boldsymbol{\nabla} \cdot \boldsymbol{J}_Q - \boldsymbol{\nabla} \cdot (\boldsymbol{P} \cdot \boldsymbol{v}) + \boldsymbol{v}(\boldsymbol{\nabla} : \boldsymbol{P}) \tag{A.40}$$

The last two terms on the right hand side of equation A.40 may be combined to give equation A.41, the internal energy continuity equation in the Lagrangian frame of reference, where the *T* superscript denotes the transpose of a tensor.

$$\rho \frac{du}{dt} = -\boldsymbol{\nabla} \cdot \boldsymbol{J}_Q - \boldsymbol{P}^T : \boldsymbol{\nabla}\boldsymbol{v} \tag{A.41}$$

A.4 Entropy Production

The total entropy S of a fluid within a given volume V can be expressed in terms of the entropy density ρs where s is the specific entropy of the fluid.

$$\frac{dS}{dt} = \int_V \frac{\partial \rho s}{\partial t} d\boldsymbol{r} \tag{A.42}$$

The total entropy can be modified by two phenomena. Firstly, the entropy may be produced within the volume, defined by the entropy source strength, ψ. Secondly, entopy may change by flow across the surface, as defined by the surface flux $\boldsymbol{J}_{ST}$.

$$\frac{dS}{dt} = \int_V \psi d\boldsymbol{r} - \int_S \boldsymbol{J}_{ST} d\boldsymbol{s} \tag{A.43}$$

Equations A.42 and A.43 are equated together to give:

$$\int_V \frac{\partial \rho s}{\partial t} d\boldsymbol{r} = \int_V \psi d\boldsymbol{r} - \int_S \boldsymbol{J}_{ST} d\boldsymbol{s} \tag{A.44}$$

The divergence theorem is used to convert the surface integral into a volume integral. As the volume is arbitrary, the volume integrals are equal to one another, therefore:

$$\frac{\partial \rho s}{\partial t} = \psi - \boldsymbol{\nabla} \cdot \boldsymbol{J}_{ST} \tag{A.45}$$

The surface flux comprises of diffusive fluxes J_S and convective fluxes $\rho s \boldsymbol{v}$. The net entropy production per unit time is therefore:

$$\frac{\partial \rho s}{\partial t} = \psi - \boldsymbol{\nabla} \cdot [\boldsymbol{J}_S + \rho s \boldsymbol{v}] \tag{A.46}$$

The left hand side of equation A.46 may be expanded using the streaming derivative relation (equation A.9) to give:

$$\rho \frac{ds}{dt} = \psi - \boldsymbol{\nabla} \cdot [\boldsymbol{J}_S + \rho s \boldsymbol{v}] - \boldsymbol{\nabla} \cdot [\rho \boldsymbol{v} s] = \psi - \boldsymbol{\nabla} \cdot \boldsymbol{J}_S \tag{A.47}$$

The first postulate of linear irreversible thermodynamics assumes that thermodynamic equilibrium will hold in a sufficiently small volume (but large enough to contain a considerable number of molecules). This is referred to the local equilibrium postulate [157]. We may therefore apply the Gibbs relation from *equilibrium* thermodynamics:

$$Tds = du + pdV \tag{A.48}$$

which in its localised form becomes:

$$T\frac{ds}{dt} = \frac{du}{dt} + p\frac{d}{dt}\rho^{-1} = \frac{du}{dt} + \frac{p}{\rho^2}\frac{d\rho}{dt} \tag{A.49}$$

where ρ^{-1} is the specific volume, $V/_M$. Inserting equation A.12 into A.49 to remove the density derivative gives:

$$T\frac{ds}{dt} = \frac{du}{dt} + \frac{p}{\rho}\boldsymbol{\nabla}\cdot\boldsymbol{v} \tag{A.50}$$

Dividing equation A.50 by T and multiplying by ρ gives:

$$\rho\frac{ds}{dt} = \frac{1}{T}\left[\rho\frac{du}{dt} + p\boldsymbol{\nabla}\cdot\boldsymbol{v}\right] \tag{A.51}$$

Equation A.41 is substituted into A.51 to remove $\rho\, du/_{dT}$, giving:

$$\rho\frac{ds}{dt} = \frac{-1}{T}\left[\boldsymbol{\nabla}\cdot\boldsymbol{J}_Q + \boldsymbol{P}^T\!:\boldsymbol{\nabla}\boldsymbol{v} - p\boldsymbol{\nabla}\cdot\boldsymbol{v}\right] \tag{A.52}$$

Equation A.52 may now be substituted back into equation A.47 to give:

$$\psi = \boldsymbol{\nabla}\cdot\boldsymbol{J}_S - \frac{1}{T}\left[\boldsymbol{\nabla}\cdot\boldsymbol{J}_Q + \boldsymbol{P}^T\!:\boldsymbol{\nabla}\boldsymbol{v} - p\boldsymbol{\nabla}\cdot\boldsymbol{v}\right] \tag{A.53}$$

The local equilibrium postulate allows the application of the second law of thermodynamics, $ds = dQ/T$, where dQ is an infinitesimal amount of heat. In its time

dependent form, this becomes $\boldsymbol{J}_s = \boldsymbol{J}_Q/T$. Taking the rate of change of the diffusive flux in this form gives:

$$\nabla \cdot \boldsymbol{J}_s = \boldsymbol{\nabla} \cdot \left(\frac{\boldsymbol{J}_Q}{T}\right) = \frac{\boldsymbol{\nabla} \cdot \boldsymbol{J}_Q}{T} - \frac{\boldsymbol{J}_Q \cdot \boldsymbol{\nabla} T}{T^2} \tag{A.54}$$

Substitute equation A.54 into equation A.53 to remove the diffusive flux now gives:

$$\psi = -\frac{\boldsymbol{J}_Q \cdot \boldsymbol{\nabla} T}{T^2} - \frac{1}{T}[\boldsymbol{P}^T : \boldsymbol{\nabla v} - p\boldsymbol{\nabla} \cdot \boldsymbol{v}] \tag{A.55}$$

The pressure tensor can be decomposed in terms of the hydrostatic pressure *p* and the second rank non-equilibrium pressure tensor, $\boldsymbol{\Pi}$ such that

$$\boldsymbol{P} = p\boldsymbol{I} + \boldsymbol{\Pi} \tag{A.56}$$

where $\boldsymbol{I}$ is the isotropic unit second rank tensor (the Kronecker delta tensor). Substituting A.55 into A.56 gives:

$$\psi = -\frac{\boldsymbol{J}_Q \cdot \boldsymbol{\nabla} T}{T^2} - \frac{1}{T}[\boldsymbol{\Pi}^T : \boldsymbol{\nabla v}] \tag{A.57}$$

Each of the fluxes in equation A.57 differ in tensoral character, and are uncoupled [33]. Equation A.57 clearly is of the form:

$$\psi = \sum_i J_i X_i \tag{A.58}$$

Where J_i is a thermodynamic flux and X_i a conjugate thermodynamic force. This is the second postulate of linear, irreversible thermodynamics [157].

Appendix B: Constitutive Laws for Fluids

Phenomenological equations provide relative relationships between the fluxes and forces originating within the entropy equation [157]. These relationships are empirically

determined, with common examples including Fourier's law of heat conductivity, Newton's law of viscosity, and Fick's law of diffusion.

B.1 Fourier's Law of Heat Conductivity

Fourier's law states that the rate of heat flow per unit area must be proportional to the difference in temperature, ΔT between two sources at different temperature. This empirical observation may be written as the following differential equation:

$$\boldsymbol{J}_Q = -k\nabla T \tag{B.1}$$

The relationship is linear in the driving field. The proportionality constant is the thermal conductivity *k*. The negative sign is added to ensure heat travels from a hot source to a cold sink [158].

B.2 Newton's Law of Viscosity

Newton's law of viscosity describes the velocity coupling between neighbouring sections of fluid. Consider two parallel plates distance *d* apart in the y direction of a fluid. One plate travels at constant velocity v_x in the *x* direction, maintained by constant force F_x, whilst the other plate remains stationary.

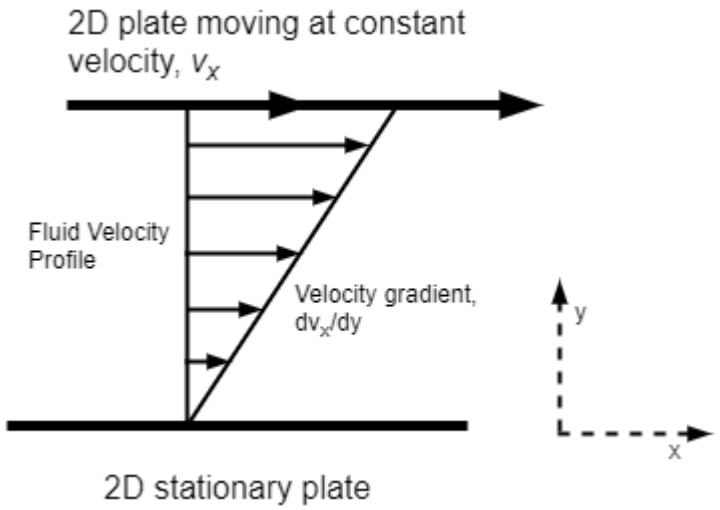

Figure B.1: The linear velocity profile between a plate moving a constant velocity v_x and a stationary plate.

Assuming both fluid plate boundaries are non-slip, the fluid medium directly adjacent both moving and stationary plates must have velocities *v* and zero respectively. The region between plates must therefore contain a gradient of velocity between v_x and zero.

It has been empirically determined that for many fluids the aforementioned velocity distribution is linear. These fluids are described as Newtonian. For such fluids velocity gradients may be conveniently described using a linear constant, referred to as fluid viscosity μ. The force applied along the x axis, perpendicular to the induced gradient of fluid in the y axis, is defined as the shear stress τ_{yx}. Shear stress is related to the velocity gradient and viscosity such that

$$\tau_{yx} = -\mu \frac{dv_x}{dy} \tag{B.2}$$

where the negative sign reflects momentum flowing from high to low velocity.

B.3 Fick's Law of Diffusion

Fick's laws of diffusion describes the rate at which mass transfers from a region of high concentration to a region of low concentration. The rate of mass transfer due to diffusion, also referred to as the diffusive flux $\boldsymbol{J}_s$, is a function of the rate of change in material concentration $\emptyset$. For a simple homogeneous fluid this relationship can be approximated as linear, such that:

$$\boldsymbol{J}_s = \zeta \nabla \emptyset \tag{B.3}$$

where ζ is the linear constant of diffusivity, or diffusion coefficient.

Appendix C: Navier-Stokes Equations in Polar and Cylindrical Polar Co-ordinates

Cylindrical Co-ordinates:

$$\rho\left(\frac{\partial v_r}{\partial t}+v_r\frac{\partial v_r}{\partial r}+\frac{v_\theta}{r}\frac{\partial v_r}{\partial \theta}+v_z\frac{\partial v_r}{\partial z}-\frac{v_\theta^2}{r}\right)$$
$$=-\frac{\partial p}{\partial r}+\mu\left[\frac{\partial}{\partial r}\left(\frac{1}{r}\frac{\partial}{\partial r}(rv_r)\right)+\frac{1}{r^2}\frac{\partial^2 v_r}{\partial \theta^2}+\frac{\partial^2 v_r}{\partial z^2}-\frac{2}{r^2}\frac{\partial v_\theta}{\partial \theta}\right]$$

$$\rho\left(\frac{\partial v_\theta}{\partial t}+v_r\frac{\partial v_\theta}{\partial r}+\frac{v_\theta}{r}\frac{\partial v_\theta}{\partial \theta}+v_z\frac{\partial v_\theta}{\partial z}+\frac{v_r v_\theta}{r}\right)$$
$$=-\frac{1}{r}\frac{\partial p}{\partial \theta}+\mu\left[\frac{\partial}{\partial r}\left(\frac{1}{r}\frac{\partial}{\partial r}(rv_\theta)\right)+\frac{1}{r^2}\frac{\partial^2 v_\theta}{\partial \theta^2}+\frac{\partial^2 v_\theta}{\partial z^2}-\frac{2}{r^2}\frac{\partial v_r}{\partial \theta}\right]$$

$$\rho\left(\frac{\partial v_z}{\partial t}+v_r\frac{\partial v_z}{\partial r}+\frac{v_\theta}{r}\frac{\partial v_z}{\partial \theta}+v_z\frac{\partial v_z}{\partial z}\right)=-\frac{\partial p}{\partial z}+\mu\left[\frac{1}{r}\frac{\partial}{\partial r}\left(r\frac{\partial v_z}{\partial r}\right)+\frac{1}{r^2}\frac{\partial^2 v_z}{\partial \theta^2}+\frac{\partial^2 v_z}{\partial z^2}\right]$$

Spherical Polar Co-ordinates:

$$\rho\left(\frac{\partial v_r}{\partial t}+v_r\frac{\partial v_r}{\partial r}+\frac{v_\theta}{r}\frac{\partial v_r}{\partial \theta}+\frac{v_\phi}{r\sin(\theta)}\frac{\partial v_r}{\partial \phi}-\frac{v_\theta^2+v_\phi^2}{r}\right)$$
$$=-\frac{\partial p}{\partial r}$$
$$+\mu\left[\frac{1}{r^2}\frac{\partial^2}{\partial r^2}(r^2v_r)+\frac{1}{r^2\sin(\theta)}\frac{\partial}{\partial \theta}\left(\sin(\theta)\frac{\partial v_r}{\partial \theta}\right)\frac{1}{r^2 sin^2(\theta)}\frac{\partial^2 v_r}{\partial \phi^2}\right]$$

$$\rho\left(\frac{\partial v_\theta}{\partial t}+v_r\frac{\partial v_\theta}{\partial r}+\frac{v_\theta}{r}\frac{\partial v_\theta}{\partial \theta}+\frac{v_\phi}{r\sin(\theta)}\frac{v_\theta}{\partial \phi}+\frac{v_\theta v_r-v_\phi^2 cot\,(\theta)}{r}\right)$$
$$=-\frac{1}{r}\frac{\partial p}{\partial \theta}$$
$$+\mu\left[\frac{1}{r^2}\frac{\partial}{\partial r}\left(r^2\frac{\partial v_\theta}{\partial r}\right)+\frac{1}{r^2}\frac{\partial}{\partial \theta}\left(\frac{1}{\sin(\theta)}\frac{\partial}{\partial \theta}(v_\theta\sin(\theta)\right)+\frac{1}{r^2 sin^2(\theta)}\frac{\partial^2 v_\theta}{\partial \phi^2}\right.$$
$$\left.+\frac{2}{r^2}\frac{\partial v_r}{\partial \theta}-\frac{2\cot(\theta)}{r^2\sin(\theta)}\frac{\partial v_\phi}{\partial \phi}\right]$$

$$\rho\left(\frac{\partial v_\phi}{\partial t}+v_r\frac{\partial v_\phi}{\partial r}+\frac{v_\theta}{r}\frac{\partial v_\phi}{\partial \theta}+\frac{v_\phi}{r\sin(\theta)}\frac{v_\phi}{\partial \phi}+\frac{v_\phi v_r-v_\phi v_\theta cot\,(\theta)}{r}\right)$$
$$=-\frac{1}{r\sin(\theta)}\frac{\partial p}{\partial \theta}$$
$$+\mu\left[\frac{1}{r^2}\frac{\partial}{\partial r}\left(r^2\frac{\partial v_\phi}{\partial r}\right)+\frac{1}{r^2}\frac{\partial}{\partial \theta}\left(\frac{1}{\sin(\theta)}\frac{\partial}{\partial \theta}(v_\phi\sin(\theta)\right)\right.$$
$$\left.+\frac{1}{r^2 sin^2(\theta)}\frac{\partial^2 v_\phi}{\partial \phi^2}+\frac{2}{r^2\sin(\theta)}\frac{\partial v_r}{\partial \theta}-\frac{2\cot(\theta)}{r^2\sin(\theta)}\frac{\partial v_\theta}{\partial \phi}\right]$$

Appendix D: Timing-gate Arduino Code:

```
//Six channel IR sensor detection and TimingLED
   //Assign Arduino pins


int ReadyLED = 14;       //Timer Ready LED
int Start = 15;          //Start Sensor
int TimingLED = 6;       //TimingLED indicator
int pass1 = 2;           //sensor 1
int pass2 = 3;           //sensor 2
int pass3 = 16;          //sensor 3
int pass4 = 7;           //sensor 4
int pass5 = 8;           //sensor 5
int pass6 = 17;          //sensor 6
int reset = 9;           //Reset button
int EndLED = 5;          //Last sensor passed indicator


//Declare Timing variables
unsigned long time1 = 0;          //sensor 1 Timing data
unsigned long time2 = 0;          //sensor 2 Timing data
unsigned long time3 = 0;          //sensor 3 Timing data
unsigned long time4 = 0;          //sensor 4 Timing data
unsigned long time5 = 0;          //sensor 5 Timing data
unsigned long time6 = 0;          //sensor 6 Timing data
unsigned long Starttime = 0;      //Start time (Sample detected)
int decimal1;                     //sensor 1 Timing integer
int decimal2;                     //sensor 2 Timing integer
```

```
int decimal3;                   //sensor 3 Timing integer
int decimal4;                   //sensor 4 Timing integer
int decimal5;                   //sensor 5 Timing integer
int decimal6;                   //sensor 6 Timing integer
    //Declare sensor variables
int StartSens = LOW;          //Start sensor status (active LOW)
int rst = HIGH;               //reset switch status
int detect1;                 //sensor 1 pass detected (active HIGH)
int detect2;                 //sensor 2 pass detected (active HIGH)
int detect3;                 //sensor 3 pass detected (active HIGH)
int detect4;                 //sensor 4 pass detected (active HIGH)
int detect5;                 //sensor 5 pass detected (active HIGH)
int detect6;                 //sensor 6 pass detected (active HIGH)
int Timing = 0;               //Timing control
int sensor1 = 0;              //initialise sensor 1
int sensor2 = 0;              //initialise sensor 2
int sensor3 = 0;              //initialise sensor 3
int sensor4 = 0;              //initialise sensor 4
int sensor5 = 0;              //initialise sensor 5
int sensor6 = 0;              //initialise sensor 6
int crst = 0;                //computer reset
int readdata = 0;             //force data send

void setup()
{
  pinMode(TimingLED, OUTPUT);       //assign pin status for Timing indicator LED
```

```
  pinMode(StartSens, INPUT);        //assign pin status for Start sensor
  pinMode(pass1, INPUT);            //assign pin status Sensor 1
  pinMode(pass2, INPUT);            //assign pin status Sensor 2
  pinMode(pass3, INPUT);            //assign pin status Sensor 3
  pinMode(pass4, INPUT);            //assign pin status Sensor 4
  pinMode(pass5, INPUT);            //assign pin status Sensor 5
  pinMode(pass6, INPUT);            //assign pin status Sensor 6
  pinMode(reset, INPUT);           //assign pin status Reset button
  pinMode(ReadyLED, OUTPUT);        //assign pin status Ready LED
  pinMode(EndLED, OUTPUT);         //assign pin status End LED


  digitalWrite(reset, HIGH);        //indicate ready to start
  Serial.begin(9600);
}

void loop()
{
  if (Serial.available() > 0 && Timing == 0) {
    crst = Serial.read();           //initial reset from software
  }

  rst = digitalRead(reset);         //read reset switch
  if (crst == 65 && Timing == 0 || rst == LOW && Timing == 0) {
    Serial.println("SAMPLE");
    digitalWrite(ReadyLED, HIGH);   //Ready LED lit
```

```
  Timing = 1;
  crst = 0;
  delay(100);
 }

 StartSens = digitalRead(Start);
 rst = digitalRead(reset);
  if (StartSens == HIGH && rst == HIGH && Timing == 1 && crst == 0) {    //timer
Started
  Starttime = millis();
  digitalWrite(TimingLED, HIGH);
  digitalWrite(ReadyLED, LOW);
  Timing = 2;
  delay(10);
 }

 detect1 = digitalRead(pass1);        //TimingLED on sensor 1
 if (detect1 == HIGH && Timing == 2 && sensor1 == 0) {
  time1 = millis() - Starttime;
  sensor1 = 1;
 }
 detect2 = digitalRead(pass2);       //TimingLED sensor 2
 if (detect2 == HIGH && Timing == 2 && sensor2 == 0) {
  time2 = millis() - Starttime;
  sensor2 = 1;
 }
```

```
 detect3 = digitalRead(pass3);        //TimingLED sensor 3
 if (detect3 == HIGH && Timing == 2 && sensor3 == 0) {
   time3 = millis() - Starttime;
   sensor3 = 1;
 }
 detect4 = digitalRead(pass4);        //TimingLED sensor 4
 if (detect4 == HIGH && Timing == 2 && sensor4 == 0) {
   time4 = millis() - Starttime;
   sensor4 = 1;
 }
 detect5 = digitalRead(pass5);         //TimingLED sensor 5
 if (detect5 == HIGH && Timing == 2 && sensor5 == 0) {
   time5 = millis() - Starttime;
   sensor5 = 1;
 }
detect6 = digitalRead(pass6);         //TimingLED sensor 6
 if (detect6 == HIGH && Timing == 2 && sensor6 == 0) {
  time6 = millis() - Starttime;
   sensor6 = 1;
 }
 if (Serial.available() > 0 && Timing == 2) {                // check for serial data received
   readdata = Serial.read();
 }
 if (readdata == 70 && sensor6 == 0 && Timing == 2) {  //ends Timing at sensor 6
 }
```

```
 if (sensor1 == 1 && sensor2 == 1 && sensor3 == 1 && sensor4 == 1 && sensor5 ==
1 && sensor6 == 1 && Timing == 2) {
   digitalWrite(EndLED, HIGH);
Serial.println("Sensor,  Time");
      //print sensor pass timings
Serial.println();
   Serial.print("  1 ,   ");     //sensor 1 time
   Serial.print( (int) (time1 / 1000L));
   Serial.print(".");
   decimal1 = (int)(time1 % 1000L);
   if (decimal1 == 0)
     Serial.print("000");
   else if (decimal1 < 10)
     Serial.print("00");
   else if (decimal1 < 100)
     Serial.print("0");
   Serial.println(decimal1);
  Serial.print("  2 ,   ");             //sensor 2 time (comma inserted for csv file)
   Serial.print( (int) (time2 / 1000L));
   Serial.print(".");
   decimal2 = (int)(time2 % 1000L);
   if (decimal2 == 0)
     Serial.print("000");
   else if (decimal2 < 10)
     Serial.print("00");
```

```
else if (decimal2 < 100)
  Serial.print("0");
Serial.println(decimal2);
    Serial.print("  3 ,   ");              //sensor 3 time
Serial.print( (int) (time3 / 1000L));
Serial.print(".");
decimal3 = (int)(time3 % 1000L);
if (decimal3 == 0)
  Serial.print("000");
else if (decimal3 < 10)
  Serial.print("00");
else if (decimal3 < 100)
  Serial.print("0");
Serial.println(decimal3);
    Serial.print("  4 ,   ");              //sensor 4 time
Serial.print( (int) (time4 / 1000L));
Serial.print(".");
decimal4 = (int)(time4 % 1000L);
if (decimal4 == 0)
  Serial.print("000");
else if (decimal4 < 10)
  Serial.print("00");
else if (decimal4 < 100)
  Serial.print("0");
Serial.println(decimal4);
    Serial.print("  5 ,   ");              //sensor 5 time
```

```
    Serial.print( (int) (time5 / 1000L));
    Serial.print(".");
    decimal5 = (int)(time5 % 1000L);
    if (decimal5 == 0)
      Serial.print("000");
    else if (decimal5 < 10)
      Serial.print("00");
    else if (decimal5 < 100)
      Serial.print("0");
    Serial.println(decimal5);
       Serial.print("  6 ,   ");              //sensor 6 time
    Serial.print( (int) (time6 / 1000L));
    Serial.print(".");
    decimal6 = (int)(time6 % 1000L);
    if (decimal6 == 0)
      Serial.print("000");
    else if (decimal6 < 10)
      Serial.print("00");
    else if (decimal6 < 100)
      Serial.print("0");
    Serial.println(decimal6);
    digitalWrite(TimingLED, LOW);       //Timing LED off
   Serial.println();
  Serial.println("END");               //End of run LED on
Serial.println();
    Timing = 3;
```

```
}
if (Serial.available() > 0 && Timing == 3) {                //computer timer reset
  crst = Serial.read();
}
rst = digitalRead(reset);                                   //manual timer reset

if (crst == 65 && Timing == 3 || rst == LOW && Timing == 3) {
  Starttime = 0;
  time1 = 0;
   time2 = 0;
    time3 = 0;
     time4 = 0;
      time5 = 0;
       time6 = 0;
  Timing = 4;
  sensor1 = 0;
   sensor2 = 0;
    sensor3 = 0;
     sensor4 = 0;
      sensor5 = 0;
       sensor6 = 0;
  digitalWrite(EndLED, LOW);
  digitalWrite(ReadyLED, HIGH);
  crst = 0;
  readdata = 0;
  Serial.flush();
```

```
  }


  if (crst == 0 && Timing == 4) {                    //serial ReadyLED status
    Serial.println("SAMPLE");
    Timing = 1;
}
}
```

Appendix E: Cylinder Results

Table E.1: Conventional cylinder results, including the 5 repeated deployments and averaged velocity.

			Repitition						
Diameter (cm)	**Length (cm)**	**Material**	**1 (m/s)**	**2 (m/s)**	**3 (m/s)**	**4 (m/s)**	**5 (m/s)**	**Average (m/s)**	**Error**
4.2	10	Aluminium	0.9797	0.9804	0.9763	0.9809	0.9752	0.9785	0.004
4.2	15	Aluminium	1.1688	1.1711	1.1675	1.1624	1.1708	1.1681	0.005
4.2	20	Aluminium	1.3490	1.3421	1.3429	1.3468	1.3451	1.3452	0.006
4.2	25	Aluminium	1.5064	1.4989	1.4968	1.5005	1.5005	1.5006	0.008
4.2	10	Steel	1.5673	1.5401	1.5992	1.5650	1.5322	1.5608	0.03
4.2	15	Steel	2.2113	2.2314	2.1869	2.1973	2.2019	2.2057	0.02
4.2	20	Steel	2.6569	2.6620	2.6401	2.6434	2.6401	2.6485	0.02
4.2	25	Steel	2.8534	2.8951	2.8456	2.9031	2.8771	2.8749	0.03
5.2	5	Aluminium	0.2291	0.2297	0.2224	0.2318	0.2279	0.2282	0.004
5.2	10	Aluminium	0.4869	0.4848	0.5219	0.4897	0.4852	0.4937	0.02
5.2	15	Aluminium	0.6269	0.6049	0.6136	0.6207	0.6270	0.6186	0.009
5.2	20	Aluminium	0.7029	0.6921	0.6972	0.6998	0.6921	0.6968	0.005
5.2	25	Aluminium	0.7630	0.7633	0.7682	0.7676	0.7684	0.7661	0.003
5.2	5	Steel	0.4862	0.4775	0.4762	0.4945	0.4872	0.4843	0.008
5.2	10	Steel	0.9374	0.9604	0.9387	0.9814	0.9385	0.9513	0.02
5.2	15	Steel	1.2640	1.2507	1.2507	1.2598	1.2336	1.2517	0.01
5.2	20	Steel	1.4189	1.4209	1.4175	1.4170	1.4204	1.4189	0.007
5.2	25	Steel	1.5545	1.5499	1.5551	1.5527	1.5418	1.5508	0.008
5.7	5	Aluminium	0.1330	0.1359	0.1275	0.1328	0.1329	0.1324	0.003
5.7	10	Aluminium	0.2596	0.2587	0.2606	0.2631	0.2594	0.2603	0.002
5.7	15	Aluminium	0.3167	0.3205	0.3134	0.3181	0.3138	0.3165	0.003
5.7	20	Aluminium	0.3562	0.3555	0.3587	0.3535	0.3541	0.3556	0.002
5.7	25	Aluminium	0.3846	0.3862	0.3848	0.3834	0.3853	0.3849	0.001
5.7	5	Steel	0.3222	0.3080	0.3256	0.3252	0.3191	0.3200	0.007
5.7	10	Steel	0.4253	0.4230	0.4296	0.4248	0.4250	0.4256	0.002
5.7	15	Steel	0.6141	0.5798	0.6319	0.5820	0.5865	0.5989	0.02
5.7	20	Steel	0.7549	0.7514	0.7277	0.7379	0.7249	0.7394	0.01
5.7	25	Steel	0.7976	0.8263	0.8148	0.8047	0.8026	0.8092	0.01
6.0	5	Aluminium	0.0609	0.0605	0.0605	0.0603	0.0606	0.0606	0.0002
6.0	10	Aluminium	0.1441	0.1429	0.1431	0.1431	0.1433	0.1433	0.0005
6.0	15	Aluminium	0.1687	0.1695	0.1684	0.1687	0.1693	0.1689	0.0005
6.0	20	Aluminium	0.1740	0.1727	0.1731	0.1726	0.1732	0.1731	0.001
6.0	25	Aluminium	0.1932	0.1917	0.1904	0.1912	0.1901	0.1913	0.001
6.0	5	Steel	0.1548	0.1559	0.1528	0.1532	0.1568	0.1547	0.0004
6.0	10	Steel	0.2418	0.2495	0.2704	0.2358	0.2539	0.2503	0.001
6.0	15	Steel	0.3274	0.3206	0.3290	0.3283	0.3277	0.3266	0.001
6.0	20	Steel	0.3595	0.3641	0.3648	0.3632	0.3604	0.3624	0.001
6.0	25	Steel	0.3900	0.3908	0.3892	0.3859	0.3921	0.3896	0.001

Table E.2: Centralised cylinder results, including the 5 repeated deployments and averaged velocity.

			Repitition						
Diameter (cm)	**Length (cm)**	**Material**	**1 (m/s)**	**2 (m/s)**	**3 (m/s)**	**4 (m/s)**	**5 (m/s)**	**Average (m/s)**	**Error**
4.2328	5	Aluminium	0.6505	0.6423	0.6466	0.6453	0.6486	0.6467	0.003
4.2328	10	Aluminium	0.8854	0.9053	0.8932	0.8982	0.9041	0.8972	0.008
4.2328	15	Aluminium	1.0601	1.0726	1.0655	1.0886	1.0606	1.0695	0.01
4.2328	20	Aluminium	1.1975	1.1971	1.2132	1.2037	1.2093	1.2041	0.007
4.2328	25	Aluminium	1.3246	1.2934	1.3544	1.3378	1.3526	1.3326	0.03
4.2328	5	Steel	1.2518	1.2567	1.2842	1.2866	1.2414	1.2641	0.02
4.2328	10	Steel	1.7781	1.8113	1.8208	1.8153	1.7826	1.8016	0.02
4.2328	15	Steel	2.1585	2.1574	2.1541	2.1892	2.1519	2.1622	0.01
4.2328	20	Steel	2.4564	2.4137	2.4506	2.4491	2.4578	2.4455	0.02
4.2328	25	Steel	2.7052	2.6860	2.6912	2.6603	2.6654	2.6816	0.02
5.207	5	Aluminium	0.3570	0.3537	0.3524	0.3559	0.3545	0.3547	0.002
5.207	10	Aluminium	0.4790	0.4831	0.4829	0.4810	0.4832	0.4818	0.002
5.207	15	Aluminium	0.5663	0.5664	0.5641	0.5664	0.5721	0.5671	0.003
5.207	20	Aluminium	0.6328	0.6319	0.6362	0.6306	0.6335	0.6330	0.002
5.207	25	Aluminium	0.7024	0.6885	0.6967	0.7077	0.7068	0.7004	0.008
5.207	5	Steel	0.6632	0.7055	0.7081	0.6972	0.6995	0.6947	0.02
5.207	10	Steel	0.9893	0.9919	0.9837	0.9844	0.9865	0.9872	0.004
5.207	15	Steel	1.1732	1.1722	1.1679	1.1640	1.1742	1.1703	0.005
5.207	20	Steel	1.3192	1.3327	1.3297	1.3314	1.3310	1.3288	0.006
5.207	25	Steel	1.4475	1.4425	1.4380	1.4485	1.4455	1.4444	0.007
5.737	5	Aluminium	0.1767	0.1754	0.1663	0.1772	0.1796	0.1750	0.005
5.737	10	Aluminium	0.2427	0.2421	0.2412	0.2431	0.2406	0.2419	0.001
5.737	15	Aluminium	0.2827	0.2817	0.2800	0.2819	0.2804	0.2814	0.001
5.737	20	Aluminium	0.3134	0.3116	0.3113	0.3129	0.3098	0.3118	0.001
5.737	25	Aluminium	0.3317	0.3334	0.3354	0.3335	0.3307	0.3330	0.002
5.737	5	Steel	0.3696	0.3730	0.3591	0.3779	0.3677	0.3695	0.007
5.737	10	Steel	0.5270	0.5251	0.5273	0.5255	0.5265	0.5263	0.002
5.737	15	Steel	0.6304	0.6287	0.6288	0.6283	0.6290	0.6291	0.002
5.737	20	Steel	0.7012	0.7037	0.7013	0.6964	0.6953	0.6996	0.004
5.737	25	Steel	0.7813	0.7932	0.7837	0.7832	0.7869	0.7857	0.005

Appendix F: Detailed Derivation of the Pressure Gradient

Begin by inserting 4.20 into 4.7:

$$Q = \frac{-U\pi R^2}{2\ln(\kappa)}[(1-\kappa^2) + 2\kappa^2\ln(\kappa)] - \frac{R^4\pi(1-\kappa^2)}{8\mu}\frac{dP}{dZ}\left[(1+\kappa^2) + \frac{(1-\kappa^2)}{\ln(\kappa)}\right] \quad \text{(F.1)}$$

Which simplifies to:

$$Q = U\pi R^2\left[\kappa^2 - \frac{(1-\kappa^2)}{2\ln(\kappa)}\right] - \frac{R^4\pi(1-\kappa^2)}{8\mu}\frac{dP}{dZ}\left[(1+\kappa^2) + \frac{(1-\kappa^2)}{\ln(\kappa)}\right] \quad \text{(F.2)}$$

Now equate F.2 = 4.21:

$$\pi R^2\kappa^2 U = U\pi R^2\left[\kappa^2 - \frac{(1-\kappa^2)}{2\ln(\kappa)}\right] - \frac{R^4\pi(1-\kappa^2)}{8\mu}\frac{dP}{dZ}\left[(1+\kappa^2) + \frac{(1-\kappa^2)}{\ln(\kappa)}\right] \quad \text{(F.3)}$$

Cancelling π and subtracting the 1st RHS component:

$$R^2\kappa^2 U - UR^2\left[\kappa^2 - \frac{(1-\kappa^2)}{2\ln(\kappa)}\right] = -\frac{R^4(1-\kappa^2)}{8\mu}\frac{dP}{dZ}\left[(1+\kappa^2) + \frac{(1-\kappa^2)}{\ln(\kappa)}\right] \quad \text{(F.4)}$$

Combining the LHS terms:

$$R^2\kappa^2 U\left[1 - 1 - \frac{(1-\kappa^2)}{2\kappa^2\ln(\kappa)}\right] = -\frac{R^4(1-\kappa^2)}{8\mu}\frac{dP}{dZ}\left[(1+\kappa^2) + \frac{(1-\kappa^2)}{\ln(\kappa)}\right] \quad \text{(F.5)}$$

This simplifies to:

$$\frac{R^2U(1-\kappa^2)}{2\ln(\kappa)} = -\frac{R^4(1-\kappa^2)}{8\mu}\frac{dP}{dZ}\left[(1+\kappa^2) + \frac{(1-\kappa^2)}{\ln(\kappa)}\right] \quad \text{(F.6)}$$

1-κ^2 now cancels to give:

$$\frac{R^2U}{2\ln(\kappa)} = -\frac{R^4}{8\mu}\frac{dP}{dZ}\left[(1+\kappa^2) + \frac{(1-\kappa^2)}{\ln(\kappa)}\right] \tag{F.7}$$

Multiplying by $2\ln(\kappa) / \kappa^2$ gives:

$$U = -\frac{R^2}{4\mu}\frac{dP}{dZ}[(1+\kappa^2)\ln(\kappa) + (1-\kappa^2)] \tag{F.8}$$

Finally, making *dP / dz* the subject gives:

$$\frac{dP}{dZ} = \frac{R^2}{4\mu}\left[\frac{-U}{(1+\kappa^2)\ln(\kappa) + (1-\kappa^2)}\right] \tag{F.9}$$